# Transport Processes through Superconducting Junctions at the Atomic Scale

Implementation of a High-Frequency Circuit into a Scanning Tunneling Microscope


Dissertation

zur

Erlangung des akademischen Grades
eines Doktors der Naturwissenschaften
(Dr. rer. nat.)

Eingereicht im Fachbereich Physik
der Freien Universität Berlin

von **Jan Olof Peters**

Berlin, 2020

Diese Arbeit entstand in der Arbeitsgruppe und mit der Betreuung von
Frau Prof. Dr. Katharina J. Franke am Fachbereich Physik der Freien Universität Berlin.

Berlin, 26. Oktober 2020

Erstgutachterin: Frau Prof. Dr. Katharina J. Franke
Zweitgutachter: Herr Prof. Dr. Robert Bittl

Datum der Disputation: 10. Dezember 2020

*"Nobody ever figures out what life is all about, and it doesn't matter. Explore the world. Nearly everything is really interesting if you go into it deeply enough."*
Richard Feynman (1918-1988)

# Abstract

Tunneling across superconducting junctions is associated with a variety of different processes that transfer single electrons, Cooper pairs, or even larger amounts of electrons by multiple Andreev reflections. Resonances inside the superconducting energy gap, like e.g. induced by magnetic adatoms, add resonant Andreev reflections to the variety of tunneling processes. We have successfully established two spectroscopic methods to study the nature of tunneling processes in superconductors. In the first approach, we complement the capabilities of a scanning tunneling microscope by introducing high-frequencies (HF) up to 40 GHz into the tunnel junction. The charge carriers involved in the tunneling process can exchange energy with the radiated HF field which leads to photon-assisted tunneling. Based on the theory of Tien und Gordon it is predicted that the sideband spacing in the bias voltage is a direct fingerprint of the number of electrons transferred in a single tunneling event.

Here we have used photon-assisted tunneling to study superconducting tunnel junctions that exhibit Yu-Shiba-Rusinov states (YSR) induced by magnetic Mn adatoms on Pb(111). By exploiting the tunability of the junction conductivity we could specifically obtain insights into the contributions of single-electron tunneling and resonant Andreev processes to the YSR states. While the simple Tien-Gordon description is sufficient to describe single-electron tunneling and Cooper pair tunneling into the pure substrate, we show that the description breaks down for resonant Andreev reflections. We developed an improved theoretical model based on rate equations and the *ac* modulation of the bias voltage. Our model is in excellent agreement with our data.

In a second spectroscopic approach, we investigate Cooper pair tunneling in current-biased Josephson junctions. We show that the critical current is strongly reduced by magnetic impurities, which reflects a reduced superconducting order parameter in the vicinity of the magnetic adatom.

Our results of photon-assisted tunneling and Josephson spectroscopy show that we have established two powerful methods for the investigation of superconducting tunneling processes at the atomic scale. These methods could be particularly informative for the investigation of unconventional and topological superconductors.

# Kurzfassung

Das Tunneln von Elektronen in supraleitenden Kontakten ist mit einer Vielzahl verschiedener Prozesse verbunden, bei denen einzelne Elektronen, Cooper-Paare oder auch eine größere Anzahl von Elektronen in Form von multiplen Andreev-Reflexionen übertragen werden können. Resonanzen innerhalb der supraleitenden Energielücke, z.B. induziert durch magnetische Adatome, fügen der Vielfalt der Tunnelprozesse darüber hinaus resonante Andreev-Reflexionen hinzu. Wir stellen in dieser Arbeit zwei spektroskopische Methoden vor, die wir erfolgreich zur Untersuchung dieser Prozesse etabliert haben. Zum einen ergänzen wir die vielfältigen Möglichkeiten der Rastertunnelmikroskopie, indem wir Hochfrequenzen (HF) in den Tunnelkontakt einstrahlen. Dies ermöglicht den am Tunnelvorgang beteiligten Ladungsträgern mit dem HF-Feld Energie auszutauschen, was wiederum zu photonen-assistiertem Tunneln führt. Ausgehend von der Tien-Gordon Theorie ist zu erwarten, dass die Seitenbandabstände der Spannung einen direkten Rückschluss auf die Anzahl der im einzelnen Tunnelereignis übertragenen Elektronen zulassen.

Wir nutzen das photonen-assistierte Tunneln, um supraleitende Tunnelkontakte zu untersuchen, die durch magnetische Mn-Adatome auf Pb(111) induzierte Yu-Shiba-Rusinov-Zustände (YSR) aufweisen. Aufgrund der über mehrere Größenordnungen variabel einstellbaren Leitfähigkeit des Kontaktes können wir Einblicke in die Beiträge des Ein-Elektron-Tunnelns und der resonanten Andreev-Prozesse durch die YSR Zustände gewinnen. Während die fundamentale Tien-Gordon-Beschreibung zur Erklärung des Einzelelekronen- und Cooper-Paar-Tunnels in das reine Substrat ausreicht, zeigen wir, dass diese Beschreibung für resonante Andreev-Reflexionen fehlschlägt. Auf Basis von Ratengleichungen in Kombination mit *ac*-Spannungsmodulationen ist es uns gelungen eine neue theoretische Beschreibung zu finden, die hervorragend mit unseren Daten übereinstimmt.

Als eine weitere neue spektroskopische Methode haben wir zur Untersuchung des Cooper-Paar-Tunnelns stromgetriebene Josephson-Kontakte etabliert. Wir zeigen, dass der kritische Strom durch den Einfluss magnetischer Verunreinigungen stark reduziert wird, was auf einen Verringerung des supraleitenden Ordnungsparameters in der Nähe des magnetischen Adatoms zurückgeführt werden kann.

Unsere Ergebnisse des photonen-assistierten Tunnelns und der Josephson-Spektroskopie zeigen, dass wir zwei vielseitige Methoden zur Untersuchung supraleitender Tunnelprozesse auf atomarer Ebene etabliert haben. Diese Methoden könnten besonders aufschlussreich für die Untersuchung neuartiger und topologischer Supraleiter sein.

# Contents


**1 Motivation** 1

**2 Theoretical Background** 5
2.1 The Tunneling Effect . . . . . 5
2.1.1 The Transfer Hamiltonian Formalism . . . . . 7
2.2 Theoretical Concepts for Describing Weakly Interacting Systems - Green's Functions, Self Energy and Perturbation Theory . . . . . 9
2.2.1 Short Introduction to Green's Functions at the Example of Single Electrons . . . . . 9
2.2.2 Green's Function in Weakly Interacting Systems – Feynman Diagrams and Self Energy . . . . . 11
2.2.3 Fermi's Golden Rule and its Generalization . . . . . 15
2.3 Fundamental Introduction in Superconductivity . . . . . 15
2.3.1 Microscopic Theory of Superconductivity: BCS theory . . . . . 16
2.3.2 Green's Functions of the Superconducting State . . . . . 21
2.3.3 BCS Quasiparticle Density of States . . . . . 22
2.4 Josephson Effect . . . . . 23
2.5 Andreev Reflection . . . . . 28
2.6 Magnetic Impurities on Superconductors – Local Pair Breaking Potential 30
2.6.1 Yu-Shiba-Rusinov States . . . . . 30
2.6.2 Self Energies due to Relaxation Processes and Tunneling Processes. 33

**3 Methods** 35
3.1 Scanning Tunneling Microscopy . . . . . 35
3.1.1 Theory of Scanning Tunneling Microscopy . . . . . 38
3.2 Scanning Tunneling Spectroscopy . . . . . 40
3.2.1 Theory of Scanning Tunneling Spectroscopy . . . . . 41
3.2.2 Spectroscopy with a Lock-In Amplifier . . . . . 41
3.2.3 Energy Resolution . . . . . 44

**4 Installation and Experimental Realization of an HF-STM** 49
4.1 Chamber, STM Head and Measurement Electronics . . . . . 49
4.1.1 Magnetic Field Issues . . . . . 55

4.2 Introducing High Frequencies into the STM Junction . . . . . 57
4.3 Characterization of HF circuit . . . . . 63
4.4 Josephson Setup . . . . . 65

**5 Superconducting Lead and its Interaction with Manganese Adatoms** 67
5.1 Corrections Applied to the BCS Density of States . . . . . 69
5.1.1 Finite Lifetime Effects on the Density of States . . . . . 69
5.1.2 Phonon Structure in Strong Electron-Phonon Coupled Superconductors . . . . . 70
5.1.3 Two-Band Superconductors . . . . . 70
5.2 Mn Adatoms on Pb(111) . . . . . 71
5.2.1 Distance Dependent Measurement: From Single-Electron Tunneling to Andreev Tunneling . . . . . 72
5.2.2 Description of the Tunnel Process by Means of Rate Equations . 75
5.2.3 Expressions for the Current of Single-Electron and Resonant Andreev Tunneling . . . . . 76

**6 Theoretical Framework for Describing Photon-Assisted Tunneling** 79
6.1 General Formalism of Photon-Assisted Tunneling . . . . . 79
6.2 Photon-Assisted Tunneling into Pristine Superconductors . . . . . 82
6.2.1 Coherence Peaks . . . . . 83
6.2.2 Andreev Reflections . . . . . 84
6.2.3 Josephson Effect . . . . . 85
6.3 Extending the Theory of Photon-Assisted Tunneling in Superconductors by a Magnetic Impurity . . . . . 86
6.4 Discussion of the Tien-Gordon-Like Patterns . . . . . 92

**7 Influence of HF Radiation on Pristine Superconducting Tunnel Junctions** 95
7.1 Photon-Assisted Tunneling Through Coherence Peaks . . . . . 95
7.2 Photon-Assisted Josephson Effect . . . . . 98
7.3 Photon-Assisted Andreev Reflections . . . . . 99
7.4 Generalized Tien-Gordon Theory . . . . . 101
7.5 Influence of the Two-Band Characteristic of Pb . . . . . 104

**8 Photon-Assisted Tunneling through YSR States under the Influence of HF Radiation** 107
8.1 Differences Between Single-Electron and Resonant Andreev Tunneling in the Presence of HF Radiation . . . . . 107
8.1.1 Single-Electron Tunneling . . . . . 109
8.1.2 Resonant Andreev Reflections . . . . . 110
8.2 Simulating the Photon-Assisted Current Through the YSR States . . . . . 115
8.2.1 Simulation Parameters . . . . . 116

8.3 Advanced Data Analysis Supported by the Rate-Based Simulation . . . . 119
8.3.1 Advanced Simulations for a Better Understanding of the Double Structure in the Y-Shape . . . . . 119
8.3.2 Investigating the YSR Wave Functions Asymmetry . . . . . 121
8.4 Summary and Conclusion . . . . . 123

**9 Implementation of Josephson Spectroscopy to Investigate the Superconducting Order Parameter** 125
9.1 Josephson-Spectroscopy in Pristine Pb/Pb Junctions . . . . . 126
9.2 Influence of Magnetic Impurities on the Critical Josephson Current . . . 129
9.3 Conclusion . . . . . 131

**10 Conclusions and Outlook** 133

**A Appendix** 139
A.1 Determination of the Distances in the Internal Structure of the HF Induced Splittings . . . . . 139

**References** 141

**Acknowledgement** 157

**Curriculum Vitae** 159

**Selbständigkeitserklärung** 161

# List of Figures


Figure 2.1 The tunnel effect. . . . . 6
Figure 2.2 First order Feynman diagrams. . . . . 12
Figure 2.3 Graphical representation of Green's function in terms of the self-energy. 13
Figure 2.4 Proper self-energy and Dyson's equation. . . . . 14
Figure 2.5 Schematic illustration of the formation of a copper pair by electron-phonon coupling. . . . . 17
Figure 2.6 Formation of the superconducting gap. . . . . 20
Figure 2.7 Resistively and capacitively shunted junction (RCSJ) model. . . . . 24
Figure 2.8 Current-voltage characteristics of Josephson junctions. . . . . 26
Figure 2.9 Voltage-biased Josephson spectrum. . . . . 27
Figure 2.10 Andreev reflections and Andreev-bound states. . . . . 29
Figure 2.11 Formation of Yu-Shiba-Rusinov states. . . . . 31

Figure 3.1 Principle of a scanning tunneling microscope. . . . . 37
Figure 3.2 Model of Tersoff and Harmann. . . . . 39
Figure 3.3 Working principle of a lock-in amplifier for measuring the differential conductance. . . . . 42
Figure 3.4 Energy resolution of a scanning tunneling microscope. . . . . 45
Figure 3.5 $\mathrm{d}I/\mathrm{d}V$ spectroscopy on pristine Pb – normal versus superconducting tip. 47

Figure 4.1 Experimental setup – UHV chamber. . . . . 51
Figure 4.2 Experimental setup – STM head. . . . . 52
Figure 4.3 Detailed circuit diagram of the setup showing the wiring of all different experiments performed. . . . . 54
Figure 4.4 Sketch of the HF cabling from the signal generator down to the scanning tunneling microscope (STM) junction. . . . . 60
Figure 4.5 Installation of the new HF cables. . . . . 62
Figure 4.6 Transmission characteristics of the high-frequency (HF) circuit. . . . . 64
Figure 4.7 Equivalent circuit diagram for the Josephson setup. . . . . 66

Figure 5.1 Exemplary lead surface with vapour-deposited Mn adatoms. . . . . 68
Figure 5.2 The two-band characteristic of Pb. . . . . 71

Figure 5.3 Differential conductance spectra recorded at two different tip-substrate distances above the center of single Mn atoms on Pb(111). . . . . 72
Figure 5.4 Sketches of the tunnel processes across the YSR states. . . . . 73
Figure 5.5 Crossover of the YSR peak heights when increasing the conductance. . 74

Figure 6.1 Energy-level shift due to externally applied HF radiation. . . . . 80
Figure 6.2 Discussion of the Tien-Gordon like sideband structure occurring during photon-assisted tunneling. . . . . 93

Figure 7.1 Splitting of the BCS coherence peaks in an HF field and comparison with accompanying simulation based on the spectrum not exposed to HF. 97
Figure 7.2 Josephson peak splitting in an HF field and comparison with simulation involving Cooper pair tunneling. . . . . 98
Figure 7.3 Simulating the Josephson peak splitting with single electrons. . . . . 99
Figure 7.4 Splitting of the multiple Andreev reflection (MAR) peaks under HF radiation and comparison with the simulation. . . . . 100
Figure 7.5 Photon-assisted tunneling process leading to the first sideband of the first Andreev reflection. . . . . 102
Figure 7.6 Cuts of PAT of the Coherence, MAR and Josephson peaks. . . . . 103
Figure 7.7 Photon-assisted splitting of the coherence peaks on Pb(111). . . . . 104
Figure 7.8 Comparison of photon-assisted tunneling for the Coherence peaks and the Josephson effect on Pb(111). . . . . 105

Figure 8.1 Photon-assisted tunneling into the YSR state under HF irradiation. . . 108
Figure 8.2 Portfolio of photon-assisted resonant Andreev tunneling processes illustrating various thresholds. . . . . 112
Figure 8.3 Individual spectra of the HF splitting of the YSR states at small and large junction conductance together with the corresponding simulations of photon-assisted tunneling. . . . . 118
Figure 8.4 Study of the origin of the double structure by comparing the electron and hole threshold. . . . . 120
Figure 8.5 Investigation of the influence of the YSR-state wave functions ratio and YSR-state energy to frequency ratio on the photon-assisted splitting. . 122

Figure 9.1 Determination of the critical Josephson current on pristine Pb. . . . . 127
Figure 9.2 YSR states of $Mn_{down}$ adatom on Pb(111). . . . . 130
Figure 9.3 Mapping of the Josephson switching current of the $Mn_{down}$ adatoms. . 131

Figure 10.1 Comparison between Josephson, thermal, and charging energy. . . . . 137

Figure A.1 Illustration of the determination of photon-sideband periodicities and their error margins. . . . . 140

# List of Abbreviations

| | |
|---|---|
| $\|v\rangle$ | Dirac ket notation for a quantum state $v$ |
| $\langle v\|$ | Dirac bra notation for a quantum state $v$ |
| $\|0\rangle$ | vacuum state |
| $\|F\rangle$ | Fermi state |
| $A(\mathbf{k}\sigma, \omega)$ | spectral function |
| $ac$ | alternating current |
| $b_{\mathbf{k}}^{\dagger}$, $b_{\mathbf{k}}$ | bosonic creation and annihilation operators |
| $\beta_{\mathrm{c}}$ | Stewart-McCumber parameter |
| $\beta$ | $(k_{\mathrm{B}}T)^{-1}$ – thermodynamic temperature |
| BCS | Bardeen-Cooper-Schrieffer |
| $c_{\mathbf{k}}^{\dagger}$, $c_{\mathbf{k}}$ | fermionic creation and annihilation operators |
| $C_{\mathbf{k}}^{\dagger}$, $C_{\mathbf{k}}$ | spinor creation and annihilation operators |
| $dc$ | direct current |
| $\Delta$ | superconducting gap parameter |
| $\delta(x)$ | Dirac delta function |
| DoS | density of states |
| $E_{\mathrm{F}}$ | Fermi energy |
| $E_{\mathrm{C}}$ | capacitive energy |
| $E_{\mathrm{J}}$ | Josephson coupling energy |
| $E_{\mathrm{J0}}$ | Josephson energy |
| $E_{\mathrm{T}}$ | thermal energy |
| $e$ | elementary charge |
| $\epsilon_0$ | YSR state energy |
| ESR | electron spin resonance |
| $f$ | frequency |
| FWHM | full width at half maximum |
| $\Gamma$ | imaginary part of self-energy |
| $\Gamma_{\mathrm{L}\to\mathrm{R}}$ | transition rate from eigenstate $\|R\rangle$ to $\|L\rangle$ – Fermi's golden rule |
| $\Gamma_1$ | thermal relaxation rate from YSR state into quasiparticle continuum |

| | |
|---|---|
| $\Gamma_2$ | thermal excitation rate into the YSR state |
| $\Gamma_\mathrm{e}$ | electron tunneling rate |
| $\Gamma_\mathrm{h}$ | hole tunneling rate |
| $\gamma_\mathbf{k}^\dagger$, $\gamma_\mathbf{k}$ | quasiparticle creation and annihilation operators |
| $G$ | causal Green's function |
| $G^\mathrm{r}$, $G^\mathrm{a}$ | retarded and advanced Green's function |
| $G^<$, $G^>$ | greater and lesser Green's function |
| $G_0$ | bare Green's function |
| $G_0$ | $2e^2/h = (12.91\,\mathrm{k\Omega})^{-1} = 77.48\,\mu\mathrm{S}$ – conductance quantum |
| $\mathcal{G}$ | imaginary-time Green's function (Matsubara) |
| $\tilde{\mathcal{H}}$ | grand canonical Hamiltonian |
| $\mathcal{H}$ | transformed Hamiltonian |
| $\mathcal{H}_0$ | unperturbed part of an Hamiltonian |
| $\mathcal{H}'$ | perturbative part of an Hamiltonian |
| $\mathcal{H}_\mathrm{T}$ | tunneling Hamiltonian |
| $H_\mathrm{c}$ | critical magnetic field |
| $h$ | Planck's constant |
| $\hbar$ | reduced Planck's constant |
| h.c. | hermitian conjugate |
| He | Helium |
| HF | high-frequency |
| $I$ | current |
| $I_\mathrm{a}$ | Andreev current |
| $I_\mathrm{c}$ | Josephson critical current |
| $I_\mathrm{R}$ | retrapping current |
| $I_\mathrm{S}$ | switching current |
| $I_\mathrm{s}$ | single particle current |
| $I_\mathrm{sc}$ | Josephson supercurrent |
| i | imaginary number |
| $\mathrm{i}0^+$ | infinitesimal positive imaginary part |
| IETS | inelastic tunneling spectroscopy |
| $\mathcal{J}_n$ | n-th Bessel function |
| JJ | Josephson junction |
| $\kappa$ | decay constant of wave function |
| $\mathbf{k}$ | general momentum or wave vector |
| $\mathbf{k}_\parallel$ | component of the wave vector parallel to the surface |
| $\mathbf{k}_\perp$ | component of the wave vector perpendicular to the surface |
| $k_\mathrm{B}$ | Boltzmann's constant |

| | |
|---|---|
| $k_\mathrm{F}$ | Fermi wave vector |
| $\Lambda$ | real part of self-energy |
| LDoS | local density of states |
| $N_\mathbf{k}$ | fermionic number operator |
| $n_\mathbf{k}$ | phonon number operator |
| MAR | multiple Andreev reflection |
| $m_\mathrm{e}$ | electron mass |
| Mn | manganese |
| $\mu$ | chemical potential |
| MZM | Majorana zero modes |
| NDC | negative differential conductance |
| Ne | Neon |
| $n_\mathrm{F}(E)$ | Fermi-Dirac distribution function |
| $\omega$ | angular frequency |
| $\Omega$ | HF (angular) frequency |
| Pb | lead (from the Latin *plumbum*) |
| $\Phi$ | work function |
| $\varphi$ | complex phase of superconducting order parameter |
| $R_\mathrm{N}$ | normal state resistance |
| $\mathbf{r}$ | general space variable |
| $\rho$ | density of states |
| $\rho_\mathrm{n}$ | normal conducting density of states |
| $\rho_0$ | normal conducting density of states at chemical potential |
| $\rho_\mathrm{s}$ | superconducting density of states |
| RCSJ | resistively and capacitively shunted junction |
| RMS | root mean square |
| $\Sigma^*$ | self-energy |
| $\Sigma$ | proper self-energy |
| $\Sigma^\mathrm{r}, \Sigma^\mathrm{a}$ | retarded and advanced self-energy |
| $\sigma$ | general spin index |
| STM | scanning tunneling microscope |
| STS | scanning tunneling spectroscopy |
| $\mathbf{T}$ | T-matrix |
| $\hat{T}$ | hopping matrix |
| $T$ | temperature |
| $T_\mathrm{c}$ | critical temperature |
| $T_{\mathbf{k},\mathbf{k}'}$ | tunneling matrix element |
| $\mathcal{T}$ | time-ordering operator |

| | |
|---|---|
| $\theta(x)$ | Heaviside's step function |
| $u_\epsilon$ | electron component of YSR wave function |
| $u_{\mathbf{k}}$ | BCS coherence factor |
| UHV | ultra high vacuum |
| $V_{\text{Bias}}$ | bias voltage |
| $V_{\text{HF}}$ | amplitude of the HF radiation |
| $V_{\text{Lock-In}}$ | RMS modulation amplitude of lock-in |
| $v_\epsilon$ | hole component of YSR wave function |
| $v_{\mathbf{k}}$ | BCS coherence factor |
| $\mathcal{V}$ | normalization volume |
| WKB | Wentzel-Kramers-Brillouin |
| $\xi_{\mathbf{k},\alpha}$ | $\epsilon_{\mathbf{k}} - \mu_\alpha$ – dispersion relation |
| $\xi_{\text{GL}}$ | Ginzburg-Landau coherence length |
| $\Psi(\mathbf{r}, t)$ | wave function in real space |
| $\tilde{\Psi}(\mathbf{k}, t)$ | wave function in Fourier space |
| YSR | Yu-Shiba-Rusinov |

# 1

# Motivation

One of the major contemporary research fields deals with quantum computing. It is based on the idea of creating devices that process information by making use of the superposition and entanglement of quantum states [1, 2]. Such computers are assumed to be superior to classical computers in terms of computational power for certain applications [3–5]. Among these applications that quantum computers could potentially solve in polynomial time is the factorization of large numbers [6, 7], which is highly relevant for our current encryption algorithms [8], together with optimization algorithms such as the improvement of search algorithms [9–11], as well as quantum simulations [12], which could be of great importance in the future for the simulation of the behavior of atoms and particles. In quantum computers, the information is stored in quantum bits (qubits). In the simplest case, this can be a two-level quantum mechanical system, like the spin of an electron, which can take the values up and down. These can be interpreted as "0" and "1", similar to classical computer technology. However, since these are quantum states, the qubit represents a superposition $|\uparrow\rangle + |\downarrow\rangle$ of both eigenvalues. Operations are done by connecting several qubits in so-called quantum gates and calculations by combining several of these gates. The result of a calculation is obtained from a "simple" measurement of the system. It is only this measurement that makes the system collapse into one of its eigenstates. Under laboratory conditions, a realization of quantum computers with currently up to 50 to 72 qubits has already succeeded [13, 14]. Despite rapid progress, scientists still face many unsolved problems such as error correction and the development of quantum computers is only in its infancy [15], as can be seen from the still large number of potentially promising implementation for qubits, which includes an entire zoo of technologies, like Josephson circuits [16, 17], trapped ions [18], quantum dots [19], Bose-Einstein condensates [20], and Majorana zero modes [21] to name only a few.

An inherent problem of all approaches realized so far is quantum decoherence, i.e. the loss of the defined phase between the states [22]. It turns out that this decoherence is one of the biggest challenges for the construction and upscaling of usable quantum computers.

Different approaches exist to address or avoid this problem. On the one hand, it is possible to reduce the decoherence with software-based quantum error corrections [23]. On the other hand, the approaches on the hardware side try to decouple the systems from any external influences of their environment in the best possible way [24]. A further approach concentrates on generating error-resistant qubits, which are protected by their topology and therefore promise longer coherence times [25, 26]. The concepts for such topological quantum computers are based on the use of exotic quasi-particles in topological materials, most prominent Majorana zero modes in topological superconductors [27].

The recent systems in which Majorana fermions have been detected [28], as well as many of the (potential) systems for quantum computing, are based on superconductivity [29]. Here, the superconducting gap is of great importance, as it contributes to the decoupling and thus to the protection of the states within the energy gap. Several different states can arise in this energy gap. For example, Yu-Shiba-Rusinov (YSR) states [30–34], which are of great interest because they are the building blocks for Majorana zero modes [35] and as quantum spin states themselves potential candidates for qubits. YSR states are formed in the interaction between a magnetic impurity and a superconductor, as the impurity binds a spin-polarized electron within the gap of the superconductor. Studying them opens up a large field of interesting physics at the boundary between the two incompatible effects of magnetism and superconductivity. In addition to the YSR states, several other subgap states such as Andreev bound states, but also the already mentioned Josephson peaks and Majorana zero modes occur in superconductors. Investigations on all of these provide a local probe for the various interactions that affect superconductivity, making their exploration relevant for quantum computing applications.

A lot of information about subgap states can be gained in tunnel experiments. The differential conductance reveals information as the bound-state energy [34, 36], gives access to the inelastic relaxation rates underlying the quasiparticle poisoning [37, 38], and the BCS order parameter by Josephson spectroscopy [39]. Accessing them by scanning probe methods additionally enables spatial resolution, like mapping the electron- and hole components of the bound state wave functions [40, 41] or mapping variations in the superconducting order parameter [39]. We would like to extend the possibilities of studying subgap states by introducing two further spectroscopic methods. First, we combine tunnel experiments with high-frequency (HF) radiation for investigations based on photon-assisted tunneling. Second, we advance Josephson spectroscopy by using current-biased Josephson junctions. For the realization of these experiments, we have developed a new machine, based on scanning tunneling microscopy (STM) and scanning tunneling spectroscopy (STS). The former gives us access to spatially resolved information on conductive surfaces down to the atomic level and the latter uses this atomic resolution to perform spatially-resolved conductance measurements. The spatial resolution is of great importance as it allows us to address individual spins on surfaces.

The combination with HF radiation enables us to gain a better understanding of the underlying tunneling processes using photon-assisted tunneling. The first observations of this effect have been made in superconducting junctions [42, 43], as well as in semiconductor

junctions [44]. Although we are also explicitly interested in superconductors, it is important to note that the precise materials used in the tunnel contacts are irrelevant. Photon-assisted tunneling is an effect that is directly and exclusively sensitive to the tunneling processes involved. Thus, in contrast to normal tunnel spectroscopy, it makes the effective charge transported in the tunnel event directly measurable. This is done by evaluating the sideband splitting that occurs in the resulting characteristic patterns when the HF amplitude is varied in addition to the bias voltage. Since single-electron tunneling in superconductors always requires the necessary energy to excite quasiparticle into the superconducting drain and source, the transport at low energies is dominated by multi-electron processes. These include Cooper pair tunneling near zero-bias [45–47], and multi-electron processes in the form of (multiple) Andreev reflections at higher subgap energies [48–51]. Photon-assisted tunneling now offers us the possibility to distinguish between these processes, even if they occur at the same energies. The implementation, characterization, and application of this technique form the core of this thesis. A quantitative understanding of these processes is provided by the model of Tien and Gordon, which applies the HF radiation to the junction as a further *ac* voltage [52]. We extend this model to subgap states and apply it to pristine superconductor-superconductor junctions, as well as to manganese-induced YSR states on Pb(111).

In order to realize current-biased Josephson spectroscopy, we have converted our voltage source to an effective current source. This is done by connecting a resistor of significantly higher resistance of 1 MΩ in series with the junction resistance. Additionally, this measurement requires a very sensitive and low capacitive voltage amplifier, which measures the voltage drop of the junction in a four-point configuration. This allows us, compared to voltage-biased Josephson spectroscopy, to directly quantify the retrapping and switching currents characterizing the Josephson junction. Since these currents are proportional to the critical Josephson current, we can use the STM to detect changes in this current and thus draw conclusions about the intrinsic order of the superconducting ground state. This was not possible with single-electron experiments, as they are only able to measure the excited quasi-particle states. Likewise, we can use Josephson spectroscopy to study the local effects of magnetic impurities on superconductors, which we have successfully demonstrated by initial measurements on the magnetic Mn atoms on Pb(111)

Looking forward, both of our established spectroscopy techniques have other promising future applications. Shapiro steps, occurring in Josephson junction under the influence of high-frequency radiation, can be used for the detection of Majorana fermions. For these, the characteristic voltage in the *ac* Josephson effect should double. Furthermore, photon-assisted tunneling can be used to distinguish Majorana fermions from very low energy YSR states by different sideband splittings upon high-frequency variation. In another application, the irradiated radio frequencies could be used for ESR-STM. This would enable direct measurements of coherence times, explicitly the transverse relaxation time ($T_2$). Besides, it also allows the direct excitation and control of single spins with a much higher energy resolution compared to normal STM.

This work is organized as follows: Chapter 2 provides a general overview of the theoretical concepts underlying this work. This is followed in Chapter 3 by an introduction into the fundamentals of scanning tunneling microscope (STM) and scanning tunneling spectroscopy (STS) as our experimental measurement methods. Chapter 4 is the purely technical description of the machine we put into operation. It also describes all modifications made for the introduction of high-frequency (HF) radiation in the STM junction and characterizes the HF circuit. Chapter 5 represents the transition to our results by introducing lead (Pb) as a substrate and tip material and discussing the tunneling processes through the YSR states caused by Mn adatoms on Pb. Next, we will present our results obtained using phonon-assisted tunneling. We briefly introduce the model of Tien and Gordon used to describe photon-assisted tunneling and then extend this model for subgap states in Chapter 6. In Chapter 7 we investigate the effects of HF radiation on coherence peaks, the Josephson effect, and Andreev reflections in pristine superconductor junctions. We demonstrate the validity of the simple Tien-Gordon model for these subgap states. Afterward, we investigate the influence of the HF radiation on resonant Andreev reflections in Chapter 8. Here, we use our extended theoretical model to describe the current through the YSR states on Pb(111). In Chapter 9 follows a change of topic to current-biased Josephson spectroscopy, which we first introduce and then use to measure the change in the superconducting order parameter induced by the Mn adatoms. The work ends in Chapter 10 with a summary of our results and an outlook on further applications of the spectroscopic methods we introduced.

# 2

# Theoretical Background

This chapter provides an overview of the basic theoretical concepts used in this thesis. We start with the tunneling effect, which is the underlying principle of the scanning tunneling microscope. In this context the formalism of the transfer Hamiltonian is introduced, on which our theoretical descriptions of photon-assisted tunneling in Chapter 6 are based. To describe the dynamics within a physical system and its interactions with its environment, an introduction to Green's functions and the associated self energies follows. Besides the transfer Hamiltonian formalism, this is the second time we make use of perturbation theory. Since we are mainly interested in superconducting materials, a brief overview of their theory follows. This includes the microscopic BCS theory in the description of the mean-field approximation, as well as a short section on the equivalent description of superconductivity using Green's functions. Afterward, the Josephson effect and the Andreev reflections are introduced as possibilities to transport superconducting currents through a tunneling junction. Finally, the theoretical part closes with a description of YSR states, which are results of the interaction of magnetic impurities with superconductors – our central point of research.

## 2.1 The Tunneling Effect

The tunneling effect is a prime example of a quantum mechanical effect and one of the most impressive examples of the differences between classical and quantum mechanics. It describes the possibility that particles can pass through a potential barrier. Unlike in classical physics, this becomes possible, even if the particle does not have the necessary energy to overcome the barrier. We refer to this as *tunneling through* the barrier – an analogy to a tunnel within a mountain, which also allows a passage without climbing the summit. In total five Nobel Prizes in Physics were awarded for research related to tunneling: Either for tunneling in semi- or superconductors or the invention of scanning tunneling microscopy.

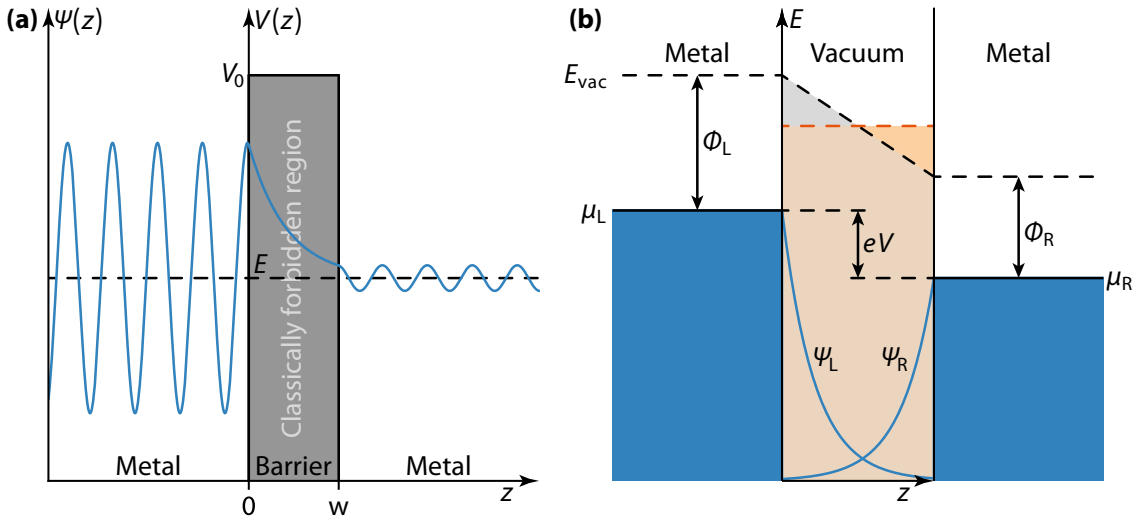


**Figure 2.1 | The tunnel effect. (a)** The wave function $\Psi(z)$ of an electron, described as an exemplary sinusoidal wave function coming from left, tunnels through a barrier of height $V_0$. It may pass through the barrier with a finite probability even though it is classically forbidden. **(b)** Energy diagram of a tunnel contact consisting of two metal electrodes separated by vacuum. The *blue* areas represent the filled electron states, with their chemical potentials $\mu$ shifted by the applied voltage $V$. The overlap of the wave functions $\Psi$ allows tunneling of electrons, resulting in a current flow across the vacuum. In *orange* the square barrier of the WKB approximation is shown, with a height of $E = \mu_R + (eV + \Phi_L + \Phi_R)/2$, where $\Phi$ denotes the work functions.

The latter (described in Section 3.1), as well as the Josephson effect (described in Section 2.4), are fundamental to this thesis.

On the microscopic level, the state of an elementary particle or a system is described by its wave function $\Psi(\mathbf{r}, t)$ in real space or $\tilde{\Psi}(\mathbf{k}, t)$ in Fourier space respectively. The wave functions absolute square $|\Psi|^2$ describes the probability density to measure the particle at the location $\mathbf{r}$ or with a momentum $\mathbf{p} = \hbar\mathbf{k}$, where $\mathbf{k}$ is the wave vector. Fig. 2.1(a) illustrates that the wave function of a particle with energy $E < V_0$ is not reflected completely, but penetrates into the barrier, provided the barrier has a finite width $w$ and a finite height $V_0$. In the barrier, the amplitude of the wave function decreases exponentially $\Psi(z) \propto \exp(-\kappa z)$, with the decay constant $\kappa = \sqrt{2m_e(V_0 - E)/\hbar^2}$. Accordingly, the particle is found on the other side of the barrier with a finite, but a much smaller probability. Note that the energy of the particle does not change during this process. In classical physics, this process is forbidden and the particle must have an energy $E > V_0$ to reach the other side of the barrier.

For us, the tunnel barrier usually is a simple vacuum gap between two electrical contacts. The wave function $\Psi$ of these metal electrodes will decay at the interface within a few nanometers. Thus, if the two electrodes are brought into close enough proximity, the wave functions overlap, as shown in Fig. 2.1(b), and the tunneling of electrons becomes possible. A *tunnel contact* is formed. By applying a voltage $eV = \mu_L - \mu_R$ to the tunnel contact, the

electrode's chemical potentials $\mu_{L,R}$ are shifted with respect to each other. As electrons tunnel from occupied states of one electrode into unoccupied states of the second electrode a net current $I$ is measured. This current provides a measure for the quantum mechanical tunneling effect and forms the basis of scanning tunneling microscopy. Besides the applied voltage, the distance $z$ between the two electrodes and their work function $\Phi_L$ and $\Phi_R$ also determine the shape of the tunnel barrier.

### 2.1.1 The Transfer Hamiltonian Formalism

For a complete description of the tunnel contact, a single Hamiltonian including both electrodes as well as all interactions between them would be needed. Attempting to find such a Hamiltonian is much too complicated for practical purposes. In addition, there is no analytical solution, even though it would naturally include the value of the tunnel current. In fact, the most common approach addressing the tunnel problem for many-particle systems is the *transfer Hamiltonian formalism* [53–55]. The fundamental assumption of this theory is that tunneling between electrodes can be described by time-dependent perturbation theory. The transfer Hamiltonian for two electrodes separated by the barrier reads

$$\tilde{\mathcal{H}} = \tilde{\mathcal{H}}_0 + \tilde{\mathcal{H}}' = \tilde{\mathcal{H}}_L + \tilde{\mathcal{H}}_R + \tilde{\mathcal{H}}_T \qquad \text{with} \qquad \tilde{\mathcal{H}}_0 = \tilde{\mathcal{H}}_L + \tilde{\mathcal{H}}_R \quad \text{and} \quad \tilde{\mathcal{H}}' = \tilde{\mathcal{H}}_T\,. \tag{2.1}$$

Each electrode forms an almost independent subsystem $\tilde{\mathcal{H}}_\alpha$, $\alpha \in \{L, R\}$. The interaction between these two subsystems is described as a weak residual perturbation $\tilde{\mathcal{H}}' = \tilde{\mathcal{H}}_T$. It couples the ground state to an excited state, whereby a single electron is transferred between the two electrodes. The grand canonical Hamiltonian for the uncoupled left and right electrode is

$$\tilde{\mathcal{H}}_\alpha = \sum_{\mathbf{k}\sigma} \epsilon_{\mathbf{k}} c^\dagger_{\alpha,\mathbf{k}\sigma} c_{\alpha,\mathbf{k}\sigma} = \mu_\alpha N_\alpha + \sum_{\mathbf{k}\sigma} \xi_{\mathbf{k},\alpha} c^\dagger_{\alpha,\mathbf{k}\sigma} c_{\alpha,\mathbf{k}\sigma} = \mu_\alpha N_\alpha + \mathcal{H}_\alpha\,, \tag{2.2}$$

where $c^\dagger_{\alpha,\mathbf{k}\sigma}$ and $c_{\alpha,\mathbf{k}\sigma}$ are the creation and annihilation operators for an electron with momentum $\mathbf{k}$ and spin $\sigma$. $N_\alpha = c^\dagger_{\alpha,\mathbf{k}\sigma} c_{\alpha,\mathbf{k}\sigma}$ is the corresponding number operator. Here, the normal state dispersion relation $\xi_{\mathbf{k},\alpha} = \epsilon_{\mathbf{k}} - \mu_\alpha$ sets a single particle eigenenergy $\epsilon_{\mathbf{k}}$ in relation to the chemical potential $\mu_\alpha$ of the respective electrode. The second quantization representation of the time independent tunneling Hamiltonian is

$$\tilde{\mathcal{H}}_T = \mathcal{H}_T = \sum_{\mathbf{k}\mathbf{k}'\sigma} \left[ T_{\mathbf{k}\mathbf{k}'} c^\dagger_{R,\mathbf{k}'\sigma} c_{L,\mathbf{k}\sigma} + \text{h.c.} \right], \tag{2.3}$$

where $T_{\mathbf{k}\mathbf{k}'}$ is the tunneling matrix element describing the probability amplitude of transferring an electron across the barrier. Bardeen showed, that the tunneling matrix element results from the overlap of the wave functions, integrated over any surface $\mathbf{S}$ that lies com-

pletely within the barrier [53]

$$T_{\mathbf{k}\mathbf{k}'} = -\frac{\hbar^2}{2m_\mathrm{e}} \int \mathrm{d}\mathbf{S} \cdot \left(\psi_\mathrm{L}^*(\mathbf{k}) \nabla \psi_\mathrm{R}(\mathbf{k}') - \psi_\mathrm{R}(\mathbf{k}') \nabla \psi_\mathrm{L}^*(\mathbf{k})\right) . \tag{2.4}$$

All distance dependence of the tunneling process caused by the separation $z$ between the electrodes is described by this matrix element. The integral can be solved within the semi-classical approximation of Wentzel, Kramers and Brillouin (WKB) [56–58]. This approximation simplifies the tunnel barrier to a rectangular energy barrier with an average height $\bar{\Phi} + eV/2$ (see Fig. 2.1). $\bar{\Phi} = (\Phi_\mathrm{L} + \Phi_\mathrm{R})/2$ corresponds to the average work function and we assume without loss of generality that the right electrode is grounded $\mu_\mathrm{R} = 0$. With this simplification, the expression of the matrix element can be transformed into the following form for the tunnel probability [59, 60]

$$|T_{\mathbf{k}\mathbf{k}'}|^2 \propto e^{-2\kappa z}, \quad \text{with} \quad \kappa = \sqrt{\frac{2m_\mathrm{e}}{\hbar^2}\left(\bar{\Phi} + \frac{eV}{2} - \xi_{\mathbf{k}'}\right)}. \tag{2.5}$$

The tunneling probability decays exponentially as a function of $z$. Moreover it shows that tunneling will be strongest for states near the chemical potential.

The tunnel current $I = -e\left\langle \dot{N}_\mathrm{L} \right\rangle$ corresponds to the change in the number of electrons in one of the two electrodes. The Heisenberg equation of motion $\dot{N}_\mathrm{L} = \mathrm{i}/\hbar \left[\tilde{\mathcal{H}}, N_\mathrm{L}\right] = \mathrm{i}/\hbar \left[\tilde{\mathcal{H}}_\mathrm{T}, N_\mathrm{L}\right]$, gives the time derivative of the number operator, as $N_\mathrm{L}$ commutes with $\tilde{\mathcal{H}}_0$. Therefore the current reads [61]

$$I(V) = \frac{e}{\hbar} \int_{-\infty}^{\infty} \frac{\mathrm{d}\omega}{2\pi} \sum_{\mathbf{k}\mathbf{k}',\sigma} |T_{\mathbf{k}\mathbf{k}'}|^2 A_\mathrm{L}(\mathbf{k}\sigma, \omega) A_\mathrm{R}(\mathbf{k}\sigma, \omega + eV) \left[n_\mathrm{F}(\hbar\omega) - n_\mathrm{F}(\hbar\omega + eV)\right] . \tag{2.6}$$

This expression contains the spectral density function $A(\mathbf{k}\sigma, \omega)$, being the probability density of a state existing at momentum $\mathbf{k}$ and energy $\hbar\omega$. It describes the tunneling electrons energy dissipation due to their coupling to the environment. In the idealized case of non-interacting free electrons the energy of a state is a proper function of its momentum only. Therefore, the spectral function $A_0(\mathbf{k}\sigma, \omega) = 2\pi\, \delta(\omega - \xi_{\mathbf{k}\sigma}/\hbar)$ becomes a Dirac delta function and the current simplifies to

$$I(V) = \frac{4\pi e}{\hbar} \sum_{\mathbf{k}\mathbf{k}'} |T_{\mathbf{k}\mathbf{k}'}|^2 \left[n_\mathrm{F}(\xi_\mathbf{k}) - n_\mathrm{F}(\xi_{\mathbf{k}'} + eV)\right] \delta(\xi_\mathbf{k} - \xi_{\mathbf{k}'} + eV) . \tag{2.7}$$

As we are dealing with electrons, both expressions for the current include the fermionic distribution function, commonly referred to as the Fermi-Dirac distribution function

$$n_\mathrm{F}(E) = \left[\mathrm{e}^{\beta E} + 1\right]^{-1} , \tag{2.8}$$

which provides the average thermal occupation number of the single-particle states $|\Psi\rangle$ at the inverse temperature $\beta = (k_B T)^{-1}$.

## 2.2 Theoretical Concepts for Describing Weakly Interacting Systems - Green's Functions, Self Energy and Perturbation Theory

Green's single-particle functions are an important tool for analyzing the temporal evolution of systems after a particle has been added or removed. Our tunnel experiments as well as those on magnetic impurities embedded in a metal host are prominent examples for the use of this method. Green's functions indicate the reaction that a physical system generates to a Dirac delta function type input. Figuratively speaking, one can imagine a drum and the sound produced by striking it with a drumstick. As a result of striking, waves propagate and a sound is generated. But when the drum is struck with another mallet such as a hammer or brush, it produces very different sounds. The idea of Green's functions is to use the reaction to the drumstick to represent the impact of the other mallets. So the drumstick is represented by the Green's function and the general sound the drum produces can be obtained as an integral combination of all possible stick situations. Mathematically speaking, Green's functions can be used to solve inhomogeneous linear differential equations by finding the solution for a single sharp impulse on the system. From this, the complete solution of the problem for more complicated impulse responses is generated.

### 2.2.1 Short Introduction to Green's Functions at the Example of Single Electrons

The *causal* time-ordered single-particle Green's function of an electron is [62]

$$G(\mathbf{k}\sigma, \tau, \tau') = -\mathrm{i}\left\langle \mathcal{T}\left[c_{\mathbf{k}\sigma}(\tau)c^{\dagger}_{\mathbf{k}\sigma}(\tau')\right]\right\rangle , \tag{2.9}$$

with the time-ordering operator $\mathcal{T}$ and $\langle O\rangle = Z_G^{-1}\,\mathrm{Tr}\left[\exp(-\beta\tilde{\mathcal{H}})O\right]$ being the grand canonical ensemble average of the operator $O$. The denominator $Z_G = \mathrm{Tr}\left[\exp(-\beta\tilde{\mathcal{H}})\right]$ is the grand canonical partition function.

In addition to the causal Green's function, two other Green's functions are of importance, since many physical quantities can be more easily extracted from them. These are the *retarded* and *advanced* Green's functions. Those are defined for times $\tau > \tau'$ which are far in the past prior to the considered moment in time $\tau'$, or for times $\tau < \tau'$ which are far in the

future, as follows [62]

$$G^{\mathrm{r}}(\mathbf{k}\sigma,\tau,\tau') = -\mathrm{i}\theta(\tau-\tau')\left\langle\left[c_{\mathbf{k}\sigma}(\tau)c^{\dagger}_{\mathbf{k}\sigma}(\tau')\right]\right\rangle \tag{2.10}$$

$$G^{\mathrm{a}}(\mathbf{k}\sigma,\tau,\tau') = \mathrm{i}\theta(\tau'-\tau)\left\langle\left[c_{\mathbf{k}\sigma}(\tau)c^{\dagger}_{\mathbf{k}\sigma}(\tau')\right]\right\rangle . \tag{2.11}$$

Here $\theta(x)$ denotes the Heaviside function[1], thus $G^{\mathrm{r}}$ is only nonzero for $\tau > \tau'$, so that we can calculate the reaction of the system after it has been perturbed. By determining one of the two functions, the other can be calculated directly, since these are adjoint $(G^{\mathrm{r}})^{\dagger} = G^{\mathrm{a}}$. These Green's functions carry information about the system's excitations, since their time evolution is determined by the Hamiltonian of the system. Additionally, two further functions are introduced, as they play an important role in transport, namely the *greater* and *lesser* Green's functions [62]

$$G^{<}(\mathbf{k}\sigma,\tau,\tau') = \mathrm{i}\left\langle\left[c^{\dagger}_{\mathbf{k}\sigma}(\tau')c_{\mathbf{k}\sigma}(\tau)\right]\right\rangle \quad \text{and} \quad G^{>}(\mathbf{k}\sigma,\tau,\tau') = -\mathrm{i}\left\langle\left[c_{\mathbf{k}\sigma}(\tau)c^{\dagger}_{\mathbf{k}\sigma}(\tau')\right]\right\rangle . \tag{2.12}$$

Here $G^{<}$ can be understood as the conditional probability amplitude for an electron generated at time $\tau'$ to be found at time $\tau$ with a momentum difference of $\mathbf{k}$. The previous Green's functions can be expressed as a combination of the greater and lesser $G^{\mathrm{r}}(\mathbf{k}\sigma,\tau,\tau') = \theta(\tau,\tau')(G^{>}(\mathbf{k}\sigma,\tau,\tau') - G^{<}(\mathbf{k}\sigma,\tau,\tau'))$. In general all these functions are related by $G^{\mathrm{r}} - G^{\mathrm{a}} = G^{>} - G^{<}$.

So far we have only considered the Green's functions in the time domain. Very often it is useful to represent them in the energy domain. For instance, when the system is in equilibrium or when the Hamiltonian is time-independent. In such cases, Green's functions depend only on the time difference of $\tau - \tau'$, and we can perform a Fourier transformation. Thus the retarded and advanced Green's functions in momentum-frequency representation become [62]

$$G^{\mathrm{r,a}}(\mathbf{k}\sigma,\omega) = \lim_{\eta\to 0^{+}} \int_{-\infty}^{\infty} \frac{\mathrm{d}\xi}{2\pi} \frac{A(\mathbf{k}\sigma,\xi/\hbar)}{\omega - \xi/\hbar \pm \mathrm{i}\eta} , \tag{2.13}$$

where $\mathrm{i}0^{+}$ is an infinitesimal positive imaginary part for $\eta$ converges to zero from above. The single-particle spectral density function $A(\mathbf{k}\sigma,\xi/\hbar)$ is essentially the imaginary part of $G^{\mathrm{r}}$ or related to $G^{<}$ by the Fermi function $(n_{\mathrm{F}})$ [61]

$$A(\mathbf{k}\sigma,\omega) = -\frac{1}{\pi}\,\mathrm{Im}\,G^{\mathrm{r}}(\mathbf{k}\sigma,\omega) \quad \text{or} \quad G^{<}(\mathbf{k}\sigma,\omega) = 2\pi\mathrm{i}n_{\mathrm{F}}(\omega)A(\mathbf{k}\sigma,\omega) . \tag{2.14}$$

[1]The Heaviside step function is defined as

$$\theta(x) = \begin{cases} 1, & x \geq 0 \\ 0, & x < 0 \end{cases} .$$

It is discontinuous at $x = 0$ and its derivative is the Dirac delta distribution $\delta(x)$.

We already know that in a non-interacting system this simplifies to $A_0(\mathbf{k}\sigma, \omega) = 2\pi\,\delta(\omega - \xi_{\mathbf{k}\sigma}/\hbar)$ so the retarded and advanced *bare* Green's functions read

$$G_0^{\mathrm{r,a}}(\mathbf{k}\sigma, \omega) = \frac{1}{\omega - \xi_{\mathbf{k}\sigma}/\hbar \pm \mathrm{i}0^+}\,, \tag{2.15}$$

with their interacting counterpart $G^{\mathrm{r,a}}$ being often referenced to as *dressed*.

As already mentioned, many physical properties can be extracted from Green's functions. Two are of great relevance for us: First, for the non-interacting Hamiltonian, the poles of the Green's functions correspond exactly to its eigenenergies $\tilde{\epsilon}_{\mathbf{k}\sigma}$, as $\xi_{\mathbf{k}\sigma}$ is related to the single-particle eigenenergy $\epsilon_{\mathbf{k}\sigma}$. Secondly, from the imaginary part of the retarded Green's functions we obtain the local density of states $\rho(E)$ of our system. The local density of states is essentially gained by adding all states $|k\rangle$ of the spectral function $A(\mathbf{k}\sigma, \omega)$ which have the same energy $E = \hbar\omega$:

$$\rho(E) = \frac{1}{\mathcal{V}}\sum_{\mathbf{k}\sigma} A(\mathbf{k}\sigma, E/\hbar) = -\frac{1}{\pi\mathcal{V}}\sum_{\mathbf{k}\sigma} \mathrm{Im}\, G^{\mathrm{r}}(\mathbf{k}\sigma, E/\hbar) = -\frac{1}{\pi\mathcal{V}}\sum_{\mathbf{k}\sigma} \mathrm{Im}\, \mathcal{G}(\mathbf{k}\sigma, E/\hbar + \mathrm{i}0^+)\,, \tag{2.16}$$

with $\mathcal{V}$ being the normalization volume.

### 2.2.2 Green's Function in Weakly Interacting Systems – Feynman Diagrams and Self Energy

In a real conductor, the electrons do not move completely free but are exposed to disturbances. These include the Coulomb interaction with the ion lattice (electron-phonon interactions) and the interaction with each other (electron-electron interactions). In order to understand the influence of these effects on tunnel spectra, we have to study the behavior of small perturbations on the spectral function. This allows us to explain why small energy shifts and finite lifetimes (and thus finite line widths) occur for measured excitations.

The calculation of physically interesting quantities, such as retarded Green's functions and associated spectral functions, is non-trivial in most interacting systems. Usually, this is only possible approximately, e.g. in terms of the many-body perturbation theory. It turns out that direct calculations of the retarded Green's functions are not practicable at finite temperatures. Therefore it is useful to introduce *imaginary-time* Green's functions, also referred to as *Matsubara* or *thermal* Green's functions [62]

$$\mathcal{G}(\mathbf{k}\sigma, \tau, \tau') = -\left\langle \mathcal{T}\left[c_{\mathbf{k}\sigma}(\tau)c^{\dagger}_{\mathbf{k}\sigma}(\tau')\right]\right\rangle\,. \tag{2.17}$$

With these it becomes possible to apply perturbation theory by a series expansion if the Green's function formalism. The imaginary-time Green's functions have a rather simple mathematical relation to the retarded and advanced Green's functions. The latter can be obtained by the simple replacement of the form $\omega \pm \mathrm{i}0^+ \to \mathrm{i}\omega_n$. So Eq. (2.15) can be extended

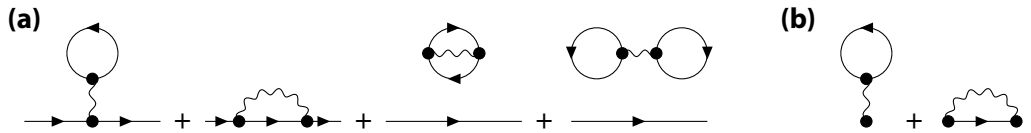

**Figure 2.2 | First order Feynman diagrams. (a)** All different $1^{\text{st}}$ order diagrams. Solid lines represent $\mathcal{G}_0(\mathbf{k}\sigma, \omega_n)$ and wavy lines the two-particle interaction. The first two are classified as *connected* diagrams and the last two as so-called *unconnected* diagrams, with the latter having no weight in the overall expansion. **(b)** The self-energy diagrams belonging to the connected diagrams: Hartree term on the left (classical mean-field) and Fock term on the right (exchange). In the style of [62].

into

$$\mathcal{G}_0(\mathbf{k}\sigma, \mathrm{i}\omega_n) = G_0^{\mathrm{r/a}}(\mathbf{k}\sigma, \omega \pm \mathrm{i}0^+ \to \mathrm{i}\omega_n) = \frac{1}{\mathrm{i}\omega_n - \xi_{\mathbf{k}\sigma}/\hbar}, \tag{2.18}$$

with $\omega_n$ being the Matsubara frequencies.

A very elegant and descriptive way to calculate the expansion of the Green's functions is in the notation of Feynman diagrams. R. P. Feynman used Feynman propagators in his formulation of quantum mechanics based on path integrals [63, 64]. The propagator's normalization is chosen so that they are identical to the Green's functions. Feynman found a graphical representation for his propagators, called *Feynman diagrams*. With these diagrams, he developed a technique to rigorously represent lengthy mathematical calculations in a pictorial and geometric form, using only lines and vertices.

Wick's theorem[2] can be used to calculate the imaginary-time Green's function between interacting electrons via an expansion of pairwise exchange diagrams and thus makes the drawing of Feynman diagrams meaningful. The $0^{\text{th}}$ order term corresponds to the bare imaginary-time Green's function $\mathcal{G}_0$ of Eq. (2.18). In Feynman's formalism, it is represented by a straight propagating line

$$\mathcal{G}_0(\mathbf{k}\sigma, \mathrm{i}\omega_n) \equiv \longrightarrow . \tag{2.19}$$

The 1st order terms are shown in Fig. 2.2(a). Here the connected diagrams theorem leads to the first simplification. This states that the complete Green's function is given by the sum over all connected diagrams with two external bare Green's functions as ends [62]. All unconnected diagrams cancel against the vacuum diagrams from the development of $Z_{\mathrm{G}}(\mathbf{k}\sigma, \omega_n)$ in the denominator of Eq. (2.17). Without the two external ends the diagrams are referred to as *self-energy diagrams*, as depicted in Fig. 2.2(b). Each connected diagram represents an algebraic value obtained by $\mathcal{G}_0(\mathbf{k}\sigma, \mathrm{i}\omega_n)B(\mathbf{k}\sigma, \mathrm{i}\omega_n)\mathcal{G}_0(\mathbf{k}\sigma, \mathrm{i}\omega_n)$, where $B(\mathbf{k}\sigma, \mathrm{i}\omega_n)$ is determined by the structure of the respective self-energy diagram. Hence the

---

[2] Wick's theorem allows to write the time-ordered many-particle Green's function as a sum of all possible pairwise products of the time-ordered single-particle Green's functions [61].

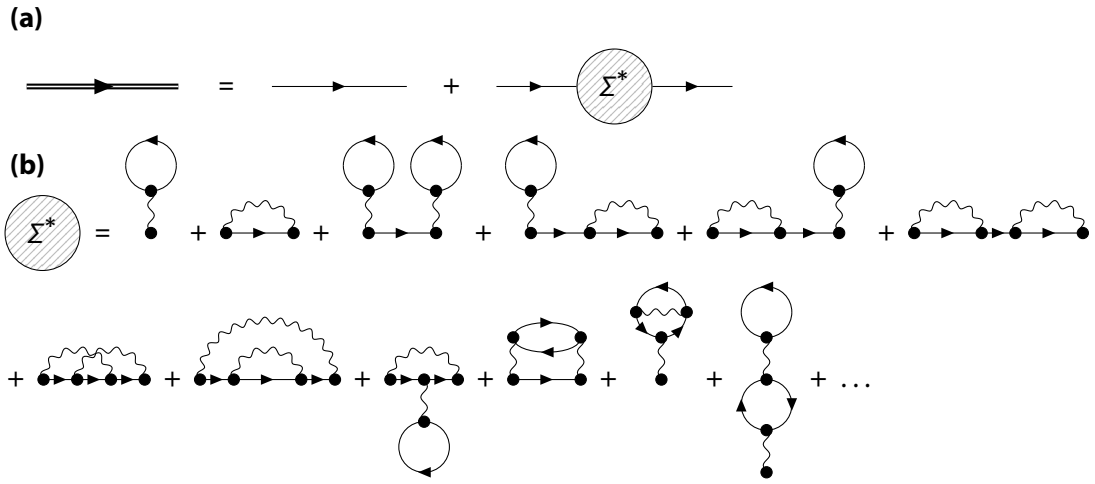


**Figure 2.3 | Graphical representation of Green's function in terms of the self-energy. (a)** The solid double-line represents $\mathcal{G}(\mathbf{k}\sigma, \mathrm{i}\omega_n)$ and the hashed circle the self-energy $\Sigma^*(\mathbf{k}\sigma, \mathrm{i}\omega_n)$. **(b)** Representation of the self-energy as infinite sum over all self-energy diagrams, here specified up to 2nd order. In the style of [62].

dressed Green's function can be written as [62]

$$\mathcal{G}(\mathbf{k}\sigma, \mathrm{i}\omega_n) = \mathcal{G}_0(\mathbf{k}\sigma, \mathrm{i}\omega_n) + \mathcal{G}_0(\mathbf{k}\sigma, \mathrm{i}\omega_n)\Sigma^*(\mathbf{k}\sigma, \mathrm{i}\omega_n)\mathcal{G}_0(\mathbf{k}\sigma, \mathrm{i}\omega_n)\,, \tag{2.20}$$

where $\Sigma^*(\mathbf{k}\sigma, \mathrm{i}\omega_n)$ is introduced as particle self-energy, which results from the sum over all $B(\mathbf{k}\sigma, \mathrm{i}\omega_n)$ from all connected, topographically different diagrams of all orders in the perturbation. Graphically, Eq. (2.20) is illustrated in Fig. 2.3, where the self-energy $\Sigma^*(\mathbf{k}\sigma, \mathrm{i}\omega_n)$ is written as infinite sum over all self-energy diagrams. Some of these diagrams can be split into two valid lower-order diagrams by cutting a single-particle line. Diagrams for which this is not possible are called *irreducible* diagrams, see Fig. 2.4(a). By adding up all these irreducible diagrams one gets the proper, or irreducible, self-energy $\Sigma(\mathbf{k}\sigma, \mathrm{i}\omega_n)$. It can be seen that this results in a further simplification (Fig. 2.4(b)) [62]

$$\Sigma^*(\mathbf{k}\sigma, \mathrm{i}\omega_n) = \Sigma(\mathbf{k}\sigma, \mathrm{i}\omega_n) + \Sigma(\mathbf{k}\sigma, \mathrm{i}\omega_n)\mathcal{G}_0(\mathbf{k}\sigma, \mathrm{i}\omega_n)\Sigma(\mathbf{k}\sigma, \mathrm{i}\omega_n) + \dots\,. \tag{2.21}$$

Accordingly, the Green's function may be written as (Fig. 2.4(c))

$$\mathcal{G}(\mathbf{k}\sigma, \mathrm{i}\omega_n) = \mathcal{G}_0(\mathbf{k}\sigma, \mathrm{i}\omega_n) + \mathcal{G}_0(\mathbf{k}\sigma, \mathrm{i}\omega_n)\Sigma(\mathbf{k}\sigma, \mathrm{i}\omega_n)\mathcal{G}(\mathbf{k}\sigma, \mathrm{i}\omega_n)\,, \tag{2.22}$$

which is known as Dyson's equation [65, 66]. In effect, this equation corresponds to a geometric series and thus an exact expression for the dressed Green's function can be given,

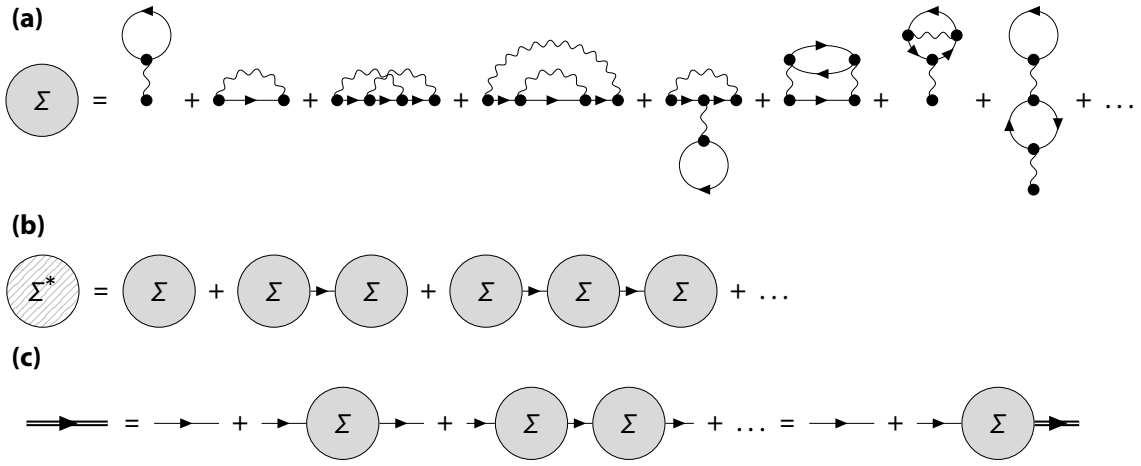


**Figure 2.4 | Proper self-energy and Dyson's equation. (a)** Proper self-energy $\Sigma(\mathbf{k}\sigma, \omega_n)$ represented by the shaded circle as composition of irreducible diagrams. **(b)** Expansion of the self-energy in terms of the proper self-energy. **(c)** Dyson's equation. In the style of [62].

in terms of the proper self-energy [62]

$$\mathcal{G}(\mathbf{k}\sigma, \mathrm{i}\omega_n) = \frac{1}{\mathrm{i}\omega_n - \xi_{\mathbf{k}\sigma}/\hbar - \Sigma(\mathbf{k}\sigma, \omega_n)}\,. \tag{2.23}$$

### Energy Shift and the Lifetime of Excitations

We now return to the retarded and advanced Green's functions, which can be obtained from their imaginary-time counterpart by a transformation $\mathrm{i}\omega_n \to \omega + \mathrm{i}0^+$, similar to Eq. (2.18)

$$G^{\mathrm{r,a}}(\mathbf{k}\sigma, \omega) = \frac{1}{\omega - \xi_{\mathbf{k}\sigma}/\hbar - \Sigma^{\mathrm{r,a}}(\mathbf{k}\sigma, \omega)} = \frac{1}{\omega - \xi_{\mathbf{k}\sigma}/\hbar - \Lambda(\mathbf{k}\sigma, \omega) \mp \mathrm{i}\Gamma(\mathbf{k}\sigma, \omega)/2}\,. \tag{2.24}$$

Here it was considered that the proper self-energy is in general a complex quantity and accordingly the retarded and advanced proper self-energies is separated into its real and imaginary part $\Sigma^{\mathrm{r,a}}(\mathbf{k}\sigma, \omega) = \Sigma(\mathbf{k}\sigma, \mathrm{i}\omega_n \to \omega + \mathrm{i}0^+) = \Lambda(\mathbf{k}\sigma, \omega) \pm \mathrm{i}\Gamma(\mathbf{k}\sigma, \omega)/2$ [61]. The real part of the self-energy $\Lambda$ is causing a shift of the eigenenergies, whereby the new poles $\omega_0$ result as the solutions of the equation $\omega - \xi - \Lambda(\mathbf{k}\sigma, \omega) = 0$. The spectral density function (see Eq. (2.14)) is given by

$$A(\mathbf{k}\sigma, \omega) = -\frac{1}{2\pi}\frac{\Gamma(\mathbf{k}\sigma, \omega)}{(\omega - \xi_{\mathbf{k}\sigma}/\hbar - \Lambda(\mathbf{k}\sigma, \omega))^2 + (\Gamma(\mathbf{k}\sigma, \omega))^2/4}\,. \tag{2.25}$$

While the spectral function for the non-interacting case is a Dirac delta function, this expression represents a Lorentz curve. Hence, including interactions between the electrons the excitations exhibit a finite line width with the full width at half maximum (FWHM) of

$\Gamma(\mathbf{k}\sigma, \omega_0)$. The finite line width can be interpreted as the lifetime $\tau = \hbar/\Gamma(\mathbf{k}\sigma, \omega_0)$ of the many-body quasiparticle state, which is antiproportional to the line width because of the Heisenberg uncertainty principle.

### 2.2.3 Fermi's Golden Rule and its Generalization

If a system is in an initial eigenstate $|\mathrm{L}\rangle$ the transition rate $\Gamma_{\mathrm{L}\to\mathrm{R}}$ to the final eigenstate $|\mathrm{R}\rangle$ of the non-interacting Hamiltonian $\tilde{\mathcal{H}}_0$ is given by [61]

$$\Gamma_{\mathrm{L}\to\mathrm{R}} = \frac{2\pi}{\hbar} |T_{\mathrm{R,L}}|^2 \, \delta(E_\mathrm{R} - E_\mathrm{L}) \qquad \text{with} \qquad T_{\mathrm{R,L}} = \langle \mathrm{R}|\mathcal{H}'|\mathrm{L}\rangle = \langle \mathrm{R}|\mathcal{H}_\mathrm{T}|\mathrm{L}\rangle \,. \tag{2.26}$$

Fermi called this result, which holds up to lowest (second) order in the perturbation $\tilde{\mathcal{H}}'$, the golden rule. The rule gives the transition probability per time unit between the states, with $|T_{\mathrm{R,L}}|^2 = |\langle \mathrm{R}|\mathcal{H}'|\mathrm{L}\rangle|^2$ being the tunneling probability. It can be generalized in case of multiple scattering events at the perturbation in terms of the so-called T-matrix [61]

$$\mathbf{T} = \mathcal{H}' + \mathcal{H}' G_0 \mathcal{H}' + \mathcal{H}' G_0 \mathcal{H}' G_0 \mathcal{H}' + \cdots = \mathcal{H}' + \mathcal{H}' G_0 \mathbf{T} \,, \tag{2.27}$$

with $G_0$ being the bare Green's function. This results in the generalized form of Fermi's golden rule

$$\Gamma_{\mathrm{L}\to\mathrm{R}} = \frac{2\pi}{\hbar} |\langle \mathrm{R}|\mathbf{T}|\mathrm{L}\rangle|^2 \, \delta(E_\mathrm{R} - E_\mathrm{L}) \,. \tag{2.28}$$

## 2.3 Fundamental Introduction in Superconductivity

The discovery of superconductivity goes back to H. K. Onnes in 1911. He was the first to succeed in cooling helium below its boiling point of 4.2 K. Using the Hampson-Linde cycle, which is based on the Joule-Thomson effect, he reached temperatures around 1.5 K. This allowed access to a large number of novel experiments that were previously inaccessible on Earth. Among other things, Onnes observed a sudden disappearance of the resistance, when lowering the temperature from mercury beneath 4.2 K [67]. For this discovery, today known as superconductivity, he was awarded the Nobel Prize in Physics in 1913. The temperature $T_\mathrm{c}$ at which a material becomes superconducting is called the critical temperature. A large number of metals and alloys are superconductors, with critical temperatures in the range of less than 1 K to 18 K.

In the 1930s to 1950s, great progress was made in the field of superconductivity. In 1933 Meissner and Ochsenfeld discovered that superconductors are perfect diamagnets with a susceptibility of $\chi = -1$, meaning they expel magnetic fields up to a critical magnetic field $H_\mathrm{c}$. This unique magnetic property is fundamental for the characterization of the superconducting state. It also distinguishes between superconductors and ideal conductors, where the latter capture magnetic fluxes inside the material during cooling instead of expelling them. The first phenomenological theory of superconductivity was developed

in 1935 by F. and H. London. The London theory was able to explain the Meissner effect as a consequence of minimizing the electromagnetic free energy of the superconducting current. It took until 1950, when E. Maxwell and C. A. Reynolds independently discovered the isotopic effect [68, 69] and found the proportionality of $T_c$ and $H_c$ to the isotopic mass $M^{-\alpha}$ of the lattice atoms, where the exponent $\alpha$ being typically close to 0.5:

$$T_c M^{-\alpha} = \text{const.} \quad \text{and} \quad H_c M^{-\alpha} = \text{const.} \tag{2.29}$$

Their experiments were the first indication that electron-phonon coupling causes superconductivity. In the same year V. L. Ginzburg and L. D. Landau extended the London theory by studying the macroscopic properties of superconductors with a general thermodynamic approach [70]. This was a pure phenomenological theory on which Abrikosov based his important analysis of magnetic field dependence in Type I and Type II superconductors. J. Bardeen, L. N. Cooper and J. R. Schrieffer succeeded in developing the BCS theory [71], one of the most important achievements in the field of classical superconductors, for which they were awarded the Nobel Prize in Physics in 1972. In their microscopic many-body theory, they explain superconductivity in metals in terms of electron pairs ($\mathbf{k}\uparrow, -\mathbf{k}\downarrow$) – the Cooper pairs [72]. These are grouped around the Fermi energy in an energy range of $\hbar\omega_D$[3] due to electron-phone interaction. The theory was supplemented by the works of Gorkov, Abrikosov, and Eliashberg.

The more recent discoveries point towards high-temperature superconductors. In 1986 J. Bednorz and K. Müller demonstrated superconductivity in a copper oxide compound at temperatures up to 32 K [73]. Although these high-temperature superconductors are still based on electron pairing, their critical temperatures are beyond what can be explained by electron-phonon coupling within BCS theory [74]. The discovery of this new class of materials, classified as cuprates, led to a true race that produced more and more superconducting materials with higher and higher transition temperatures. Today the record temperature for superconductivity in a cuprate is around 140 K. Towards these temperatures, the exceeding of the boiling point of liquid nitrogen at 77 K was a milestone, making superconductors more attractive for industrial applications.

### 2.3.1 Microscopic Theory of Superconductivity: BCS theory

The essential physical idea, introduced by Cooper in 1956, showed that any attraction, however weak, between pairs of electrons will lead to the creation of a new ground state [72]. In this new state, the Fermi sea of electrons is unstable towards the formation of such bound pairs of electrons, the so-called Cooper pairs.

One possibility for such an attraction is the electron-phonon interaction. The Cooper pair formation is illustrated in Fig. 2.5(a-c). A first electron polarizes the lattice of the positive ion cores in the crystal lattice, leading to lattice vibrations, which are called phonons.

[3] The Debye frequency $\omega_D$ is the theoretical maximum frequency of the lattice-atom vibrations, called phonons. It limits the electron-phonon interaction.

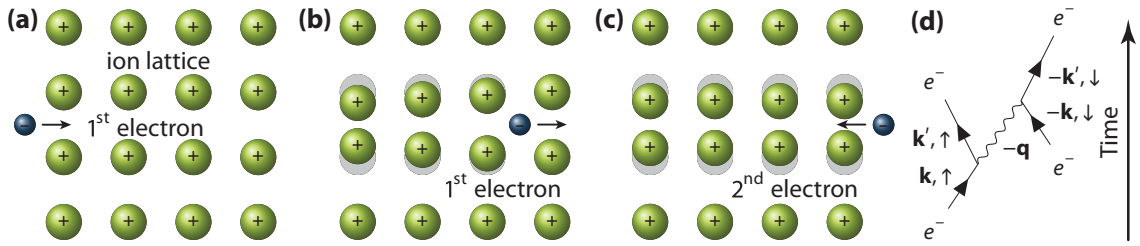


**Figure 2.5 | Schematic illustration of the formation of a copper pair by electron-phonon coupling. (a)** Unperturbed ion lattice consisting of positively charged atomic cores *(green)* and an exemplary electron *(blue)* passing through the lattice. **(b)** The negatively charged electron interacts with the positive nuclei by an attractive electrostatic force. The attraction between them leads to the excitation of lattice vibrations in the crystal, so-called phonons. The displacement of atomic cores is shown relative to their resting positions *(grey)*. **(c)** A second electron is attracted by the phonons and moves along the positive space charge zone formed by the cores. The time scale on which the phonons take place is so long compared to the speed of the electrons that the electrons do not influence each other and thus the second electron only interacts with the ion lattice. **(d)** Feynman diagram of the electron-phonon coupling: The electron with momentum **k** and spin up emits a phonon of wave-vector $-\mathbf{q}$. This phonon is absorbed later by a second electron with $-\mathbf{k}$ and spin down.

These phonons create an effective attractive interaction that results in a second electron with opposite momentum being dragged along the trajectory of the first electron at a later time. Superconductivity occurs when this attraction is strong enough to compensate for the repulsive Coulomb interaction between the electrons. The interaction can further be illustrated in the Feynman diagram in Fig. 2.5(d). The Coulomb interaction can be regarded as an instantaneous process, in comparison to the slow electron-phonon interaction. The former process is mediated by photons, which have a significantly shorter lifetime than phonons. For this reason, the first electron can travel a long distance in the metal before a second electron scatters off the excited lattice. This is why the second electron experiences only a very weak Coulomb repulsion from the very distant first electron, while the phonon has hardly decayed at all. Momentum conservation implies that for an electron scattered from $\mathbf{k}$ to $\mathbf{k}'$, the generated phonon must have the moment $\mathbf{q} = \mathbf{k} - \mathbf{k}'$ associated with an frequency $\omega_{\mathbf{q}}$. The Debye frequency $\omega_{\mathrm{D}}$ as maximum phonon energy acts as the upper limit for the maximal transferable energy. These diagrams illustrate how important the time scales associated with the processes are. The importance of electron-phonon interaction for explaining superconductivity was first proposed by Fröhlich [75] in 1950. The first clear indication of a phonon-forwarded interaction was the already mentioned isotope effect (see Eq. (2.29)) discovered in the same year [68, 69]. Since the isotope mass only influences the lattice oscillations, but not the electronic conductivity, this observation is a clear indication that electron-phonon interaction, plays an essential role in superconductivity.

In BCS theory, the total Hamiltonian of a metal is considered to be the sum of the ground state energies of electrons and phonons, the Coulomb repulsion and the electron-phonon

interaction [76]

$$\begin{aligned}\tilde{\mathcal{H}} = &\sum_{\mathbf{k}} \epsilon_{\mathbf{k}} N_{\mathbf{k}} + \sum_{\mathbf{k}} \omega_{\mathbf{k}} n_{\mathbf{k}} && \text{(GS energy)} \\ &+ \sum_{\mathbf{k}\mathbf{k}'\mathbf{q}} V_{\text{Coulomb}}(\mathbf{k},\mathbf{k}') c^{\dagger}_{\mathbf{k}+\mathbf{q}} c^{\dagger}_{\mathbf{k}'-\mathbf{q}} c_{\mathbf{k}} c_{\mathbf{k}'} && (\mathrm{e}^- - \mathrm{e}^- \text{ interaction}) \\ &+ \sum_{\mathbf{k}\mathbf{k}'} M_{\mathbf{k},\mathbf{k}'} b_{\mathbf{k}'-\mathbf{k}} c^{\dagger}_{\mathbf{k}'} c_{\mathbf{k}} + \sum_{\mathbf{k}\mathbf{k}'} M^{*}_{\mathbf{k},\mathbf{k}'} b^{\dagger}_{\mathbf{k}'-\mathbf{k}} c^{\dagger}_{\mathbf{k}} c_{\mathbf{k}'}\,, && (\mathrm{e}^- - \text{ph interaction})\end{aligned} \tag{2.30}$$

with $\mathbf{k}$ and $\mathbf{k}'$ being the individual electron momentum, $\epsilon_{\mathbf{k}}$ the electron energy, $\omega_{\mathbf{k}}$ the phonon energy, $c^{\dagger}_{\mathbf{k}}$, $c_{\mathbf{k}}$ and $b^{\dagger}_{\mathbf{k}}$, $b_{\mathbf{k}}$ the fermionic electron and bosonic phonon creation and annihilation operators, and $N_{\mathbf{k}} = c^{\dagger}_{\mathbf{k}} c_{\mathbf{k}}$ and $n_{\mathbf{k}} = b^{\dagger}_{\mathbf{k}} b_{\mathbf{k}}$ the corresponding electron and phonon number operators.

The BCS theory assumes that the Debye frequency is much smaller than the Fermi energy $E_{\mathrm{F}}$, which limits the interaction to a small energy interval $E_{\mathrm{F}} \pm \hbar\omega_{\mathrm{D}}$. Due to the indistinguishability of electrons and due to the Pauli exclusion principle, the wave functions of the Cooper pair's are antisymmetric for the permutation of electrons. This means that also the spins within the electron pairs must be antisymmetric, leading to a spin singlet with opposite spin. The singlet wave function is given by [77]

$$|\psi_0\rangle = \sum_{k>k_{\mathrm{F}}} g_{\mathbf{k}} c^{\dagger}_{\mathbf{k}\uparrow} c^{\dagger}_{-\mathbf{k}\downarrow} |F\rangle\,, \tag{2.31}$$

where $|F\rangle$ is the Fermi sea with all states filled up to $k_{\mathrm{F}}$ and $g_{\mathbf{k}}$ is the expansion coefficient. In Eq. (2.31) the creation and annihilation operators get an additional index indicating the spin of the electron. This wave function describes the process of adding a Cooper pair to the Fermi sea.

With the introduction of Cooper pairs, the complexity of the Hamiltonian from eq.(2.30) can be simplified to the *pairing Hamiltonian* [77]

$$\mathcal{H} = \sum_{\mathbf{k}\sigma} \xi_{\mathbf{k}} N_{\mathbf{k}\sigma} + \sum_{\mathbf{k}\mathbf{k}'} V_{\mathbf{k},\mathbf{k}'} c^{\dagger}_{\mathbf{k}\uparrow} c^{\dagger}_{-\mathbf{k}\downarrow} c_{-\mathbf{k}'\downarrow} c_{\mathbf{k}'\uparrow}\,, \tag{2.32}$$

with the matrix element of the interaction potential $V_{\mathbf{k},\mathbf{k}'}$ including the electron-phonon interaction as described above.

### Mean-Field Approach to Superconductivity

To determine the ground state of the pairing Hamiltonian a mean-field approach may be used. This BCS mean-field approach is also based on a perturbative treatment of the many-body problem, with the electron-phonon interaction regarded as small perturbation [61, 62]. In contrast to normal metals, quantities such as $\left\langle c^{\dagger}_{\mathbf{k}\uparrow} c^{\dagger}_{-\mathbf{k}\downarrow} \right\rangle$ and $\left\langle c_{-\mathbf{k}'\downarrow} c_{\mathbf{k}'\uparrow} \right\rangle$ do not vanish in superconductors. Hence, the BCS ground state is no longer an eigenstate of the

number operator and it becomes useful to rewrite the pair creation operator [62]

$$c_{-\mathbf{k}'\downarrow}c_{\mathbf{k}'\uparrow} = \langle c_{-\mathbf{k}'\downarrow}c_{\mathbf{k}'\uparrow}\rangle + c_{-\mathbf{k}'\downarrow}c_{\mathbf{k}'\uparrow} - \langle c_{-\mathbf{k}'\downarrow}c_{\mathbf{k}'\uparrow}\rangle = \langle c_{-\mathbf{k}'\downarrow}c_{\mathbf{k}'\uparrow}\rangle + d_{\mathbf{k}}\,. \tag{2.33}$$

The introduced fluctuation operator $d_{\mathbf{k}}$ represents the deviation of $c_{-\mathbf{k}'\downarrow}c_{\mathbf{k}'\uparrow}$ from its average in the ground state. Following the same arguments, the annihilation operator can be defined. These fluctuations are expected to be small because of the large number of particles involved in the ground state. In terms of the fluctuation operators, the interaction Hamiltonian reads

$$\mathcal{H}' = \sum_{\mathbf{k}\mathbf{k}'} V_{\mathbf{k},\mathbf{k}'}\left[\langle c^\dagger_{\mathbf{k}\uparrow}c^\dagger_{-\mathbf{k}\downarrow}\rangle\, d_{\mathbf{k}} + \langle c_{-\mathbf{k}'\downarrow}c_{\mathbf{k}'\uparrow}\rangle\, d^\dagger_{\mathbf{k}} + \langle c^\dagger_{\mathbf{k}\uparrow}c^\dagger_{-\mathbf{k}\downarrow}\rangle\langle c_{-\mathbf{k}'\downarrow}c_{\mathbf{k}'\uparrow}\rangle + d^\dagger_{\mathbf{k}}d_{\mathbf{k}}\right]. \tag{2.34}$$

Within the mean-field approximation, we neglect the last term because it is bilinear in the fluctuation. By introducing the gap parameter

$$\Delta_{\mathbf{k}} = -\frac{1}{N}\sum_{\mathbf{k}'} V_{\mathbf{k},\mathbf{k}'}\langle c_{-\mathbf{k}'\downarrow}c_{\mathbf{k}'\uparrow}\rangle\,, \tag{2.35}$$

the mean-field Hamiltonian may be written as

$$\mathcal{H} = \sum_{\mathbf{k},\sigma}\left[\xi_{\mathbf{k}}c^\dagger_{\mathbf{k}\sigma}c_{\mathbf{k}\sigma} + \left(\Delta c^\dagger_{\mathbf{k}\uparrow}c^\dagger_{-\mathbf{k}\downarrow} + \text{h.c.}\right)\right], \tag{2.36}$$

or using the rather convenient matrix notation as [61]

$$\mathcal{H} = \sum_{\mathbf{k}}\left[\begin{pmatrix} c^\dagger_{\mathbf{k}\uparrow} & c_{-\mathbf{k}\downarrow}\end{pmatrix}\begin{pmatrix}\xi_{\mathbf{k}} & \Delta_{\mathbf{k}}\\ \Delta^\dagger_{\mathbf{k}} & -\xi_{\mathbf{k}}\end{pmatrix}\begin{pmatrix} c_{\mathbf{k}\uparrow}\\ c^\dagger_{-\mathbf{k}\downarrow}\end{pmatrix} + \xi_{\mathbf{k}} + \langle c^\dagger_{\mathbf{k}\uparrow}c^\dagger_{-\mathbf{k}\downarrow}\rangle\,\Delta_{\mathbf{k}}\right] = \sum_{\mathbf{k}}\mathbf{C}^\dagger_{\mathbf{k}}\mathbf{H}_{\mathbf{k}}\mathbf{C}_{\mathbf{k}} + \text{const.}\,. \tag{2.37}$$

This is also known as the Bogoliubov-de Gennes Hamiltonian for non-magnetic superconductors. On the right hand side the spinors $\mathbf{C}^\dagger_{\mathbf{k}}$ and $\mathbf{C}_{\mathbf{k}}$, as well as the energy matrix $\mathbf{H}_{\mathbf{k}}$ are introduced as

$$\mathbf{C}^\dagger_{\mathbf{k}} = \begin{pmatrix} c^\dagger_{\mathbf{k}\uparrow} & c_{-\mathbf{k}\downarrow}\end{pmatrix}, \quad \mathbf{C}_{\mathbf{k}} = \begin{pmatrix} c_{\mathbf{k}\uparrow}\\ c^\dagger_{-\mathbf{k}\downarrow}\end{pmatrix}, \quad \mathbf{H}_{\mathbf{k}} = \begin{pmatrix}\xi_{\mathbf{k}} & \Delta_{\mathbf{k}}\\ \Delta^*_{\mathbf{k}} & -\xi_{\mathbf{k}}\end{pmatrix}. \tag{2.38}$$

To calculate the eigenvalue spectrum of the superconducting ground state it is necessary to diagonalize $\mathbf{H}_{\mathbf{k}}$, which can be done by means of a canonical unitary transformation $\mathbf{U}_{\mathbf{k}}$ – the Bogoliubov–Valatin transformation [78, 79]

$$\mathbf{B}_{\mathbf{k}} = \begin{pmatrix}\gamma_{\mathbf{k}\uparrow}\\ \gamma^\dagger_{-\mathbf{k}\downarrow}\end{pmatrix} = \mathbf{U}^{-1}_{\mathbf{k}}\mathbf{C}_{\mathbf{k}}\,, \quad \mathbf{U}_{\mathbf{k}} = \begin{pmatrix} u_{\mathbf{k}} & -v_{\mathbf{k}}\\ v^*_{\mathbf{k}} & u^*_{\mathbf{k}}\end{pmatrix}, \tag{2.39}$$

resulting in

$$\mathbf{U}^\dagger_{\mathbf{k}}\mathbf{H}_{\mathbf{k}}\mathbf{U}_{\mathbf{k}} = \begin{pmatrix} E_{\mathbf{k}} & 0\\ 0 & \tilde{E}_{\mathbf{k}}\end{pmatrix}. \tag{2.40}$$

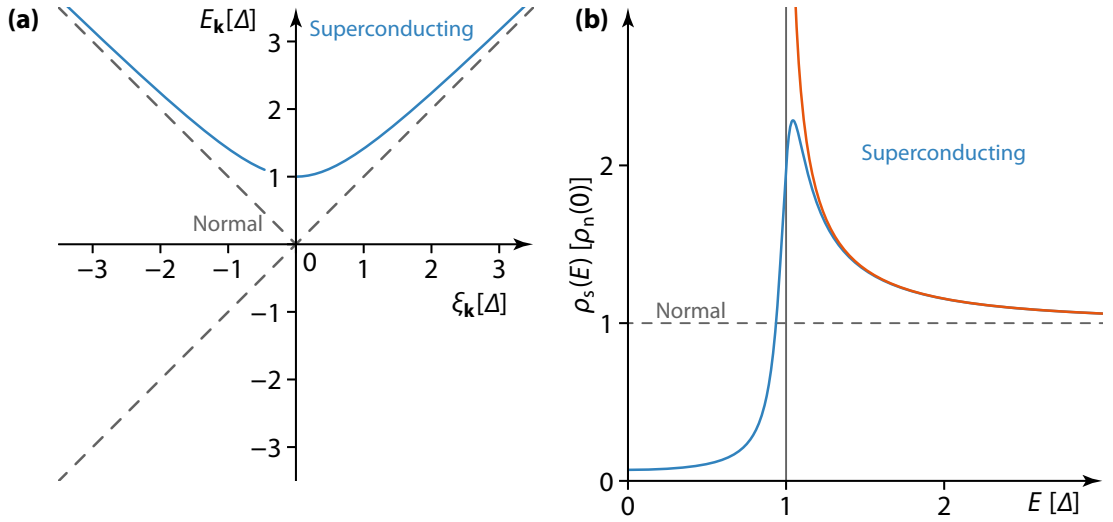


**Figure 2.6 | Formation of the superconducting gap. (a)** Energies of the elementary excitations in the normal and superconducting states as a function of $\epsilon_{\mathbf{k}}$. **(b)** Quasiparticle density of states $\rho_s$ (*orange*) normalized to the metallic density of states $\rho_n$ as a function of energy. Additional effects can lead to a broadening of the superconducting density of states (*blue*), e.g. the depairing of the quasiparticles near the superconducting gap, which is described by the Dynes parameter (see section 5.1). In the style of [77].

The solution for $u$, $v$ with energies $E$ and $\tilde{E}$ may be found as [61]

$$|u_{\mathbf{k}}|^2 = \frac{1}{2}\left[1 + \frac{\xi_{\mathbf{k}}}{E_{\mathbf{k}}}\right], \quad |v_{\mathbf{k}}|^2 = \frac{1}{2}\left[1 - \frac{\xi_{\mathbf{k}}}{E_{\mathbf{k}}}\right], \quad E_{\mathbf{k}} = \sqrt{\xi_{\mathbf{k}}^2 + |\Delta_{\mathbf{k}}|^2} = -\tilde{E}_{\mathbf{k}}\,. \tag{2.41}$$

The transformation between the old and new set of operators is given by Eq. (2.39) as

$$\begin{pmatrix} \gamma_{\mathbf{k}\uparrow} \\ \gamma^\dagger_{-\mathbf{k}\downarrow} \end{pmatrix} = \begin{pmatrix} u^*_{\mathbf{k}} & v_{\mathbf{k}} \\ -v^*_{\mathbf{k}} & u_{\mathbf{k}} \end{pmatrix} \begin{pmatrix} c_{\mathbf{k}\uparrow} \\ c^\dagger_{-\mathbf{k}\downarrow} \end{pmatrix}. \tag{2.42}$$

Finally, the Hamiltonian in terms of these new operators is

$$\mathcal{H} = \sum_{\mathbf{k}} E_{\mathbf{k}} \left(\gamma^\dagger_{\mathbf{k}\downarrow}\gamma_{\mathbf{k}\downarrow} + \gamma^\dagger_{\mathbf{k}\uparrow}\gamma_{\mathbf{k}\uparrow}\right) + \sum_{\mathbf{k}} \left(\xi_{\mathbf{k}} - E_{\mathbf{k}} + \Delta_{\mathbf{k}} \left\langle c^\dagger_{\mathbf{k}\uparrow} c^\dagger_{-\mathbf{k}\downarrow} \right\rangle\right). \tag{2.43}$$

The second term on the right hand side is constant and describes the ground state energy. In contrast, the first term describes excitations above this ground state as the creation of a Bogoliubov quasiparticle from the ground state condensate – also referred to as *Bogoliubons*. It is evident, that no fermion excitation is possible with an energy less than $|\Delta|$, shown in Fig. 2.6(a). Therefore this mean field parameter results in a energy gap around $\mu$ – called

superconducting energy gap. The BCS wave function for the ground state has the form

$$|\Psi_{\mathrm{BCS}}\rangle = \prod_{\mathbf{k}} (|u_{\mathbf{k}}| + |v_{\mathbf{k}}| \, \mathrm{e}^{\mathrm{i}\varphi} c^{\dagger}_{\mathbf{k}\uparrow} c^{\dagger}_{-\mathbf{k}\downarrow}) |0\rangle \,, \tag{2.44}$$

where $|0\rangle$ is the vacuum state with no particles present. The wave function is normalized if $|u_{\mathbf{k}}|^2 + |v_{\mathbf{k}}|^2 = 1$. In the BCS ground state the occupations of $|\mathbf{k}, \uparrow\rangle$ and $|-\mathbf{k}, \downarrow\rangle$ are fully correlated - either both are occupied or both are empty. Therefore the superconducting ground state consists of pairs of electrons with opposite momentum and spin, with $|v_{\mathbf{k}}|^2$ being the probability that a pair $(\mathbf{k}\uparrow, \mathbf{k}\downarrow)$ is occupied and $|u_{\mathbf{k}}|^2$ being the probability that it is empty. All Cooper pairs with the same momentum are in phase and thus form a macroscopic quantum state similar to a Bose-Einstein condensate. Consequently, Cooper pairs do not experience electrical resistance because the wave function cannot scatter at microscopic defects. Another important property derived directly from the Hamiltonian is the particle-hole symmetry of superconductors. The degrees of freedom of the condensate allow an electron to be transformed into a hole by the creation of a Cooper pair and vice versa. This property becomes of interest when impurities are added to the superconductor that lead to a symmetry breaking as described in Section 2.6.

### 2.3.2 Green's Functions of the Superconducting State

We can also describe superconductors with the help of Green's functions, first introduced by Gorkov. This allows us to describe magnetic impurities in superconductors (see Section 2.6) in the context of the Dyson equation, as described in Section 2.2.2. Here we follow the generalized Green's function formalism in Nambu space [80], which is very convenient for describing the single-particle excitation spectrum of a superconducting system, since its calculations become quite analogous to those for normal metals [31]. Using the spinors introduced in the mean-field approximation in Eq. (2.38), the Nambu Green's function is defined as a $2 \times 2$ matrix [61]

$$\underline{\mathcal{G}}(\mathbf{k}, \tau) = -\left\langle T\left[C_{\mathbf{k}}(\tau) C^{\dagger}_{\mathbf{k}}(0)\right]\right\rangle = \begin{pmatrix} \mathcal{G}(\mathbf{k}\uparrow, \tau) & \mathcal{F}^{\dagger}(\mathbf{k}, \tau) \\ \mathcal{F}(\mathbf{k}, \tau) & \mathcal{G}^{\dagger}(\mathbf{k}\downarrow, \tau) \end{pmatrix}. \tag{2.45}$$

Here the *anomalous* Green's function is defined as $\mathcal{F}_{\downarrow\uparrow}(\mathbf{k}, \tau) = -\left\langle T\left[c_{\mathbf{k}\uparrow}(\tau) c^{\dagger}_{\mathbf{k}\downarrow}(0)\right]\right\rangle$. As already mentioned, such terms vanish in normal metals, whereas in superconductors they describe the pairing average, so $\Delta_{\mathbf{k}} = -1/N \sum_{\mathbf{k}'} V_{\mathbf{k},\mathbf{k}'} \mathcal{F}_{\downarrow\uparrow}(\mathbf{k}', 0)$. The Green's function is found to be [61]

$$\underline{\mathcal{G}}(\mathbf{k}, \mathrm{i}\omega_n) = \frac{1}{(\mathrm{i}\omega_n)^2 - (E_{\mathbf{k}}/\hbar)^2} \begin{pmatrix} \mathrm{i}\omega_n + \xi_{\mathbf{k}}/\hbar & \Delta_{\mathbf{k}}/\hbar \\ -\Delta^*_{\mathbf{k}}/\hbar & \mathrm{i}\omega_n - \xi_{\mathbf{k}}/\hbar \end{pmatrix}. \tag{2.46}$$

The poles of $\mathcal{G}(\mathbf{k}\uparrow, \mathrm{i}\omega_n)$ are $\mathrm{i}\omega_n = E_{\mathbf{k}}$, which is consistent with the previous derivation in Section 2.3.1. A rewriting of the Green's function using $u^2_{\mathbf{k}}$ and $v^2_{\mathbf{k}}$ shows the connection to

the Bogoliubov transformation [81]

$$\mathcal{G}(\mathbf{k}, \mathrm{i}\omega_n) = \frac{u_\mathbf{k}^2}{\mathrm{i}\omega_n - E_\mathbf{k}/\hbar} + \frac{v_\mathbf{k}^2}{\mathrm{i}\omega_n + E_\mathbf{k}/\hbar}\,, \tag{2.47}$$

so the spectral density function that is probed by STM is [62]

$$A(\mathbf{k}, \omega) = u_\mathbf{k}^2\,\delta(\omega - E_\mathbf{k}/\hbar) + v_\mathbf{k}^2\,\delta(\omega + E_\mathbf{k}/\hbar)\,. \tag{2.48}$$

This function consists of two delta function peaks at $\pm E_\mathbf{k}$ corresponding to the energies for adding or removing one electron. The bare retarded Green's function of a BCS superconductor in Nambu space is [82]

$$\underline{G}_0^\mathrm{r}(\mathbf{k}, \omega) = \left[\omega - \xi_\mathbf{k}\tau_z/\hbar - \Delta\tau_x/\hbar\right]^{-1}, \tag{2.49}$$

where

$$\tau_x = \begin{pmatrix} 0 & 1 \\ 1 & 0 \end{pmatrix}, \quad \tau_y = \begin{pmatrix} 0 & -\mathrm{i} \\ \mathrm{i} & 0 \end{pmatrix} \quad \text{and} \quad \tau_z = \begin{pmatrix} 1 & 0 \\ 0 & -1 \end{pmatrix}, \tag{2.50}$$

denote the Pauli matrices in Nambu space. Computing the bare Green's function and evaluate it at its origin yields.

$$\underline{G}^\mathrm{r}(\omega) = \frac{1}{\mathcal{V}}\sum_k \underline{G}^\mathrm{r}(\mathbf{k}, \omega) = \rho_0 \int \mathrm{d}\xi_\mathbf{k} \frac{\hbar\omega + \xi_\mathbf{k}\tau_z + \Delta\tau_x}{(\hbar\omega)^2 - \xi_\mathbf{k}^2 - \Delta^2} = -\frac{\pi\rho_0(\hbar\omega + \Delta\tau_x)}{\sqrt{\Delta^2 - (\hbar\omega)^2}}\,. \tag{2.51}$$

In summary, the perturbation series of the Greens function is the same as that of the normal state by using Nambu space, resulting in identical Feynman diagrams compared to those of the normal state.

### 2.3.3 BCS Quasiparticle Density of States

For the interpretation and simulation of a superconducting spectrum we need an exact formulation of the superconducting density of states. In the two previous sections we showed that Cooper pairs can be described as quasiparticles with fermionic creation and annihilation operators $\gamma_\mathbf{k}^\dagger$ and $\gamma_\mathbf{k}$, which are directly related to $c_\mathbf{k}^\dagger$ and $c_\mathbf{k}$ of a normal metal. Quasiparticle excitations from the BCS ground state are single electrons that are no longer part of the condensate of pairs. We learned in Eq. (2.16) that the density of states of these quasiparticles can be derived from the Matsubara Green's functions or respectively from the spectral function. From equation Eq. (2.51) the density of states can be read directly as (see Fig. 2.6(b))

$$\rho_\mathrm{s}(E) = -\frac{1}{\pi\mathcal{V}}\sum_\mathbf{k} G^\mathrm{r}(\mathbf{k}, E/\hbar) = \rho_0\,\mathrm{Im}\left(\frac{E}{\sqrt{\Delta_\mathbf{k}^2 - E^2}}\right) = \rho_0\frac{E}{\sqrt{E^2 - \Delta_\mathbf{k}^2}}\theta(E - \Delta_\mathbf{k})\,. \tag{2.52}$$

Here $\rho_n(0) = \rho_0 = m_e k_F/2\pi^2\hbar^2$ is the normal conducting density of state at the chemical potential. Note, that $\Delta_{\mathbf{k}}$ is $\mathbf{k}$-dependent. Classical superconductors are all s-wave superconductors and therefore $\Delta_{\mathbf{k}} \to \Delta$, raising all excitations with momenta $\mathbf{k}$ to energies above $\Delta$. This is no longer true for unconventional superconductors in particular, since the $d_{x^2-y^2}$ symmetry of the $\mathbf{k}$ vectors is reflected in the symmetry of the gap parameter.

## 2.4 Josephson Effect

So far we have only considered single quasiparticle tunneling across a tunneling barrier. However, the overlap of the BCS wave functions of two superconductors allows also the tunneling of Cooper pairs, resulting in a superconducting tunnel current, also referred to as *supercurrent* $I_{sc}$. B. Josephson made two important predictions for such supercurrents [83]. First, that the current will continue to flow, even without applied voltage. As long as there is a phase difference $\varphi = \varphi_L - \varphi_R$ between the two superconducting leads this current will be proportional to the critical current $I_c$ in the form of [83]

$$I_{sc}(t) = I_c \sin\varphi(t)\,. \tag{2.53}$$

This first Josephson relation describes the *dc Josephson effect*. The second relation states, that in the presence of a nonzero bias voltage $V$, the phase difference evolve in time [83]

$$V = \frac{\Phi_0}{2\pi}\dot{\varphi}(t) \quad \Rightarrow \quad \varphi(t) = \varphi_0 + \frac{2\pi V}{\Phi_0}t\,, \tag{2.54}$$

with $\Phi_0 = h/2e$ being the flux quantum. A direct consequence is that a constant *dc* voltage $V_{dc}$ applied to the junction leads to an alternating current, the so called *ac Josephson effect*. Their corresponding frequency $\omega = 2\pi V_{dc}/\Phi_0$ is typically in the microwave regime ($\omega/V_{dc} = 2\pi/\Phi_0 \approx 3\,\mathrm{GHz/\mu V}$). Conventional tunnel experiments are not sensitive to changes in this frequency range and will average them out over time. The relevant quantity to consider for analyzing the ac Josephson effect is therefore the time-averaged voltage $\langle V(t)\rangle$.

Being a *zero voltage state*, no energy dissipation is associated with the *dc* Josephson effect. This means that the supercurrent is an equilibrium quantity, unlike for normal conducting junctions, in which a current is always associated with energy dissipation. Nevertheless, finite energy $E_J$ is stored in the junction, which can be regarded as the electrical work done by a current source in changing the phase. This stored (free) energy corresponds to the integrated power from time $t = 0$ when starting to increase the current to time $t = t_0$, when reaching the final value $I$ [84]

$$E_J(\varphi) = \int_0^{t_0} I_{sc} V\,\mathrm{d}t = \int_0^{t_0} (I_c \sin\tilde{\varphi})\left(\frac{\Phi_0}{2\pi}\frac{\mathrm{d}\tilde{\varphi}}{\mathrm{d}t}\right)\mathrm{d}t\,. \tag{2.55}$$

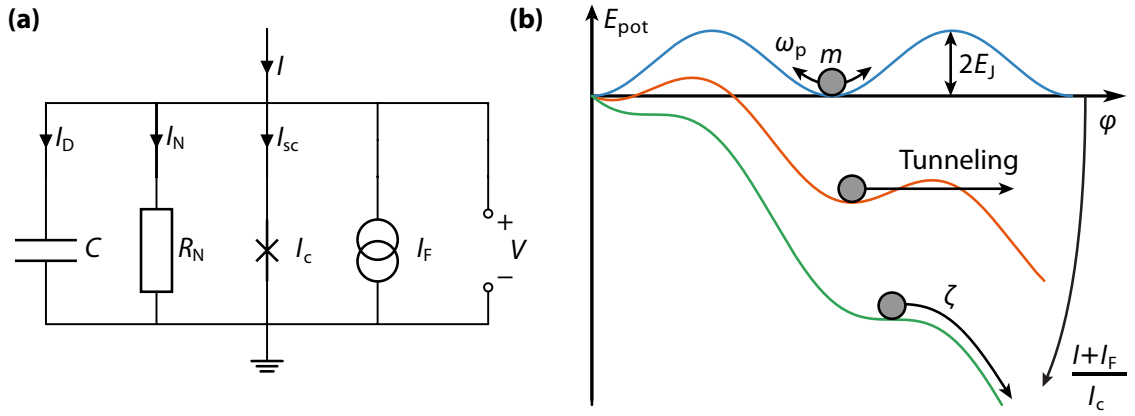


**Figure 2.7 | Resistively and capacitively shunted junction (RCSJ) model. (a)** Equivalent circuit. The RCSJ model divides the Josephson current into a parallel circuit of supercurrent $I_{sc}$, quasiparticle current $I_N$, and displacement current $I_D$. Additionally a thermal current noise source $I_F$ is included. **(b)** The tilted washboard potential, in which the phase moves as a particle with mass $m$ and friction $\zeta$, is shown for different normalized currents. At zero current the potential is flat and the particle is trapped (*blue* curve). When the critical current is exceeded, the potential has no more minima and the particle enters a running state, where changing its phase over time (*green* curve). Figure (b) in the style of [84].

During this time the phase difference is changed from $\varphi(0) = 0$ to $\varphi(t_0) = \varphi$. Thus the integral can be solved by a change of variables

$$E_J(\varphi) = \frac{\Phi_0 I_c}{2\pi} \int_0^{\varphi} \sin\tilde{\varphi}\, \mathrm{d}\tilde{\varphi} = E_{J0}(1 - \cos\varphi)\,, \tag{2.56}$$

where the *Josephson energy* $E_{J0} = \Phi_0 I_c/2\pi$ is a characteristic parameter of the Josephson junction. The energy $E_J$ is also referred to as the *Josephson coupling energy* as it results from the overlap (or coupling) of the wave functions of the two superconducting electrodes. This energy has to be applied once to accelerate the Cooper pairs before they can flow across the junction without resistance.

From the current-phase relation in Eq. (2.53) it can be concluded that also a current-biased junction where a constant external *dc* current is added to the Josephson junctions leads to a constant phase difference. Therefore the junction remains in the *zero voltage state*. The stability of the zero voltage state results from the potential energy $E_{pot}$ of the system consisting of Josephson junction and current source. Analogous to the calculation of the Josephson coupling energy in (2.56) the potential energy of the system is given by [84]

$$E_{pot}(\varphi) = E_{J0}(1 - \cos\varphi - \tilde{I}\varphi)\,, \tag{2.57}$$

with the normalized current $\tilde{I} = I/I_c$. This potential is called tilted washboard potential because of its shape (compare Fig. 2.7(b)).

### Dynamics of Josephson Junctions – Resistively and Capacitively Shunted Junction (RCSJ) model

We will now have a closer look at the dynamics of the phase difference. For a realistic description it is crucial that we consider yet again the influences of the junction environment resulting in additional current contributions:

*i.* At finite temperatures, the thermal break-up of Cooper pairs results in normal conducting quasiparticles. These follow Ohm's law and lead to a normal conductance $G_\mathrm{N} = 1/R_\mathrm{N}$ within the Josephson junction whenever a voltage is applied.

*ii.* A tunnel contact made of two metals facing each other forms a capacitor with a capacity of $C$. Therefore time changing voltages ($\dot{V} \neq 0$) produce a displacement current $I_\mathrm{D} = C\dot{V}$.

*iii.* Additionally, fluctuations can lead to currents represented by a current noise source $I_\mathrm{F}$.

The *resistively and capacitively shunted junction* (RCSJ) model takes all these three components together with the supercurrent into account, resulting in the equivalent circuit shown in Fig. 2.7(a). The total current is determined using Kirchhoff's law as

$$I(t) + I_\mathrm{F} = I_\mathrm{c} \sin\varphi(t) + \frac{\hbar}{2eR_\mathrm{N}}\dot{\varphi}(t) + C\frac{\hbar}{2e}\ddot{\varphi}(t)\,. \tag{2.58}$$

Rewriting this equation leads to the still nonlinear but traceable differential equation

$$\left(\frac{\hbar}{2e}\right)^2 C\ddot{\varphi} + \left(\frac{\hbar}{2e}\right)^2 \frac{1}{R_\mathrm{N}}\dot{\varphi} + \frac{\mathrm{d}}{\mathrm{d}\varphi}\left[E_\mathrm{J0}\left[1 - \cos\varphi - \tilde{I}\varphi + \tilde{I}_\mathrm{F}\varphi\right]\right] = 0\,. \tag{2.59}$$

In this equation we recover the classical equation of motion $m\ddot{x} + \zeta\dot{x} + \nabla E_\mathrm{pot} = 0$ for a particle with mass $m$, moving under the influence of Stokes friction $\zeta$ in a one-dimensional potential $E_\mathrm{pot}$. The mass, the friction, and the potential can be identified as

$$m = \left(\frac{\hbar}{2e}\right)^2 C\,, \quad \zeta = \left(\frac{\hbar}{2e}\right)^2 \frac{1}{R_\mathrm{N}}\,, \quad E_\mathrm{pot} = E_\mathrm{J0}\left[1 - \cos\varphi - \tilde{I}\varphi + \tilde{I}_\mathrm{F}\varphi\right]\,. \tag{2.60}$$

We recognize the tilted washboard potential again, supplemented by a term for the fluctuation current. This can now be interpreted as shown in Fig. 2.7(b). If zero current flows through the junction the potential is flat (*blue* curve) and the phase is trapped in a potential minimum, meaning it is constant. By increasing the current, the potential will tilt[4]. If the critical current is exceeded, the local extrema disappear and the junction enters a running phase state (*green* curve). Hence this current where the transition from the trapped in the running state happens is often referred to as switching current $I_\mathrm{S}$. A trapped phase is

[4]From the mathematically correct point of view this is a shear transformation.

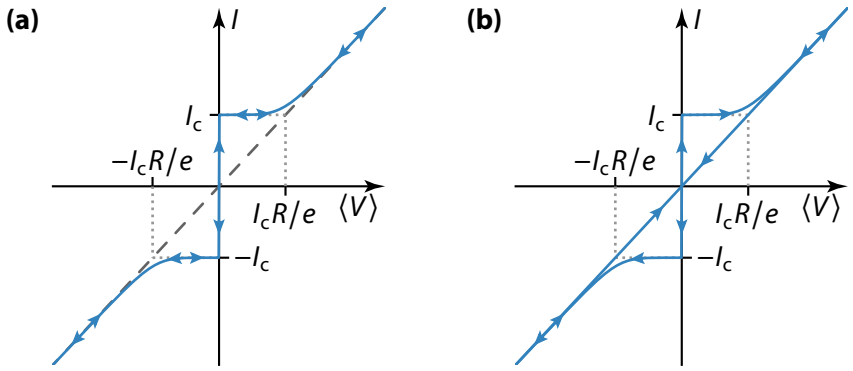


**Figure 2.8 | Current-voltage characteristics of Josephson junctions. (a)** Overdamped junction. **(b)** Underdamped junction. The direction of the current variation is indicated by arrows. In the style of [84].

associated with the dc Josephson effect and a running phase with the ac Josephson effect. In the transition area (*orange* curve) where the potential still exhibits minima, the phase remains constant, but the probability increases that the phase can tunnel through the potential or overcome it by thermal excitation. Depending on the damping $\zeta$, this inertia can be sufficient to change the junction into the running state. Therefore $I_S$ is a statistical quantity, which explains why a distinction from the critical current is useful.

When the current is subsequently reduced again, the phase is retrapped in one of the reappearing minima. The exact retrapping current $I_R$ at which this happens depends on the momentum associated with the phase in the RCSJ model, i.e. the mass and friction of the phase. With the help of the Stewart-McCumber parameter $\beta_c = 2eI_cR_N^2C/\hbar$, the two cases of an overdamped and underdamped junction can be distinguished. For $\beta_c \ll 1$ the junction capacitance and (or) the resistance is small and thus in the analogy the mass $m \propto C$ is small and (or) the damping $\zeta \propto 1/R_N$ is large. In this case the phase will quickly leave the running state and will be trapped in a minimum at $I_R \approx I_c$ (see Fig. 2.8(a)). We call this an overdamped junction [84]. In the opposite case of $\beta_c \gg 1$ (shown in Fig. 2.8(b)) the junction is underdamped, if the capacitance and (or) resistance is large and thus the mass is large and (or) the friction is small. Thereby the retrapping will occur much later $I_R \ll I_c$, the latest when the slope of the washboard changes sign by reversing the polarity. The difference between $I_S$ and $I_R$ introduces a hysteresis in measurements. The time-averaged voltage of the *ac* Josephson effect takes the form $\langle V(t)\rangle = I_cR_N\sqrt{(I/I_c)^2 - 1}$. Therefore it is possible to determine the critical current from the time-averaged voltage-current measurement. The product of critical current and normal state resistance itself is a constant. For a junction with identical superconductors on either side of the barrier, this constant is given by the Ambegaokar-Baratoff relation [85]

$$I_cR_N = \frac{\pi}{2e}\Delta(T)\tanh\left(\frac{\Delta(T)}{2k_BT}\right). \tag{2.61}$$

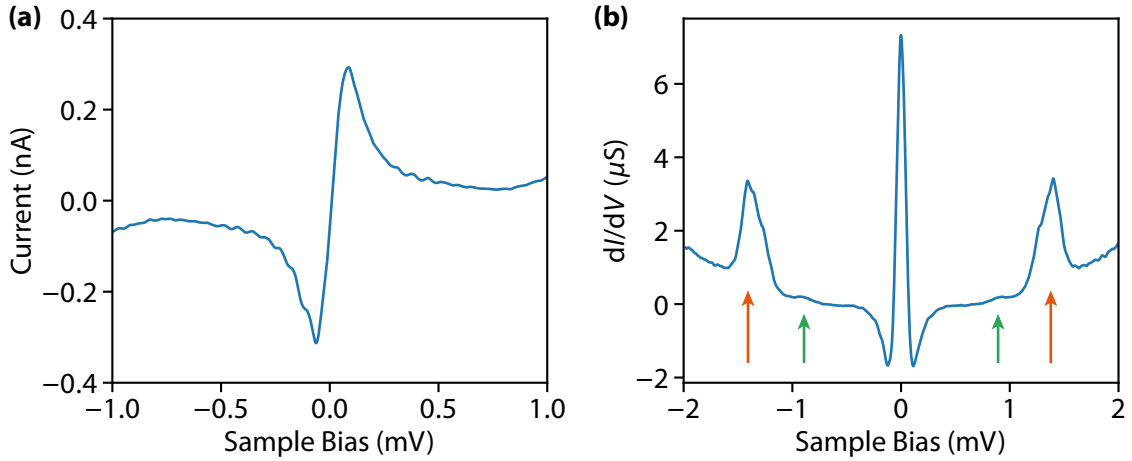


**Figure 2.9 | Voltage-biased Josephson spectrum. (a)** $I(V)$ characteristic of the Josephson effect in a Pb-Pb tunnel junction. The maximum Josephson current is not reached at $V = 0$ but shortly above it. **(b)** Corresponding differential conductance of (a). The negative differential conductance is a sign of an underdamped junction $\beta_c > 1$. The arrows mark the positions of Andreev resonances for $k = 2$ (*orange*) and $k = 3$ (*green*) (see section 2.5). Current and $dI/dV$ were recorded in a scanning tunneling microscope junction above a Pb(111) surface (see methods in Chapter 3). Setpoint: $V_{Bias} = 5$ mV, $I = 60$ nA, $V_{Lock\text{-}in} = 20$ μeV.

As the critical current is directly related to the superconducting order parameter $\Delta$, this spectroscopy is a measure to probe the superconducting ground state on the local scale [39].

## Voltage-Biased Josephson junctions

In the previous section, the description of Josephson junctions was based on current-biased junctions, where the voltage $V(I)$ is a function of the current. The spectroscopic features change if the junctions are operated with a voltage source instead of a current source, hence the current $I(V)$ becomes a function of the voltage. For a McCumber parameter $\beta_c < 1$, the $V(I)$ dependence has the voltage jump to $V = 0$ at $I = I_c$ (Fig. 2.8(a)). The $I(V)$ dependence has the corresponding current plateau $I = I_c$ at voltages a bit higher than zero. In contrast, for a McCumber parameter $\beta_c > 1$, this shift of the maximal current to $V \neq 0$ is still present as can be seen in the shown voltage-biased Josephson spectra in Fig. 2.9(a). In the $V(I)$ dependence the underdamped junction exhibits a hysteresis as shown in (Fig. 2.8(b)). A corresponding range with a negative differential conductance is observed in the I(V) dependence due to the difference between retrapping and critical current. This negative differential conductance (NDC) accompanying the Josephson peak is a very characteristic feature present in the $dI/dV$ measurements of voltage-biased junctions (Fig. 2.9(b)). In these junctions also the maximum current is no longer a direct measure of the critical current.

By considering the electromagnetic environment in a model-like form as shown in Fig. 2.7(a) the complicated behavior of the supercurrent in a voltage-biased junction can be described in the framework of the P(E) theory [86]

$$I(V) = 2e\left(\frac{E_{J0}}{2\hbar}\right)^2 2\pi\hbar\left[P(2V) - P(-2V)\right], \tag{2.62}$$

where

$$P(E) = \frac{1}{2\pi\hbar}\int \mathrm{d}\tau e^{\mathrm{i}E\tau/\hbar + J(\tau)}. \tag{2.63}$$

This function represents the probability that a tunneling electron will generate an excitation by interacting with its environment. It contains the equilibrium phase correlation function, in which the junction capacitance was neglected for simplicity [87]

$$J(\tau) = 2\int \frac{\mathrm{d}\omega}{\omega}\frac{R}{R_Q}\left\{\coth\frac{\beta\hbar\omega}{2}\left[\cos\omega\tau - 1\right] - \mathrm{i}\sin\omega\tau\right\}. \tag{2.64}$$

## 2.5 Andreev Reflection

An interface effectively represents a potential at which particles can be reflected. The situation at an interface containing a superconductor is even more special. We now take a closer look at an electron coming from the normally conducting side towards a normal-superconductor interface.

Seen from the energetic perspective, an electron can enter the quasiparticle states of the superconducting material as long as its energy is above the gap $|E| > \Delta$. The situation differs for energies smaller than the gap $|E| < \Delta$. Because of the lack of available quasiparticle states, the superconductor is like an insulator for such electrons and one would think that only the reflection of the electron remains (Fig. 2.10(a)). The solution of the Bogoliubov-de Gennes Hamiltonian in Eq. (2.37) has another surprising solution, known as Andreev reflections. With a certain probability, a hole is reflected with opposite spin and opposite momentum relative to the incoming electron (Fig. 2.10(b)). As a counterpart for the reflected hole, an electron is added to the superconducting condensate and forms a Cooper pair with the incident electron. The reverse process with the annihilation of a Cooper pair works equivalent. Since the number of electrons in the superconductor is not an exactly defined quantity, the superconductor can absorb or emit electrons and holes without changing its state, but it can only do so in pairs [88].

### Andreev Bound States

When we return to the superconductor-superconductor junction, we get a situation where this process of Andreev reflection can be repeated by itself. It is reflected back and forth between the two superconductors by continuously annihilating Cooper pairs on one side

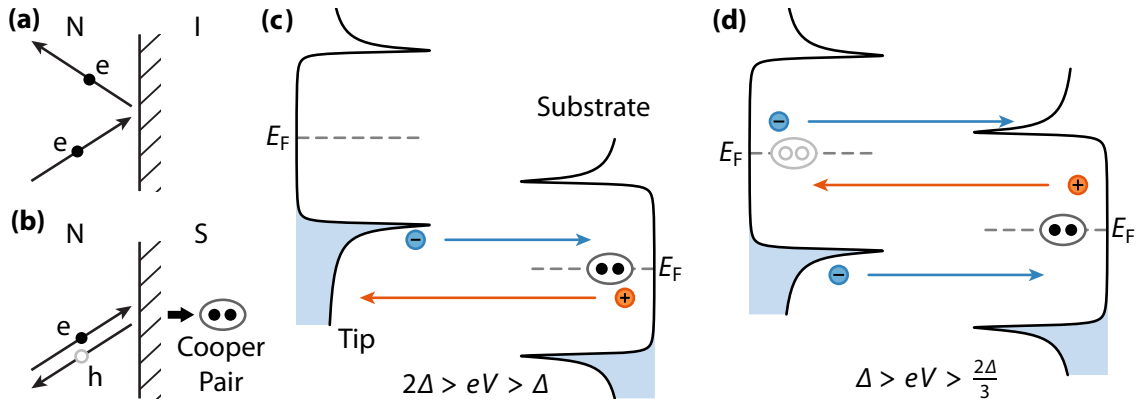


**Figure 2.10 | Andreev reflections and Andreev-bound states. (a)** Reflection of an electron at an normal-insulator interface. **(b)** At a NS interface the electron can be reflected as a hole in the process of Andreev reflections creating a Cooper pair in the superconductor. **(c)** and **(d)**: Andreev-bound states with an applied bias voltage $V$ for one reflection or correspondingly two reflections.

and generating them on the other (theoretically treated in [89]). In fact, this describes a supercurrent over the junction and thus contributes to the Josephson effect.

If a finite voltage $V$ is applied to the junction, the energy of the tunneling electron or the reflected hole is increased by $eV$ with each tunneling. Therefore a multiple Andreev reflection of electrons and holes can increase its energy arbitrarily for finite bias voltages. With an odd number of reflections, an electron-like quasi-particle from the occupied states of one of the two superconductors can therefore be transferred as a hole into unoccupied states of the same superconductor (shown in Fig. 2.10(c) for a single reflection, using that the unoccupied states of the hole density of states are the occupied states of the electron density of states). For an even number of reflections, the electron-like quasi-particle is transferred to the empty states of the opposite superconductor (shown in Fig. 2.10(d) for two reflections). It can be seen that new transport channels are opened at multiples of $eV$, which leads to so-called Andreev bound states at

$$2\Delta = k\, e\,|V| \quad \Rightarrow \quad e\,|V| = \frac{2\Delta}{k} \quad \text{with} \quad k = 2, 3, 4, \ldots , \tag{2.65}$$

as can be seen in Fig. 2.9(b) for $k = 2$ (*orange* arrow) and $k = 3$ (*green* arrow) as resonance in the tunneling spectrum. For $k = 1$ the quasiparticles are transferred directly from one superconductor to the other. As higher orders of multiple Andreev reflections result in repeated passing of the tunnel barrier, their probability decreases $\propto |T|^{2k}$ in its strength accordingly.

## 2.6 Magnetic Impurities on Superconductors – Local Pair Breaking Potential

Single magnetic adatoms in s-wave superconductors scatter conduction electrons, which will affect the order parameter. This problem in the theory of superconductivity was first investigated in the late 1960s by L. Yu, H. Shiba, and A. I. Rusinov (YSR) [30–33]. The magnetic impurities inserted can bind in-gap, spin-polarized electrons, in the so-called localized Yu-Shiba-Rusinov (YSR) states. Early pioneering experimental STM studies investigating these states on single Manganese (Mn) and Gadolinium (Gd) adatoms on a Niobium (Nb) single crystal surface at 4 K were conducted by A. Yazdani in the group of D. M. Eigler [34, 90] followed by investigations on high-$T_c$ superconductors [90–92]. The use of superconducting tips enabled experiments with increased energy resolution [36, 93], which provided the foundation of recent developments on YSR states [35]. Especially, since YSR states have been proposed as building blocks for topological superconductors, they have become a very active field of research.

### 2.6.1 Yu-Shiba-Rusinov States

First of all, an impurity atom has a different electronic configuration than the substrate and therefore interacts with the conduction electrons via a Coulomb potential $V$. In metals, the Coulomb interaction of an impurity at $\mathbf{r}_0$ is screened by the conduction electrons on length scales of the atomic lattice spacing, so the potential can be assumed to be local $V(\mathbf{r}) = V_0\,\delta(\mathbf{r}-\mathbf{r}_0)$. In Nambu space it has the same matrix structure as the chemical potential (compare Eq. (2.49)), thus also like $\xi_{\mathbf{k}}$[81], so that

$$V(\mathbf{r}) = V_0\tau_z\,\delta(\mathbf{r}-\mathbf{r}_0)\,. \tag{2.66}$$

Furthermore, if the impurity atom has a magnetic moment, there is an exchange interaction $V_{\mathrm{mag}}$ between the local spin and the conduction electrons on top of the electrostatic interactions. This magnetic interaction will break the time-reversal symmetry in the superconductor and thus locally disturb the Cooper pair condensate, creating a bound state – what we refer to as the YSR state. The local magnetic moment of an atom results from single occupied states. In a classical spin model, the spin $\mathbf{S}$ of the atom is bound to the electrons of the superconductor by an exchange coupling $J(\mathbf{r})$. Hence, the exchange interaction becomes $V_{\mathrm{mag}} = J(\mathbf{r})\mathbf{S}\cdot\mathbf{s}$, with the electron spin operator $\mathbf{s}$ in four-component vector notations [94]. This interaction leads to electrons with opposite spin compared to the atom's spin being attracted – a parallel spin is repelled. Consequently, this interaction competes with the pairing energy $\Delta$ of the superconductor. Depending on the strength of the coupling compared to the pairing energy, two regimes can be distinguished. The *free-spin* state (Fig. 2.11(a)) if the coupling is small compared to the pairing energy and the Cooper pairs are hardly disturbed. And the *screened-spin* state (Fig. 2.11(c)), in which a Cooper pair is broken due to the coupling and the spin of the impurity is shielded by a

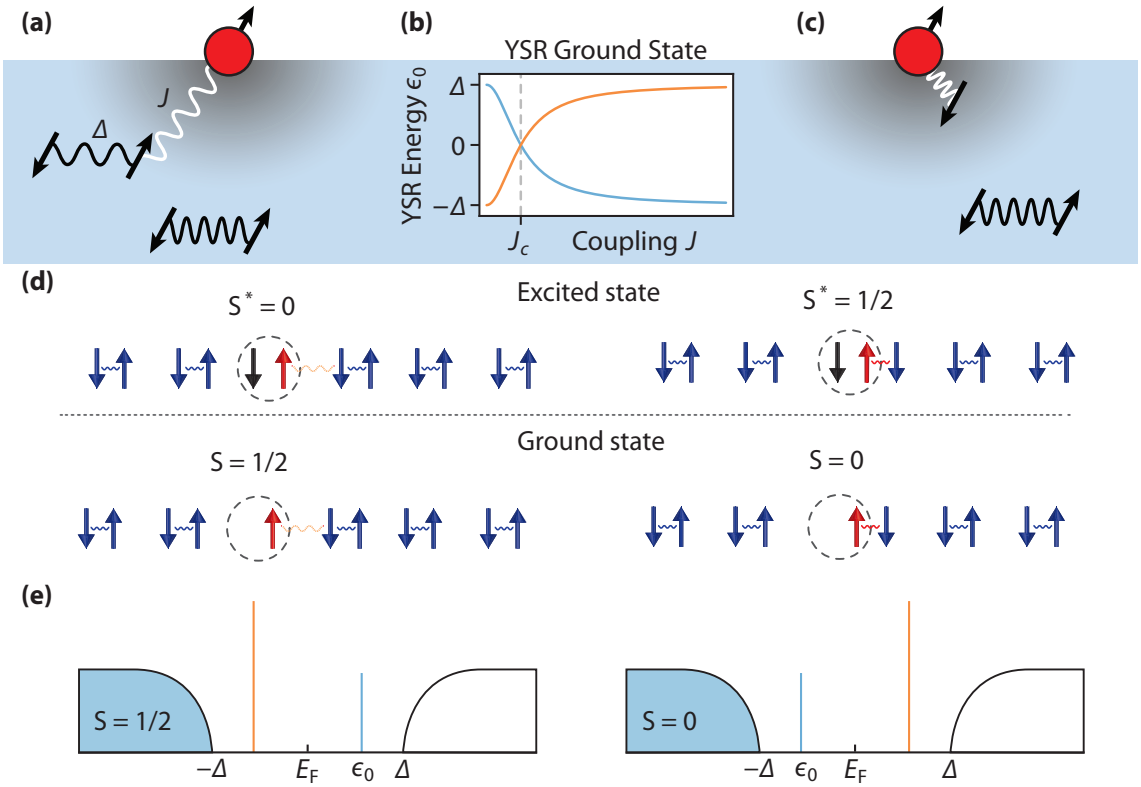


**Figure 2.11 | Formation of Yu-Shiba-Rusinov states.** Depending on the relationship between exchange coupling $J$ and pairing energy $\Delta$, the impurity is found in **(a)** *free-spin* (corresponding to the left side of the figure) or **(c)** *screened-spin* state (right side). **(b)** Dependence of the YSR energy $\epsilon_0$ on the exchange coupling. **(d)** Excitation processes induced by tunneling electrons (*Black* arrows). In the case of a free spin, the electron induces a transition from the coherent many-body ground state with spin $S = 1/2$ to the excited state with $S^* = 0$. In the screened spin state, the screening exchanges the spin values associated with the ground and excited states. **(e)** $|u_\epsilon|^2$ and $|v_\epsilon|^2$ can be probed as in-gap states in the BCS local density of states. In the style of [35].

quasiparticle. By adjusting the coupling strength the system can undergo a quantum phase transition [95], as shown in Fig. 2.11(b).

Both described interactions can be included into the Hamiltonian by means of the Dyson equation $\left[G_{\mathrm{R}}^{\mathrm{r}}\right]^{-1} = \left[G_{\mathrm{R0}}^{\mathrm{r}}\right]^{-1} + J\mathbf{S}\cdot\mathbf{s} - V_0\tau_{\mathrm{z}}$. The Bogoliubov-deGennes Hamiltonian of the magnetic moment embedded in the superconductor is given by [81, 96]

$$\mathcal{H} = \xi_{\mathbf{k}}\tau_{\mathrm{z}} + \left[V_0\tau_{\mathrm{z}} - J\mathbf{S}\cdot\sigma\right]\delta(\mathbf{r}-\mathbf{r}_0) + \Delta\tau_{\mathrm{x}}\,, \tag{2.67}$$

where $\sigma = (\sigma_{\mathrm{x}}, \sigma_{\mathrm{y}}, \sigma_{\mathrm{z}})$ are the Pauli matrices that act in the spin space. By choosing the impurity spin $S$ to point along the z direction, this $4\times4$ Hamiltonian can be split into two independent $2\times2$ blocks $\mathcal{H}_{\pm}$ for spin up $(+)$ and spin down $(-)$ [35, 82]

$$\mathcal{H}_{\pm} = \xi_{\mathbf{k}}\tau_{\mathrm{z}}\left[V_0\tau_{\mathrm{z}} \mp JS\right]\delta(\mathbf{r}-\mathbf{r}_0) + \Delta\tau_{\mathrm{x}}\,. \tag{2.68}$$

Solving for the bound-state spectrum results in finding of a subgap solution of $\mathcal{H}_{\pm}$ at energy $\epsilon_0$ corresponding to the poles of the Green's function $G^{\mathrm{r}}$ [81]

$$\epsilon_0 = \pm\Delta\frac{1-\alpha^2+\beta^2}{\sqrt{(1-\alpha^2+\beta^2)^2+4\alpha^2}}\,, \tag{2.69}$$

with introducing the dimensionless parameters $\alpha = \pi\rho_0 JS > 0$ and $\beta + \pi\rho_0 V_0$. The wave function $\langle\mathbf{r}|\psi_{\mathrm{YSR}}\rangle = \begin{pmatrix} u_\epsilon(r) & v_\epsilon(r)\end{pmatrix}^T$, which corresponds to these eigenvalues, describes a quasiparticle, that can be excited by the tunnel current (Fig. 2.11(d)). The excitation is given by the Bogoliubov operator $\gamma = u_\epsilon^* c_\uparrow - v_\epsilon c_\downarrow^\dagger$. The individual wave functions $u_\epsilon$ and $v_\epsilon$ of the electron-like and hole-like YSR excitations are described as [35]

$$u_\epsilon(r), v_\epsilon(r) \propto \frac{\sin(k_{\mathrm{F}}r + \delta^{\pm})}{k_{\mathrm{F}}r}\exp\left[-\frac{r}{\xi_{\mathrm{GL}}}\left|\sin(\delta^+ - \delta^-)\right|\right]. \tag{2.70}$$

The YSR wave functions are typically phase shifted by $\delta^{\pm}$. They have an oscillating character, determined by the Fermi wave vector $k_{\mathrm{F}}$ and their total decay length is given by the superconducting Ginzburg-Landau coherence length $\xi_{\mathrm{GL}}$ and $k_{\mathrm{F}}$. The energy of the bound states is related to the difference of the scattering phase shift, namely [35]

$$\epsilon_0 = \Delta\cos(\delta^+ - \delta^-)\,. \tag{2.71}$$

Particularly, with a STM we have the possibility to probe $|u_\epsilon|^2$ and $|v_\epsilon|^2$ as amplitudes of the in-gap peaks that form symmetrically around the Fermi energy in the quasiparticle spectrum (Fig. 2.11(e)).

## 2.6.2 Self Energies due to Relaxation Processes and Tunneling Processes.

According to Section 2.2.2 the line width of excitations in a tunneling experiment is determined by the coupling of the electrons to their environment. For the YSR state, we want to discuss two couplings. One is the coupling to the phonons of the hosting substrate and the other is the coupling to the other tunneling electrode which is described by the tunneling coupling.[5]

### Self Energy due to Relaxation Processes

Phonons as well as photons are able to induce relaxation processes of the YSR state, introducing a self energy $\Sigma_{\mathrm{ph}}$ in the substrate. The substrates Green function is approximated by the electron Green's function of Eq. (2.24), with $\epsilon_0$ as eigenenergy and in the basis of the YSR excitations $\langle \mathbf{r}|\psi_{\mathrm{YSR}}\rangle = \begin{pmatrix} u(r) & v(r) \end{pmatrix}^T$. The self energy itself is approximated by its value at $\omega = \epsilon_0$ and only the imaginary part $\Gamma_{\mathrm{Ph}} = 2\,\mathrm{Im}\langle\psi_{\mathrm{YSR}}|\Sigma_{\mathrm{ph}}(\epsilon_0)|\psi_{\mathrm{YSR}}\rangle$ is considered. Within these approximations the YSR state Green's functions read

$$G_{\mathrm{R}}^{\mathrm{r,a}}(\omega) = \frac{|\psi_{\mathrm{YSR}}\rangle\langle\psi_{\mathrm{YSR}}|}{\omega - \epsilon_0/\hbar \mp \mathrm{i}\Gamma_{\mathrm{Ph}}(\epsilon_0)/2}\,. \tag{2.72}$$

We can introduce the rates with which the YSR state is emptied or occupied as $\Gamma_1 = \mathrm{i}\Sigma_{\mathrm{ph}}^{>}(\epsilon_0) = (1 - n_{\mathrm{F}})\Gamma_{\mathrm{Ph}}$ and $\Gamma_2 = -\mathrm{i}\Sigma_{\mathrm{ph}}^{<}(\epsilon_0) = n_{\mathrm{F}}\Gamma_{\mathrm{Ph}}$.

### Self Energy due to Tunneling Processes

The coupling to the opposite tunneling electrode gives rise to a Green's function of the same character as just explained above

$$G_{\mathrm{R}}^{\mathrm{r,a}}(\omega) = \frac{|\psi_{\mathrm{YSR}}\rangle\langle\psi_{\mathrm{YSR}}|}{\omega - \epsilon_0/\hbar \mp \mathrm{i}\Gamma(\epsilon_0)/2}\,, \tag{2.73}$$

where the imaginary part of the self energy $\Gamma(\omega) = \Gamma_{\mathrm{e}}(\omega) + \Gamma_{\mathrm{h}}(\omega) + \Gamma_1 + \Gamma_2$ also contains broadenings due to the tunneling process. These tunneling rates have the following form according to Fermi's golden rule in Eq. (2.26)

$$\Gamma_{\mathrm{e}}(\omega) = \frac{2\pi}{\hbar}T^2|u|^2\rho(\omega_-) \quad \text{and} \quad \Gamma_{\mathrm{h}}(\omega) = \frac{2\pi}{\hbar}T^2|v|^2\rho(\omega_+)\,, \tag{2.74}$$

with $\rho(\omega)$ being the electrode's density of states of the tip and $\omega_\pm = \omega \pm eV$.

[5] This section is based on Ruby *et al.* [97]. Consult the supplement for details.

# 3
# Methods

A scanning tunneling microscope is based on the tunneling effect as it is described in Section 2.1. There is a finite probability for an electron to tunnel through a classically impassable barrier when the wave functions of two electrodes overlap. By using a moving wire with a sharp apex as a tip, an STM takes advantage of this effect to examine a substrate. This chapter deals with the related measuring methods, i.e. the investigation of the substrates topographic structure by scanning tunneling microscopy and the spatial resolution of its spectroscopic features by scanning tunneling spectroscopy. In particular, the spectroscopy on superconductors and the gain in spectroscopic resolution associated with the use of superconducting tips will be discussed.

## 3.1 Scanning Tunneling Microscopy

The STM was invented by G. Binnig and H. Rohrer in 1981 [98, 99], who were awarded the Nobel Prize for their work only five years later. Its invention opened up completely new perspectives in the field of surface physics and revolutionized it. The great strength of the STM is that it works in real space and allows us to study defects and adsorbates together with their dynamics all on the atomic level. This distinguishes it from the majority of other surface techniques that work in reciprocal space and are based on scattering processes. As reciprocal techniques they average over large sample areas, making them only sensitive to periodic structures.

The spatial resolution enables the STM to study phenomena on conducting surfaces at the atomic level and thus to investigate questions such as the origin of superconductivity or magnetism down to the atomic level [100–102]. It provides the opportunity to observe the electronic and magnetic properties of single atoms and molecules on different surfaces [103–106] as well as their manipulation [107] and arrangement in larger ensembles [108, 109]. Inelastic tunneling spectroscopy (IETS) uses the signal from inelastic transport channels

to measure intramolecular vibrations [110–114], electron-phonon coupling [115–117] or chemical reactions on surfaces [118–121]. Moreover, STM has been combined with several other measurement techniques over the last two decades, which have continuously expanded its parameter space and application range. Magnetic fields are used e.g. in combination with IETS of spin excitations to determine the spin state of single atoms and molecules [122]. Pump-probe methods can be used for time-resolved measurements [123]. The combination with X-ray magnetic circular dichroism (XMCD) allowed getting chemical sensitivity on individual adatoms [124]. Shot-noise measurements allow the measurement of fluctuations in the current to investigate its dynamics [125–127]. Light sources such as lasers are used to irradiate THz pulses into the junction, also for the purpose of time-resolved measurements [128–130] and GHz radiation is used to combine STM with electron spin resonance (ESR) [131–136].

As described above, the basic concept of an STM, as shown in Fig. 3.1(a), is simple in itself. It is based on a tip moving over a surface at a vertical distance $d$ of a few Å. At these distances, a net current $I$ is generated by applying a voltage $V$ and making use of the tunnel effect. Therefore both electrodes must be electrically conductive. It is the exponential distance dependence of the current $I \propto \exp(-\kappa d)$, which leads to the high resolution of the scanning tunneling microscope (STM) since even small changes in distance lead to large changes in current. By scanning the surface while the vertical tip position $z$ remains constant, the current measured as a function of the tip's horizontal positions $x$ and $y$ reflects the electronically convolved topography of the surface (Fig. 3.1(b)). This measurement mode is called *constant height* mode and is one of two commonly used modes in STM to image surfaces. In the case of tilted samples or strong corrugations in the topography, there is the risk of accidentally crashing the tip into the surface. To avoid this, the STM can be operated in a second measuring mode, the *constant current* mode (Fig. 3.1(c)). Here, the $z$-position of the tip is readjusted above each point using a feedback loop until the current matches a predefined setpoint value. Hence the tip's $z$ position now carries the topographic information of the surface. Due to the feedback loop, this mode is slower than the constant height mode.

With the knowledge about the tunnel effect, the realization of an STM is well feasible from a physical point of view. However, there are a few things to consider from a technical point of view. Typically, the applied voltages range from several tenths of microvolts for investigating electronic excitations in superconductors to some volts for studying molecular orbitals. As a result of the small tunneling probabilities, the measured currents are only in the range of some picoamperes. To detect such small currents a very precise low noise amplifier is needed. Moreover, to take advantage of the sensitivity of the STM, the tip must be positioned very accurately. Therefore the tip is controlled by three piezo elements, one for each direction in space. By applying a voltage to the piezo elements, the piezoelectric effect causes strain in the sub-nanometer range, allowing for the required degree of precision control. Yet accurate measurement electronics and tip control are useless if external influences introduce large amounts of noise that superimpose the small signals. It is therefore important to protect the system from mechanical vibrations and to filter out electrical interference.

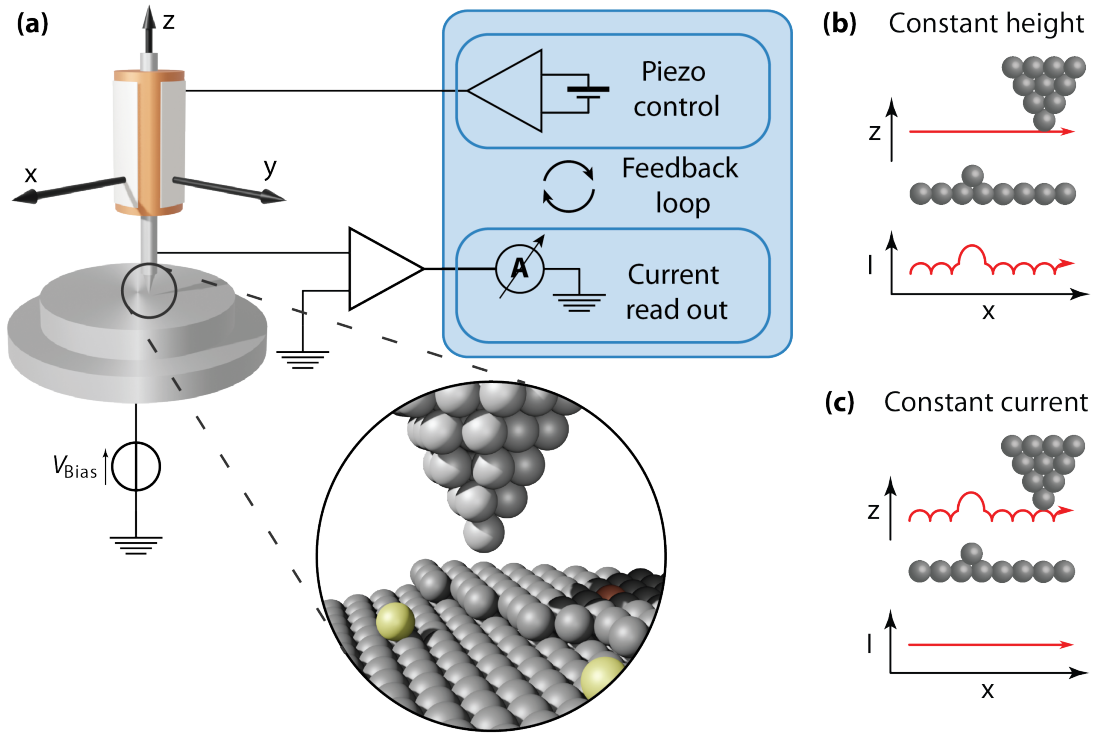


**Figure 3.1 | Principle of a scanning tunneling microscope. (a)** Schematic view of an STM. In the junction between a sharp tip and a surface, a current is measured when applying a voltage $V$. The tip can be moved over the surface by a piezo tube. The tips position can be controlled via a feedback loop, which regulates the height of the tip depending on the measured current. **(b)** & **(c)** The two measurement modes of an STM: In (b) the tip is scanning at a constant height above the sample and is measuring the resulting current due to changes in the topography and electronic structure. In the other mode (c) the height of the tip is regulated via the feedback-loop such that the current is always constant. Therefore the $z$ signal is carrying the topographic information of the sample. In the style of [137].

### 3.1.1 Theory of Scanning Tunneling Microscopy

In Section 2.1.1 we have shown that the tunnel current depends on the spectral functions of tip and sample (see Eq. (2.6)). We also discussed how the spectral function is related to the local density of states (see Eq. (2.16)). Therefore the band structure is considered, in which all states $|k\rangle$ with the same energy are summed up, whereby the exact momentum information is lost ($T_{\mathbf{k}\mathbf{k}'} \to T_\xi$). By means of this approximation we can rewrite the tunneling current as

$$I(V) = \frac{4\pi e}{\hbar} \int_{-\infty}^{\infty} \mathrm{d}\xi \, |T_\xi|^2 \, \rho_\mathrm{L}(\xi) \rho_\mathrm{R}(\xi + eV) \left[ n_\mathrm{F}(\xi) - n_\mathrm{F}(\xi + eV) \right] , \tag{3.1}$$

where $n_\mathrm{F}$ is the Fermi-Dirac distribution and $\xi = \epsilon - \mu$ gives the dispersion relation for measuring the energies $\epsilon$ with respect to the chemical potential $\mu$. This expression can be even further simplified by the assumption of low temperatures, as the Fermi distribution at low temperatures approaches a Heaviside step function and thus the current becomes

$$I(V) = \frac{4\pi e}{\hbar} \int_{0}^{eV} \mathrm{d}\xi \, |T_\xi|^2 \, \rho_\mathrm{L}(\xi) \rho_\mathrm{R}(\xi + eV) \, . \tag{3.2}$$

For small voltages the matrix element $|T_\xi| \to |T|$ does not change significantly over the integration range. Thus, we can approximate it as energy independent and put it in front of the integral. In essence we have learned that we can conceptually interpret the tunneling current as a convolution of tip and substrate density of states.

Nevertheless it is crucial for the interpretation of the topographies to have an understanding of the tunneling matrix element, so that a comparison between different measuring points becomes possible. The WKB approximation from Eq. (2.5) provides a first estimation for the tunneling matrix element. It assumes that only electron states near the $\Gamma$ point of the surface Brillouin zone contribute to tunneling. If the latter condition is not met, the equation should be supplemented by the parallel momentum $k_\parallel$ of the surface electronic state [138]

$$\kappa = \sqrt{\frac{2m_\mathrm{e}}{\hbar^2} \left( \bar{\Phi} + \frac{eV}{2} - \xi_{\mathbf{k}'} \right) + k_\parallel^2} , \tag{3.3}$$

where $\bar{\Phi} + eV/2$ gives the average barrier height including the average work function $\bar{\Phi}$.

Additionally, the well-defined geometry of the STM contact allows us to further specify the tunneling matrix element. Tersoff and Hamann developed a complex, but essentially more accurate model compared to the very fundamental WKB approach [139]. In their work, they used the transfer Hamiltonian formalism and extended it by assuming explicit wave functions for tip and substrate. The model is valid for tips with an *s*-wave character. Furthermore, they characterized the tip only by the *s*-wave orbital of its last atom, which is a justified assumption, because due to the exponential distance dependence it can be assumed that almost all tunneling current flows through this last atom. By this, they reduced the geometry of the tip, as shown in the schematic drawing in Fig. 3.2(a), to a sphere with

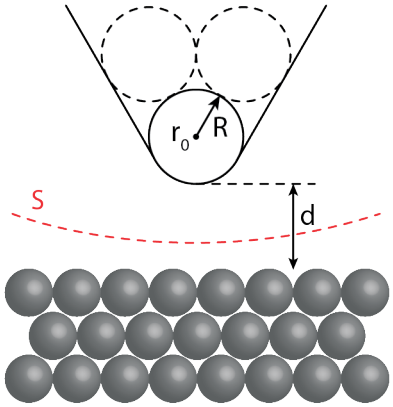


**Figure 3.2 | Model of Tersoff and Harmann.** Schematic of the assumed tunneling geometry. The end of the tip is approximated by a sphere with a radius of *R*. The shortest distance to the sample is marked *d* and the center of the curvature is $\mathbf{r}_0$. The surface **S** indicates a possibility for the differential to calculate the matrix element. In the style of [139].

radius $R$ at location $\mathbf{r}_0$. This is to approximate the curvature of the tip apex at the closest point to the substrate. The local spherical wave function has the form

$$\Psi_{\mathrm{L}}(\mathbf{k},\mathbf{r}) = \frac{1}{\sqrt{\mathcal{V}_{\mathrm{L}}}} c_{\mathrm{L}} \kappa R e^{\kappa R} \frac{e^{-\kappa|\mathbf{r}-\mathbf{r}_0|}}{\kappa\,|\mathbf{r}-\mathbf{r}_0|}\,, \tag{3.4}$$

where $\mathcal{V}_{\mathrm{L}}$ is the volume of the probe and $\kappa = \sqrt{2m_{\mathrm{e}}\Phi/\hbar^2}$ is the inverse decay length with the work function $\Phi$. For the wave function of the substrate they assumed a Bloch wave, which decays exponentially into vacuum along the normal direction $\mathbf{r}_\perp$

$$\Psi_{\mathrm{R}}(\mathbf{k},\mathbf{r}) = \frac{1}{\sqrt{\mathcal{V}_{\mathrm{R}}}} \sum_{\mathbf{G}} a_{\mathbf{G}} e^{-\sqrt{\kappa^2+|\mathbf{k}_\parallel+\mathbf{G}|^2}|\mathbf{r}_\perp|} e^{\mathrm{i}(\mathbf{k}_\parallel+\mathbf{G})\cdot\mathbf{r}_\parallel}\,, \tag{3.5}$$

where $\mathcal{V}_{\mathrm{R}}$ is the sample volume, $\mathbf{k}_\parallel$ the surface Bloch wave vector and $\mathbf{G}$ the reciprocal surface lattice vector with some normalization factors $a_{\mathbf{G}}$. In addition, the work function for the probe and substrate are assumed to be identical for the sake of simplicity. Using the two expressions for the wave functions, the tunnel matrix element is calculated on the basis of Eq. (2.4) by integrating over the surface **S** as

$$T_{\mathbf{k}\mathbf{k}'} = \frac{\hbar^2}{2m_{\mathrm{e}}} \frac{4\pi}{\kappa\sqrt{\mathcal{V}_{\mathrm{L}}}} \kappa R e^{\kappa R} \Psi_{\mathrm{R}}(\mathbf{k}',\mathbf{r}_0)\,. \tag{3.6}$$

The current now takes the form

$$I(V) \propto \frac{e^2 V}{\hbar} \Phi^2 \rho_{\mathrm{L}}(\mu) \rho_{\mathrm{R}}(\mu, \mathbf{r}_0), \quad \text{with} \quad \rho_{\mathrm{R}}(\xi, \mathbf{r}_0) = \sum_{\mathbf{k}'} |\Psi_{\mathrm{R}}(\mathbf{k}', \mathbf{r}_0)|^2 \, \delta(\xi_{\mathbf{k}',\mathrm{R}} - \xi). \quad (3.7)$$

In conclusion this shows, that the tunneling current is directly proportional to the DoS $\rho_{\mathrm{L}}(\xi)$ of the tip and the LDoS $\rho_{\mathrm{R}}(\xi, \mathbf{r}_0)$ of the substrate at the position $\mathbf{r}_0$ of the tip. The exponential decay of the tunnel current is reflected in the location dependency of $\rho_{\mathrm{R}}$ as defined in Eq. (3.5). By means of controlled tip formings, the DoS can be optimized. Especially for metallic tips and small bias ranges around the chemical potential it is possible to get a constant DoS. Therefore Eq. (3.7) allows the straightforward interpretation of the measured constant-current image as topography of the sample LDoS at the chemical potential.

It is worth noting that while the assumption of an *s*-wave tip is a good approximation for most metal tips, modifying the tip material so that it exhibits *p*- or *d*-orbital character may have additional benefits. For example, with the very common tungsten tips, the d-wave orbitals contribute a large part of the tunnel current, which leads to better topographic resolution [140]. Additionally, studies with functionalized tips have shown that chlorine atoms [141] at the apex of the tip can significantly increase the lateral resolution through their *p*-wave orbital. To describe this in the context of Tersoff and Harmann, adapted matrix elements are needed.

Evaluating the tunneling current given by Eq. (3.1) for two normal conducting metal electrodes gives

$$I_{\mathrm{N}} = \frac{4\pi e}{\hbar} |T|^2 \rho_{\mathrm{n,L}}(0) \rho_{\mathrm{n,R}}(0) \int_{-\infty}^{\infty} \mathrm{d}\xi [n_{\mathrm{F}}(\xi) - n_{\mathrm{F}}(\xi + eV)] \quad (3.8)$$

$$= \frac{4\pi e}{\hbar} |T|^2 \rho_{\mathrm{n,L}}(0) \rho_{\mathrm{n,R}}(0) eV = G_{\mathrm{N}} V. \quad (3.9)$$

Since the normal conducting density of states is usually energy independent, it is possible to put it in front of the integral, like the tunneling probability, for which we just discussed, that it can be considered energy independent for small bias voltages. The junction becomes an ohmic contact with a clearly defined normal state conductance, which is independent of the voltage $V$. Assuming two identical electrodes, the normal state conductance is

$$G_{\mathrm{N}} = G_0 4\pi^2 (\rho_0 |T|)^2, \quad (3.10)$$

with $G_0 = 2e^2/h = (12.91\,\mathrm{k\Omega})^{-1} = 77.48\,\mu\mathrm{S}$ being the conductance quantum.

## 3.2 Scanning Tunneling Spectroscopy

Apart from the ability of an STM to resolve the sample's topographic information with atomic resolution, scanning tunneling spectroscopy (STS) is another major application and

a powerful tool to study locally the electronic properties of the surface. Therefore the tip is positioned over the location to be examined before disabling the feedback loop for the constant height mode. Subsequently, the current or differential conductance is recorded while the bias voltage is swept through the desired range of values. Its main working principle is presented in the following part, together with a discussion of some details of its practical implementation, such as the lock-in technique and the energetic resolution that can be achieved within STS.

### 3.2.1 Theory of Scanning Tunneling Spectroscopy

The dependence of the tunnel current on the LDoS of the tip and substrate has already been discussed in the previous section and can be seen in Eq. (3.2). The integration considers all states between the chemical potential and the energy $eV$ to calculate the total current. To resolve the contribution of the states to the current as a function of their respective energy, we study the derivative of the current with respect to the bias voltage [138, 142]

$$\begin{aligned}\frac{\mathrm{d}I}{\mathrm{d}V} \propto\ & |T|^2 \rho_\mathrm{L}(\xi)\rho_\mathrm{R}(\xi+eV) \\ & + \int_0^{eV} \mathrm{d}\xi \frac{\mathrm{d}|T|^2}{\mathrm{d}V} \rho_\mathrm{L}(\xi-eV)\rho_\mathrm{R}(\xi) \\ & + \int_0^{eV} \mathrm{d}\xi |T|^2 \rho_\mathrm{R}(\xi) \frac{\mathrm{d}\rho_\mathrm{L}(\xi')}{\mathrm{d}\xi'}\,.\end{aligned} \tag{3.11}$$

Assuming small bias voltages ($eV \ll \Phi$) and also small longitudinal tunnel energies $\xi_\nu - \frac{\hbar^2 k_\parallel^2}{2m_\mathrm{e}}$ in comparison to the barrier height, the matrix element becomes constant and the second term on the right hand side in Eq. (3.11) is negligible. In general, the tunnel conductance contains convoluted information of the band structures of tip and sample. In the special case of constant LDoS of the tip the differential conductance becomes

$$\frac{\mathrm{d}I}{\mathrm{d}V} \propto |T|^2 \rho_\mathrm{L}(0)\rho_\mathrm{R}(\xi+eV) \propto \rho_\mathrm{R}(\xi+eV)\,, \tag{3.12}$$

which may be the case for normal conducting metallic tips as already mentioned. For such tips, the $\mathrm{d}I/\mathrm{d}V$ signal is a direct measure of the LDoS of the substrate.

### 3.2.2 Spectroscopy with a Lock-In Amplifier

To measure the differential conductance ($\mathrm{d}I/\mathrm{d}V$) we use a lock-in amplifier. This measurement method is generally used to measure very small *ac* signals. Precise measurements of these signals are possible even if the signal is obscured by noise, which can be orders of magnitude larger than the signal of interest [143]. As a result, measurements with a lock-in amplifier benefit from an improved signal-to-noise ratio.

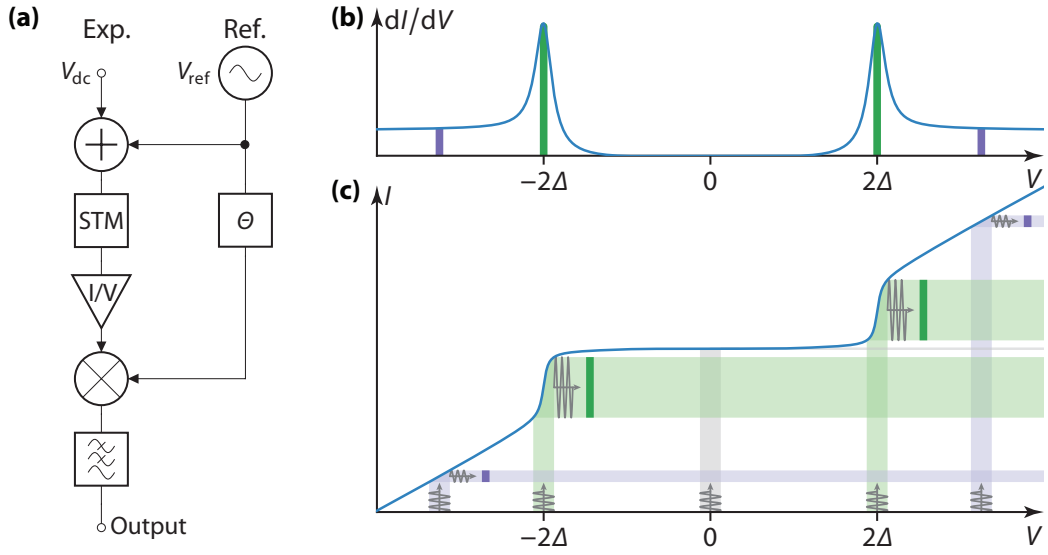


**Figure 3.3 | Functional principle of a lock-in amplifier for measuring the differential conductance. (a)** Equivalent circuit diagram of a lock-in consisting of adder, phase sensitive detection unit (PSD) and additional signal path for the reference signal. **(b)** and **(c)**: Here, the functional principle is demonstrated at a superconductor-superconductor spectrum. A sinusoidal *ac* voltage $V_{ac}(t)$ is added as modulation to the *dc* bias voltage $V_{dc}$. This also makes the current oscillate $I(V_{dc} + V_{ac}(t))$. The lock-in amplifier is sensitive to the *ac*-component of this current, which for small modulations is proportional to the slope of the $I(V)$ curve and thus reflects the $dI/dV$ signal shown in (b). In the regions of the coherence peaks, the slope is highest, which leads to a strong $dI/dV$ signal, compared to the disappearance signal in the gap where the current slope is zero (compare ratio between *green* and *violet* bars in the curves for $I(V)$ and $dI/dV$ $(V)$). In the style of [144].

In order to understand how an *ac* signal is generated in the junction, which can then be detected with the lock-in technique, a block diagram of the measurement is shown in Fig. 3.3(a). In an adder a small sinusoidal *ac* modulation $V_{ac}(t)$ is added to the *dc* bias voltage $V_{dc}$. After it has passed through the STM, the measured current is converted by the low noise amplifier into a voltage proportional to the current. In parallel to the experimental signal path, the *ac* modulation is carried as a reference and after a phase shifter, it is multiplied with the experimental signal in the core of the lock-in, the phase sensitive detection unit (PSD). Once it has passed a low-pass filter, the output signal is proportional to the $dI/dV$ signal. The *ac* modulation is given by

$$V_{ac}(t) = \sqrt{2}V_{\text{Lock-In}}\cos(\omega_{mod}t + \Theta_{mod}) = \frac{V_{\text{Lock-In}}}{\sqrt{2}}\left[e^{i(\omega_{mod}t+\Theta_{mod})} + e^{-i(\omega_{mod}t+\Theta_{mod})}\right], \quad (3.13)$$

making use of the complex definition of the cosine. In lock-in amplifiers all input signals are generally measured in units of $V_{RMS}$ (RMS: root mean square). For this reason, the

lock-in modulation amplitude $V_{\text{Lock-In}} = V_{\text{mod}}/\sqrt{2}$ is to be understood as the effective value of the peak-to-peak amplitude $V_{\text{mod}}$.

For small modulation amplitude we can expand the modulated tunnel current in a Taylor series around the *dc* bias voltage $V_{\text{dc}}$, resulting in

$$I(t) = I\left(V_{\text{dc}} + V_{\text{ac}}(t)\right) = I(V_{\text{dc}}) + \underbrace{\left.\frac{\mathrm{d}I}{\mathrm{d}V}\right|_{V=V_{\text{dc}}} V_{\text{ac}}(t)}_{1^{\text{st}}\text{ harmonic}} + \underbrace{\left.\frac{1}{2}\frac{\mathrm{d}^2 I}{\mathrm{d}V^2}\right|_{V=V_{\text{dc}}} \left(V_{\text{ac}}(t)\right)^2}_{2^{\text{nd}}\text{ harmonic}} + \dots . \tag{3.14}$$

Besides the *dc* tunnel current, higher harmonic *ac* current components were generated by modulating the voltage. The first harmonic is proportional to the $\mathrm{d}I/\mathrm{d}V$ signal at $V_{\text{dc}}$. Fig. 3.3(b) illustrates this generation of the first harmonic. Alternatively it is also possible to lock in the second harmonic, which measures the change in conductance.

The device response $I(t)$ and the reference signal are used by the lock-in amplifier to determine the amplitude $R$ and phase $\Theta$ of the response. This is achieved by a so-called dual-phase demodulation circuit within the PSD unit [145]. As the phase relation between response and reference is lost in the STM, we assume the reference also in its general form to be

$$V'_{\text{ref}}(t) = \sqrt{2} V_{\text{Lock-In}} \cos(\omega_{\text{ref}} t + \Theta_{\text{ref}}) . \tag{3.15}$$

The dual-phase demodulation circuit splits the input signal and multiplies it separately with the reference signal and a 90° phase-shifted copy of it. Mathematically this corresponds to a mixing with the complex reference signal

$$V_{\text{ref}}(t) = \sqrt{2} V_{\text{Lock-In}} e^{-\mathrm{i}(\omega_{\text{ref}} t + \Theta_{\text{ref}})} = \sqrt{2} V_{\text{Lock-In}} \left[\cos(\omega_{\text{ref}} t + \Theta_{\text{ref}}) - \mathrm{i}\sin(\omega_{\text{ref}} t + \Theta_{\text{ref}})\right] . \tag{3.16}$$

By focusing on the first harmonic of the tunnel current in Eq. (3.14) one can see that the response of the STM after mixing is a complex signal of the form

$$\begin{aligned} Z(t) = X(t) + \mathrm{i}Y(t) &= \frac{\mathrm{d}I}{\mathrm{d}V} V_{\text{ac}}(t) V_{\text{ref}}(t) \qquad (3.17) \\ &= \frac{\mathrm{d}I}{\mathrm{d}V} V_{\text{Lock-In}}^2 \Big[ \underbrace{e^{\mathrm{i}\left[(\omega_{\text{mod}} - \omega_{\text{ref}})t + (\Theta_{\text{mod}} - \Theta_{\text{ref}})\right]}}_{=\text{const. for } \omega_{\text{mod}} = \omega_{\text{ref}}} + e^{-\mathrm{i}\left[(\omega_{\text{mod}} + \omega_{\text{ref}})t + (\Theta_{\text{mod}} + \Theta_{\text{ref}})\right]} \Big] , \end{aligned}$$

with $X$ being the in-phase component and $Y$ the quadrature component. Here the working principle of the lock-in amplifier becomes apparent because only if the frequency of the response matches that of the reference signal $\omega_{\text{mod}} = \omega_{\text{ref}}$ the first exponential term is a constant. Since only signals that are nearly time-independent can pass the low pass filter, this is the only remaining signal

$$Z = R \cdot e^{\mathrm{i}\Theta} = \frac{\mathrm{d}I}{\mathrm{d}V} V_{\text{Lock-In}}^2 e^{\mathrm{i}(\Theta_{\text{mod}} - \Theta_{\text{ref}})} . \tag{3.18}$$

The elegance of this method is that all other terms except the first harmonic are also eliminated by the low pass filter, including any arbitrary noise $S(\omega)$, as long as its frequency does not coincide accidentally with that of the modulation. Naturally, the signal-to-noise ratio can be optimized by trying to use modulation frequencies that are as crooked as possible and try to avoid frequencies of known noise sources such as multiples of the electrical 50 Hz noise. To measure the second harmonic the mixing is done twice so that only terms proportional to $\left[\sin(\omega_{\mathrm{mod}} t + \Theta_{\mathrm{mod}})\right]^2$ remain after the filter.

In summary, the output signals of the Lock-in are

$$\begin{aligned} R = |Z| = \sqrt{X^2 + Y^2} = \frac{\mathrm{d}I}{\mathrm{d}V} V_{\text{Lock-In}}^2 ; \qquad & X = \mathrm{Re}(Z) = \frac{\mathrm{d}I}{\mathrm{d}V} V_{\text{Lock-In}}^2 \cos(\Theta_{\mathrm{mod}} - \Theta_{\mathrm{ref}}) \\ \Theta = \arg(Z) = \mathrm{atan2}(Y, X) = \Theta_{\mathrm{mod}} - \Theta_{\mathrm{ref}} ; \quad & Y = \mathrm{Im}(Z) = \frac{\mathrm{d}I}{\mathrm{d}V} V_{\text{Lock-In}}^2 \sin(\Theta_{\mathrm{mod}} - \Theta_{\mathrm{ref}}) . \end{aligned} \tag{3.19}$$

In our measurements we always record the in-phase component $X$ and the quadrature component $Y$, whereby we adjust the phase difference by means of the phase shifter to remove the capacitive signal by shifting it into $Y$.

### 3.2.3 Energy Resolution

Spectroscopic features have an intrinsic width $\Gamma_{\mathrm{int}}$. This is often of physical interest because it gives direct information about the lifetime of states (see Section 2.2.2). The experimentally determined width $\Gamma_{\mathrm{exp}}$ will always be larger than the intrinsic width, because different factors can lead to a broadening of the experimental features, namely:

*i.* Thermal broadening $\Gamma_{\mathrm{T}}$

*ii.* Lock-In broadening $\Gamma_{\text{Lock-In}}$

*iii.* Broadening $\Gamma_{\mathrm{HF}}$ due to high-frequency noise

*iv.* Broadening $\Gamma_{\mathrm{s}}$ due to lifetime effects

Consequently, the knowledge about these broadenings is of great relevance to get an estimation of the intrinsic width and the energy resolution we can achieve in spectroscopy. The energy resolution is a measure of how far two spectral features must be separated in energy in order to be able to distinguish them clearly in a spectrum. A common convention is that they are distinguishable if they are separated by the full width at half maximum (FWHM), see Fig. 3.4(c). In case of Gaussian line shapes, the experimental broadening is the square root of the sum of the individual widths of all contributions to the particular system

$$\Gamma_{\mathrm{exp}} = \sqrt{\Gamma_{\mathrm{int}}^2 + \sum_i \Gamma_i^2} . \tag{3.20}$$

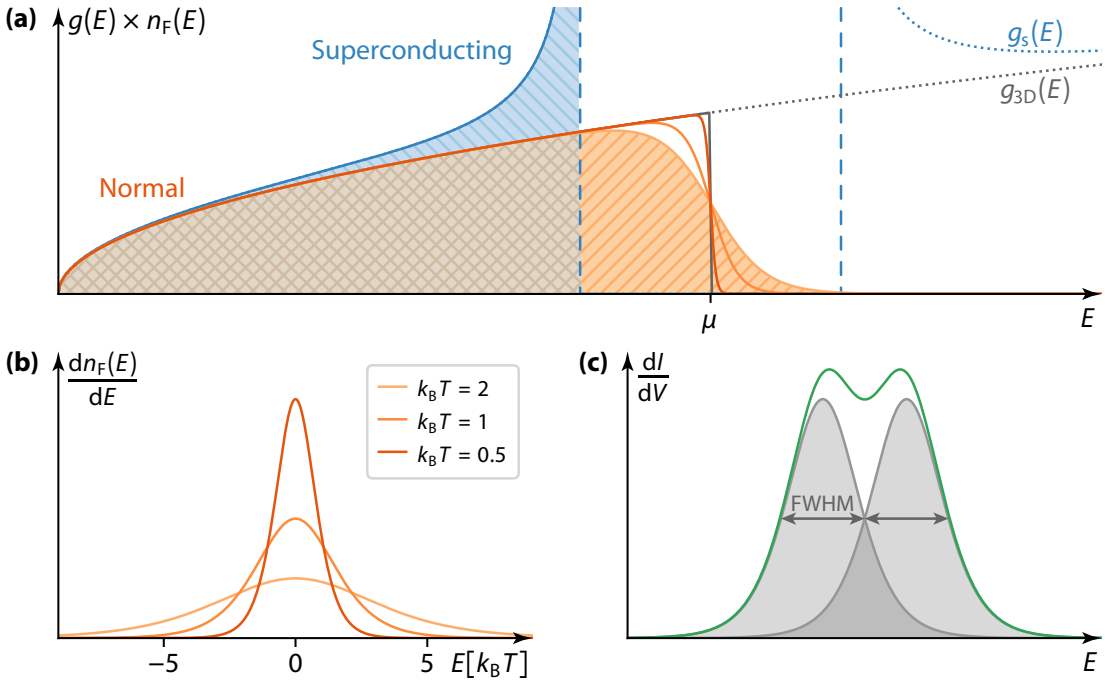


**Figure 3.4 | Energy resolution of a scanning tunneling microscope. (a)** Density of states weighted with the thermal distribution as function of energy. The higher the temperature, the more the Fermi edge smears out. **(b)** Derivative of the Fermi-Dirac distribution functions, showing the broadening with temperature. **(c)** Distinctness of two peaks in the spectrum. A typical rule of thumb is that the peaks can be separated from each other if the distance is at least one full FWHM.

This corresponds to the Gaussian error propagation. For Lorentzian line forms, the half widths add up

$$\Gamma_{\text{exp}} = \Gamma_{\text{int}} + \sum_i \Gamma_i \,, \tag{3.21}$$

since the Lorentzian distribution is a convolutional half group. Usually not all sources of broadening are known, which is why we generally refer to the system unknown parts of broadening as instrumental broadening $\Gamma_{\text{setup}}$. For our experiments we could estimate an energy resolution of ~400 µeV for normally conducting tips and ~80 µeV for superconducting Pb-Pb junctions.

### Thermal Broadening

At a temperature of $T = 0$ a physical system is in its ground state. As electrons are fermions, states are always filled up with one electron starting from the lowest energy level, because the Pauli principle forbids the filling of a single particle state with more than one fermion. For this reason, the descriptive picture of a Fermi sea is often used. Accordingly, at $T = 0$

all states are filled up to an upper limit, which is called Fermi energy $E_F$ and corresponds to the chemical potential at absolute zero temperature (see Fig. 3.4(a)). Hence, the Fermi energy is the energy it takes to add another electron to the system.

Regarding finite temperatures $T > 0$, electrons can be excited thermally to energy levels above $E_F$. As fermions, electrons obey the Fermi-Dirac statistic $n_F$ (see Eq. (2.8)), which indicates the electron distribution around the chemical potential. Fig. 3.4(a) shows clearly how the Fermi edge becomes more and more smeared with increasing temperatures. Spectroscopy uses the derivation of the Fermi-Dirac statistics, shown in Fig. 3.4(b), to probe the substrate. The broadening caused by the thermal distribution of the electrons can be determined as the FWHM of its derivative

$$\Gamma_T(T) = \mathrm{FWHM} = \left[\ln(3+2\sqrt{2}) - \ln(3-2\sqrt{2})\right] k_B T \approx 3.53 k_B T\,. \tag{3.22}$$

At for us typical temperatures of 1.35 K this corresponds to a broadening of about 410 µeV.

### Energy Resolution in SIS Junctions

The energy resolution resulting from the thermal broadening is not sufficient to investigate e.g. YSR states in superconductors, at least not without drastically reducing the measuring temperature. Fig. 3.4(a) illustrates that the thermal broadening can be avoided by using a superconducting tip as a probe. If the width of the superconducting gap is much larger than the thermal broadening, $\Delta \gg \Gamma_T(T)$, the smearing of the Fermi edge falls completely into the gap, where no states exist. A superconductor with a sufficient gap is e.g. lead with $\Delta = 1.35\,\mathrm{meV}$ so that the thermal broadening in a Pb/Pb junction no longer plays a role. The difference between normal conducting tips and superconducting tips can be seen in Fig. 3.5. A spectrum with an etched tungsten tip in Fig. 3.5(a) is compared to a superconducting tip coated with lead in Fig. 3.5(b). For metallic tips the spectrum resembles the superconducting BCS density of states as illustrate in Fig. 2.6(b), with a clearly defined gap of $\Delta = 1.35\,\mathrm{meV}$. For the superconducting tip, the gap region is doubled because also Cooper pairs in the tip must be broken to allow single-electron tunneling into the coherence peaks. The comparison between the coherence peaks broadening shows a significant increase in energy resolution.

Without thermal broadening, two other types of broadenings determine the energy resolution of such junctions. First, the quasiparticles at the edge of the gap have a finite lifetime, see Section 5.1, which is given by the broadening $\Gamma_s$. Moreover, high-frequency noise coupled into the measurement setup leads to a broadening $\Gamma_{HF}$. The underlying mechanism is similar to the photon-assisted tunneling we describe in this thesis, except that the high-frequency background radiation occurs with very large bandwidth. From the fit of the spectrum in Fig. 3.5(b) we can extract these broadening. Typical values for our setup are $\Gamma_s = 20\,\mu\mathrm{eV}$ and $\Gamma_{HF} = 60\,\mu\mathrm{eV}$.

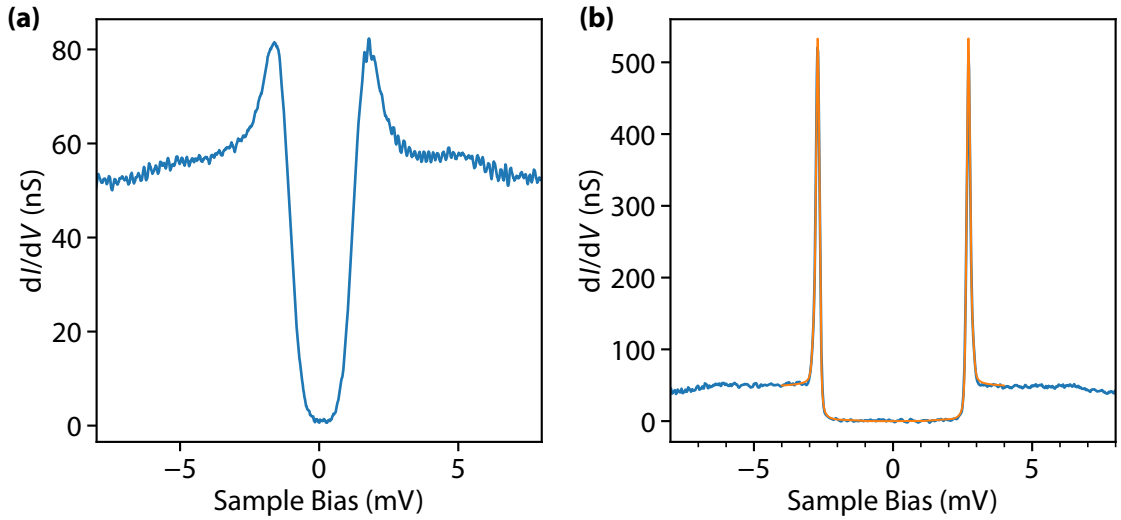


**Figure 3.5 | d$I$/d$V$ spectroscopy on pristine Pb – normal versus superconducting tip. (a)** With a normal conducting tungsten tip the displayed d$I$/d$V$ spectrum represents the sample DoS. The superconducting gap of lead with $\Delta$ = 1.35 meV prominently determines the differential conductance. **(b)** With a superconducting tip the shape changes significantly. Now the spectrum is to be understood as a convolution of tip and substrate DoS and thus the coherence peaks appear at an energy of $e|V| = 2\Delta$. The increase in resolution is evident as the superconducting tip allows to beat the thermal Fermi-Dirac limit. In *orange* a fit of the spectrum is shown, from which the broadening due to lifetime effects and external HF noise can be determined. Setpoint and measurement parameters: $V_{\text{Bias}}$ = 10 mV, $I$ = 400 pA, $V_{\text{Lock-in}}$ = 25 µV and $f_{\text{Lock-in}}$ = 873 Hz.

### Broadening through Lock-In Modulation

The broadening of the lock-in modulation can be taken into account by using its instrumental broadening function $\chi_{\text{m}}$,

$$\chi_{\text{m}}(V) = \begin{cases} \frac{2}{\pi}\frac{\sqrt{V_{\text{mod}}^2 - V^2}}{V_{\text{mod}}^2} & \text{for } |V| \leq V_{\text{mod}} \\ 0 & \text{for } |V| > V_{\text{mod}}\,, \end{cases} \tag{3.23}$$

and convolve it with the differential conductance [146–148]. This corresponds mathematically to a convolution with a semicircle

$$\frac{\mathrm{d}I}{\mathrm{d}V}(V) = \frac{2}{\pi}V_{\text{mod}}^2 \int_{-V_{\text{mod}}}^{V_{\text{mod}}} \mathrm{d}V' \frac{\mathrm{d}I}{\mathrm{d}V}(V+V')\sqrt{V_{\text{mod}}^2 - V'^2}\,. \tag{3.24}$$

This results in $\Gamma_{\text{Lock-In}} = \text{FWHM} = 1.7\,V_{\text{mod}} = 2.4\,V_{\text{Lock-In}}$ as broadening.

# 4

# Installation and Experimental Realization of an HF-STM

Our goal was to design a setup for addressing single spins and their dynamics on surfaces with high-frequency radiation. Such a machine would allow for example the combination of electron spin resonance (ESR) measurements with the spatial resolution of scanning tunneling microscope (STM). A sufficiently good vacuum and low temperatures are of utmost necessity to study spins on the level of single atoms. This chapter describes the overall concept of the machine, its specifications, and the design and implementation of the installed HF circuit to shine GHz radiation into the STM junction.

## 4.1 Chamber, STM Head and Measurement Electronics

For stable measurements of surfaces with atomic resolution, STMs have to meet some requirements. In particular for studying the interaction of single atoms with surfaces. To achieve resolution on these length scales, a very sensitive and noise stable circuit is needed to measure currents in the pA range and to move the tip with pm precision. Besides, a sophisticated damping system is necessary to prevent mechanical vibrations from interfering with the atomic resolution. For the study of single atoms also an ultra-high vacuum (UHV) is used, to protect the sample from contamination. Furthermore, the thermal energy in the measuring system has to be reduced to such an extent that the thermal diffusion of the atoms on the surface is frozen in order to keep the samples unchanged during the measurements. The usual method is to cool the microscope down to the boiling temperature of liquid helium, i.e. 4.2 K, enabling measurements on the same preparation over a long time (weeks to months).

For addressing individual magnetic moments on superconducting materials, the machine design must meet additional requirements beyond those of 'simple' low-temperature STMs,

operating at 4 K. For measurements on superconductors, the temperature should be kept far below their critical temperature in order to reduce thermal influences. One of our preferred superconducting materials is lead with a comparatively high critical temperature of $T_c$ = 7.2 K. Other classical BCS superconductors are not even in the superconducting phase at He temperatures. For this purpose, we have installed an additional cooling stage that reduces the thermal energy by another three quarters to 1.3 K. This reduction also enables us to achieve the energy resolution needed for the investigation of subgap states in superconductors by avoiding all thermal influences on the superconducting gap as far as possible, thus making the use of superconducting tips advantageous (see Section 3.2.3).

To address individual spins with high-frequency radiation also a magnetic field is needed to reverse and lift the degeneracy of spin states, as well as cables that are capable of conducting electromagnetic waves in the GHz range. Here small magnetic fields of a few 100 mT are perfectly adequate since a large number of our experimental proposals are based on Pb as tip and substrate material. The superconductor Pb has a critical magnetic field of about 80 mT at a temperature of 1.2 K. Spin splits in magnetic fields of this magnitude are in the GHz range. For this reason, we want to install a GHz light source in the form of a signal generator to excite these spin transitions. Using these frequency bands for detection would result in a further increase in energy resolution. To give an order of magnitude, each gigahertz corresponds to a photon energy of 4 μeV, which is several times smaller than the thermal energy of about 100 μeV at 1.2 K.

### Vacuum Chamber and Cold Gases

An overview of the entire setup is given in Fig. 4.1. The entire experiment is enclosed in a UHV chamber, as shown in Fig. 4.1, and can be divided into three sections: A STM-chamber, a preparation chamber, and a load-lock. The base pressure of the system is $< 1 \times 10^{-10}$ mbar. Sample preparation takes place in the preparation chamber to prevent contamination of the microscope. Ion pumps, titanium sublimation pumps, and cold traps are used for pumping, and a helium flow cryostat in the manipulator allows the samples to be cooled down to < 60 K during preparation. A mass spectrometer, leak valves, a sputter gun, and two ovens for heating are available for the characterization and preparation of the samples. One of the ovens is specially designed for Pb with its low melting point. Therefore, it works exclusively by thermal radiation and has a temperature diode for monitoring. The other oven is based on ion beam heating and can reach temperatures up to 2000 K. In this temperature range, the temperature is controlled solely by the spectral composition of the emitted radiation. Different positions around the preparation chamber allow the mounting of evaporators. For the evaporation of metal atoms, we use EFM3 ion beam evaporators from Omicron. In order to be able to load samples into the vacuum as quickly as possible and to maintain the UHV at the same time, we use the load-lock.

The basis of our setup is a microscope from CreaTec, which we customize according to our requirements. It is a 1 K setup with an integrated vector magnet up to 1 T. The cryostat from CryoVac is based on a multi-stage cooling process using liquid nitrogen and helium. In the

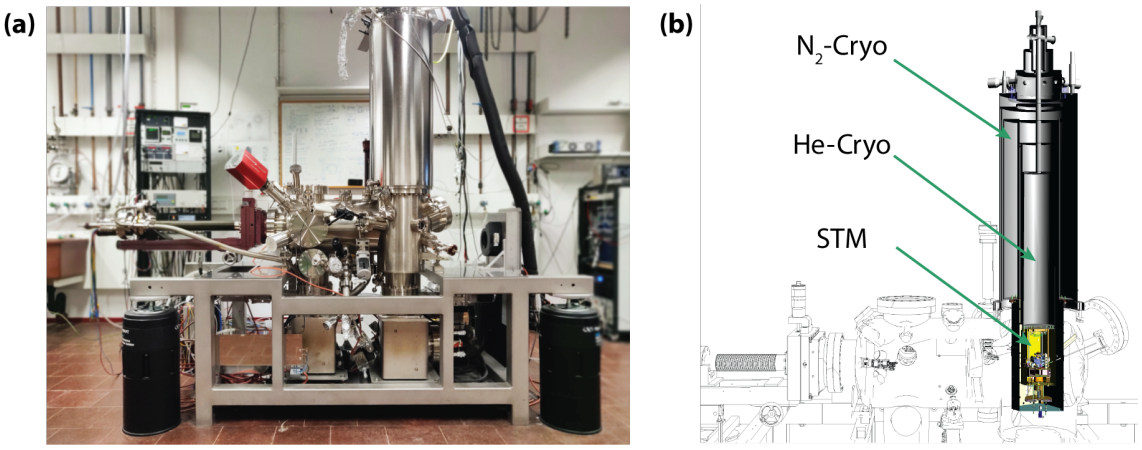


**Figure 4.1 | Experimental setup – UHV chamber.** **(a)** Shown is the UHV chamber with all instruments necessary for its operation. It can be divided into three parts: The STM chamber, the preparation chamber, and the load-lock. The left part of the chamber is the preparation chamber, where metal evaporators, the mass spectrometer, and gas leak valves are mounted. A large manipulator on the far left enables the transfer through the chamber. **(b)** Cross-section through the cryostat showing the cooling stages with the different liquid gases. The 1 K-stage together with the STM head (*yellow*) is attached to the bottom of the He-cryostat itself. ((b) used with the permission of CreaTec)

first stage, the nitrogen cools to 77 K followed by the helium stage cooling to a temperature of 4.2 K. A subsequent cooling cycle further reduces the temperature of the microscope down to 1.3 K. Therefore a powerful rotary vane pump is used to pump a $^4$He reservoir for reducing its vapor pressure. The consumed helium gas is used by a sophisticated system of heat changers to pre-cool all incoming lines of the system. Besides, all supply lines are intercepted at the respective cooling shields before they reach the STM so that no external thermal loads heat the experiment. For this purpose, good thermal conductance must be ensured at all interception points. For this, the area must be maximized to allow the greatest possible heat flow, but also applying high contact pressure helps for microscopically increasing the area.

### STM Head and Magnetic Field

The head of the STM is attached to the base plate of the 1 K cooling stage. For vibration decoupling the STM is suspended on springs. Three radiation shields surround the head and are interconnected to the three cooling reservoirs. The central component of the STM head is a scanning unit which enables the tip to be positioned accurately anywhere on the sample, shown in Fig. 4.2. The scanning unit has two piezo-electric motors for coarse positioning – a combined motor for the $x$ and $y$ positioning and a motor for the $z$ positioning. The latter is constructed in the very compact pan style [149, 150]. All piezo motors are based on the stick-slip effect. The microscopic movement of the tip is achieved by a piezo tube. This tube

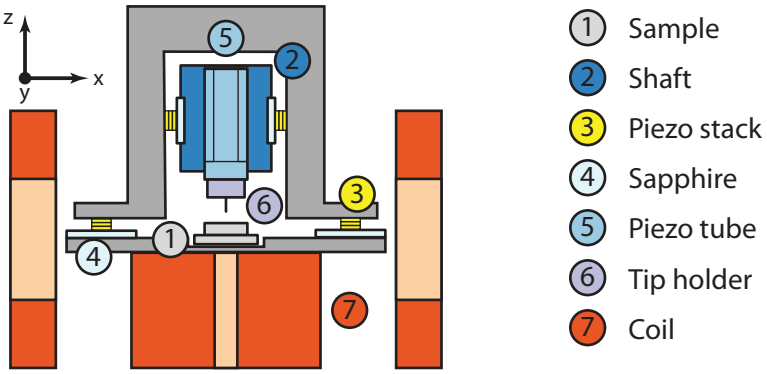


**Figure 4.2 | Experimental setup – STM head.** Shown is the scanning unit of the STM together with the magnetic field coils. The tip can be attached to the bottom end of the *piezo tube* by means of a *tip holder*. The tube provides the microscopic positioning via elongation and bending. It is located inside a *shaft* that can be moved up and down for macroscopic tip approach via *piezo stacks* that run on *sapphire* plates via stick-slip. Further piezo stacks allow macroscopic positioning of the entire tip unit in *x* and *y* direction. The three magnetic *coils* are shown in *red*, right and left a pair for the parallel magnetic field and one below the *sample* for the vertical field. The sample is specially mounted in a recess to minimize the distance to the lower coil. *Sketch is not true to scale and perspective.*

can be bent and elongated with sub-picometer precision due to the piezoelectric effect. The tip itself is mounted in a tip holder and clamped into a small cage at the bottom end of the tube. With a pair of tweezers, this clamping can be released which allows tip transfers.

Besides, three magnetic coils are integrated into the STM head, for generating a parallel and a perpendicular field component with respect to the surface. A pair of coils in an almost Helmholtz arrangement generates the horizontal magnetic field (the distance between the two coils is slightly increased to increase the experimental volume). A separate coil directly underneath the sample is responsible for generating the vertical magnetic field. Compared to other STM construction types, this design is rather unusual. These other designs tend to separate head and coils by placing the magnets into the He-cryostat. Here, the cooling power is considerably higher compared to that of the 1 K pot and thus heat loads can be dissipated much better. The small cooling power has turned out to be a significant problem in our setup (see Section 4.1.1). On the other hand, the hoped-for advantages of our design due to its spatial proximity between the coils and the microscope are a possible reduction of the coil dimensions and therefore also a reduction in the required currents for generating the magnetic field. Consequently, the energy stored in the magnetic field is much lower and, in the event of an unintended quench, the risk of damage is reduced. Besides, this design also allows using eddy current damping, as permanent magnets can be attached to the head. The use of eddy-current damping is useful because it very effectively dampens the remaining mechanical vibrations reaching the STM, thus further reducing the noise level of the system. Since head and coils as a whole are screwed and therefore building a

stiff connection, there will be no displacement due to unwanted interaction between the magnetic field and the permanent magnets.

As the vertical magnetic field consists of only one coil, it is quite inhomogeneous. This makes it all the more important that its distance to the sample is as small as possible and that the measurements take place along the coil axis. The latter can be ensured by selecting a proper tip position on the sample. The former we tried to optimize by minimizing the thickness of all samples by milling out the sample plates to lower the crystals as far as possible. Furthermore, we are using the flattest possible crystals of only 1 mm.

Another advantage of this STM design compared to those with magnetic fields embedded in the cryostat is its good accessibility. Samples and tips are transferred through openings in the shields using a wobble stick. The openings in the 77 K and 4 K shielding are realized by closable doors to protect the STM from thermal radiation during operation. These doors are also operated with the wobble stick. Due to this uncomplicated handling, transfers are relatively fast and straightforward. Combined with the use of small and light sample plates, crystals can be transferred and cooled in a relatively short time. The junction is optically well accessible. There is optical access from the front, for transferring sample and tip. Moreover, there is optical access from both sides through the core holes of both Helmholtz coils. It may be used to directly deposit adsorbates onto the sample in the STM or to integrate a laser into the system. We use one of these two accesses to have more control over the tip during the sample transfer and the subsequent approach of the tip. For this, we use a CCD camera with a corresponding zoom lens.

Although the head is already quite compact, CreaTec's design still offers us space and freedom to make modifications. Overall, the accessibility and the available space make the setup flexible for possible extensions in more advanced experiments, such as the realization of high-frequency integration.

### Cabling and Measurement Electronics

A STM can detect currents of a few picoamperes. To separate these currents from background noise it is not only necessary to provide mechanical damping, it is also necessary to use sophisticated wiring, high precision measurement electronics, and to filter electronic noise to a minimum. A detailed layout of the cabling circuit is shown in Fig. 4.3. The STM, at the heart of the experiment, is depicted as an equivalent circuit diagram (with *blue* background), consisting of a parallel circuit of a resistor, a capacitor, and a tunnel barrier. It is surrounded by the UHV chamber, illustrated by a *grey* area with a dashed outline. All wiring inside the chamber must pass at least a distance of 1.5 m through the cryostat, along which the cables are cooled before reaching the STM. This long path results in a typical resistance of about 200 Ω for all of these cables. The chamber itself acts as a Faraday cage, preventing the entry of external radiation that could be picked up as noise. This is mainly high-frequency radiation, like radio waves, but also fluctuations due to the *ac* mains voltage which is typically transposed at 50 Hz. All cable feedthroughs into the vacuum provide a gateway for such noise. For this reason, we filter all supply lines, except for the HF lines,

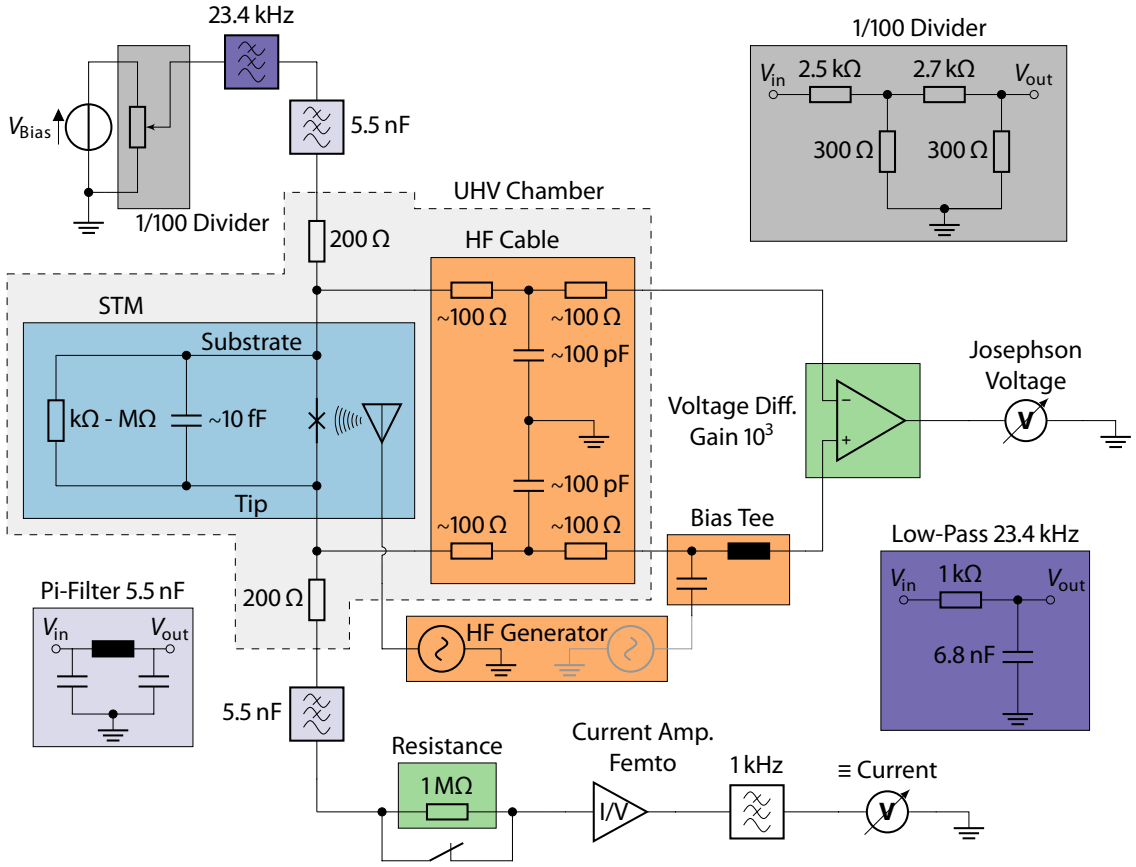


**Figure 4.3 | Detailed circuit diagram of the setup showing the wiring of all different experiments performed.** The core of the experiment is the STM (blue) consisting of tip and substrate which is shown here as an equivalent circuit diagram in the format of the RCSJ model as a parallel arrangement of a resistor, a capacitor, and a tunnel barrier. The UHV chamber is indicated as a *grey* area with a dashed outline. Filters for noise reduction are highlighted in *purple*. All components with HF reference are highlighted in *orange* and those of the Josephson setup in *green*.

directly at the feedthroughs. This is illustrated here by Pi-filters of 5.5 nF (Tusonix/CTS) at the supply for bias voltage and current. These are used as well at the high-voltage piezo-control lines. The bias line, which is connected to the sample, is additionally filtered with a home-built 23.4 kHz $R$-$C$ low pass filter. We use a Nanonis™control system, to provide the bias voltage and for data acquisition. The current is pre-amplified by a variable-gain low-noise amplifier (Femto, DLPCA 200) and then filtered by a 1 kHz $R$-$C$ low-pass filter.

$\mathrm{d}I/\mathrm{d}V$ spectra were recorded using an external lock-in amplifier (Ametek, 7270 DSP lock-in amplifier). Its $ac$ reference signal was divided by a factor of 100 before being added to the $dc$ bias-voltage output of the Nanonis controller. A second voltage divider reduces the noise on the bias signal even further. As an example, the 1/100 divider is depicted, which scales the signal from the ±10 V of the Nanonis™to ±100 mV and reduces the noise accordingly by the same ratio.

The performance of the filtering and shielding concept is directly reflected in the effective energy resolution of a Pb/Pb junction as high-frequency noise would lead to energy broadening. The $\mathrm{d}I/\mathrm{d}V$ spectra of superconductor–superconductor junctions are ideal test systems for probing the effective energy resolution because they are not limited by Fermi-Dirac broadening (see Section 3.2.3). We routinely obtain peak widths of ~ 80 μV and coherence peak to normal conductance ratios > 10 due to the well-designed filtering scheme.

In addition to this basic setup, Fig. 4.3 contains the components for our two implemented spectroscopy methods. On the one hand the components for our Josephson setup (with *green* background), with an amplifier, which outputs the voltage difference over the junction and an additional 1 MΩ resistor. This setup is described in detail in 4.4. The Josephson resistor is shorted in normal operation. On the other hand, all components that are related to the creation of HF radiation are marked with a *orange* background. There are two ways to bring this radiation into the junction. The HF signal from the signal generator (R&S® SMB 100A) is either emitted from an antenna or with the help of a bias tea (SHF BT45-B) directly applied to the tip. For the latter transmission path, we assume that technically speaking the tip also functions as an antenna. In the course of our experiments, we have found that feeding the HF via the antenna is the path with fewer losses and less noise compared to the tip path. Both ways are similar in terms of cabling, the details of which can be found in the next Section 4.2. Since each coaxial cable automatically acts as a filter because it contains a capacitance and can therefore be considered a simple $R$-$C$ filter, the HF cables inside the UHV chamber are shown in an equivalent circuit diagram.

### 4.1.1 Magnetic Field Issues

In their present state, the magnetic fields are unusable. The magnets generate a large amount of heat and noise during their operation, due to the non-superconductive joints. This is a clear design flaw of CreaTec. We have invested a lot of time in identifying and solving this issue and have tried to acquire the expertise ourselves to create superconducting

connections between coil-wires. Unfortunately, we could not find a satisfactory solution without redesigning the STM from scratch.

In summary, the problem can be ascribed to ohmic heating, caused by the high coil currents. This heat input is so significant that the regular operation of the STM is no longer possible. The coils themselves are wound from superconducting Nb-Ti wires that are embedded into a Cu matrix and therefore support a loss-free current flow. NbTi is particularly suitable for the production of superconducting magnets with a critical temperature of about 10 K [151] and critical magnetic fields of about 15 T [152]. For the installation of the coils, however, the wires are soldered on the corresponding cooling shields to the supply lines running through the cryostat. These soldered joints are not superconducting and as a normal conducting contact, they obey Ohm's law. Due to a finite resistance, this leads to the generation of heat when a current flows through the contact. This heat has to be dissipated mainly by the 1 K cooling stage. A rough estimate of the maximum resistance of the solder joints can be made: The cooling power of the JT stage is approximately 10 mW to 20 mW, which corresponds to a permitted resistance of 10 μΩ per contact (five in total). This is to be understood as an upper limit and is based on the assumption that the entire cooling capacity is available to the magnet and that no further heat input exists.

In order to reduce the heat input, we have conducted a detailed study and investigated various connection techniques between the NbTi wires, based on the work of Brittles *et al.* [153]. The greatest challenge is that Nb-Ti forms an oxide layer on its surface when exposed to air. Nb has a very high oxygen affinity and consequently forms a NbO layer very quickly. Subsequently, the slow formation of a very stable $Nb_2O_5$ layer follows [154]. It requires temperatures of ~2000 K under ultra-high vacuum conditions to remove the oxide layer. Alternatively, it can be dissolved in hazardous hydrofluoric acid (HF) [154, 155]. Both methods are not feasible for us, since the connections must be made directly at the STM head. There is only very limited access to these joints, combined with the difficulty of different spatial orientations. The use of hydrofluoric acid for us is impossible because we do not have the facilities to use it in our laboratory. This prefabrication would therefore have to be done in specially equipped chemical laboratories. However, this contradicts the idea of dividing the supply lines in order to protect the cables from bending during installation and to be able to replace broken cables later on.

In total, the methods for creating a low-resistance connection between two NbTi cables can be divided into three connection techniques: These are soldering, cold-pressing, or welding. Direct soldering of the pure NbTi filaments is not a possibility, as we have already discovered. The standard method of soldering is the Thornton matrix replacement method. The idea is that the individual filaments in the copper matrix have not formed an oxide layer during production. A successful joint could therefore be achieved by replacing the copper matrix with a soldering tin without exposing the filaments to an oxygen atmosphere. This is exactly what happens in Thornton's method. The copper matrix is dissolved in molten Sn and the Sn layer is afterward replaced by superconducting tin solder in a second bath of molten metal. The wires are finally joined in a solder pot of the same superconducting tin. Both, the handling of molten Sn and larger quantities of molten tin solder, combined with

the limited accessibility of the joints have led us to distance ourselves from this bonding method. Cold pressing of the joints is based on the idea that NbTi can be metallurgically joined as a soft alloy by simply crimping the filaments at room temperature. This method unfortunately fails due to the fragility of our wires. With a diameter of a few tenths of a micrometer, we were not able to fix the wires and then apply the necessary force without damaging the wires. The final bonding method is spot welding. It is hoped that the high current that flows during welding will break the oxide barrier due to resistive heating and thus lead to a connection of the two NbTi cores. Because it is not possible to verify whether the joining was successful, it is advantageous to make the connection with several spot weld joints. We have been able to produce welded joints of ~5 μΩ in a test setup. This is far from the values described in the literature of up to $<10^{-13}$ Ω. [156]. Nevertheless, these values are an improvement and therefore we installed new coils. Unfortunately, the heat input was still excessive and the STM proved to be unsuitable for the use of magnetic fields. Neither was the consultation of external help in the form of specialized companies successful. All companies contacted have refused to manufacture the joints outside their laboratories.

## 4.2 Introducing High Frequencies into the STM Junction

The following section describes the selection, installation, and characterization of the used coaxial cables. We will explain why coaxial cables in their design are for us the best compromise for the transmission of high frequencies. Besides, a detailed technical description of the installation follows, together with a summary of all the precautions we have taken to avoid unnecessary heat and noise input into the microscope.

### Comparison Between Waveguides and Coaxial Cables for High-Frequency Transmission into the STM

Exposing a STM to high-frequency (HF) radiation in the GHz range requires a dedicated circuit [131, 157–159]. Typical cables used in low-temperature STMs are specially designed for efficient filtering of environmental radiation, which would otherwise induce noise in the tunneling junction. As such, they are very bad conductors for high-frequency signals. In total, a distance of ~2 m must be covered from the *ac* source to the junction, making low-loss transmission important. High-frequency signals in the GHz require specially designed cables. Despite all the specifications that the cables must meet, they are not allowed to compromise the stability and resolution criteria of the STM.

It is important to take a closer look at the requirements that must be met for a cable to conduct alternating currents. In free space, an electromagnetic wave, such as our HF radiation, propagates in all directions as a spherical wave. Its power decreases with one over the distance square. A normal cable consisting of a single copper core is no longer able to guide such alternating currents because it effectively acts as a long antenna. Hence it radiates electromagnetic waves in all directions along its entire length, causing massive

signal losses. In order to transmit HF radiation directionally, the wave must remain spatially constrained. Conductors that are capable of doing this are called waveguides. They confine and channel the waves along one direction due to total reflection from their walls. Under ideal conditions, this propagation occurs free of energy loss. Waveguides are widely used in physics and are used for acoustic waves, radar waves, as well as for light, which is transmitted over long distances in optical fibers.

We have chosen coaxial cable as transmission lines. Coaxial cables are a type of electrical cable consisting of an inner conductor surrounded by a concentric conductive shield. At this shield, also called the outer conductor, the total reflection takes place, which confines the electromagnetic wave. Inner and outer conductors are separated by a dielectric material which is an insulating material, usually polytetrafluoroethylene (PTFE). We want to transmit a very wide spectrum of frequency over these cables, ranging from some ~100 MHz up to ~50 GHz. From a physical point of view, the interesting spectrum is that of the centimeter waves, from 3 GHz to 30 GHz, because electron spin signals fall into this frequency band. However, coaxial cables are not necessarily suitable for the majority of this frequency range. Since the power losses in the dielectric increase with frequency, coaxial cables start to transmit increasingly poorly above 1 GHz. Unwanted higher frequency modes occur, which fundamentally change the principle of transmission as soon as the inner circumference of the coaxial shielding becomes smaller than the wavelength to be transmitted. For this reason, microwaves of sufficiently short wavelengths are normally guided in hollow waveguides, as these have lower losses. In the following, we will explain why coaxial cables are nevertheless the best compromise for our application.

For this purpose we will first take a look at the advantages and disadvantages of waveguides: Waveguides are hollow metal tubes with a mostly rectangular, circular, or elliptical cross-section. They can transmit electrical power in the frequency range above 1 GHz with much smaller losses than electrical cables like coaxial cables. The minimum width of a rectangular waveguide corresponds to about half the wavelength of the transmitted frequency – this is exactly when only a single antinode fits in the transverse direction. Consequently, for a frequency range of 1 GHz to 30 GHz the width of the waveguide would vary between 16 cm to 7 cm. It is possible to transmit higher frequencies on oversized waveguides, although in addition to the transmission of the desired fundamental mode, undesired higher modes are also transmitted. However, this problem applies equally to coaxial cables. The main disadvantage is the size and stiffness of the waveguides. Apart from the complications of accommodating such cross-sections near the tip, they must also be guided through the thermal shields. Holes of this size would lead to a high thermal load to the STM and have a noticeable effect on the achievable final temperature and the helium consumption. The latter is of major relevance from an economic point of view since liquid helium is expensive and accounts for a large part of operating costs. Another problem is that waveguides are relatively rigid in design, with corresponding large bending radii, leading to the propagation of vibrations into the STM. A solution would have to be found here which appears not to be obvious. Moreover, this stiffness would also lead to enormous stresses in the materials during the cooldown of the machine due to different thermal expansion coefficients. In

summary, although we have made slight sacrifices in attenuation with coaxial cables, we have ensured that we can keep the measurement temperature and the vibrational noise under control. Also, the handling of much smaller cross-sections during installation is a decisive argument in favor of coaxial cables.

### Coax Cable Installation and Optimization

When planning the machine, we concluded that one single uninterrupted cable from the top of the cryostat to the STM was the best solution. This was based on the motivation that any transition between two cables, typically realized as SMK connectors, would lead to losses on the one hand and the formation of unwanted higher modes due to reflections on the other. Our demands on the cable were very high for the reasons already described – low thermal conductivity should minimize the heat input and certain flexibility should minimize the input of mechanical vibrations. Our choice was the cryogenic semi-rigid coaxial cable (type SR) distributed by LakeShore. This was installed by CreaTec during assembly and ended at one of the PTFE connection pads at the head (see Fig. 4.5(f)). For the remaining distance to the tip, the HF signal was transmitted on the wire for the direct current, thus no longer meeting the requirements of a waveguide. This configuration turned out to be almost completely useless with attenuations in the range of 65 dB to 80 dB (over a range of 1 GHz to 40 GHz).

We could not find the reason for the poor attenuation values, but we could make two important observations with the LakeShore cables. Firstly, despite these high attenuations, we were still able to detect HF signals in the junction. Secondly, we had to conclude that a clean transmission of the high frequencies without the generation of higher modes was an unrealistic prospect. Most likely, the geometries of the head and shields alone generate a large number of standing waves, leading to higher modes. Since it was technically not possible to ensure a smooth transmission curve as a function of frequency, we solved the problem by implementing a control loop. By measuring the power at the junction, we can ensure a constant output regardless of frequency. For this purpose, we record the specific attenuation for each irradiated frequency in a data table and use this lookup table to correct the power later during data acquisition. This table has to be refreshed at regular intervals but is a practical solution under the condition that the attenuation changes slowly and continuously. With the implementation of such a measurement compensation, we could now also accept reflections at connectors and our requirement for a single continuous cable was no longer necessary. Also, the power losses at the connectors of about ~1 dB are negligible compared to our total losses.

The possibility of using different cables led to a complete re-evaluation and optimization of the selected cables in terms of thermal conductivity and rigidity. A scheme of the improved transmission line is shown in Fig. 4.4. By dividing the cabling into several segments, we were able to start with a low-loss cable for the major part of the distance that has to be covered through the cryostat, for which we could tolerate a higher thermal conductance and larger cable diameter, see Tab. 4.1. This is followed by a superconducting

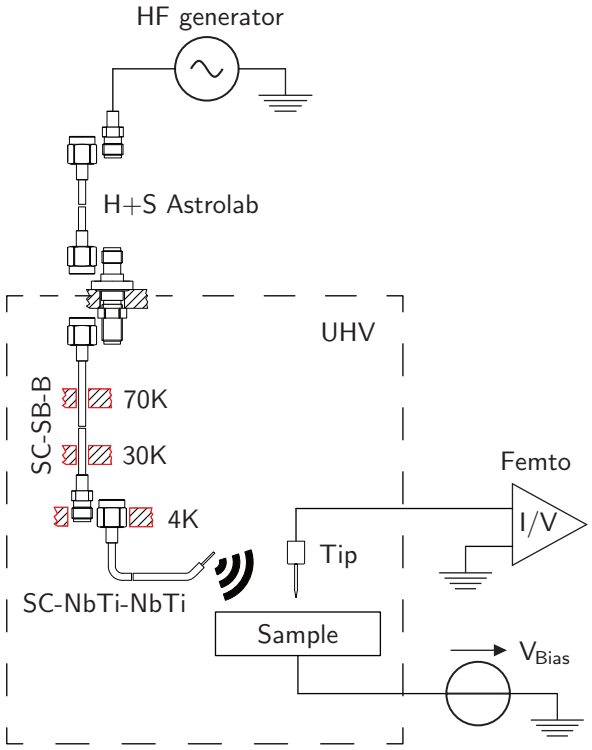


**Figure 4.4 | Sketch of the HF cabling from the signal generator down to the STM junction.** The high frequencies generated at the signal generator are brought to the STM junction via a cable route optimized for this purpose. The cables are thermally intercepted at multiple points on the cooling shields (*red* areas). The signal is transmitted contactless onto the sample via an antenna. The antenna is realized by an open-ended coaxial cable. All connectors are assembled as SMK connectors and are therefore designed for frequencies up to 40 GHz.

coaxial cable with a much smaller diameter, which is nearly loss-free and also superb in terms of low heat conductance. The cable path is realized as follows: The high frequencies are generated at the signal generator followed by a semi-flexible H+S Astrolab cable (H+S Astrolab KK-SF240-2X11SK, $l$ = 0.5 m) forming the low-vibration connection to the ultra high vacuum (UHV) chamber. All connectors outside and inside the chamber as well as the feedthrough (Allectra 242-SMAD40G-C16) are designed as SMK 2.92 mm, suitable for frequencies up to 40 GHz. Inside the UHV chamber, a silver-plated beryllium-copper coaxial cable (SC-219/50-SB-B, $l$ = 1.25 m) is passed through the cryostat and attached to the cryostat's radiation shields for thermal equalization. At the bottom of the 4 K-plate it is connected (via SMK connectors) to a superconducting niobium titanate (NbTi) coaxial cable (SC-086/50-NbTi-NbTi, $l$ = 0.4 m), which has negligible attenuation losses at low temperature. This cable terminates close to the STM junction with the outer conductor being removed over a length of 5 mm $\approx \lambda_{30\,\mathrm{GHz}}/2$ and bent up ~45°.

**Table 4.1 | Comparison of the installed cable types.** Performance data of the installed cables regarding dimensions, thermal conductivity, and attenuation.

| Company | | LakeShore | Coax Co., LTD. | | | |
|---|---|---|---|---|---|---|
| Cable | | type SR | SC-219/50-SB-B | | SC-086/50-NbTi-NbTi | |
| **Material** | | | | | | |
| Center conductor | | Carbon steel[a] | Beryllium copper | | NbTi | |
| Dielectric | | PTFE[b] | PTFE | | PTFE | |
| Outer conductor | | 304 stainless steel[c] | Silver-plated beryllium copper | | NbTi | |
| **Dimensions** | | | | | | |
| ∅ Center conductor [mm] | | 0.114 | 0.51 | | 0.203 | |
| ∅ Dielectric [mm] | | 0.38 | 1.67 | | 0.66 | |
| ∅ Outer conductor [mm] | | 0.51 | 2.19 | | 0.90 | |
| **Properties** | | | | | | |
| Thermal conductivity @ 4K [W/(m K)] | | $4 \times 10^{-1}$ | $4.88 \times 10^{-2}$ | | $4.63 \times 10^{-4}$ | |
| Attenuation [dB/m] | $f$ | n.a. | 300 K | 4 K | 300 K | 4 K |
| | 0.5 GHz | 4.43 | 0.6 | 0.2 | 6.8 | < 0.5 |
| | 1.0 GHz | 6.27 | 0.8 | 0.3 | 9.6 | |
| | 5.0 GHz | 14.09 | 1.8 | 0.6 | 21.6 | |
| | 10.0 GHz | 20.01 | 2.5 | 0.9 | 30.5 | |
| | 20.0 GHz | 28.45 | 3.5 | 1.2 | 43.1 | |

[a] Silver plated copper clad carbon steel (0.103 mm outer diameter carbon steel covered by 0.0057 mm thick copper cladding covered by 0.001 mm thick silver plating.
[b] Polytetrafluoroethylene (PTFE)
[c] A seamless tubular metal jacket serves as the outer conductor/shield

In figure Fig. 4.5 the technical precautions taken to thermally intercept the HF cable and to avoid mechanical vibrations are documented. Fig. 4.5(a) and (b) show the thermal coupling of the copper-beryllium cable with a cross-section of 2.2 mm. This cable is winded with copper wires and silver conductive lacquer is applied to the windings for good thermal contact (*blue* arrows). These wires act as cooling fingers and are firmly screwed to the corresponding 30 K and 70 K shields (*orange* arrow). In Fig. 4.5(c) and (d) the transition between the copper-beryllium cable and the superconducting NbTi cable is shown. The SMK connector is pressed onto an angle acting as a cooling finger by using a clamping device. The angle itself is firmly screwed to the bottom plate of the 4 K cryostat. It is important for all thermal contacts that they are connected with a large force so that as much contact as possible exists at the microscopic level. In Fig. 4.5(e) the much larger cross-section of the NbTi cable compared to all other cables that reach the STM head can be seen, including the previous HF cable (see Tab. 4.1). For this reason, the cable is wound

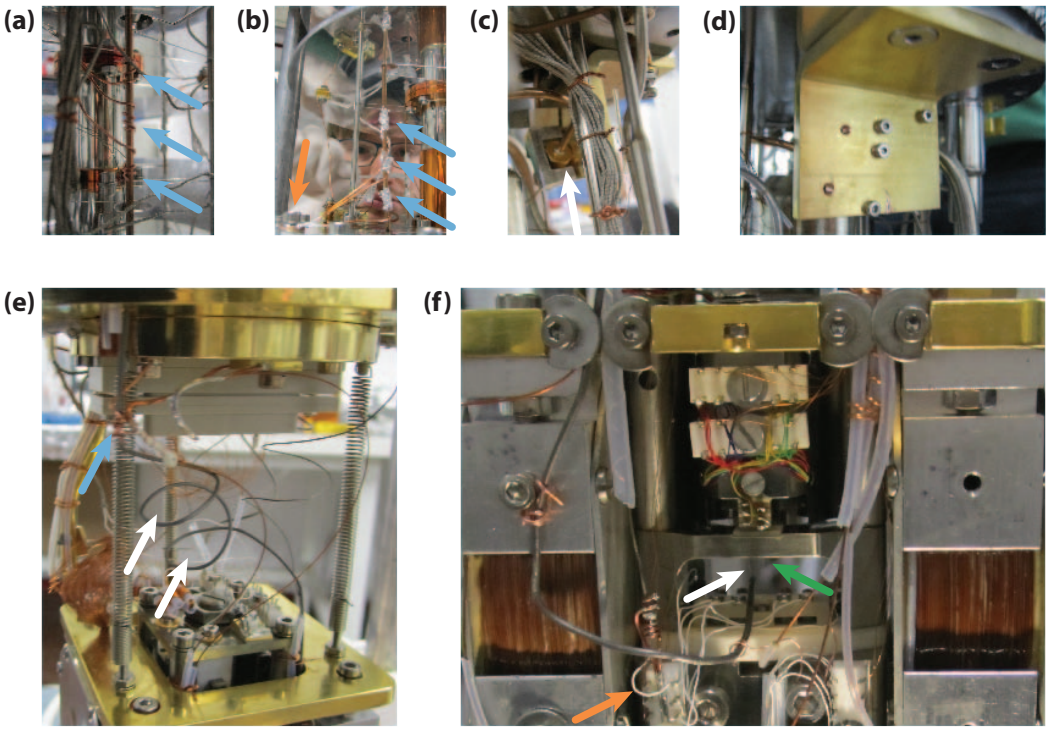


**Figure 4.5 | Installation of the new HF cables.** The figure shows the technical precautions that have been taken to ensure good thermal contact between the HF line and the antenna and to avoid the transmission of mechanical vibrations. **(a)** Thermal coupling of the copper-beryllium cable by copper wires acting as cooling fingers (*blue* arrows) **(b)** Furthermore, the thermal contact of the wires to the coaxial cable was increased with silver conductive epoxy adhesive. These wires are firmly screwed to the corresponding 30 K and 70 K shields (*orange* arrow). **(c)** and **(d)** show the transition between the copper-beryllium cable and the superconducting NbTi cable. The SMK connector is pressed tightly to a Au-coated copper angle with a clamping device. The angle itself acts as a cooling finger and is firmly screwed to the base plate of the 4 K cryostat. **(e)** The much larger cross-section of the NbTi cable can be seen in comparison to all other cables that go to the STM head. For this reason, the cable is wound like a spring in several loops (*white* arrows) that are intended to dampen the mechanical transmission of vibrations. Another cooling finger couples the line to the 1 K stage (blue arrow). **(f)** On the head itself the HF cable is only loosely attached to hold it in position. The end is stripped and serves as an antenna (*white* arrow). A comparison with the position of the tip (*green* arrow) shows the spatial proximity. PTFE connection pad as an interface between the old HF line and the tip cable (*orange* arrow).

like a spring in several loops, which are intended to dampen mechanical vibration. On the head itself (see Fig. 4.5(f)), the HF cable is only loosely attached to hold it in position, but without strong mechanical coupling. The cable ends with the stripped part that acts as an antenna (*white* arrow). The proximity to the tip position (indicated by *green* arrow) is < 15 mm.

## 4.3 Characterization of HF circuit

To determine the attenuation of our HF setup we use a nonlinearity in the current-voltage dependence. By measuring the current while modulating the fixed *dc* bias with the HF voltage we can determine the strength of the HF amplitude. A comparison with the set HF power at the source gives directly the value for the attenuation. As shown in Fig. 4.6(a) we use the highly nonlinear current-voltage characteristics of the pristine superconducting Pb-Pb tunnel junction. Similarly, other nonlinearities such as inelastic spin excitations could also be used [131].

In detail, we set the *dc* bias at $V = 2.6\,\mathrm{mV}$, just below the onset of the quasi-particle current at $eV = 2\Delta$. Thus, we expect to measure a vanishing current within the gap. For large enough applied HF amplitudes, the *ac* voltage $V_{\mathrm{ac}}(t)$ added to the *dc* bias generates a current contribution as it is entering the nonlinearities. Since the bandwidth of our current amplifier[1] is not sufficient for detecting current changes in the frequency range of GHz, we will measure only the time-averaged current $\overline{I(t)} = \langle I \rangle$. Here the demand of a nonlinearity becomes obvious because otherwise the contribution of the HF voltage is averaged out. A representative measurement of time-averaged current as a function of HF power is shown in Fig. 4.6(b). The indicated power level refers to the output level at the signal generator. Since the electrical power varies over several orders of magnitude, it is given in logarithmic form as power level $L(\mathrm{dBm}) = 10\log_{10}(\frac{P}{1\,\mathrm{mW}})$ based on a reference power of 1 mW.

We determine the attenuation of our signal path by modeling this current-power dependence. The model is based on the *dc* voltage $V_{\mathrm{dc}}$ and the precisely determined current-voltage relation $I^{(0)}(V)$ without applied high frequencies from Fig. 4.6(a). The time averaged current is by definition

$$\langle I \rangle = \frac{1}{\tau} \int_0^\tau \mathrm{d}\tau'\, I^{(0)}\left( V_{\mathrm{dc}} + V_{\mathrm{ac}}(\tau') \right) . \tag{4.1}$$

Since the HF voltage modulation $V_{\mathrm{ac}}(\tau) = V_{\mathrm{PK}} \sin(\omega\tau)$ is a periodic function, it is sufficient to integrate over one of its periods. The amplitude (peak voltage) is related to the power as

[1] Variable Gain Low Noise Current Amplifier DLPCA-200: For this measurement, we use the highest sensitivity with a trans-impedance of $10^9$ V/A (also referred to as gain 9). At this gain the −3 dB bandwidth of the amplifier is 1.1 kHz.

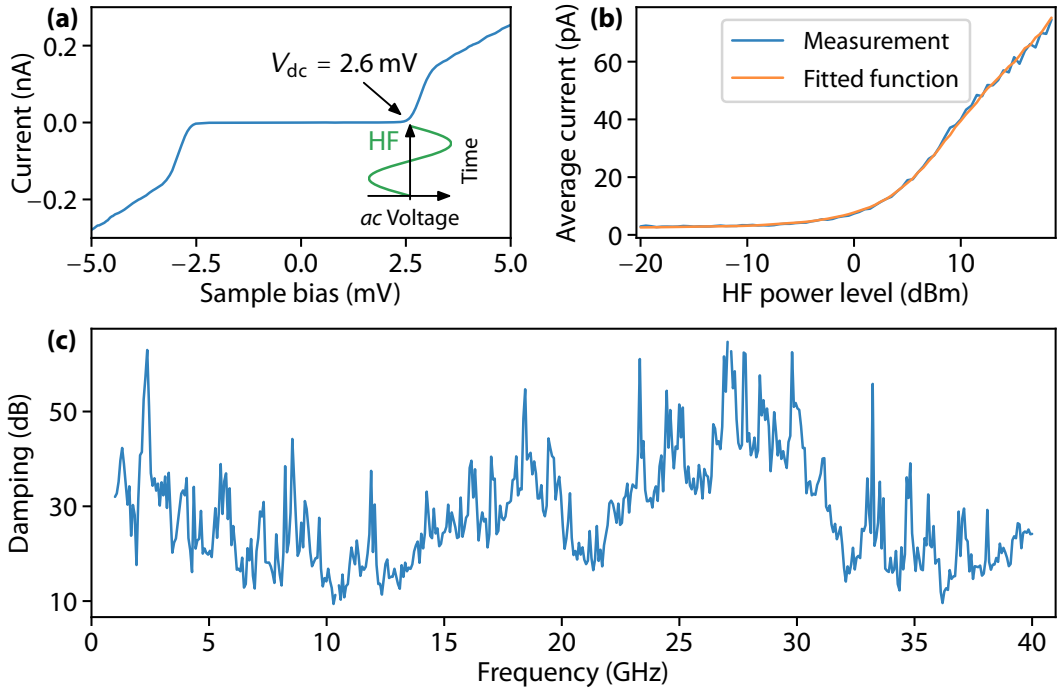


**Figure 4.6 | Transmission characteristics of the HF circuit. (a)** Example of an I(V) characteristic with pronounced nonlinearities. In this case the I(V) dependence of a superconducting Pb-Pb tunnel junction at $G_N = 3.7 \times 10^{-1}\,G_0$, shown in *blue*. Schematically as an inset the HF voltage modulated on top is shown in green. Its amplitude indicates the window in which the current is averaged. **(b)** Exemplary measurement of the time-averaged current as a function of the HF power level (*blue* curve) and the corresponding fit using Eq. (4.4) (*orange* curve) to determine the power in the junction and thus also the attenuation. **(c)** Transmission curve of the setup. The attenuations determined from (b) are plotted over the complete range of frequencies available to us up to 40 GHz.

follows

$$P = I V_{\mathrm{RMS}} = \frac{V_{\mathrm{RMS}}^2}{R} \tag{4.2}$$

$$\Leftrightarrow \quad V_{\mathrm{PK}} = \sqrt{2R \cdot P}\,, \tag{4.3}$$

where $R$ is the impedance, which is 50 Ω for our setup. The root mean square of a sinusoidal function $V_{\mathrm{RMS}} = V_{\mathrm{PK}}/\sqrt{2}$ is the peak amplitude divided by $\sqrt{2}$. Thus the time averaged current can be calculated as

$$\langle I(L) \rangle = \frac{1}{2\pi} \int_0^{2\pi} \mathrm{d}\phi\, I^{(0)} \left( V_{\mathrm{dc}} + \sin(\phi) \sqrt{2R \cdot 10^{\frac{L(\mathrm{dBm}) - g(\mathrm{dB})}{10}} 1\,\mathrm{mW}} \right). \tag{4.4}$$

Here $g(\mathrm{dB})$ is the damping of the setup, which reduces the incoming power level at the junction accordingly. In Fig. 4.6(b) the fit using Eq. (4.4) is shown next to the data. The comparison between the experiment (*blue* curve) and the fit (*orange* curve) shows a good agreement. Thus, this model is sufficiently well suited for the determination of the attenuation. The fit procedure proved to be very robust and stable with error rates below 5 %. The fit is most error-prone when the attenuation is so large that hardly any signal is received, which is a systematic error and cannot be attributed to the model.

The extracted damping over a wide range of frequencies is shown in Fig. 4.6(c). To generate small enough *ac* modulations we have to artificially increase the damping of the transmission line with a ~40 dB attenuator. This value is subsequently subtracted in Fig. 4.6(c). Overall we get a very discontinuous frequency response with many fine structures due to standing waves. Given the design of the setup, with all the shields and connectors, we expected similar results. In general, our attenuation fluctuates between 10 dB to 60 dB over the entire frequency range. Besides many small spikes, we also notice more wider range structures. Two attenuation bands can be identified between 13 GHz to 20 GHz, and 22 GHz to 32 GHz.

In the range from 30 GHz to 40 GHz, which is important for our experiments, the frequency response is particularly loss-free with attenuations <20 dB. We note that also during data acquisition, we artificially increased the damping of the transmission line with a ~40 dB attenuator. We observe that the total attenuation at 40 GHz slowly fluctuates between 53 dB to 57 dB over time (13 dB to 17 dB without the attenuator). We attribute these fluctuations to external influences such as the He level of the cryostat. For the duration of one measurement sweep, however, we find the attenuation to be constant to a good approximation.

An alternative way of measuring the HF energy-level in the junction offers a comparison with the theory of Tien and Gordon. The microwave radiation leads to a distinct V-shaped splitting. So, for example, the coherence peaks in the power-dependent $\mathrm{d}I/\mathrm{d}V$ maps can be used to make an accurate measurement of the power level at the junction by evaluating the resulting photon-assisted tunneling pattern (see Section 7.1). This method is very precise and is well suited for single maps. We determine the attenuation of each map in Chapters 7 and 8 by fitting one of the spectra of each sweep with the corresponding Tien-Gordon-like expressions in Eqs. (6.12), (6.17), and (6.19). Although this method works very well for a single frequency, it is too time-consuming to characterize the complete frequency response due to the large amount of data required. Both ways of determining the attenuation were cross-checked and provide consistent results.

## 4.4 Josephson Setup

To measure current-biased Josephson spectra we have added a 1 MΩ resistor to our experimental setup. The reduced circuit diagram is shown in Fig. 4.7. This Josephson resistor is connected in series to the junction (again shown within the resistively and capacitively shunted junction (RCSJ) model, explained in Section 2.4). The resistor is significantly

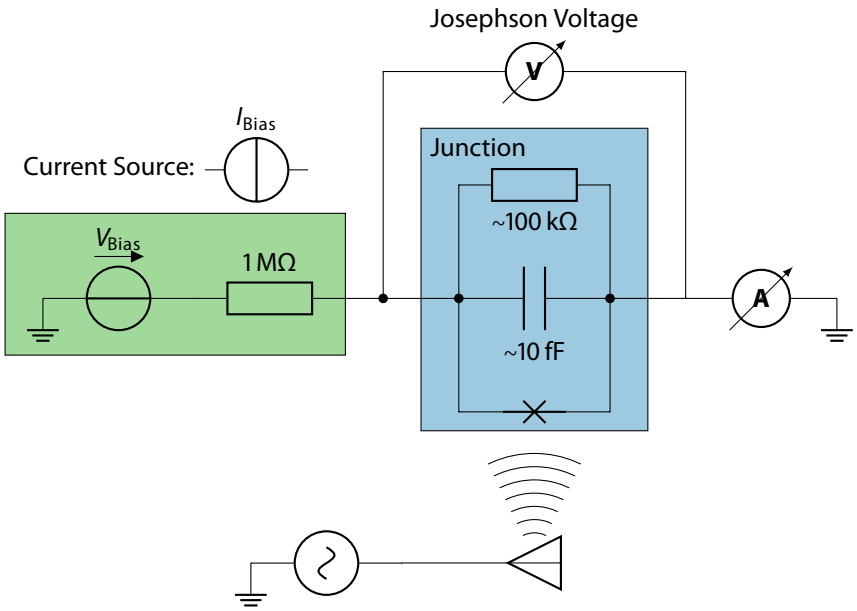


**Figure 4.7 | Equivalent circuit diagram for the Josephson setup.** Voltage source and resistance of 1 MΩ together form a constant current source (*green*). The voltage across the junction (*blue*, shown in the RCSJ model) is measured by an additional amplifier (labeled: Josephson Voltage). HF radiation can be emitted into the junction via the antenna.

larger than the junction resistance itself, which in these Josephson experiments is around 100 kΩ and less. Accordingly, almost all the bias voltage drops across the Josephson resistor, which acts effectively as a constant-current source. In order to record $V(I)$ characteristics of the Josephson junction, a highly precise measurement of the junction voltage is necessary. For this, we use an additional amplifier with an amplification gain of $10^3$, connected in a four-point configuration. The amplifier itself has a floating ground, which means that the zero-level adapts to the input signal over time. For this reason, the spectra should be recorded at times of $< 1$ s so that effects due to the offset does not have any impact on the measured data.

# 5

# Superconducting Lead and its Interaction with Manganese Adatoms

All measurements presented in this thesis use lead (Pb) as a substrate. Lead is a superconducting material at low temperatures, which has been studied intensively in our group for many years. The two-band nature of lead has been established [160], but also the interaction of magnetic adatoms [97, 161, 162] and magnetic molecules [95, 141, 163–167] with this superconductor has been studied extensively and many new insights into YSR states have been gained [35]. These studies form the basis for further investigations such as the research on the coupling of iron and cobalt chains and the Majorana zero modes arising at their ends [37, 168].

Lead is a type I superconductor with a critical temperature of $T_c = 7.2\,\mathrm{K}$. Studies on bulk Pb show typical London penetration depths $\lambda_L$ of 32 nm to 39 nm and Ginzburg-Landau coherence length $\xi_{GL}$ of 51 nm to 83 nm [169]. We use single crystals as substrates in our experiments. These are cleaned in several cycles, where one cycle consists of successive $Ne^+$ ion sputtering at a Ne pressure of $2 \times 10^{-4}$ mbar and subsequently heating to about 400 K for approximately 30 min.

In Fig. 5.1(a) a typical STM topography of the surface is shown. It contains several very typical characteristics: The surface shows flat terraces that are confined by step-edges, which usually have a height of exactly one atomic layer. With our preparation procedure, we achieve a terrace size of up to several 100 nm, which are very well suited for STM studies. Vapor-deposited atoms appear as small round protrusions on the surface. Also Ne inclusions are visible, which are trapped underneath the surface during the sputtering process. These show up as hexagonal depressions and protrusions, where the exact shape and electronic properties depend on their depth and the corresponding scan parameters.

The strength of a scanning tunneling microscopes (STMs) is the combination of the spatial resolution with its spectroscopic possibilities in scanning tunneling spectroscopy (STS).

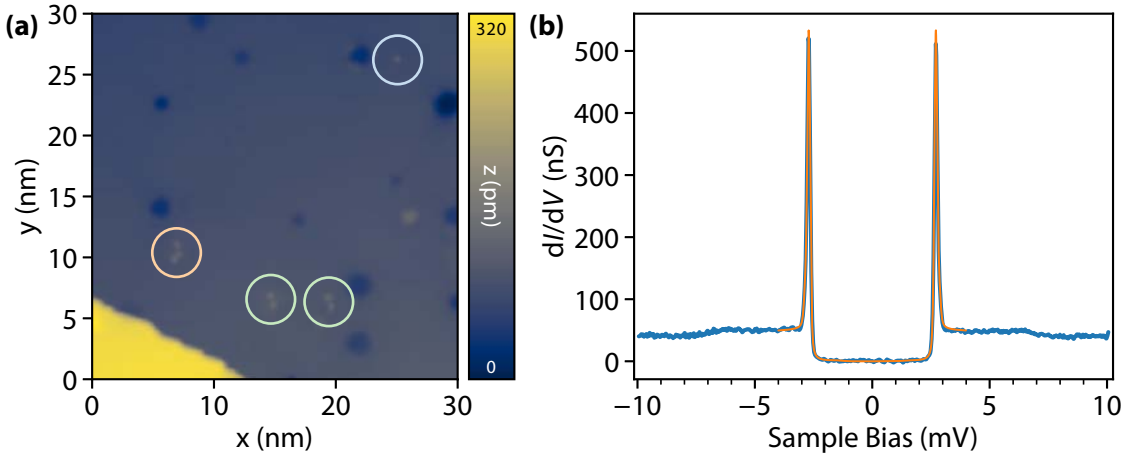


**Figure 5.1 | Exemplary lead surface with vapour-deposited Mn adatoms. (a)** The image shows a 30 nm × 30 nm large segment of the surface of a lead single crystal. It was cleaned and heated under special conditions to form large terraces. In the lower-left corner a single atomic terrace step can be seen. As a consequence of the cleaning process, the surface is covered with numerous hexagonal depressions of different sizes, which originate from Ne impurities. The vapor-deposited Mn atoms are seen as small protrusions and are encircled. In this segment there is one single atom (*blue* circle), but also collections of Mn atoms in the form of two dimers (*green* circles) and one trimer (*orange* circle). Setpoint $V_{\text{Bias}} = 5\,\text{mV}$, $I = 100\,\text{pA}$. **(b)** $\text{d}I/\text{d}V$ spectrum (*blue*) and fit (*orange*) of the plain lead surface recorded with a superconducting Pb tip. The spectrum is the result of the convolution of the BCS density of states of substrate and tip and therefore shows a gap of $e|V| = \Delta_t + \Delta_s = 2\Delta$, with a superconducting pairing parameter of Pb of $\Delta = 1.35\,\text{meV}$. At $e|V| \approx 7\,\text{meV}$ begins the onset of the phonon shoulders. Setpoint and measurement parameters: $V_{\text{Bias}} = 10\,\text{mV}$, $I = 400\,\text{pA}$, $V_{\text{Lock-in}} = 25\,\mu\text{V}$ and $f_{\text{Lock-in}} = 873\,\text{Hz}$.

The STS spectra must always be regarded as a convolution of the densities of states of both electrodes. The assumption that the signal is a direct reflection of the sample density of states (DoS) is only valid for a flat density of states in the tip, where the resolution $3.5k_{\text{B}}T \approx 400\,\mu\text{eV}$ is limited by the experimental temperature of $T = 1.35\,\text{K}$. We can circumvent this thermal restriction and go beyond the Fermi-Dirac limit by using superconducting tip material with their BCS coherent peaks as a probe. Therefore we coat tungsten tips with a thin layer of lead by controlled submersion of the tip into the surface. Fig. 5.1(b) shows a spectrum (*blue*) of such a pristine Pb-Pb junction. It becomes apparent that now the BCS density of states of tip and sample are convoluted and an energy of $e|V| = \Delta_t + \Delta_s = 2\Delta$ is needed to break a Cooper pair in the tip and substrate each, before quasi-particle transport between the coherence peaks can take place. From the fit of the superconductor-superconductor spectrum (*orange*), we can determine an instrumental broadening of $\Gamma_{\text{setup}} = 60\,\mu\text{eV}$ and a Dynes parameter of $\Gamma_s = 20\,\mu\text{eV}$, which is one of the corrections needed to describe the density of state of lead as described in the next section. With these two broadenings we are able to estimate our resolution to 80 µeV (see Section 3.2.3). So far, we

could not detect an influence of the Ne impurities on the spectroscopy. Nevertheless, we avoid measurements in their vicinity, so that our results can always be separated from the impurities.

## 5.1 Corrections Applied to the BCS Density of States

Although the BCS theory provides a robust basis for the understanding of superconductors, early experiments in planar tunneling junctions showed that the experimental density of states deviates from the theory even in elementary superconductors such as lead, vanadium, or tantalum. These deviations are small and can be introduced as correction terms to Eq. (2.52). For the Pb superconductors we use, three corrections have to be considered: A finite lifetime effect, a strong electron-phonon coupling, and that Pb is a tow-band superconductor.

### 5.1.1 Finite Lifetime Effects on the Density of States

To consider pair breaking of the quasiparticles at the edge of the superconducting gap, a small imaginary energy $E \to E + \mathrm{i}\Gamma_\mathrm{s}$ (Dynes parameter [170]) is introduced to account for final lifetime effects[171]:

$$\rho_\mathrm{s}(E) = \rho_0 \,\mathrm{Im}\left(\frac{E + \mathrm{i}\Gamma_\mathrm{s}}{\sqrt{\Delta_\mathbf{k}^2 - (E + \mathrm{i}\Gamma_\mathrm{s})^2}}\right). \tag{5.1}$$

$\Gamma_\mathrm{s}$ is usually small compared to the minimum excitation energy $\Delta_\mathbf{k}$. The effects of this correction are demonstrated in Fig. 2.6(b). It is known, that the simplest way to create such a correction is to assume an energy-dependent gap function of the form $\Delta(E) = \Delta_0 E/(E + \mathrm{i}\Gamma_s)$ [172, 173]. Various effects are imaginable that lead to such a pair breaking processes. Electron-photon scattering alone has a pair breaking character at finite temperatures [172]. However, the expected temperature dependence of this mechanism is not consistent with experimental observations [174–176], which measured only a weak temperature dependence nor did the effect disappear in the low-temperature limit. Elastic pair-breaking processes due to the scattering at magnetic impurities [177] or the fluctuation of the order parameter [178] are other possibilities. The latter can be excluded due to the spatial homogeneity of the observed tunnel spectra [174]. More generally, however, it can be shown, that by assuming a very weak random scattering potential disorder occurs and is accounted for by the self-energy, resulting in a correction as Dynes suggested [173].

### 5.1.2 Phonon Structure in Strong Electron-Phonon Coupled Superconductors

For materials with strong electron-phonon coupling, the gap parameter can also become a function of energy $\Delta(E)$. This effect was first observed by Giaever on Pb [179] and discussed in detail by Rowell *et al.* [180]. They showed that the Eliashberg phonon interaction between electrons causes $\Delta(E)$ to exhibit structures at energies determined by the phonon energies. Especially at the gap $\Delta$ plus multiples of the phonon frequencies. We also see such phonon shoulders on lead at $e|V| \approx 7$ meV, visible in Fig. 5.1(b). The agreement between the theory and the experiments in materials like lead and mercury has also clarified the last doubts on the assumption, that electron-phonon mechanisms are the cause of superconductivity in these materials.

### 5.1.3 Two-Band Superconductors

Lead is a so-called tow-band superconductor. This fact has been theoretically predicted by density functional theory by Floris *et al.* [181] and experimentally confirmed by Ruby *et al.* [160] in our group. They found that the Fermi surface of Pb consists of a compact Fermi sheet mainly with *s-p* character and a tubular Fermi sheet with *p-d* character, both are illustrated in Fig. 5.2. The differences in the origin of the Fermi sheets lead to different electron-phonon coupling strengths [183] and thus to different pairing energies in the superconducting condensate. These two different superconducting pairing energies can be seen for Pb(111), Pb(110), and Pb(100), as a double structure in their coherence peaks representing tunneling into the two Fermi sheets. Depending on the orientation of the lead crystal, tunneling occurs with different amplitudes. This becomes clear if we recall that the wave function $\Psi \propto \exp(-\kappa z)$ is decaying exponentially with a decay constant $\kappa = \sqrt{\mathbf{k}_\perp^2 + \mathbf{k}_\parallel^2}$. This constant is a combination of the vector component $\mathbf{k}_\perp$ which is necessary to overcome the tunneling barrier and the vector component $\mathbf{k}_\parallel$ which is parallel to the surface (see Eq. (3.3)). Consequently, wave functions will decay slower from the $\Gamma$ point, since $\mathbf{k}_\parallel = 0$ and tunneling takes place mainly in the direction of $\mathbf{k}_\perp$. Due to the exponential form of the decay, it even follows that the larger the tunnel barrier becomes, the smaller the contribution of $\mathbf{k}_\parallel$ will be. The comparison of the Fermi surfaces in Fig. 5.2 shows that we always tunnel into the *s-p*-like band, whereas we need a $\mathbf{k}_\parallel \neq 0$ for tunneling into the *p-d*-like band. The only exception here is the Pb(110) direction. Due to these distinctions in the Fermi-sheets, the ratio of the peak heights is different. With increasing conductivities and thus increasing tunnel probabilities, the ratio becomes equal, since tunneling in the direction of $\mathbf{k}_\parallel$ leads to a less significant decay in the wave function.

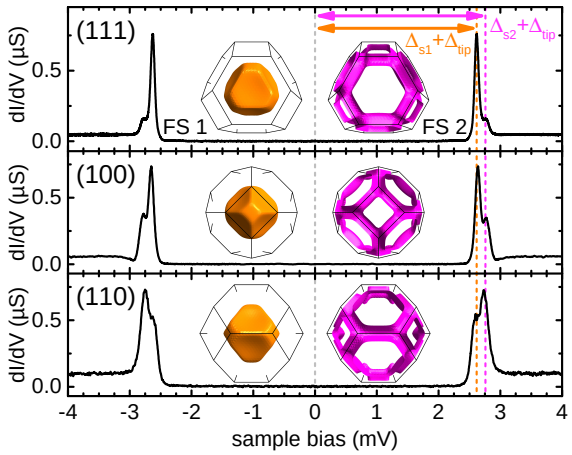


**Figure 5.2 | The two-band characteristic of Pb.** Figure is taken from Ref. [160]. Shown are d$I$/d$V$ spectra, taken on clean terraces of Pb(111), Pb(100) and Pb(110) single crystals (top to bottom). The quasiparticle coherence peaks surrounding the gap consist of two peaks which are 150 µeV apart. The peak energy is the sum of the pairing energies of the tip (here called $\Delta_{tip}$) and the substrate (here called $\Delta_{s1}$ and $\Delta_{s2}$ respectively). The insets in the middle show the corresponding top views of the two different Fermi surfaces (FS) of the two bands of Pb crystal. The *orange* one has a *s-p* character, while the *purple* one has a *p-d* character. These 3D models are taken from Ref. [182]. Depending on the shape of the Fermi surface in tunneling direction, the associated coherence peaks are respectively stronger or weaker.

## 5.2 Mn Adatoms on Pb(111)

To induce YSR states in the s-wave superconductor Pb(111) we use magnetic Mn adatoms. This system has already been studied in detail by Ruby *et al.* [97]. In the following, we will summarize some of their results because we will use them as a reference to discuss our results on photon-assisted tunneling.

The adatoms are evaporated under ultra high vacuum (UHV) conditions in the preparation chamber. We use the possibility to cool down the sample in the evaporation position to approximately 60 K with the He flow cryostat. We deposited a coverage of less than 20 atoms per $100 \times 100\,\mathrm{nm}^2$ (Fig. 5.1 shows a typical preparation). For spectroscopy, we always make sure that we measure isolated adatoms that have nothing but clean lead surface in a surrounding radius of at least 5 nm. The Mn can sit in two different absorption states on the lead surface, the *down* and *up* adsorption side. These differ in their apparent height and different spectroscopic fingerprints. After the evaporation process, all atoms have the same apparent height and are on the lower adsorption side, which was investigated by Ji *et al.* [36]. It is possible to manipulate an adatom back and forth between the two states by tip manipulation. By contacting the adatoms with the tip while applying a bias voltage of 5 mV a change to the higher configuration is induced. This process can be well monitored

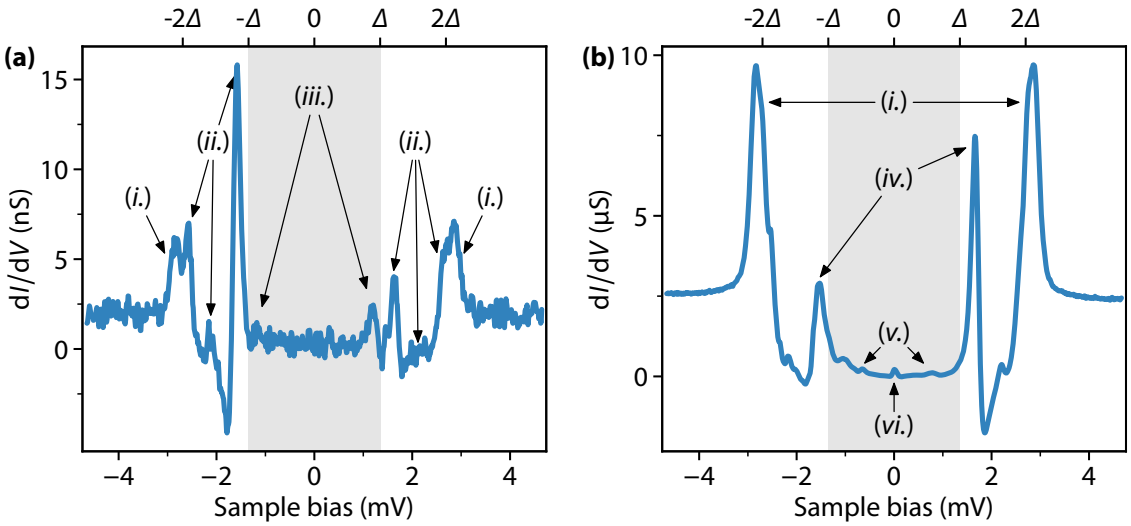


**Figure 5.3 | Differential conductance spectra recorded at two different tip-substrate distances above the center of single Mn atoms on Pb(111).** **(a)** Spectrum with low normal state conductance of $G_N^{low} = 2.6 \times 10^{-5}\, G_0$ and **(b)** spectrum with high conductance $G_N^{high} = 5.2 \times 10^{-2}\, G_0$. All spectra on top of Mn have the following features (in descending order, from high to low bias voltages): The BCS coherence peaks at $2\Delta$ (*i.*) are followed by the tunneling into the three YSR states (*ii.*). The tip's gap is represented by the gray-shaded area. The tunneling of thermally excited quasiparticles (*iii.*) falls within this area. At high junction conductances – panel **(b)** – we additionally observe resonant Andreev reflections (*iv.*), next to multiple Andreev reflections (*v.*), and Josephson tunneling (*vi.*).

and controlled during a z-approach of the tip while applying the voltage. To reverse the adsorption side the atom is contacted by the tip at a bias of −180 mV.

### 5.2.1 Distance Dependent Measurement: From Single-Electron Tunneling to Andreev Tunneling

In order to observe different tunneling processes through the YSR states we perform tip approaches on the Mn adatoms. We use the Mn atoms in the *up* adsorption side, because they were found to be more stable upon tip approach. Differential conductance spectra at two different tip-substrate distances on a Mn adatom are shown in Fig. 5.3 giving an overview of the observed basic tunneling processes. The two spectra stand exemplarily for the extremal points of a distance-dependent measurement and represent two opposite tunnel regimes as described below. The shape of $\mathrm{d}I/\mathrm{d}V$ spectra is composed of different tunneling processes, some of which can be found in both spectra, others only becoming apparent at high tunnel coupling. The following six tunneling processes can be distinguished in the spectra:

*i.* Quasiparticle tunneling from the coherence peaks at $e|V| = \Delta_t + \Delta_s = 2\Delta$

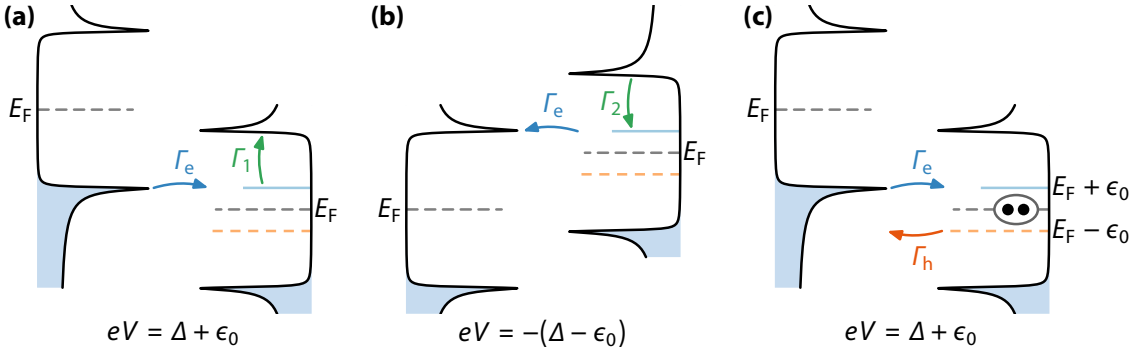


**Figure 5.4 | Sketches of the tunnel processes across the YSR states. (a)** At $eV = \Delta + \epsilon_0$, single-electron tunneling transfers an electron with rate $\Gamma_e$ into the positive-energy YSR state, which is then excited with rate $\Gamma_1$ into the positive-energy quasiparticle continuum of the substrate. **(b)** Thermal occupation of the YSR state with rate $\Gamma_2$ followed by single-electron tunneling with rate $\Gamma_e$ leads to a thermal replica of the experimental YSR resonance at $eV = -(\Delta - \epsilon_0)$. **(c)** Resonant Andreev reflections transfer a Cooper pair to the substrate via electron tunneling with rate $\Gamma_e$ and hole tunneling with rate $\Gamma_h$. The process takes place at $eV = \Delta + \epsilon_0$ like the single- electron process; the analogous hole processes take place at $eV = -(\Delta + \epsilon_0)$ for the process of panel **(a)**, $eV = +(\Delta - \epsilon_0)$ for the process of panel **(b)**, and $eV = -(\Delta + \epsilon_0)$ for the process of panel **(c)**.

*ii.* Quasiparticle tunneling into the YSR subgap states at $e|V| = \Delta + \epsilon_0$

*iii.* Tunneling of thermally excited quasiparticles at $e|V| = \Delta - \epsilon_0$

*iv.* resonant Andreev reflections at $e|V| = \Delta + \epsilon_0$

*v.* (multiple) Andreev reflections at $e|V| = 2\Delta/k$ for $k = 2, 3, \ldots$

*vi.* Josephson effect: Tunneling of Cooper pairs at $e|V| = 0$

In more detail: (*i.*) Above the threshold of $e|V| = 2\Delta$ the energy is sufficient to excite a Cooper pair in the tip and substrate each, similar to the spectra of plain superconductor-superconductor junctions in Fig. 5.1(b). (*ii.*) In addition to the coherence peaks, the YSR subgap states can be seen symmetrically around the Fermi energy at $e|V| = \Delta + \epsilon_0$ in Fig. 5.3. As described in section 2.6, magnetic atoms like Mn can induce YSR states in the superconductor. In the case of Mn in the high absorption configuration, three YSR states are induced at energies of $\epsilon_0 = 0.25$ meV, 0.77 meV and 1.2 meV. In the following, our main focus lies on the energetically lowest of these three YSR states, which we label as $\alpha$, with $\alpha_\pm$ at the corresponding polarity. The tunneling process into such a YSR state is described in the scheme in Fig. 5.4(a). As soon as enough voltage is applied so that electrons from the quasi-particle continuum of the tip can tunnel into YSR resonances, peaks become visible in the spectrum. (*iii.*) A thermal YSR state can be detected at $e|V| = \Delta - \epsilon_0$. Thermal excitation of the YSR state, as shown in Fig. 5.4(a), results in a current already below $e|V| < \Delta$. For Mn, only the thermal YSR states of the lowest lying YSR state can be detected.

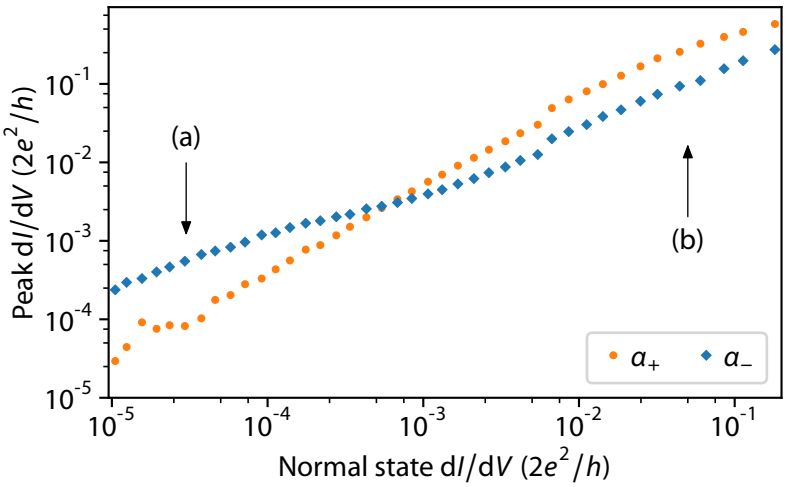


**Figure 5.5 | Crossover of the YSR peak heights when increasing the conductance.** Peak heights $\alpha_{\pm}$ of the two resonances associated with the energetically lowest YSR state as a function of normal-state conductance at $T = 1.35$ K. The labels (a) and (b) mark the conductance values at which the spectra in the corresponding panels of Fig. 5.3 and Fig. 8.1 were taken.

In addition to the single-electron processes, multi-electron processes can take place, if the conductance and thus the tunneling probability is increased. In an Andreev reflection an electron (hole) is reflected as a hole (electron), and thus a Cooper pair is transported over the junction. (*iv.*) If a YSR state is involved in this process, *resonant* Andreev processes are obtained by resonantly transported Cooper pairs across the barrier. The energy $e|V| = \Delta + \epsilon_0$ at which this process occurs is the same as for the single-particle processes including the YSR state (compare (*ii.*)). (*v.*) Without a YSR states regular (multiple) Andreev processes occur at voltages of $e|V| < 2\Delta$. Depending on the number of charge carriers $k$ involved in the process, the corresponding threshold values are $e|V| = 2\Delta/k$ for $k = 2, 3, \ldots$ (see Section 2.5). The resonant Andreev reflections already occur at much lower tunneling conductance than the once not including a YSR state, since an electron (hole) can virtually enter the state. One also expects to observe resonant multiple Andreev reflections involving the YSR state occurring at $e|V| = (\Delta + \epsilon_0)/k$. It is difficult to assign these peaks marked multiple Andreev reflection (MAR) to specific processes, due to the large number of possible resonant processes involved with three YSR states, as well as (multiple) non-resonant MARs. (*vi.*) In addition to the Andreev processes, Cooper pairs can also tunnel directly from the tip into the sample. This Josephson current is observed at zero energy.

A closer look at the YSR resonances at $\epsilon_0 = 0.25$ meV reveals that their shape changes significantly during the tip approach. When comparing their amplitudes $\alpha_{\pm}$ it appears that their ratio is inverted. In Fig. 5.5 the amplitudes are plotted against the normal state conductance confirming the crossover and revealing that it is a continuous process. The crossover can be explained by the change in the predominant tunneling process. In the low conductance case, single-electron processes dominate the current, whereas for high

conductance they become negligible compared to the resonant Andreev processes, see Section 5.2.3. For large tip-substrate distances, the ratio of the amplitudes $\alpha_{\pm}$ corresponds to the ratio of electron and hole wave functions $u$ and $v$ of the YSR states as the tunneling process consists only of single-electron tunneling [97]. From Fig. 5.3(a) a ratio of $\alpha_+/\alpha_- = (u/v)^2 = 0.253$ can be determined. With the knowledge of the YSR wave functions, we can describe the tunneling processes through the YSR states theoretically. Following Fermi's golden rule we obtain rate equations for the transition from tip states to the YSR state described by $u$ and $v$. These rate processes will be discussed in the following section and theoretically in chapter 6.

## 5.2.2 Description of the Tunnel Process by Means of Rate Equations

An important difference between single-electron and the Andreev processes is the change in the occupation of the YSR state [184]. The single-electron processes change the occupation while Andreev processes just transfer Cooper pairs into the condensate. For this reason, a continuous current flow carried by single-electron processes requires a relaxation process, which empties (fills) the state after it has been occupied from (emptied into) the tip. The description of these processes is done by rate equations which follow Fermi's golden rule. In Fig. 5.4 these rates are included in the illustration of the processes. Fig. 5.4(a) shows that the YSR state at $eV = \Delta + \epsilon_0$ is filled at the rate $\Gamma_e$ from the tip. In order for this process to be repeated, the YSR state must first be emptied again. This can be realized by an inelastic excitation into the quasiparticle continuum of the substrate at the rate $\Gamma_1$. If $\Gamma_1$ becomes smaller than $\Gamma_e$, this process saturates. The equivalent is the formulation for the thermally excited YSR states, happening at a rate $\Gamma_2$ and at an energy of $eV = -(\Delta - \epsilon_0)$, see Fig. 5.4(b). Another possible process is that the electron with rate $\Gamma_e$ is reflected as a hole with the rate $\Gamma_h$, as shown in Fig. 5.4(c). This leaves two electrons in the substrate, which can be formed into a Cooper pair and enter the condensate. This process is possible once a threshold value of $eV = \Delta + \epsilon_0$ is reached. If the bias is below the threshold, these resonant Andreev reflections are not possible, because of the lack of a free state in the tip for the hole to tunnel into.

### Thermal Relaxation Processes

The $\Gamma_1$ and $\Gamma_2$ rates that describe the occupation of the YSR state also determine its intrinsic line width. These two rates are added to the theory as phenomenological parameters, as their origin can be caused by various microscopic mechanisms. We believe that they can be attributed to phonon processes because Ruby *et al.* [97] has seen that the crossover point between the linear and sublinear regime in Fig. 5.5 is strongly temperature-dependent. This would lead to a thermal distribution of the YSR state $f(E) = n_F(\epsilon_0)$ in the absence of any tunneling coupling to the tip, where $f(E) = \Gamma_2/(\Gamma_1 + \Gamma_2)$ (see Section 2.6.2).

For purely thermal relaxations we can assume in general

$$\frac{\Gamma_1}{\Gamma_2} = e^{\beta\epsilon_0}\,, \tag{5.2}$$

with $\beta$ being the inverse temperature. The simplest relaxation process involves a direct transition between YSR state and quasiparticle continuum. For such processes it has been shown that the relaxation rate is given by [185]

$$\Gamma_1 \sim \sqrt{\frac{1}{\beta\Delta}} e^{-\beta(\Delta-\epsilon_0)} \left[(\Delta-\epsilon_0) + (\Delta+\epsilon_0)e^{-\beta\epsilon_0}\right], \tag{5.3}$$

$$\Gamma_2 \sim \sqrt{\frac{1}{\beta\Delta}} e^{-\beta\Delta} \left[(\Delta-\epsilon_0) + (\Delta+\epsilon_0)e^{-\beta\epsilon_0}\right]. \tag{5.4}$$

The relaxation rate $\Gamma_1$ has the thermal factor $\exp(-\beta(\Delta-\epsilon_0))$, which contains the required phonon energy $\Delta-\epsilon_0$ for the transition to the continuum. In contrast, $\Gamma_2$ is only limited by the thermal occupation $\exp(-\beta\Delta)$. The ratio of the two results in Eq. (5.2). The fact that there is more than one subgap state makes complicated relaxation dynamics possible, such as pairs of quasiparticles from subgap states, that can relax inelastically in the form of Cooper pairs. The possibility and effects of such processes were discussed further in Ref. [97]. Another plausible process would including the transitions assisted by photons as a relaxation mechanisms.

#### Electron and Hole Tunneling Rates

The electron and hole tunnel rates $\Gamma_\mathrm{e}$ and $\Gamma_\mathrm{h}$ describe the tunneling process across the vacuum barrier of the junction. They follow Fermi's golden rule (see Section 2.6.2)

$$\Gamma_\mathrm{e}(\omega) = \frac{2\pi}{\hbar} T^2 |u|^2 \rho(\omega_-)\,, \tag{5.5}$$

$$\Gamma_\mathrm{h}(\omega) = \frac{2\pi}{\hbar} T^2 |v|^2 \rho(\omega_+)\,, \tag{5.6}$$

with the notation $\omega_\pm = \omega \pm eV$. The electron and hole wave functions of the YSR states $u$ and $v$ are included as well as the DoS $\rho(\omega)$ of the tip and the tunnel coefficient $T$.

### 5.2.3 Expressions for the Current of Single-Electron and Resonant Andreev Tunneling

In general, the total tunneling current via YSR states is the sum of single- and two-electron (resonant Andreev) processes, $I = I_\mathrm{s} + I_\mathrm{a}$. Ruby *et al.* [97] derived the expression for the

current by using a non-equilibrium Green function method resulting in

$$I_{\mathrm{s}}(V) = \frac{e}{h} \int \mathrm{d}\omega \frac{\Gamma_1 \left[\Gamma_{\mathrm{e}}^{n_{\mathrm{F}}}(\omega) - \Gamma_{\mathrm{h}}^{n_{\mathrm{F}}}(\omega)\right] - \Gamma_2 \left[\Gamma_{\mathrm{e}}^{1-n_{\mathrm{F}}}(\omega) - \Gamma_{\mathrm{h}}^{1-n_{\mathrm{F}}}(\omega)\right]}{(\omega - \epsilon_0)^2 + \Gamma(\omega)^2/4}, \tag{5.7}$$

$$I_{\mathrm{a}}(V) = \frac{2e}{h} \int \mathrm{d}\omega \frac{\Gamma_{\mathrm{h}}(\omega)\Gamma_{\mathrm{e}}^{n_{\mathrm{F}}}(\omega) - \Gamma_{\mathrm{e}}(\omega)\Gamma_{\mathrm{h}}^{n_{\mathrm{F}}}(\omega)}{(\omega - \epsilon_0)^2 + \Gamma(\omega)^2/4}, \tag{5.8}$$

where $\Gamma(\omega) = \Gamma_{\mathrm{e}}(\omega) + \Gamma_{\mathrm{h}}(\omega) + \Gamma_1 + \Gamma_2$, together with the tunneling rates weighted by the Fermi distribution $n_{\mathrm{F}}(\omega)$

$$\Gamma_{\mathrm{e}}^{n_{\mathrm{F}}}(\omega) = \Gamma_{\mathrm{e}}(\omega) n_{\mathrm{F}}(\omega_-), \tag{5.9}$$

$$\Gamma_{\mathrm{e}}^{1-n_{\mathrm{F}}}(\omega) = \Gamma_{\mathrm{e}}(\omega)[1 - n_{\mathrm{F}}(\omega_-)]. \tag{5.10}$$

The single-electron current contains products of the form $\Gamma_{1/2}\Gamma_{\mathrm{e/h}} \propto T^2$, i.e. a tunnel process combined with thermal relaxation. In contrast, the Andreev current contains two tunnel processes, represented by the products of the form $\Gamma_{\mathrm{e}}\Gamma_{\mathrm{h}} \propto T^4$. Given the dependence on the tunnel coefficient, it can be summarized why in the distance-dependent measurement the single-electron process dominates, for large tip-substrate distances, because $\Gamma_{1/2} \gg \Gamma_{\mathrm{e/h}}$. Once this ratio is reversed, the Andreev current becomes the dominant process, due to the higher power in the tunneling coefficient. The two spectra shown in Fig. 5.3 reflect situations in which one of the two processes dominates.

# 6

# Theoretical Framework for Describing Photon-Assisted Tunneling

Within this chapter, we summarize the theoretical considerations about photon-assisted tunneling in superconductor-superconductor junctions. After a short description of photon-assisted tunneling in the most general way, we start with a summary of photon-assisted tunneling from a superconducting tip into a pristine superconducting substrate. This includes the three processes for which we show experimental data in chapter 7: (i) the tunneling of single electrons at $e|V| \simeq 2\Delta$ (coherence peaks), (ii) Andreev reflections at $e|V| \simeq \Delta$, and (iii) the Cooper pair tunneling (Josephson peak) at $e|V| \simeq 0$. We will use a Fermi's golden rule approach for all three of these processes based on the theory of Tien and Gordon [52]. Then we will present our derivation of the single-particle and Andreev currents through Yu-Shiba-Rusinov (YSR) states, in case the junction is exposed to HF radiation. For this purpose, we rework the rate-based description from Section 5.2.2 under the same assumption that Tien and Gorden met. This rate-based model provides the background for the discussion of photon-assisted resonant Andreev reflections through YSR states in chapter 8. Finally, a short discussion of the recurring Tien-Gordon-like patterns follows. I follow the description my colleagues and I used in González *et al.* [186] and Peters *et al.* [187] in large parts.

## 6.1 General Formalism of Photon-Assisted Tunneling

Photon-assisted tunneling is caused by the interaction of the tunneling electrons with high-frequency radiation in the MHz/GHz range. In the simplest case, these high frequencies radiated into the scanning tunneling microscope (STM) junction can be regarded as an electromagnetic field. In the presence of this field with frequency $\Omega$, the electrons can exchange energy with it by absorbing or emitting $n$ photons of energy $E_{\mathrm{ph}} = \hbar\Omega$ during

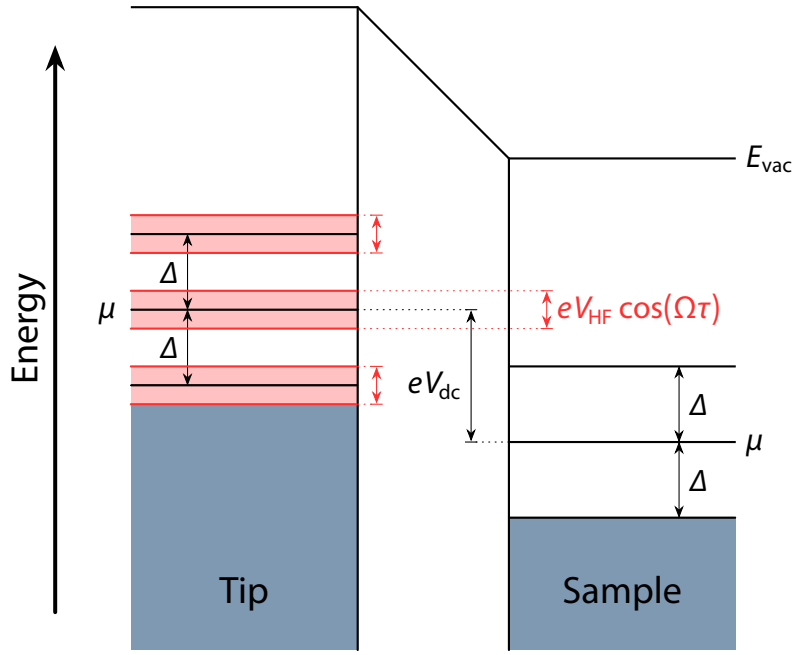


**Figure 6.1 | Energy-level shift due to externally applied HF radiation.** Visualization of the periodic shift of the quasiparticle energy levels in a superconductor-superconductor tunneling junction due to HF radiation. In general, this shift affects all energy levels, here indicated by shifting the chemical potential. The HF field acts as a time-dependent *ac* voltage of amplitude $V_{\mathrm{HF}}$ applied in addition to the *dc* bias voltage $V_{\mathrm{dc}}$. We apply this additional modulation to the energy levels of the tip, without loss of generality. In the style of [84].

tunneling. The maximum exchangeable energy is given by the amplitude $V_{\mathrm{HF}}$ of the field, which forms an upper boundary. We describe this by the maximum number of photons $\Lambda = eV_{\mathrm{HF}}/\hbar\Omega \geq n$.

Tien and Gordon were the first to model qualitatively the effects of such an electric field on the conduction electrons in superconductors.[52] Their assumption was that the field creates a time-dependent potential difference

$$V_{\mathrm{ac}}(\tau) = V_{\mathrm{HF}} \cos(\Omega\tau) \tag{6.1}$$

between the two superconductors in tip and substrate. Fig. 6.1 illustrates the effect of this time-dependent potential. As usual for light, within the wave-particle dualism, it can be described as a time-dependent wave as well as a photon of energy $E_{\mathrm{ph}}$. Both descriptions are valid and correct and we alternate between them, according to which one is more comprehensible. By choosing the quasiparticle energy levels in the substrate as a reference, the irradiated high-frequency solely leads to a potential change of the form described in Eq. (6.1) to the electrons in the tip. This reduces the threshold voltage $e|V_{\mathrm{dc}}| = 2\Delta - \Lambda\hbar\Omega$ above which the electrons from outside the energy gap can tunnel.

The general theoretical framework for describing photon-assisted tunneling starts from the transfer Hamiltonian used for the tunneling process (see Section 2.1.1)

$$\tilde{\mathcal{H}} = \tilde{\mathcal{H}}_{\mathrm{L}} + \tilde{\mathcal{H}}_{\mathrm{R}} + \tilde{\mathcal{H}}_{\mathrm{T}}\,, \tag{6.2}$$

which is composed of three parts. The two superconducting contacts are each described by their Hamiltonian $\tilde{\mathcal{H}}_\alpha$, where $\alpha \in \{\mathrm{L}, \mathrm{R}\}$ stands in the most general form for the left and right contact of the junction, in the case of an STM they are a reference to the tip and substrate. In the scope of this thesis, we will always refer to the left side as the tip and the right side as the substrate, without loss of generality. The Hamiltonian measures the energies on an absolute scale and conserves the total number of particles $N = N_{\mathrm{L}} + N_{\mathrm{R}}$.

Assuming that tip and substrate charge carriers are each a grand canonical ensemble, as is the case with superconductors in the Bardeen-Cooper-Schrieffer (BCS) theory, the chemical potential is the energy associated with adding a particle to the system. Therefore the grand canonical Hamiltonians $\tilde{\mathcal{H}}_{\mathrm{L}} = \mathcal{H}_{\mathrm{L}} + \mu_{\mathrm{L}} N_{\mathrm{L}}$ and $\tilde{\mathcal{H}}_{\mathrm{R}} = \mathcal{H}_{\mathrm{R}} + \mu_{\mathrm{R}} N_{\mathrm{R}}$ measure the single-particle energies in tip and substrate with their corresponding chemical potentials $\mu_{\mathrm{L}}$ and $\mu_{\mathrm{R}}$ as a reference point. The applied voltage $V$ leads to a shift of the chemical potentials against each other

$$eV = \mu_{\mathrm{L}} - \mu_{\mathrm{R}}\,. \tag{6.3}$$

As illustrated in Fig. 6.1 the high-frequency radiation causes the chemical potentials to be time-dependent and thus the voltage $V \to V(\tau)$ becomes time-dependent as well. It consists of a time-independent *dc* voltage $V_{\mathrm{dc}}$, the bias voltage, and a time-dependent *ac* voltage $V_{\mathrm{ac}}$ of frequency $\Omega$

$$V(\tau) = V_{\mathrm{dc}} + V_{\mathrm{HF}} \cos(\Omega\tau)\,. \tag{6.4}$$

This *ac* voltage can be seen as a modulation of the *dc* voltage caused by the external radiation field as described in Eq. (6.1) [52].

Consequently, the tunnel barrier also becomes time-dependent and in order to apply the usual BCS mean-field description we perform a time-dependent canonical transformation

$$U(\tau) = \exp\left\{\frac{\mathrm{i}}{\hbar}\int_0^\tau \mathrm{d}\tau' \left[\mu_{\mathrm{L}}(\tau')\, N_{\mathrm{L}} + \mu_{\mathrm{R}}(\tau')\, N_{\mathrm{R}}\right]\right\}. \tag{6.5}$$

This transformation converts the Hamiltonian from Eq. (6.2) to a form $\mathcal{H} = U\tilde{\mathcal{H}}U^\dagger - \mathrm{i}\hbar U\partial_\tau U^\dagger$, like

$$\mathcal{H} = \left(\tilde{\mathcal{H}}_{\mathrm{L}} - \mu_{\mathrm{L}} N_{\mathrm{L}}\right) + \left(\tilde{\mathcal{H}}_{\mathrm{R}} - \mu_{\mathrm{R}} N_{\mathrm{R}}\right) + U\tilde{\mathcal{H}}_{\mathrm{T}}U^\dagger\,. \tag{6.6}$$

Here explicitly the property that $\tilde{\mathcal{H}}_{\mathrm{L}}$ and $\tilde{\mathcal{H}}_{\mathrm{R}}$ each conserve their corresponding particle number $N_{\mathrm{L}}$ and $N_{\mathrm{R}}$ is used so that $U\tilde{\mathcal{H}}_\alpha U^\dagger = \mathcal{H}_\alpha$ is valid. However, the tunneling Hamiltonian for our system only conserves the total number of electrons $N$. $N_{\mathrm{L}}$ and $N_{\mathrm{R}}$ on their own are not a conserved quantity. Because of this, the transformed tunneling Hamiltonian

$\mathcal{H}_\mathrm{T} = U\tilde{\mathcal{H}}_\mathrm{T}U^\dagger$ becomes time dependent

$$\mathcal{H}_\mathrm{T} = \sum_{\mathbf{k}\mathbf{k}'\sigma}\left[T_{\mathbf{k}\mathbf{k}'}e^{\mathrm{i}\varphi(\tau)}c^\dagger_{\mathrm{R},\mathbf{k}'\sigma}(\mathbf{R})c_{\mathrm{L},\mathbf{k}\sigma}(\mathbf{R}) + \mathrm{h.c.}\right], \tag{6.7}$$

whereby the time-dependent phase

$$\varphi(\tau) = \frac{1}{\hbar}\int_0^\tau \mathrm{d}\tau' eV(\tau') = \frac{eV_\mathrm{dc}}{\hbar}\tau + \frac{eV_\mathrm{HF}}{\hbar\Omega}\sin(\Omega\tau) \tag{6.8}$$

includes all effects of the applied time-dependent voltage. In Eq. (6.7) the electron creation and annihilation operators $c^\dagger_{\alpha,\mathbf{k}\sigma}(\mathbf{r})$ and $c_{\alpha,\mathbf{k}\sigma}(\mathbf{r})$ at a position $\mathbf{r}$ represent the transfer of an electron with a spin of $\sigma$ between the electrodes. The position of the tip is denoted by $\mathbf{R}$ and the probability of this process occurring is described by the tunneling matrix element $T_{\mathbf{k}\mathbf{k}'}$. No momentum dependence is considered in the matrix element because for the small energies in superconducting tunnel spectroscopy the matrix element can be assumed to be approximately constant (see Section 3.1.1).

It is now possible to treat the transformed Hamiltonian from equation Eq. (6.6) within the framework of the mean-field approximation in the form of $\mathcal{H} = \mathcal{H}_0 + \mathcal{H}'$, where $\mathcal{H}'$ contains the tunneling Hamiltonian as a small perturbation.

## 6.2 Photon-Assisted Tunneling into Pristine Superconductors

Being able to use mean-field approximation we can describe the two pristine superconducting leads of our junction by the mean-field Hamiltonian from Eq. (2.36) and thus the unperturbed Hamiltonian $\mathcal{H}_0$ becomes

$$\mathcal{H}_0 = \mathcal{H}_\mathrm{L} + \mathcal{H}_\mathrm{R} = \sum_{\mathbf{k},\alpha}\sum_\sigma\left[\xi_{\mathbf{k},\alpha}c^\dagger_{\alpha,\mathbf{k}\sigma}c_{\alpha,\mathbf{k}\sigma} + \left(\Delta c^\dagger_{\alpha,\mathbf{k}\uparrow}c^\dagger_{\alpha,-\mathbf{k}\downarrow} + \mathrm{h.c.}\right)\right]. \tag{6.9}$$

The Hamiltonian contains the creation and annihilation operators $c^\dagger_{\alpha,\mathbf{k}\sigma}$ and $c_{\alpha,\mathbf{k}\sigma}$ for an electron with momentum $\mathbf{k}$, the normal state dispersion $\xi_{\mathbf{k},\alpha} = \epsilon_\mathbf{k} - \mu_\alpha$ and the superconducting gap $\Delta$. The latter is assumed to be the same in tip and substrate for this description, which is a justified presumption since in our experiment both are made of lead and are exposed to the same external conditions.

As we will see below, photon-assisted tunneling depends on the number of charge carriers involved in the tunneling process. Therefore, we will perform a single derivation of the tunnel current in the presence of HF radiation for all three processes for which we will show data in the next chapter, namely the tunneling into the coherence peaks, the Andreev reflections, and the Josephson effect.

### 6.2.1 Coherence Peaks

The coherence peaks follow from single-electron tunneling through the superconducting junction. For this, a Cooper pair must be broken and a quasi-particle must be formed in both the source and drain electrodes. This breaking requires excitation energies of $\Delta$ each, which results in a corresponding higher threshold voltage of $V = 2\Delta/e$ at which the coherence peaks appear. To discuss the influence of high frequency a series expansion of the time-dependent phase in the tunneling Hamiltonian Eq. (6.7) within a Fourier series is performed. By using the definition of the time-dependent phase from Eq. (6.8) and the Jacobi Anger expansion[1] one obtains

$$e^{\mathrm{i}\varphi(\tau)} = \sum_{n=-\infty}^{\infty} \mathcal{J}_n\left(\frac{eV_{\mathrm{HF}}}{\hbar\Omega}\right) e^{\mathrm{i}(eV/\hbar + n\Omega)\tau}, \tag{6.10}$$

with the coefficients involving the Bessel functions $\mathcal{J}_n(x)$. Under the for this experiment valid assumption that the temperature is small compared to the superconducting gap, no thermally excited quasiparticles exist, and tunneling will only occur from source to drain. When using the sum identities for the Bessel functions $[\sum \mathcal{J}_n(x)]^2 = \sum \mathcal{J}_n^2(x) = 1$, Fermi's golden rule (Eq. (2.26)) yields for the tunneling current

$$I = \frac{2e}{h} \sum_n \mathcal{J}_n^2\left(\frac{eV_{\mathrm{HF}}}{\hbar\Omega}\right) \sum_{\mathbf{k}} \sum_{\mathbf{k}'} |T_{\mathbf{k}\mathbf{k}'}|^2 u_{\mathbf{k}}^2 v_{\mathbf{k}'}^2 \delta(\xi_{\mathbf{k}} + \xi_{\mathbf{k}'} - eV - n\hbar\Omega), \tag{6.11}$$

with the factor of two accounting for the spin and $u_{\mathbf{k}}$ and $v_{\mathbf{k}}$ being the coefficients of the Bogoliubov transformation (see Eq. (2.39)). This can be written as [52]

$$I(V) = \sum_n \mathcal{J}_n^2\left(\frac{eV_{\mathrm{HF}}}{\hbar\Omega}\right) I^{(0)}(V + n\hbar\Omega/e), \tag{6.12}$$

with $I^{(0)}(V)$ being the current-voltage characteristic in the absence of any radiation field. By using the superconducting density of states from Eq. (2.52)[2]

$$\rho(E) = \rho_{\mathrm{L}}(E) = \rho_{\mathrm{R}}(E) = \rho_0 \frac{|E|\,\theta(|E| - \Delta)}{\sqrt{E^2 - \Delta^2}}, \tag{6.13}$$

with $\rho_0$ being the normal-state density of states per spin direction and $\theta(x)$ the Heaviside function[3], it is possible to bring all the terms belonging to $I^{(0)}(V)$ in Eq. (6.11) into the

[1] Jacobi Anger expansion: $e^{\mathrm{i}z\sin(\varphi)} = \sum_{n\in\mathbb{Z}} \mathcal{J}_n(z)\, e^{\mathrm{i}n\varphi}$

[2] This theoretical expression for the density of states is identical to the previous description in Eq. (5.1), if the Dynes parameter responsible for depairing is set to zero.

[3] The Heaviside step function is defined as

$$\theta(x) = \begin{cases} 1, & x \geq 0 \\ 0, & x < 0 \end{cases}.$$

known form for the tunneling current from Eq. (3.1)

$$I^{(0)}(V) = \frac{4\pi e}{\hbar}|T|^2 \int_{-\infty}^{\infty} \mathrm{d}\xi \rho_{\mathrm{L}}(\xi)\rho_{\mathrm{R}}(\xi + eV)\left[n_{\mathrm{F}}(\xi) - n_{\mathrm{F}}(\xi + eV)\right] . \tag{6.14}$$

We will refer to this mathematical form derived in Eq. (6.12) and all its variations as Tien-Gordon-like terms. It always contains two components, the Bessel function squares and the current without HF radiation, or in the case of $\mathrm{d}I/\mathrm{d}V$ spectra, the conductance without HF radiation. Performing the discrete sum leads to the formation of sidebands around the coherence peaks. The sidebands, in this case of single-electron tunneling, have a separation of $\hbar\Omega/e$ in the *dc* bias voltage direction. A complete discussion of the splitting pattern resulting from this Tien-Gordon-like equation can be found in section 6.4.

### 6.2.2 Andreev Reflections

At subgap voltages and sufficiently low temperatures, the elementary tunneling processes involve the transfer of multiple electrons. Here we focus on Andreev processes transferring two electrons across the transition, which are still clearly resolved in our experiment. The transfer can be treated as a scattering process and thus within the Born approximation. As the tunneling amplitude can be related to the T-matrix, the amplitude for transferring multiple electrons can be obtained from higher-order terms in the Born series for the T-matrix, $\mathbf{T} = \mathcal{H}_{\mathrm{T}} + \mathcal{H}_{\mathrm{T}} G_0 \mathcal{H}_{\mathrm{T}} + \ldots$. The intermediate state contains two quasiparticles, which clearly distinguishes it from processes in which two electrons tunnel one after the other since here both electrons share the same phase of the intermediate state. One quasiparticle each is in the source and drain electrode, and the electron tunneling gains energy in the order of $\Delta$ due to the applied bias voltage. Thus, the energy denominator of the Green's operator $G_0$ is in the order of $\Delta$ in the absence of HF radiation (compare with Eq. (2.49) for $G_0$). The *ac* bias changes the energy denominator by at most $eV_{\mathrm{HF}}$ due to photon emission and absorption. Concentrating now on the term $\mathcal{H}_{\mathrm{T}} G_0 \mathcal{H}_{\mathrm{T}}$ of second order, which transfers two electrons at a time, it is possible to approximate its contribution to the $T$-matrix

$$\mathbf{T} \simeq -\mathcal{H}_{\mathrm{T}} \frac{1}{\Delta} \mathcal{H}_{\mathrm{T}} , \tag{6.15}$$

as long as $eV_{\mathrm{HF}}$ and $\hbar\Omega$ are small compared to $\Delta$. Both tunneling Hamiltonians contribute a time-dependent phase factor $e^{\mathrm{i}\varphi(\tau)}$, which can be expressed as

$$e^{2\mathrm{i}\varphi(\tau)} = \sum_{n=-\infty}^{\infty} \mathcal{J}_n\left(\frac{2eV_{\mathrm{HF}}}{\hbar\Omega}\right) e^{\mathrm{i}(2eV/\hbar + n\Omega)\tau} . \tag{6.16}$$

A calculation similar to the one in the previous section based on Fermi's golden rule shows that the Andreev reflections also form sidebands (see [188] for an alternative Blonder-

It is discontinuous at $x = 0$ and its derivative is the Dirac delta distribution $\delta(x)$.

Tinkham-Klapwijk approach)

$$I(V) = \sum_n \mathcal{J}_n^2 \left( \frac{2eV_{\mathrm{HF}}}{\hbar\Omega} \right) I^{(0)}(V + n\hbar\Omega/2e) \,. \tag{6.17}$$

$I^{(0)}(V)$ again describes the current-voltage dependence in the absence of any HF radiation. Again we get a form similar to Tien-Gordon (see section 6.4 for a complete discussion). This form already includes the two-electron character of the tunneling process, to be found within the spacing of the sidebands. Compared to the single-electron tunneling, these now have a halved distance of $\hbar\Omega/2e$ as a function of the *dc* bias voltage and a period of $\hbar\Omega/2e$ as a function of $V_{\mathrm{HF}}$.

### 6.2.3 Josephson Effect

In superconducting tunneling contacts, small tunneling barriers cause the incoherent transfer of Cooper pairs, known as the Josephson effect [45]. Since two charge carriers are transferred in the tunneling process, the Cooper pairs gain or lose $2eV$ in energy. This transfer takes place with the help of an intermediate state in which a quasi-particle is located in both the source and the drain electrode. Since the Josephson peak occurs at energies $eV \ll \Delta$, the denominator of the Green's operator can be approximated by $2\Delta$. Following the same line of reasoning, the denominator remains unchanged due to photon absorption or emission as long as $eV_{\mathrm{HF}} \ll 2\Delta$. As already seen for the Andreev reflections, both of the Hamiltonians have a time-dependent phase factor, which makes the amplitude for the Cooper pair transfer from the tip to the substrate

$$\frac{E_{\mathrm{J}}}{2} e^{-\mathrm{i}2\varphi(\tau)} = \frac{E_{\mathrm{J}}}{2} e^{-\mathrm{i}2\tilde{\varphi}} \sum_n \mathcal{J}_n \left( \frac{2eV_{\mathrm{HF}}}{\hbar\Omega} \right) e^{-\mathrm{i}2eV\tau/\hbar - \mathrm{i}n\Omega\tau} \,. \tag{6.18}$$

Here $E_{\mathrm{J}}$ is the Josephson energy which satisfied the usual Ambegaokar-Baratoff relations. To describe the coupling to the environment, the tunneling Hamiltonian needs to be complemented by the operator $e^{-\mathrm{i}2\tilde{\varphi}}$, which describes the charge transfer $2e$ associated with the transfer of the Cooper pair. Once again, Fermi's golden rule yields an expression for the current similar to the one used by Tien-Gordon (see [86] for a functional integral approach)

$$I(V) = \sum_n \mathcal{J}_n^2 \left( \frac{2eV_{\mathrm{HF}}}{\hbar\Omega} \right) I^{(0)}(V + n\hbar\Omega/2e) \,, \tag{6.19}$$

which directly encodes the transfer of Cooper pairs between tip and substrate. The current in the absence of the HF radiation for a perfectly voltage biased source without series resistance or capacitance takes the form [87] (see section 2.4)

$$I^{(0)}(V) = \frac{I_c^2 R}{2} \frac{V}{V^2 + \left( \frac{2e}{\beta\hbar} R \right)^2} \,, \tag{6.20}$$

where the current is written in terms of the critical current $I_c = 2eE_J/\hbar$.

## 6.3 Extending the Theory of Photon-Assisted Tunneling in Superconductors by a Magnetic Impurity

Within this section, we will describe the formalism used to simulate the photon-assisted processes associated with resonant Andreev reflections. All simulations in this thesis of the YSR subgap states and Peters *et al.* [187] are based on the hypothesis that the tunneling rates for the tunneling through the YSR states must be substituted by Tien-Gordon like terms. This approximation is based on the work of Ruby *et al.* [97], whereby we have added the photon-assisted processes to their derived expressions for the tunneling current. This assumption was validated afterward by S. Acero González and L. Melischek following Ruby *et al.* but include an external HF field to the tunneling Hamiltonian. Furthermore, they completed the approximation even further by including the real part of the self-energy into the calculation.

For the purpose of deriving the photon-assisted tunneling current the consideration from section 6.1 is continued and a magnetic adatom is added on the substrate side. Eq. (6.9) is therefore extended for a classical impurity with spin $S$

$$\mathcal{H}_0 = \sum_{\mathbf{k},\alpha}\sum_{\sigma}\left[\xi_{\mathbf{k},\alpha}c^{\dagger}_{\alpha,\mathbf{k}\sigma}c_{\alpha,\mathbf{k}\sigma} + \left(\Delta c^{\dagger}_{\alpha,\mathbf{k}\uparrow}c^{\dagger}_{\alpha,-\mathbf{k}\downarrow} + \text{h.c.}\right)\right] + \sum_{\mathbf{k},\mathbf{k}'}\sum_{\sigma}(V_0 - JS\sigma)c^{\dagger}_{\mathrm{R},\mathbf{k}\sigma}c_{\mathrm{R},\mathbf{k}'\sigma}\,. \quad (6.21)$$

Here the impurity couples to the substrate electrons by the potential scattering of strength $V_0$ and the exchange coupling $J$. The quantization axis of the electron spins is chosen such that it is parallel to the spin of the impurity.

For the conductivity measurements carried out, we have to provide an expression of the current flowing through the junction. In the actual description, the current can be determined for example using the expectation value of the temporal change of the number of electrons in the tip. We obtain the current using that $\mathrm{i}\hbar\,\mathrm{d}N_\mathrm{L}/\,\mathrm{d}t = [N_\mathrm{L}, H]$, and that $N_\mathrm{L}$ commutes with $H_\mathrm{L}$ and $H_\mathrm{R}$

$$\begin{aligned} I &= -e\left\langle\frac{\mathrm{d}N_\mathrm{L}}{\mathrm{d}t}\right\rangle = \mathrm{i}\frac{e}{\hbar}\langle[N_\mathrm{L}, H_\mathrm{T}]\rangle \\ &= \mathrm{i}\frac{e}{\hbar}\sum_{\mathbf{k}\mathbf{k}'\sigma}\left(T_{\mathbf{k}\mathbf{k}'}e^{\mathrm{i}\varphi(\tau)}\langle c^{\dagger}_{\mathrm{L},\sigma}(\mathbf{R})c_{\mathrm{R},\sigma}(\mathbf{R})\rangle - \text{h.c.}\right). \end{aligned} \quad (6.22)$$

This expression can be rewritten using the lesser Green's functions in Nambu space

$$G^{<}_{\alpha\beta}(\tau_1,\tau_2) = \mathrm{i}\begin{pmatrix} \langle c^{\dagger}_{\beta\uparrow}(\tau_2)c_{\alpha\uparrow}(\tau_1)\rangle & \langle c_{\beta\downarrow}(\tau_2)c_{\alpha\uparrow}(\tau_1)\rangle \\ \langle c^{\dagger}_{\beta\uparrow}(\tau_2)c^{\dagger}_{\alpha\downarrow}(\tau_1)\rangle & \langle c_{\beta\downarrow}(\tau_2)c^{\dagger}_{\alpha\downarrow}(\tau_1)\rangle \end{pmatrix}, \quad (6.23)$$

so the current reads

$$I(\tau) = \frac{e}{\hbar}\mathrm{Tr}\left\{\tau_z\left[\hat{T}(\tau)G^<_{\mathrm{RL}}(\tau,\tau) - G^<_{\mathrm{LR}}(\tau,\tau)\hat{T}^*(\tau)\right]\right\}. \tag{6.24}$$

Here the Pauli matrix $\tau_z$ in Nambu space is used and the hopping matrix

$$\hat{T}(\tau) = \begin{pmatrix} T_{\mathbf{k}\mathbf{k}'}e^{\mathrm{i}\varphi(\tau)} & 0 \\ 0 & -T^*_{\mathbf{k}\mathbf{k}'}e^{-\mathrm{i}\varphi(\tau)} \end{pmatrix}, \tag{6.25}$$

is introduced. All electron operators, as well as Green's functions and self energies, which have no explicit momentum or location argument, always refer to the tip position $\mathbf{R}$.

The YSR state in the substrate amplifies the Andreev processes, leading to the formation of resonances at the YSR energies $\epsilon_0$. However, there is no amplification in the tip due to the absence of the YSR bound state. In contrast to the resonant Andreev reflections, the non-resonant ones in the tip can be neglected, which is achieved by neglecting all off-diagonal contributions of the pure Nambu Green's function $g_{\mathrm{L}}$ of the tip in the following calculation. As a consequence, also all multiple Andreev reflections are not regarded in this approximation.

Writing Dyson equations for the Keldysh Green's function and using the Langreth rules, the lesser Green's functions can be written as

$$\begin{aligned} G^<_{\mathrm{LR}} &= (g_{\mathrm{L}}\hat{T}G_{\mathrm{R}})^< = g^<_{\mathrm{L}}\hat{T}G^a_{\mathrm{R}} + g^r_{\mathrm{L}}\hat{T}G^<_{\mathrm{R}} \\ G^<_{\mathrm{RL}} &= (G_{\mathrm{R}}\hat{T}^*g_{\mathrm{L}})^< = G^<_{\mathrm{R}}\hat{T}^*g^a_{\mathrm{L}} + G^r_{\mathrm{R}}\hat{T}^*g^<_{\mathrm{L}}, \end{aligned} \tag{6.26}$$

with the superscripts $r$ and $a$ labeling the retarded and advanced Green's functions. Here, the bare Nambu space Green's function of tip and substrate without tunneling is given by $g_\alpha$ with $\alpha$ = L,R. In particular, the Green's function for the substrate includes the coupling to the spin of the impurity (compare Eq. (6.21)), which is accounted for in the corresponding Dyson equation $g_{\mathrm{R}}^{-1} = g_0^{-1} + JS - V_0\tau_z$. If this Green's function is now expressed with the help of the Bogoliubov-deGennes formalism and its wave function $\psi^T = (u, v)$ one gets

$$g_{\mathrm{R}}(\omega) = |\psi\rangle\frac{1}{\omega - \epsilon_0}\langle\psi| \tag{6.27}$$

as an approximation. The tunneling process introduces a self-energy to the denominator of the Green's function

$$G_{\mathrm{R}} = |\psi\rangle\frac{1}{\omega - \epsilon_0 - \tilde{\Sigma}_{\mathrm{R}}}\langle\psi|, \tag{6.28}$$

with

$$\tilde{\Sigma}_{\mathrm{R}} = \langle\psi|\Sigma_{\mathrm{R}}|\psi\rangle, \tag{6.29}$$

taking into account the tip-substrate tunneling by its self-energy

$$\Sigma_{\mathrm{R}}(\tau,\tau') = \hat{T}^{*}(\tau) g_{\mathrm{L}}(\tau,\tau') \hat{T}(\tau') \,. \tag{6.30}$$

With combining Eq. (6.26) and Eq. (6.24) and using the fact that the hopping matrix $T$ commutes with the Pauli matrix $\tau_z$ the current reads

$$\begin{aligned} I(\tau) = \frac{e}{\hbar} \int \mathrm{d}\tau' \,\mathrm{Tr}\,\{\tau_z [ & G^{<}_{\mathrm{R}}(\tau,\tau')\Sigma^{a}_{\mathrm{R}}(\tau',\tau) + G^{r}_{\mathrm{R}}(\tau,\tau')\Sigma^{<}_{\mathrm{R}}(\tau',\tau) \\ & - \Sigma^{<}_{\mathrm{R}}(\tau,\tau')G^{a}_{\mathrm{R}}(\tau',\tau) - \Sigma^{r}_{\mathrm{R}}(\tau,\tau')G^{<}_{\mathrm{R}}(\tau',\tau)]\} \,. \end{aligned} \tag{6.31}$$

The time-dependent phase in the hopping matrix from Eq. (6.25) can again be developed in a Fourier series when including the HF field, similar as it is done in Eq. (6.10). By using this result and inserting it in Eq. (6.30) the self-energy becomes

$$\Sigma_{\mathrm{R}}(\tau,\tau') = |T|^2 \sum_{n,m} \mathcal{J}_n\left(\frac{eV_{\mathrm{HF}}}{\hbar\Omega}\right) \mathcal{J}_m\left(\frac{eV_{\mathrm{HF}}}{\hbar\Omega}\right) e^{-\mathrm{i}(eV/\hbar+n\Omega)\tau\tau_z} g_{\mathrm{L}}(\tau-\tau') e^{\mathrm{i}(eV/\hbar+m\Omega)\tau'\tau_z} \,. \tag{6.32}$$

This sum can be divided into a diagonal ($n = m$) and a non-diagonal ($n \neq m$) component

$$\Sigma_{\mathrm{R}} = \Sigma^{0}_{\mathrm{R}} + \Sigma^{1}_{\mathrm{R}} \,, \tag{6.33}$$

where the diagonal component reads

$$\Sigma^{0}_{\mathrm{R}}(\tau,\tau') = |T|^2 \sum_{n} \mathcal{J}_n^2\left(\frac{eV_{\mathrm{HF}}}{\hbar\Omega}\right) e^{-\mathrm{i}(eV/\hbar+n\Omega)\tau\tau_z} g_{\mathrm{L}}(\tau-\tau') e^{\mathrm{i}(eV/\hbar+n\Omega)\tau'\tau_z} \,. \tag{6.34}$$

At this point, we follow the approximation of keeping only the diagonal self-energy $\Sigma^{0}_{\mathrm{R}}$, which greatly simplifies the following calculation. The non-diagonal part of the self-energy only plays a role if the broadening of the Green's functions induced by tunneling reaches or even exceeds the photon energy. So it is to be expected that the diagonal approximation is sufficiently accurate as long as only a small broadening and well-resolved photon sidebands are present. This is sufficient for the scope of this work, and it turns out that this approximation is adequate for explaining all our data (for the more general calculation, see González *et al.* [186]).

In the context of this approximation, the Green's function $g_{\mathrm{L}}$ of the tip in Eq. (6.34) depends only on the time difference $\tau - \tau'$, so the corresponding Hamiltonian has become time-independent, and thus also the self-energy is diagonal in the frequency representation. Therefore we can perform a Fourier transformation to represent the Green's function in the energy domain. The prior and subsequent exponential functions effectively only perform as a translation operator, changing the self-energy to

$$\Sigma^{0}_{\mathrm{R}}(\omega) = |T|^2 \sum_{n} \mathcal{J}_n^2\left(\frac{eV_{\mathrm{HF}}}{\Omega}\right) g_{\mathrm{L}}\left(\omega - (eV + n\hbar\Omega)\,\tau_z\right) \,. \tag{6.35}$$

Now the Green's function $g_{\mathrm{L}}$ can be interpreted in the way, that due to the bias voltage and its *ac* field component the electrons (holes) tunneling into the substrate lose (gain) an energy of $eV + n\hbar\Omega$.

If we now focus on the retarded and advanced correlation functions, not much changes, and Eq. (6.28) becomes

$$G_{\mathrm{R}}^{r/a} = |\psi\rangle \frac{1}{\omega - \epsilon_0 - \tilde{\Sigma}_{\mathrm{R}}^{0,r/a}} \langle\psi| , \tag{6.36}$$

with the projection of the self-energy onto the YSR states split into real and imaginary part

$$\tilde{\Sigma}_{\mathrm{R}}^{r/a} = \langle\psi|\Sigma_{\mathrm{R}}^{0,r/a}|\psi\rangle = \Lambda(\omega) \mp \mathrm{i}\frac{\Gamma(\omega)}{2} . \tag{6.37}$$

Performing the projection results in

$$\tilde{\Sigma}_{\mathrm{R}}^{0,r/a}(\omega) = |T|^2 \sum_n \mathcal{J}_n^2 \left(\frac{eV_{\mathrm{HF}}}{\hbar\Omega}\right) \left[|u|^2 g_{\mathrm{L}}^{r/a}(\omega_{-n}) + |v|^2 g_{\mathrm{L}}^{r/a}(\omega_{+n})\right] , \tag{6.38}$$

where we define $\omega_{\pm i} = \omega \pm (eV + i\hbar\omega)$. With the explicit expression of the tip Green's function[4] $g_{\mathrm{L}}^{r/a}$ the imaginary part $\Gamma(\omega)$ of the self energy can be calculated by

$$\Gamma(\omega) = \sum_n \mathcal{J}_n^2 \left(\frac{eV_{\mathrm{HF}}}{\hbar\Omega}\right) \left[\Gamma_{\mathrm{h}}(\omega_{-n}) + \Gamma_{\mathrm{h}}(\omega_{+n})\right] . \tag{6.39}$$

Here electron and hole tunneling rates are defined similar to Eq. (6.40) and Eq. (6.40) in the previous chapter as

$$\Gamma_{\mathrm{e}}(\omega) = \frac{2\pi}{\hbar}|u|^2|T|^2\rho(\omega_-) \quad \text{and} \tag{6.40}$$

$$\Gamma_{\mathrm{h}}(\omega) = \frac{2\pi}{\hbar}|v|^2|T|^2\rho(\omega_+) , \tag{6.41}$$

including the BCS density of states $\rho(\omega)$ as its already defined in Eq. (6.13). This allows one to interpret $\Gamma$ as the broadening of the YSR state due to the photon-assisted tunneling of electrons and holes in the tip.

[4] The retarded and advanced Green's function of the tip is

$$g_{\mathrm{L}}^{r/a}(\omega) \simeq \begin{cases} -\pi\rho_0 \frac{\omega}{\sqrt{\Delta^2 - \omega^2}}, & |\omega| < \Delta \\ \mp \mathrm{i}\pi\rho_0 \frac{|\omega|}{\sqrt{\omega^2 - \Delta^2}}, & |\omega| > \Delta \end{cases}$$

In the same way, the real part of the self-energy can be determined as

$$\Lambda(\omega) = -\pi\rho_0|T|^2 \sum_n \mathcal{J}_n^2\left(\frac{eV_{\mathrm{HF}}}{\hbar\Omega}\right)\left[\frac{|u|^2\omega_{-n}}{\sqrt{\Delta^2-\omega_{-n}^2}}\theta(\Delta-|\omega_{-n}|)+\frac{|v|^2\omega_{+n}}{\sqrt{\Delta^2-\omega_{+n}^2}}\theta(\Delta-|\omega_{+n}|)\right], \tag{6.42}$$

describing a frequency-dependent renormalization of the energy of the YSR state.

To finally calculate the current from Eq. (6.31) the lesser self energy, which results from Eq. (6.38) and the lesser tip Green's function $g_{\mathrm{L}}^{<} \simeq 2\pi \mathrm{i} n_{\mathrm{F}}(\omega)\rho(\omega)$, is needed

$$\tilde{\Sigma}_{\mathrm{R}}^{<}(\omega) = \mathrm{i}\sum_n \mathcal{J}_n^2\left(\frac{eV_{\mathrm{HF}}}{\hbar\Omega}\right)\left[\Gamma_{\mathrm{e}}(\omega_{-n})n_{\mathrm{F}}(\omega_{-n})+\Gamma_{\mathrm{h}}(\omega_{+n})n_{\mathrm{F}}(\omega_{+n})\right]. \tag{6.43}$$

as well as the lesser Green's function of the sample, which also follows directly as

$$G_{\mathrm{R}}^{<}(\omega) = |\psi\rangle\frac{\tilde{\Sigma}_{\mathrm{R}}^{<}(\omega)}{[\omega-\epsilon_0-\Lambda(\omega)]^2+[\Gamma(\omega)/2]^2}\langle\psi|, \tag{6.44}$$

using the identity $G_{\mathrm{R}}^{<} = G_{\mathrm{R}}^{r}\Sigma_{\mathrm{R}}^{<}G_{\mathrm{R}}^{a}$. So the current can now be expressed as a function of the energy

$$\begin{aligned} I(\omega) \;=\; & \frac{e}{h}\int \mathrm{d}\omega \mathrm{Tr}\left\{\tau_z\left[G_{\mathrm{R}}^{<}(\omega)\Sigma_{\mathrm{R}}^{a}(\omega)+G_{\mathrm{R}}^{r}(\omega)\Sigma_{\mathrm{R}}^{<}(\omega)\right.\right. \\ & \left.\left.-\Sigma_{\mathrm{R}}^{<}(\omega)G_{\mathrm{R}}^{a}(\omega)-\Sigma_{\mathrm{R}}^{r}(\omega)G_{\mathrm{R}}^{<}(\omega)\right]\right\}. \end{aligned} \tag{6.45}$$

and by using the further identity $G_{\mathrm{R}}^{r} - G_{\mathrm{R}}^{a} = G_{\mathrm{R}}^{r}(\Sigma_{\mathrm{R}}^{r}-\Sigma_{r}^{a})G_{\mathrm{R}}^{a}$, as well as the fact that the self energy $\Sigma_{\mathrm{R}}$ is diagonal in the Nambu space and commutes with $\tau_z$, we can rewrite it one last time to

$$\begin{aligned} I \;=\; & \frac{e}{h}\int \mathrm{d}\omega \mathrm{Tr}\left\{\tau_z\left[G_{\mathrm{R}}^{r}(\omega)(\Sigma_{\mathrm{R}}^{r}(\omega)-\Sigma_{\mathrm{R}}^{a}(\omega))G_{\mathrm{R}}^{a}(\omega)\Sigma_{\mathrm{R}}^{<}(\omega)\right.\right. \\ & \left.\left.-G_{\mathrm{R}}^{r}(\omega)\Sigma_{\mathrm{R}}^{<}(\omega)G_{\mathrm{R}}^{a}(\omega)\left(\Sigma_{\mathrm{R}}^{r}(\omega)-\Sigma_{\mathrm{R}}^{a}(\omega)\right)\right]\right\}. \end{aligned} \tag{6.46}$$

By evaluating this equation we obtain for the current

$$I_{\mathrm{a}} = \frac{2e}{h}\int \mathrm{d}\omega \sum_{n,m}\mathcal{J}_n^2\left(\frac{eV_{\mathrm{HF}}}{\hbar\Omega}\right)\mathcal{J}_m^2\left(\frac{eV_{\mathrm{HF}}}{\hbar\Omega}\right)\frac{\Gamma_{\mathrm{e}}(\omega_{-n})\Gamma_{\mathrm{h}}(\omega_{+m})[n_{\mathrm{F}}(\omega_{-n})-n_{\mathrm{F}}(\omega_{+m})]}{[\omega-\epsilon_0-\Lambda(\omega)]^2+[\Gamma(\omega)/2]^2}. \tag{6.47}$$

So far we have only considered the coupling between the tip and YSR state due to tunneling. The current resulting from this interaction is carried by Andreev processes. No single particle processes are possible at zero temperature ($T = 0$). But the YSR state also couples to the substrate itself as described in section 2.6.2. This leads to relaxation and excitation processes mediated by phonons or photons for finite temperatures ($T \neq 0$), which themselves contribute a self-energy $\Sigma_{\mathrm{ph}}$ to the Green's function of the substrate. These

processes enable single-electron (hole) tunneling processes which occupy (empty) the YSR state by being thermally relaxed into the continuum (excited from the continuum) with the new introduced rate $\Gamma_1$ ($\Gamma_2$). For the theoretical description of these processes, we consider this time only the imaginary part of the self-energy

$$\mathrm{Im}(\tilde{\Sigma}_{\mathrm{ph}}) = \mathrm{Im}(\langle\psi|\Sigma_{\mathrm{ph}}|\psi\rangle) = \frac{1}{2}\Gamma_{\mathrm{ph}} = \frac{1}{2}(\Gamma_1 + \Gamma_2)\,. \tag{6.48}$$

Thus the projected self-energy from Eq. (6.38) becomes

$$\tilde{\Sigma}_{\mathrm{R}}^{0,r/a}(\omega) = |T|^2 \sum_n \mathcal{J}_n^2\left(\frac{eV_{\mathrm{HF}}}{\hbar\Omega}\right)\left[|u|^2 g_{\mathrm{L}}^{r/a}(\omega_{-n}) + |v|^2 g_{\mathrm{L}}^{r/a}(\omega_{+n})\right] + \frac{1}{2}(\Gamma_1 + \Gamma_2)\,, \tag{6.49}$$

and the imaginary part from Eq. (6.39) changes to

$$\Gamma(\omega) = \sum_n \mathcal{J}_n^2\left(\frac{eV_{\mathrm{HF}}}{\hbar\Omega}\right)\left[\Gamma_{\mathrm{e}}(\omega_{-n}) + \Gamma_{\mathrm{h}}(\omega_{+n})\right] + \Gamma_1 + \Gamma_2\,. \tag{6.50}$$

Finally the lesser self-energy from Eq. (6.43) is transformed into

$$\tilde{\Sigma}_{\mathrm{R}}^{<}(\omega) = \mathrm{i}\left[\sum_n \mathcal{J}_n^2\left(\frac{eV_{\mathrm{HF}}}{\hbar\Omega}\right)\left[\Gamma_{\mathrm{e}}(\omega_{-n})n_{\mathrm{F}}(\omega_{-n}) + \Gamma_{\mathrm{h}}(\omega_{+n})n_{\mathrm{F}}(\omega_{+n})\right] + \Gamma_2\right], \tag{6.51}$$

including $\Gamma_2$. $\Gamma_1$ enters accordingly into the greater self-energy $\tilde{\Sigma}_{\mathrm{R}}^{>}$. So we are now getting a single particle current

$$\begin{aligned} I_{\mathrm{s}} = \frac{e}{h}\int \mathrm{d}\omega \sum_n \mathcal{J}_n^2\left(\frac{eV_{\mathrm{HF}}}{\hbar\Omega}\right)\Gamma_1 \frac{\Gamma_{\mathrm{e}}(\omega_{-n})n_{\mathrm{F}}(\omega_{-n}) - \Gamma_{\mathrm{h}}(\omega_{+n})n_{\mathrm{F}}(\omega_{+n})}{[\omega - \epsilon_0 - \Lambda(\omega)]^2 + [\Gamma(\omega)/2]^2} \\ - \sum_m \mathcal{J}_m^2\left(\frac{eV_{\mathrm{HF}}}{\hbar\Omega}\right)\Gamma_2 \frac{\Gamma_{\mathrm{e}}(\omega_{-m})(1 - n_{\mathrm{F}}(\omega_{-m})) - \Gamma_{\mathrm{h}}(\omega_{+m})(1 - n_{\mathrm{F}}(\omega_{+m}))}{[\omega - \epsilon_0 - \Lambda(\omega)]^2 + [\Gamma(\omega)/2]^2} \end{aligned} \tag{6.52}$$

next to the Andreev current which add up to the total current $I = I_{\mathrm{s}} + I_{\mathrm{a}}$. By making the replacements

$$\Gamma_{\mathrm{e}}(\omega) = 2\pi T^2|u|^2 \sum_n \mathcal{J}_n^2\left(\frac{eV_{\mathrm{HF}}}{\hbar\Omega}\right)\rho(\omega_{-n})\,, \tag{6.53}$$

$$\Gamma_{\mathrm{e}}^{n_{\mathrm{F}}}(\omega) = 2\pi T^2|u|^2 \sum_n \mathcal{J}_n^2\left(\frac{eV_{\mathrm{HF}}}{\hbar\Omega}\right)\rho(\omega_{-n})n_{\mathrm{F}}(\omega_{-n}) \quad \text{and} \tag{6.54}$$

$$\Gamma_{\mathrm{e}}^{1-n_{\mathrm{F}}}(\omega) = 2\pi T^2|u|^2 \sum_n \mathcal{J}_n^2\left(\frac{eV_{\mathrm{HF}}}{\hbar\Omega}\right)\rho(\omega_{-n})[1 - n_{\mathrm{F}}(\omega_{-n})]\,, \tag{6.55}$$

together with the similar replacements for $\Gamma_{\mathrm{h}}$, where $|u|^2 \to |v|^2$ and $\omega_{-n} \to \omega_{+n}$ has to be substituted, Eq. (6.47) and Eq. (6.52) can be reduced to the already known form from Eq. (5.7) and Eq. (5.8). The electron and hole tunneling rates $\Gamma_{\mathrm{e,h}}(\omega)$, which also influence

the resulting broadening, now include the absorption and emission of photons. Here, these tunneling rates each take on a structure similar to the one of Tien-Gordon (see section 6.4). It should be noted that although these individual processes described by the rates have a Tien-Gordon like form, it can be directly seen from Eqs. (6.47) and (6.52), that this no longer applies to the entire tunneling current, as combinations of the rates are included in the expressions as well as the width of the bound state resonance in the denominator. This last point, that the width of the bound state resonance is given by the sum of the single rates, which in the case of the Andreev reflections are dominated by the electron and hole tunneling rate, is only describable by low order perturbation theory in the tunneling Hamiltonian.

## 6.4 Discussion of the Tien-Gordon-Like Patterns

In the description of photon-assisted tunneling processes, one encounters a very specific mathematical form, no matter if regarding the tunneling current $I$, the conductance $G$, or the tunneling rates $\Gamma_{\mathrm{e,h}}$. All of them contain a sum over the squared Bessel function $\mathcal{J}_n^2(\alpha)$, like for example the conductivity

$$G(V) = \frac{\mathrm{d}I}{\mathrm{d}V} = \sum_n \mathcal{J}_n^2\left(\frac{V_{\mathrm{HF}}}{V_{\mathrm{ph}}}\right) G^{(0)}(V + nV_{\mathrm{ph}}), \tag{6.56}$$

where the Bessel functions argument $\alpha$ consists of the ratio between HF amplitude $V_{\mathrm{HF}}$ and the voltage $V_{\mathrm{ph}} = \hbar\Omega/ke$ associated with the photon energy per tunneling electron. The absorbed (emitted) energy is thereby distributed over all $k$ electrons involved in a tunneling process. The squares of the Bessel functions of the first kind are shown in Fig. 6.2(a) up to the fourth-order $n$. The graphs of Bessel functions resemble oscillating sine or cosine functions for large $\alpha$, decaying proportionally to $\alpha^{-\frac{1}{2}}$.

If one recalls the integral definition of the Bessel function

$$\mathcal{J}_n(\alpha) = \frac{1}{\pi}\int_0^\pi \mathrm{d}\tau \cos(n\tau - \alpha\sin(\tau)) \tag{6.57}$$

one can see that the integrand only becomes relevant when $\alpha \approx n$. While $\alpha < n$ the oscillations are strongly suppressed and the Bessel functions are as good as zero, since the sine can be neglected compared to $n\tau$ and thus the integral of the cosine disappears since it is integrated over integer multiples of a half-period. Only starting at $\alpha \gtrapprox n$ the oscillations are formed.

Next to the sum of the Bessel function squares, there is always the corresponding term without the influence of high frequency, in this case, the conductivity without HF radiation $G^{(0)}$. This term is not evaluated at the voltage $V$ itself but shifted by $nV_{\mathrm{ph}}$, where $n$ is the order of the Bessel function.

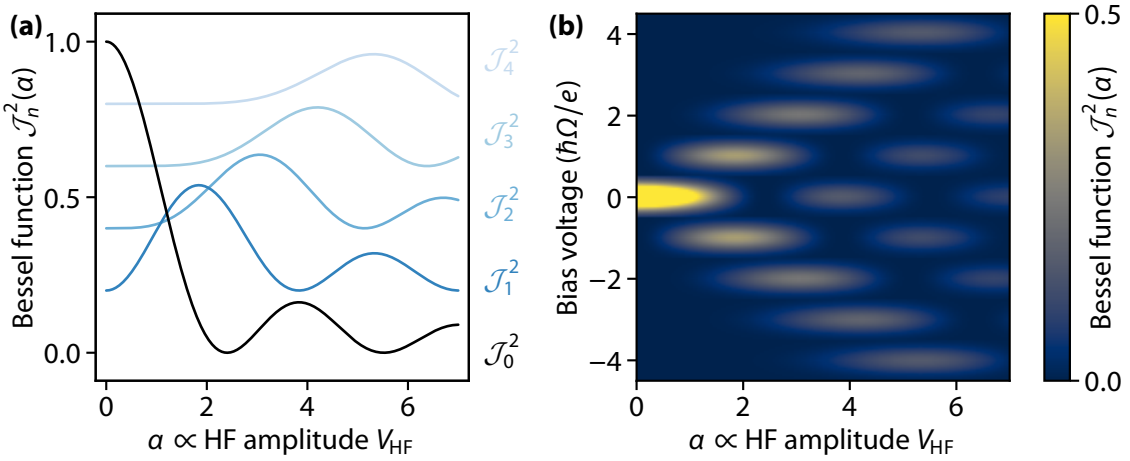


**Figure 6.2 | Discussion of the Tien-Gordon like sideband structure occurring during photon-assisted tunneling. (a)** Bessel function squares $\mathcal{J}_n^2(\alpha)$ up to order $n = 4$. Its argument is proportional to the HF amplitude $V_{HF}$. **(b)** Theoretical composition of the 2D plots by horizontal plotting of the Bessel function. Thereby the n-th Bessel function is shifted along the bias voltage by $\pm n$.

There is also the possibility to understand the V-shape as a visual composition of several shifted Bessel functions as shown in the 2D representations in Fig. 6.2(b). Here, the idealized representation of the Bessel function is shown as a function of the HF amplitude and the bias voltage, where $G^{(0)}$ is assumed as a Lorentz peak with an amplitude of one. Taking a horizontal cut in the middle of the spectrum at $V_{dc} = 0$, one gets the zeroth order of the Bessel function $\mathcal{J}_0^2$ along the horizontal line. The first order $\mathcal{J}_1^2$ is also mapped along a horizontal cut, but now shifted by $V_{ph}$ along the vertical direction. Generalized, the Bessel function $\mathcal{J}_n^2$ is being shifted by $nV_{ph}$. It becomes apparent that the frequency $\Omega$ of the HF wave enters at two points. On the one hand, it determines the distance of the shift and thus the spacing of the pattern of the internal structure of this splitting, on the other hand, it also enters the argument of the Bessel function as a compression factor, which leads to the fact that the splitting always has an opening angle of $\sim 1\, V_{HF}/V_{dc}$.

# 7

# Influence of HF Radiation on Pristine Superconducting Tunnel Junctions

Within this chapter, I will describe how photon-assisted tunneling can be used to gain detailed knowledge about the tunneling process across a scanning tunneling microscope (STM) junction. For this purpose, we examined three different processes. First, we used photon-assisted tunneling to study single-electron tunneling into superconducting substrates. Then we looked at two-electron processes, like Cooper pair tunneling in the Josephson effect or Andreev reflections. We use the simulation based on the method of Tien and Gordon from Section 6.2 as a theoretical basis to describe these processes. This is of relevance for understanding the tunneling in subgap states in the following Chapter 8.

## 7.1 Photon-Assisted Tunneling Through Coherence Peaks

With large junction resistances, tunneling into a superconductor-superconductor junction takes place primarily above a threshold value of $|V| = 2\Delta/e$. Beyond this voltage, it is possible to excite a quasi-particle in both, tip and substrate, which is necessary for a single-electron tunnel process in a superconducting junction. This process leads to the formation of so-called Bardeen-Cooper-Schrieffer (BCS) coherence peaks at the threshold $\Delta_{\mathrm{tip}} + \Delta_{\mathrm{sample}} = 2\Delta$. For bias voltages below this threshold, the tunneling process would have to involve either tunneling into subgap states that are not existing in clean superconductors or Cooper pairs would have to be transmitted directly, e.g. in the Josephson effect or as Andreev reflections. As two-electron processes, these two latter processes are far less probable at large junction resistances as the probability for each tunneling process is proportional to the square of the tunneling amplitude $T^2 \ll 1$ (Fermi's golden rule, Eq. (2.26)). Therefore the current for single-electron processes is proportional to $T^2$, compare with Eq. (3.1). Two-electron processes, in contrast, scale to the fourth power ($\propto T^4$) as two tunnel processes

take place and can be neglected for large junction resistances as in this case for 20 MΩ, which corresponds to a junction conductivity of $G_N = 50$ nS.

Exposing the BCS coherence peaks to an HF field splits them into symmetric sidebands with a distinct pattern of maxima and minima, as shown in Figure Fig. 7.1(a) and (c), with the latter being a magnification of the first. The shape of the splitting follows a V-like shape. Within the V shape, an oscillating pattern with alternating dark and bright regions appears. The intensity of the $\mathrm{d}I/\mathrm{d}V$ signal decreases as the splitting progresses, i.e. the stronger the irradiated HF is. Along the bias voltage direction, the outermost oscillations have the greatest intensity, decreasing with each maximum towards the center and thus having the maximum with the lowest intensity near the center. The opening angle of the shape is approximately ~1 V/V.

The distance of adjacent maxima along the bias voltage direction is 161(10) μV. To determine this distance, we placed vertical lines by eye through several maxima along the direction of increasing HF amplitude $V_{HF}$. We then averaged over several of these distances between adjacent lines and calculate the error from the statistical distribution of the distances (see the Appendix A.1 for more details). To make the best use of our energy resolution, we have chosen to use the maximum frequency that our setup allows, which is $f = \Omega/2\pi = 40$ GHz. This followed directly from one of the first observations we ever made, namely that the splitting is HF frequency-dependent and increases proportionally as a function of the frequency (see Section 6.4).

Within the mechanism outlined in Fig. 6.1 we can understand this splitting into sidebands as the emission and absorption of photons within the tunneling process. This leads to a modification of the threshold voltage $e|V| + n\hbar\Omega = 2\Delta$ from which on coherent tunneling is possible. The resulting V-like shape follows from the maximum number of photons $n < \Lambda = eV_{HF}/\hbar\Omega$ that a tunneling electron can exchange with HF field. The splitting of the inner structure corresponds to $\hbar\Omega/e$ and is therefore direct evidence for single-electron tunneling.

A quantitative analysis is done using the conductivity resulting from the equation (6.12)

$$G(V) = \frac{\mathrm{d}I}{\mathrm{d}V} = \sum_n \mathcal{J}_n^2 \left(\frac{eV_{HF}}{\hbar\Omega}\right) G^{(0)}(V + n\hbar\Omega/e)\,. \tag{7.1}$$

The strength of the $n$th sideband includes the Bessel function $\mathcal{J}_n$ and the function $G^{(0)}$, which represents the $\mathrm{d}I/\mathrm{d}V$ signal in the absence of HF radiation and is evaluated at a voltage shifted by $n$ times the photon energy over the electron charge. Fig. 7.1(b) and (d) show the excellent agreement between our experimental results and the simulation that is based on equation Eq. (7.1) (see also Fig. 7.6). Note that even the 2-band character of the lead, which can be seen in the zoom by the double structure of the coherence peak, is reproduced by the simulation. This property of lead is already introduced into the simulation by the spectrum without HF radiation. A detailed discussion of the influences of the two-band characteristic and a comparison with other surface orientations can be found in section 7.5. However, the fact that this property is also reflected in such a convincing form in the

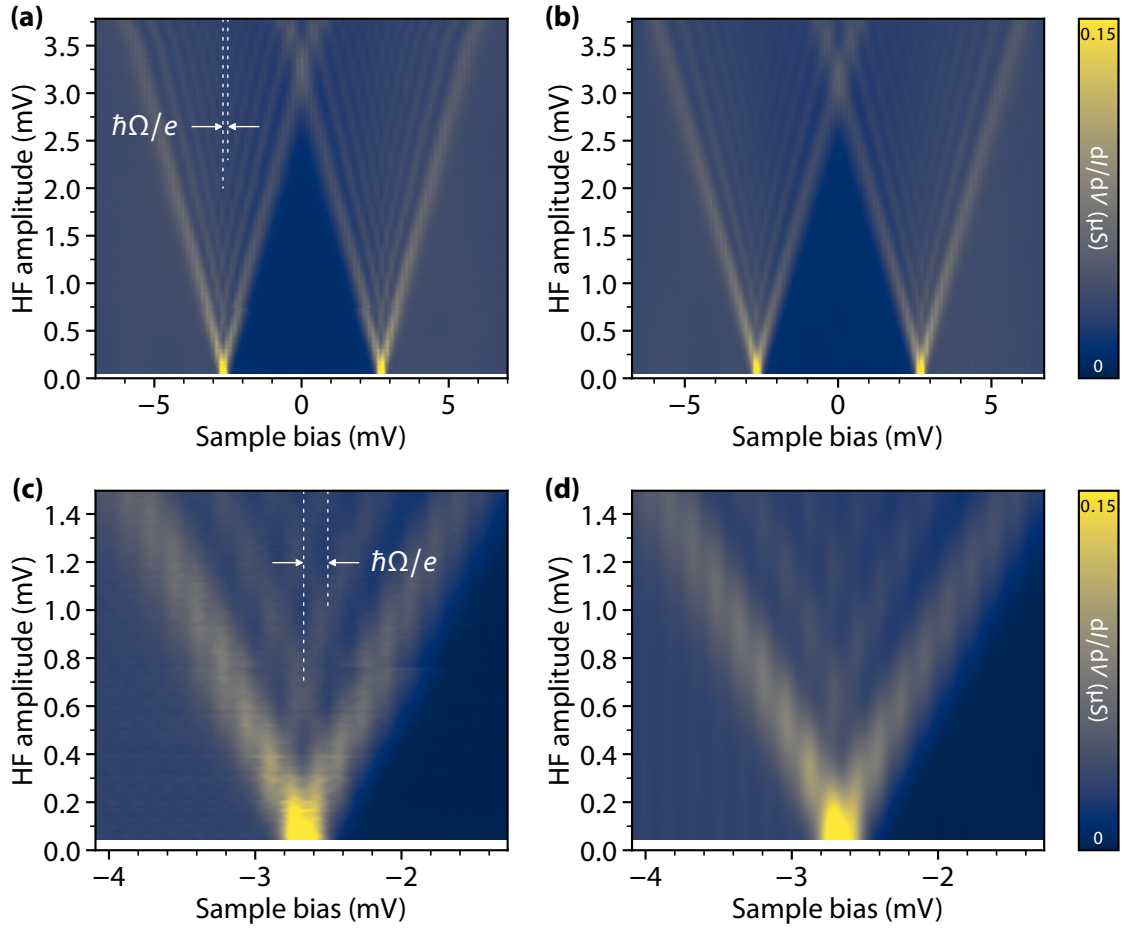


**Figure 7.1 | Splitting of the BCS coherence peaks in an HF field and comparison with accompanying simulation based on the spectrum not exposed to HF.** Color maps of the splitting of the coherence peaks in a Pb-Pb(110) junction, with the d$I$/d$V$ spectra under HF radiation of $f$ = 40 GHz (left) and their simulation (right). **(a)** The BCS coherence peaks surrounding the superconducting energy gap of $2\Delta$ split in a V-shaped pattern due to HF radiation. The sideband splitting within the pattern is $\hbar\Omega/e$, which indicates single-electron tunneling. The spectrum was recorded using the following setpoint and measurement parameters: $V_{\text{Bias}}$ = 10 mV, $I$ = 500 pA, $V_{\text{Lock-in}}$ = 40 μV and $f_{\text{Lock-in}}$ = 873 Hz. For the rescaling of the HF amplitude, an attenuation of the cable path up to the junction of 56.6 dBm was determined. **(c)** Detailed view of the splitting in (a) for the coherence peak at negative bias voltage up to an HF amplitude of 1.5 mV. **(b)** and **(d)**: Simulations corresponding to the measurements. The simulations are based on a Tien-Gordon-like expression from Eq. (7.1), which includes the HF amplitude $V_{\text{HF}}$, the frequency $\Omega$ and the measured conductance $G^{(0)}$ without HF field. It is assumed that the number of electrons $k$ involved in the tunneling process is $k$ = 1.

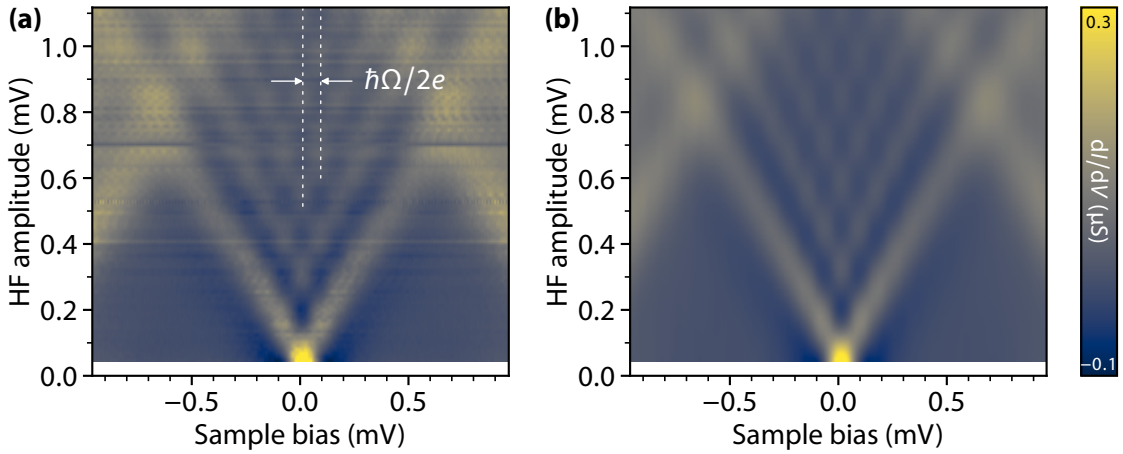


**Figure 7.2 | Josephson peak splitting in an HF field and comparison with simulation involving Cooper pair tunneling. (a)** Splitting the Josephson peak at zero bias into a V-shape with a sideband spacing of $\hbar\Omega/2e$, revealing the Cooper pair tunneling. The spectrum is recorded in the same Pb-Pb(110) junction as Fig. 7.1, with the following setpoint and measurement parameters: $V_{\text{Bias}} = 10$ mV, $I = 50$ nA, $V_{\text{Lock-in}} = 40$ μV and $f_{\text{Lock-in}} = 873$ Hz. For the rescaling of the HF amplitude, an attenuation of 57.3 dBm was determined. **(b)** Simulation that shows the splitting of the Josephson peak. It is based on the Tien-Gordon like expression from Eq. (7.2). To reflect the Cooper pair tunneling $k = 2$ charge carriers per elementary tunneling process are assumed.

results is proof that the model of photon absorption and emission captures the regime set by large tunnel resistances and adequate HF amplitudes ($V_{\text{HF}} \lessapprox \Delta$).

## 7.2 Photon-Assisted Josephson Effect

In contrast to single-electron tunneling, the Cooper pair tunneling in the Josephson effect does not require excitations of quasiparticles in tip and substrate. Consequently, it can be observed as a Josephson peak at zero bias voltage. Again, the HF field splits the peak into a distinct V-shape with structures of resonant sidebands, as shown in Fig. 7.2(a). These results confirm the observations also made in the investigations of Ref. [189, 190]. As a two-electron process, the effect scales with $\propto T^4$, the fourth power of the tunneling amplitude, and thus can be observed as soon as the junction conductance is large enough. The setpoint of $G_{\text{N}} = 5$ μS is chosen in such a way, that the Josephson peak is already intense, that even after the splitting and the resulting distribution of the intensity to the sidebands, these bands are still well resolved. The distance between these sidebands is now 82(5) μV, which is about half of the distance we found for the BCS coherence peaks. This is consistent with the theoretical considerations from Eq. (6.19), which predict a splitting of $\hbar\Omega/2e$ and

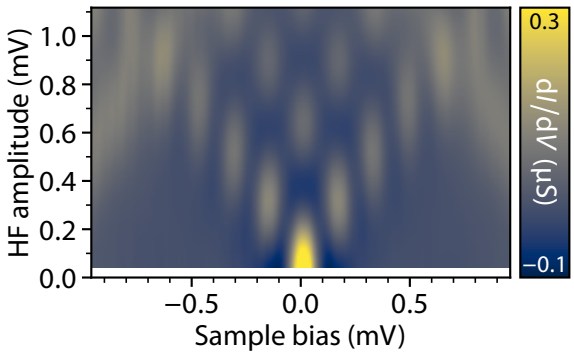


**Figure 7.3 | Simulating the Josephson peak splitting with single electrons.** Simulation analogous to Fig. 7.2(b) where this time only $k = 1$ charge carriers per elementary tunneling process were assumed, resulting in an expression similar to Eq. (7.1). The comparison shows a clear difference to the experimental data. The inner pattern has doubled in distance due to the assumption of single electrons tunneling, whereas the V-shape remains unchanged in its outer boundaries.

yields the conductivity

$$G(V) = \frac{\mathrm{d}I}{\mathrm{d}V} = \sum_n \mathcal{J}_n^2\left(\frac{2eV_{\mathrm{HF}}}{\hbar\Omega}\right) G^{(0)}(V + n\hbar\Omega/2e)\,. \tag{7.2}$$

The simulation that is based on this equation is compared to the measured data in Fig. 7.2(b) and shows excellent agreement with the data. In contrast, Fig. 7.3 shows how the simulation changes when assuming single electrons instead of Cooper pairs as it is described in Eq. (7.1). This direct comparison is in perfect agreement with the predictions discussed in Section 6.4. The opening angle of the split and the outer boundary remain identical, but the inner pattern of the split changes. There is a doubling of the distances between the regions with maxima and minima if only a one-electron process is assumed. In summary, the simulation can be seen as direct evidence for Cooper pair tunneling.

## 7.3 Photon-Assisted Andreev Reflections

To further demonstrate our ability to determine the number of elementary charge carriers in the superconducting STM junction, we next investigate multiple Andreev reflections (MARs) in the presence of an HF field. Andreev reflections appear at energies of $e|V| = 2\Delta/k$, with $k \geq 2$. The $\mathrm{d}I/\mathrm{d}V$ peak, in the case of $k = 2$, results from the transfer of a Cooper pair into the substrate, for which two quasi-particles are generated in the tip, or from the opposite process, in which two quasi-particles are generated in the substrate and a Cooper pair is transferred into the tip. For larger $k$, additional Cooper pairs are transferred by means of further reflections. While for odd $k$ a quasi-particle is generated in tip and substrate each and transferred as Cooper pair, two quasiparticles are created on the same

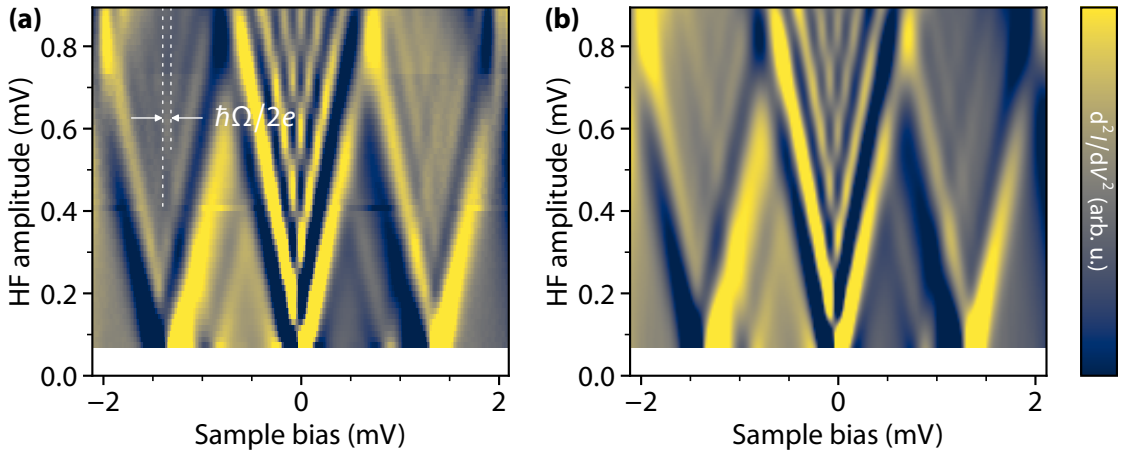


**Figure 7.4 | Splitting of the MAR peaks under HF radiation and comparison with the simulation. (a)** MARs measured on a Pb adatom on Pb(111). As explained in the text, the $d^2I/dV^2$ signal is shown here to make the rather weak splitting in the first Andreev reflections at $eV = \pm\Delta$ visible by increasing the contrast. The splitting also follows the known V-shape and splits like the Josephson effect with $\hbar\Omega/2e$, which reflects a two-electron transfer. The spectrum was recorded at rather high normal state conductance of $G_N = 40\,\mu S$ using the following setpoint and measurement parameters: $V_{Bias} = 5\,mV$, $I = 200\,nA$, $V_{Lock\text{-}in} = 20\,\mu V$ and $f_{Lock\text{-}in} = 929\,Hz$. For the rescaling of the HF amplitude, an attenuation of 53.3 dBm was determined. **(b)** Simulation, which shows the splitting of the MARs. It is based on the expression from Eq. (7.3), in which $k = 2$ represents the two-electron character.

side of the junction for even $k$ as for $k = 2$ (see Fig. 2.10 in Section 2.5). In Fig. 7.4(a), the first two (multiple) Andreev reflections for $k = 2$ and 3 can be seen next to the zero-bias Josephson peak, accordingly at energies of $eV = \pm\Delta$ and $eV = \pm 2\Delta/3$.

Compared to the two previous measurements, the measurement of the MAR was done on the Pb(111) orientation. Since the signal of MARs is relatively weak, e.g. compared to the signal of the Josephson peak, we had to adjust two things in the measurement procedure to be able to resolve the splitting of the Andreev reflections with our setup. On the one hand, we would like to increase the normal state conductance even more in order to further increase the signal-to-noise ratio. However, this is where we encounter a material-specific limit of lead, namely that it is relatively soft compared to other superconducting materials such as niobium or rhenium. This causes the junction to become unstable when the tip and the substrate are brought into too close proximity, resulting in an unsuitable signal-to-noise ratio due to increasing attractive forces between tip and substrate, which can lead to a premature deformation of the junction or even to an accidental tip crash. To prevent this we can take advantage of a general property of superconductors (as we study a purely superconductive effect with the Andreev reflections), namely that superconductivity is a macroscopic phenomenon on the order of the intrinsic Ginzburg-Landau coherence length that is for lead $\xi_{GL} = 51\,nm$ to $83\,nm$ [169]. For this reason, we are able to change the

geometry of the junction at the atomic level to increase stability. This is achieved by adding a lead adatom to the junction and since the substrate is no longer flat, the intermolecular forces are reduced when measuring above the adatom. Thus it is possible to increase the normal state conductance to a value of $G_N = 40\,\mu S$ for this measurement while maintaining the stability of the junction. A second way to increase the signal to noise ratio is to record the $d^2I/dV^2$, which gives a better resolution and makes even smaller changes visible. In the measurements of the coherence peaks and the Josephson effect, this was not necessary and we preferred the direct display of the conductivity. To further improve the signal quality, we have chosen quite high averaging times per data point for this measurement, which must be carefully weighed against the low-frequency noise that can render the measurement useless due to artifact production.

The first thing to notice when comparing the process with one reflection ($k = 2$) with the following ($k = 3$) is that the latter has a much lower intensity as a direct consequence of the additional electron transported across the junction. The influence of the HF field is again a splitting of both detectable Andreev reflections into a V-shaped pattern, as previously observed for the Josephson effect (a direct comparison with the Josephson peak at zero bias voltage is possible in Fig. 7.4). It can also be seen that although the energetically lower Andreev reflection splits in a V-shape, due to the weak intensity and the small distance to the much more intense two-electron Andreev reflection, it is not possible to investigate an internal structure in this splitting. For the more intense Andreev signal, we find a sideband spacing of $91(9)\,\mu V$, equal to $\hbar\Omega/2e$, revealing the underlying charge transfer of $2e$. Fig. 7.5 shows a schematic illustration for the photon-assisted Andreev reflections demonstrated by the formation of the first sideband of the Andreev reflection at $eV = \pm\Delta$. It is shown that with the help of the HF field it is possible to transport a Cooper pair by means of an Andreev reflection already at a voltage lowered by $\hbar\Omega/2e$. Here, the energy $\hbar\Omega$ of the absorbed photon is shared between both charge carriers involved in the process.

Also for the Andreev reflections, the simulation shown in Fig. 7.4(b) is in excellent agreement. Instead of the conductivity as in Eq. (7.2) we have here simulated its derivative, which directly results as

$$\frac{dG(V)}{dV} = \frac{d^2I}{dV^2} = \sum_n \mathcal{J}_n^2\left(\frac{2eV_{HF}}{\hbar\Omega}\right) dG^{(0)}(V + n\hbar\Omega/2e)\,, \tag{7.3}$$

where within $dG^{(0)}$ again the spectrum recorded without HF voltage forms the basis for the simulation.

## 7.4 Generalized Tien-Gordon Theory

This chapter has so far investigated photon-assisted tunneling using three characteristic transport resonances of the superconducting spectra. The splitting of all three processes is summarized in Fig. 7.6. Here selected spectra (*blue*) are presented and compared to

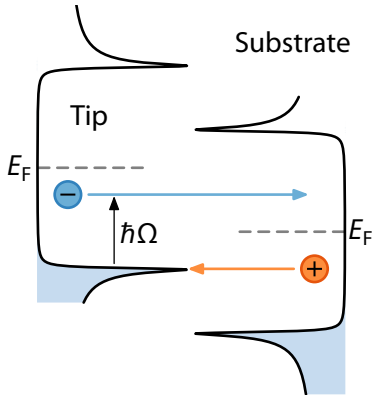


**Figure 7.5 | Photon-assisted tunneling process leading to the first sideband of the first Andreev reflection.** The Andreev reflection takes place at a bias voltage of $V = \Delta/e - \hbar\Omega/2e$. Without HF radiation the process would be prohibited at this voltage. The HF field allows an electron to be excited in the tip and tunnel at an energy increased by $\hbar\Omega$. This electron is reflected symmetrically to the Fermi energy of the substrate as a hole. Thus a Cooper pair can relax into the substrate and the reflected hole can tunnel at $-\Delta$ into the filled quasi-particle states of the tip.

their respective simulations (*red*). Once again, the impressive agreement of the data with its theoretical description is apparent. These fits can be used to determine the attenuation very precisely because the peak structure with all its details is very sensitive to the smallest changes in the HF amplitude.

The simulations are based on the Tien-Gordon-like expressions in Eq. (6.12), Eq. (6.17), and Eq. (6.19), all derived in Chapter 6. These three expressions can be generalized to a single formula for the conductance

$$G(V) = \frac{\mathrm{d}I}{\mathrm{d}V} = \sum_n \mathcal{J}_n^2\left(\frac{keV_{\mathrm{HF}}}{\hbar\Omega}\right) G^{(0)}(V + n\hbar\Omega/ke)\,, \tag{7.4}$$

where $k$ indicates the number of transferred electrons. One of the explicit advantages of this model by Tien and Gordon is that it does not require a complete understanding of the physics underlying the tunneling process to describe photon-assisted tunneling. It is sufficient to measure the effect without the influence of high frequency. Once a spectrum of the effect has been recorded, it is also possible to describe the effects of the HF field on it, despite the fact that such a spectrum, with its large number of measurement points, introduces a lot of redundant information into the simulations. In summary, this is a simplistic method to determine the number of charge carriers $k$ just by comparing the results of different simulations without the need for additional parameters, apart from the known HF frequency.

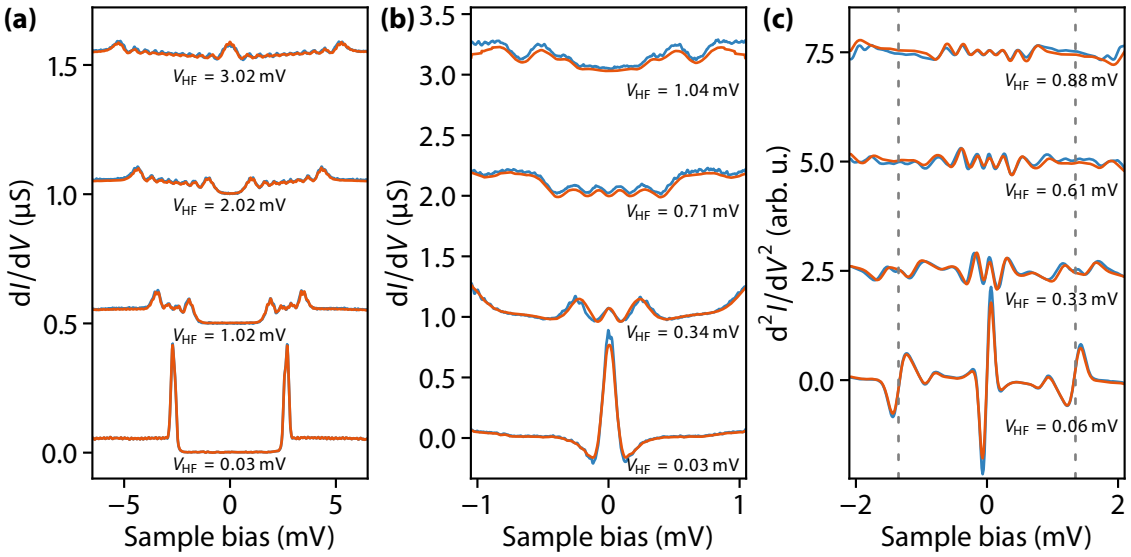


**Figure 7.6 | Cuts of PAT of the Coherence, MAR and Josephson peaks.** Selected individual $dI/dV$ and $d^2I/dV^2$ spectra from the color maps. Shown are experimental data (*blue*) at different HF amplitudes from **(a)** the BCS coherence peaks from Fig. 7.1, **(b)** the Josephson peak from Fig. 7.2, and **(c)** the MAR from Fig. 7.4. The corresponding simulations (*red*) are based on the Tien-Gordon-like expressions generalized in Eq. (7.4). For (c), the simulation was differentiated once more accordingly. The simulation includes the applied HF voltage of $V_{HF}$, the frequency $\Omega/2\pi = 40$ GHz, and $G^{(0)}(V)$ the measured spectrum without applied high frequencies as input parameters. The one-electron processes in (a) is simulated with $k = 1$, whereas the two-electron processes in (b)-(c) $k = 2$ is used. The spectra are offset for clarity. The experimental parameters can be taken from the captions of the color maps.

The question is whether the generalization remains valid for processes with $k > 2$? We have only shown examples for $k = 1$ and 2. The obvious system to test this are multiple Andreev reflections as shown schematically in Fig. 2.10(d) for $k = 3$. Although we detect these, as can be seen in Fig. 7.4(a) and Fig. 7.6(c) from the peaks at $e|V| = 2\Delta/3 = 0.9$ meV, we have not yet been able to validate the generalization. Our resolution is not sufficient to resolve the splitting in the Andreev bound states, which become weaker and weaker in intensity for higher-order Andreev processes. Two factors make this measurement difficult. First, the photon-assisted splitting reduces the signal intensity even further, and second, the signal of interest is superimposed by the splitting of neighboring peaks with most likely different $k$. To obtain conclusive results, it is advisable to avoid these interferences. This is possible by either reducing the frequency which leads to a faster formation of the inner patterns at lower HF amplitudes, but requires a higher energy resolution in order to be able to resolve the reduced distances in the pattern. Alternatively, superconductors with larger gap parameters $\Delta$ can be used to increase the separation between the Andreev peaks.

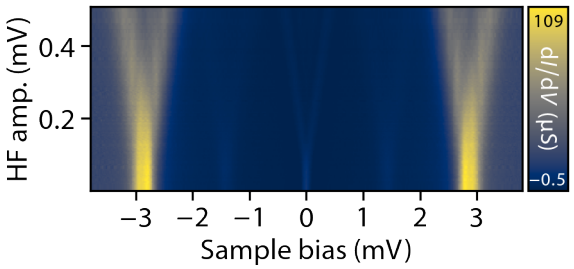


**Figure 7.7 | Photon-assisted splitting of the coherence peaks on Pb(111).** Color plot of the d$I$/d$V$ spectra on a clean Pb(111) sample. This plot contrasts with the Figs. 7.1 and 7.2 and is intended to allow comparison with a different surface orientation of the lead crystal. The junction conductance is 18 µS and the junction is exposed to radiation of 31 GHz. The splitting of the Coherence peaks, the Josephson peak and (very faint) the first MAR can be observed. The spectrum was recorded using the following setpoint and measurement parameters: $V_{\text{Bias}}$ = 5 mV, $I$ = 90 nA, $V_{\text{Lock-in}}$ = 30 µV and $f_{\text{Lock-in}}$ = 873 Hz.

However, the generalization seems plausible, since it effectively states that $k$ charge carriers share the energy $\hbar\Omega$ provided by the HF field, but it remains to be confirmed.

## 7.5 Influence of the Two-Band Characteristic of Pb

Pb is a two-band superconductor as already outlined in Section 5.1.3. In the following, we show based on our results, how the two Fermi sheets of Pb affect the photon-assisted tunneling. Therefore, in addition to the previously described data of the coherence and Josephson peaks on Pb(110), we also measured on Pb(111) shown in Fig. 7.7 and Fig. 7.8. The tunneling spectra for the two surface orientations differ only in the relative strengths of tunneling into the two distinct Fermi sheets of the Pb substrate. This leads to different relative weights of the two BCS-like coherence peaks [160]. Fig. 7.7 shows in a 2D differential conductance map the individual splitting of the two coherence peaks as a function of the HF field. This is shown in greater detail in Fig. 7.8(a) using exemplary d$I$/d$V$ spectra (*blue*) from the 2D map. The similar amplitudes of the two coherence peaks indicate that the tunneling probability in the two different Fermi sheets is approximately the same for this high-conductance data. The coherence peaks were again simulated based on Eq. (7.4) with $k$ = 1 (*orange*). Besides the coherence peaks, the first Andreev reflections and the Josephson peak are also visible due to the high conductance. In Fig. 7.8(b) the splitting of the Josephson peak is also shown as a 2D map.

Within the framework of the Tien-Gordon theory, the two coherence peaks are each individually split when exposed to HF radiation. This is included in the previously established simulation. A comparison of the experimental data with the simulations in Fig. 7.8(a) shows again an excellent agreement and thus confirms the independent splitting. Thus, we have shown that the two-band nature of Pb does not affect photon-assisted tunneling in

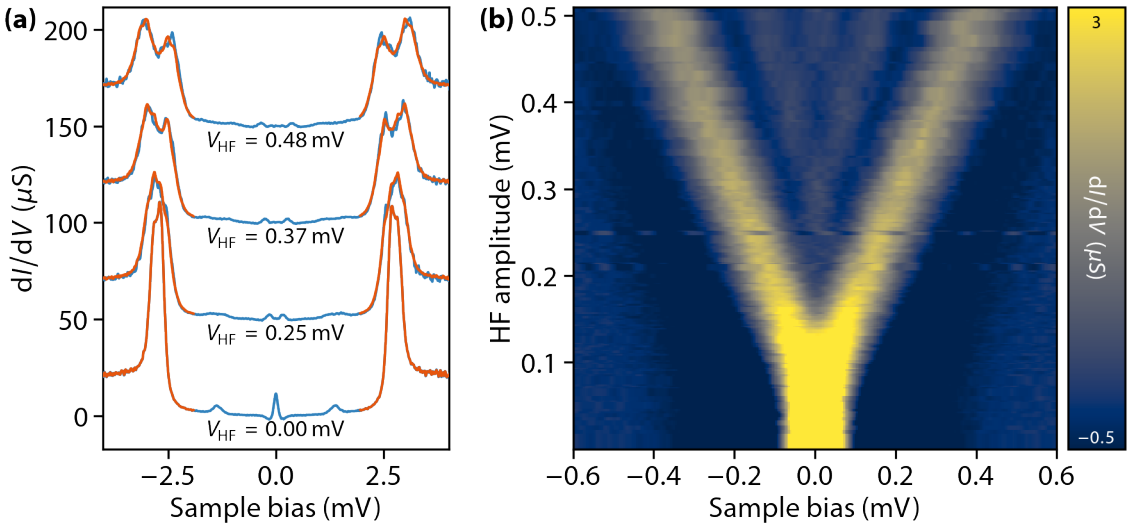


**Figure 7.8 | Comparison of photon-assisted tunneling for the Coherence peaks and the Josephson effect on another surface orientation. (a)** Single spectra showing photon-assisted tunneling for the Coherence peaks and the Josephson effect on Pb(111) surface orientation contrasting the data in Figs. 7.6(a) and (b) on Pb(110). The data (*blue*) are taken from Fig. 7.7 and are accordingly exposed to HF radiation of 31 GHz and recorded at a junction conductance of 18 μS. The two coherence peaks of the two-band superconductor split up individually by the photon-assisted tunneling, which is confirmed by the superimposed simulation (*orange*) based on our theory using Eq. (7.4) with $k = 1$. **(b)** Close-up view of the Josephson peak splitting. The spectrum was recorded using the following setpoint and measurement parameters: $V_{\text{Bias}} = 5$ mV, $I = 90$ nA, $V_{\text{Lock-in}} = 30$ μV and $f_{\text{Lock-in}} = 873$ Hz.

a particular way. As before, the splitting results from the features of the irradiation-free spectrum, which already includes the two-band character.

Moving our focus away from the coherence peaks and towards the subgap states, we do not find any influence of the two-band nature of Pb. Fig. 7.8 shows the Josephson effect analogous to the coherence peaks above also on the Pb(111) surface. We can not find any difference to the split from Fig. 7.2, as the Josephson peak is not affected by the gap structure. For the MAR we would expect an effect similar to the coherence peaks since this process involves tunneling into them as shown in Fig. 7.5. However, our resolution is not sufficient to draw any conclusions, because the MAR intensities are too small to detect the two different thresholds, regardless of the surface orientation.

# 8

# Photon-Assisted Tunneling through YSR States under the Influence of HF Radiation

In the previous chapter, we showed that the approach of Tien-Gordon, as presented in its generalized form in Eq. (7.4), is very successful in describing photon-assisted tunneling between a superconducting tip and a bulk superconducting substrate. As a direct result, it reveals the number of electrons involved in the tunneling process. In this chapter, we find that Eq. (7.4) does not apply generally for tunneling into subgap states and has to be replaced by a more elaborate description. Here, we use our extension of the theory described in Section 6.3 to describe the photon-assisted tunneling through Yu-Shiba-Rusinov (YSR) states.

## 8.1 Differences Between Single-Electron and Resonant Andreev Tunneling in the Presence of HF Radiation

In the following, we return to the system of $Mn_{up}$ adatoms on a Pb(111) surface (see Chapter 5), in which several YSR states are induced within the superconducting gap. We concentrate on the YSR state with the lowest energy at $\epsilon_0 = 0.25\,\mathrm{meV}$. The energetic position of the resonance remains unchanged even when the tip approaches the Mn atom, which is monitored by a change in conductance by three orders of magnitude. However, the relative ratio of the resonance amplitudes $\alpha_\pm$ changes and is eventually inverted, as shown in Fig. 5.5. The inversion reflects the transition from single-electron tunneling at large tip distances to a regime at close distances where the dominant processes are resonant Andreev reflections.

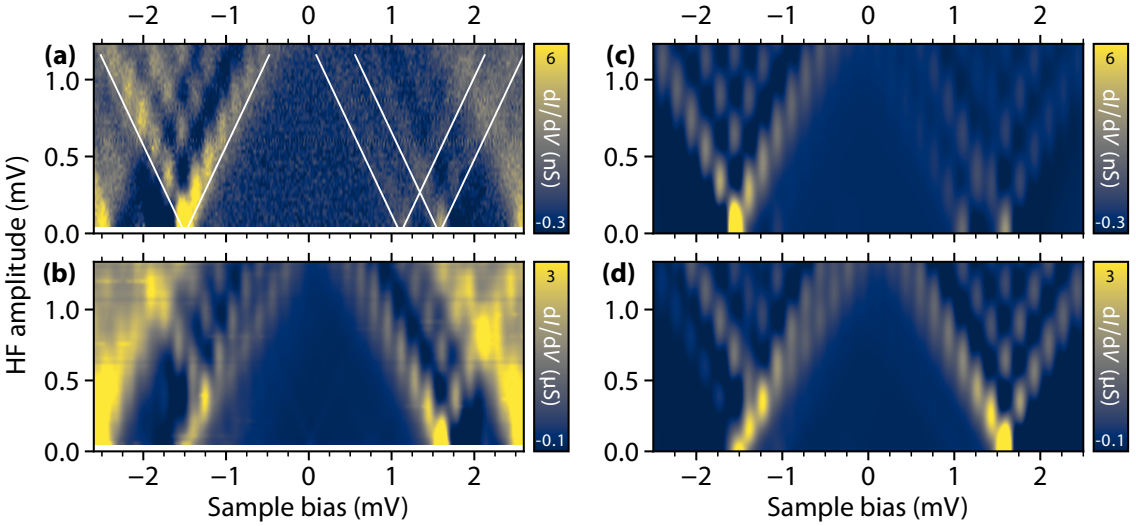


**Figure 8.1 | Photon-assisted tunneling into the YSR state under HF irradiation. (a)** Three V-shaped splittings of the YSR peaks for a low (normal-state) junction conductance ($G_N^{low}$ = 2 nS = $2.6 \times 10^{-5} G_0$ with $G_0 = 2e^2/h$). The faint structure emerging from $eV = \Delta - \epsilon_0 = 1.1$ mV is due to thermally excited quasiparticles. **(b)** At high conductance ($G_N^{high}$ = 4 μS = $5.2 \times 10^{-2} G_0$), we observe a V-shaped pattern at positive bias and a distinct Y-shaped pattern with a double-peak structure on the low-bias branch at negative bias. **(c, d)** Simulations corresponding to the junction conductances in (a, b) which are in excellent agreement with the experiment (BCS peaks were omitted for clarity). For the simulation parameters see Section 8.2.1.

The amplitude differences between $\alpha_\pm$ reveal the asymmetry in the electron wave function $u_\epsilon$ and the hole wave function $v_\epsilon$ of the YSR state, where $|u_\epsilon|^2 \ll |v_\epsilon|^2$.

The measured $\mathrm{d}I/\mathrm{d}V$ maps of the photon-assisted tunneling through the Pb–Mn–Pb junction are shown in Fig. 8.1(a) and (b) for low and high junction conductance, respectively. The normal state conductance of this data is identical to that of the data shown in Fig. 5.3. For clarity, these conductance values are also marked in the approach curve in Fig. 5.5. At low junction conductance, three V-shaped splits are distinctly visible (indicated in Fig. 8.1(a)). For high junction conductances on the other hand (shown in Fig. 8.1(b)), the YSR resonances show a clear difference in their splitting structure compared to the splitting that is expected by the Tien-Gordon theory (see Chapter 7). The map exhibits the familiar V-shaped pattern for positive bias voltages but exhibits a different pattern at negative biases. In particular, the V-shaped pattern gives way to a Y-shaped structure, which is fundamentally different from all previously discussed HF radiation patterns observed on the unstructured surfaces. However, not only for negative biases but also for positive polarity the high-conductance data is surprising. We have learned from Ruby *et al.* that at such high normal state conductance the current through the YSR state is dominated by Andreev reflections, thus by two-electron processes. This number of charge carriers, on which the tunneling process is based, should be reflected in the periodicity of the sideband spacing

with a separation of $\hbar\Omega/2e$, corresponding to 83 μV at a frequency of 40 GHz. However, the data show a splitting of 163(5) μV, which would correspond to a charge transfer of 0.99(3) $e$. This result would suggest single-electron tunneling and is therefore in clear contradiction to our expectation. It becomes obvious that our previous understanding of photon-assisted tunneling is no longer sufficient to resolve this contradiction. A third and final observation in the high-conductance data is a double structure along the low-voltage arm of the Y-shape. It appears that on this side of the outer boundary of the Y-shape, two different gradients define the splitting.

### 8.1.1 Single-Electron Tunneling

Before we go into detail on how to interpret the high conductance data with its surprising observations, we first have to discuss the low conductance data in Fig. 8.1(a). This map shows for both polarities the familiar V-shaped patterns centered around $e|V| = \Delta + \epsilon_0$. We extract a sideband spacing of 161(7) μV, corresponding to a charge transfer of 0.97(5) $e$. For this reason, we interpret the process as tunneling of a single electron, leaving a quasiparticle in the tip and occupying the YSR state at the energy $\epsilon_0$.

We have shown in Section 6.2 and demonstrated in the previous chapter, that the influence of the HF radiation can be simulated based on a radiation-free spectrum – which we will refer to as *spectrum-based* simulation. However, the information content of a single spectrum is very large. Since every data point of the spectrum can be considered as an input parameter, a large number of partly redundant information enter the simulation. This redundancy can be resolved by basing the simulation solely on rate equations for the electron and hole tunneling into the YSR state – the *rate-based* simulation. These rates together with only a few other physical quantities, such as the YSR state energy and the superconducting order parameter, characterize our system completely, as we described in Section 6.3. Hence, we have been able to reduce the number of input parameters with our new rate-based simulation significantly. In Section 8.2 we describe in detail how we determine each of these parameters. The resulting simulation is shown in Fig. 8.1(c) and demonstrates excellent agreement with the data in Fig. 8.1(a).

In a nutshell, this new type of simulation describes the conductance in terms of the tunneling rates $\Gamma_{\mathrm{e}}^{(0)}(E)$ and $\Gamma_{\mathrm{h}}^{(0)}(E)$ for electrons and holes. Here the superscript $(0)$ indicates the radiation-free rates. The energy $E \to E + n\hbar\Omega$ changes by interactions of the charge carrier with the HF field. In the case of electrons, a positive value of the integer number $n$ represents the number of absorbed photons with frequency $\Omega$ and a negative value represents their emission. The reverse is true for holes. Combining rates and energy change, the Tien-Gordon model yields

$$\Gamma_{\mathrm{e,eff}}(E) = \sum_n \mathcal{J}_n^2\left(\frac{eV_{\mathrm{HF}}}{\hbar\Omega}\right)\Gamma_{\mathrm{e}}^{(0)}(E + n\hbar\Omega) \tag{8.1}$$

as rate for electrons exposed to HF radiation (compare with Eq. (6.53)). The hole rate $\Gamma_{\mathrm{h,eff}}(E)$ results analogously. At relatively small junction conductances, inelastic thermal processes in the substrate with rates of $\Gamma_1$ and $\Gamma_2$ (see Fig. 5.4) are sufficient for the depletion of the YSR state long before the next tunneling event takes place, making the tunneling rates the current limiting factor. Therefore the total current can be calculated by integrating all rates taking into account the thermal occupations of the available states in the tip, as it is done in Eq. (6.52). In particular, our simulation even reproduces a second, much weaker V-shaped structure centered around $eV = \Delta - \epsilon_0$ originating from the thermally activated quasi-particles. Finally, it should be noted that for this case of the small junction conductance, both the spectrum-based simulation model of Section 6.2 and the rate-based simulation model of Section 6.3 yield the same results. Mathematically they are equivalent and can be transformed into each other as long $\Gamma_1$ and $\Gamma_2$ are large compared to $\Gamma_{\mathrm{e}}^{(0)}(E)$ and $\Gamma_{\mathrm{h}}^{(0)}(E)$.

Nevertheless, our rate approach has the advantage of the smaller number of input parameters, and is only based on the asymmetry of the YSR states and the particular relaxation rates. Another advantage is that the model explicitly incorporates the understanding of the tunneling process. This was not the case for the simple Tien-Gordon model of the spectrum-based simulation, where only the number of charge carriers underlying the tunneling process had to be assumed. An understanding of the physical origin of the spectral features was not necessary. Overall, we can conclude from the good agreement between the rate-based simulation and experiment that our assumption of the single-electron tunneling processes through the YSR state for small conductances is valid.

### 8.1.2 Resonant Andreev Reflections

In this section, we want to demonstrate that the rate-based simulation is also applicable for high conductances, allowing to describe tunneling processes through the YSR state in the presence of resonant Andreev reflections. Single-electron tunneling was characterized by the fact that the inelastic relaxation processes are fast compared to the electron and hole tunneling rates. By increasing the junction conductance this proportion is reversed as already described in Section 5.2.1. Thus, the statistical probability for an inelastic relaxation process of the YSR state is much lower compared to the electron and hole tunneling rates, and consequently, the resonant Andreev reflections become the dominant process for large enough conductances. As pointed out at the beginning of Section 8.1, the naive expectations for the HF splitting of a two-electron process being $\hbar\Omega/2e$ and the experimental observations in Fig. 8.1(b) contradict each other.

We need to be able to explain three things: *(i)* The origin of the Y-shape, *(ii)* the fact why the inner distances of the splitting do not reflect a charge transfer of $2e$, and *(iii)* the double structure along the low voltage arm of the Y-shape. Since the one-electron tunnel process is the subordinate process for high conductances, we neglect it for the discussion presented in this section. The influence of HF radiation within the framework of the rate-based model

results in Eq. (8.1) for the effective rates and Eq. (6.47) for the resulting current. These equations allow us to understand the HF-splitting at the level of the sub-processes involved.

Let us first focus on the Andreev processes detected at negative bias voltage forming the Y-shape in Fig. 8.1(b) that evolves from $eV = -(\Delta + \epsilon_0)$. The process under consideration consists of a hole tunneling into the resonance of the YSR state at negative energy and an electron tunneling out of the YSR state at positive energy. For this to be possible, a Cooper pair is broken in the substrate (see Fig. 5.4). The resonant nature of this process has two important implications. At first, Andreev reflections involving YSR states are stronger than those of unstructured substrates, as the YSR resonance provides in-gap states in which the electrons and holes can tunnel into. Additionally, there are clear threshold conditions for when electron and hole tunneling from the YSR resonance into the quasi-particle states of the tip is possible. These are $eV + m\hbar\Omega \leq -(\Delta + \epsilon_0)$ for holes and $eV + n\hbar\Omega \leq -(\Delta - \epsilon_0)$ for electrons (see Fig. 8.2). Here, the integers $m$ and $n$ indicate the number of absorbed or emitted photons of the hole or electron respectively. Not satisfying these inequalities means that no states in the tip are available for the tunneling process due to the superconducting tip-gap. In our terminology, we speak of *on-threshold* processes when equality occurs in the threshold conditions, meaning the tunneling process originates exactly from the sharp edge of the coherence peak. All other valid solutions of the inequality are described as *above-threshold* processes. Accordingly, in the absence of HF radiation, the electron process is automatically above-threshold at negative bias when the hole process is. With incident HF radiation, however, this no longer has to be true, as it will be the case within the *violet*-hashed cross-section in Fig. 8.2(a).

The larger the amount of energy available in the HF field becomes with increasing amplitude $V_{\mathrm{HF}}$, the more photons can be emitted and absorbed during the tunneling process. We can introduce the maximum number of photons $\Lambda = eV_{\mathrm{HF}}/\hbar\Omega$, which is representing an upper boundary for $|m| \leq \Lambda$ and $|n| \leq \Lambda$. As a result, the two thresholds define two distinct V-shaped regions in the negative bias voltage range. One may expect the *orange* V-shape in Fig. 8.2(a) from the hole threshold $|eV + (\Delta + \epsilon_0)| \leq \Lambda\hbar\Omega = eV_{\mathrm{HF}}$ and another *blue* V-shape for the electrons from the threshold $|eV + (\Delta - \epsilon_0)| \leq \Lambda\hbar\Omega = eV_{\mathrm{HF}}$. For resonant Andreev reflections to occur, both processes must be above-threshold, which means that resonant Andreev reflections can only be measured in the outer (*orange*) V-shaped region. Likewise, without HF radiation, no spectral fingerprint of the Andreev processes occurs at the energy $eV = -\Delta + \epsilon_0$, because the electron process is only possible together with the associated hole process.

We can now attribute the observation of both, the Y-shape and the unexpected spacing, to the strong asymmetry $|u_\epsilon|^2 \ll |v_\epsilon|^2$ in the YSR state amplitudes $u_\epsilon$ and $v_\epsilon$ for electrons and holes respectively. Since the tunnel rates are directly proportional to these amplitudes (compare Eq. (5.5) and Eq. (5.6)), this also implies that the hole tunnel rate $\Gamma_{\mathrm{h,eff}}$ is generally significantly larger than the electron rate $\Gamma_{\mathrm{e,eff}}$. Because we have to consider separate thresholds for the two rates, the electron tunneling can be regarded primarily as the rate-limiting component. It may be counterintuitive at first, but it is the limiting component of a current that determines its flow. This is analogous to rivers or roads, where the narrowest point also

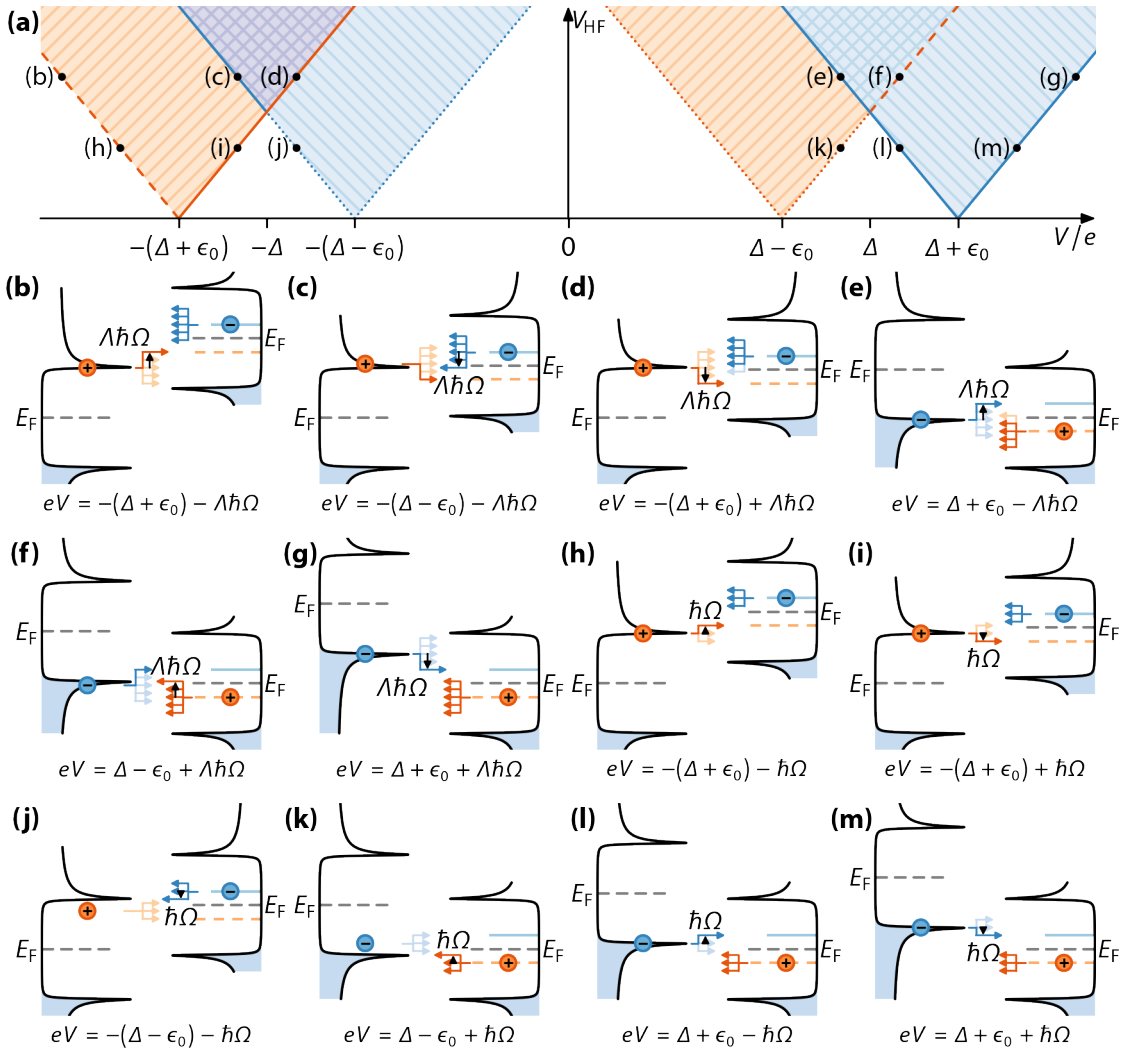


**Figure 8.2 | Portfolio of photon-assisted resonant Andreev tunneling processes illustrating various thresholds. (a)** Schematic overview of the 2D color maps. V-shaped regions with separate photon-assisted tunnel thresholds for electrons (blue; originating from $eV = \pm\Delta + \epsilon_0$) and holes (orange; originating from $eV = \pm\Delta - \epsilon_0$). For resonant Andreev reflections to occur, both electron and hole tunnels must be above-threshold, which has the consequence that only the structure within the outer V-shapes can be seen. Due to a large asymmetry between the YSR wave function of electrons and holes at the peak position, electron tunneling is effectively rate-limiting, and the photon sidebands are most visible in the (blue) electron regions. At negative biases, this makes the violet region particularly prominent, resulting in a distinct Y shape indicated by full lines. With positive bias, the outer V (blue) is the result of electron tunneling, and the sidebands are visible throughout. The dots marked **(b)**-**(m)** indicate bias and HF amplitude, for which tunneling processes are outlined in corresponding panels. In these, long arrows mark processes that are on-threshold, short *full* (*faint*) arrows mark processes above (below) the threshold. The small black arrows indicate the energy available at the corresponding HF voltage, which can be absorbed or emitted by the photons.

determines the maximum transport capacity. Hence, the features in the experiment due to $\Gamma_{\mathrm{e,eff}}$ (*blue* V-shape) are more pronounced but result only from one of the two separate threshold conditions. Therefore the distance between maxima is $\hbar\Omega/e$, although the underlying process is based on two-electron tunneling. In combination with the previously made observation that Andreev reflections can only occur within the outer *orange* V-shape, this also explains why the sidebands occur with stronger intensities in the region where both V-shapes overlap (*violet* region). While the electron rate is more important for the overall appearance of the spectrum, the hole processes can not be neglected. The threshold of the hole processes leads to a contribution along the low-voltage arm of the Y-shape (solid *orange* line in Fig. 8.2(a)). Along this line, the rates of the electron processes and the hole processes are of comparable size, since the latter is just beginning to emerge. So in essence, we explained the Y-shape in two steps, by pointing out the regions in which the rates are limited and lead to pronounced features. These are the solid *orange* line together with the violet hatched region and both combine to the Y-shape in Fig. 8.2(a). Moreover, as a result of the comparable rates along the low-voltage arm, the electron and hole thresholds become visible side by side. That region is the only one where the asymmetry is not apparent. This means that the observed double structure consists of features that can be attributed to both rate equations.

For a deeper understanding, we take a closer look at the sub-processes involved in the rate-based description for different characteristic combinations of bias voltage $V$ and HF amplitude $V_{\mathrm{HF}}$. The panels in Figs. 8.2(b)-(m) show the underlying processes for selected points marked in the schematic overview in Fig. 8.2(a). These sketches all follow the same systematic representation: The electron and hole components of the YSR states are shown as lines in the gap of the substrate (for the electrons *blue* and *solid*, the holes *orange* and *dashed*). Here the asymmetry in the amplitude of the states is characterized by the different length of the lines. Fans indicate all possible energies that the tunneling hole or electron can have after emitting or absorbing photons. Black arrows denote the HF amplitude defining the maximum number of photons $\Lambda$ that can be absorbed or emitted during the process. Tunneling processes that are on-threshold are marked by long arrows, as they are more pronounced in intensity due to the large density of states available at the tip. Processes above and below the threshold value are marked by short arrows. Since below threshold processes are forbidden, they are shown only for the sake of completeness but in a lighter color.

To understand the Y-shape, we first focus on the selected points (b)-(d), whose sketches can be found in the figures of the same name in Figs. 8.2(b)-(d). In (b) and (d), cases are shown where the hole process is on-threshold, whereas in (c) this is the case for the electron process. As the weaker of the two processes determines the shape of the spectrum, the asymmetry of the YSR amplitudes comes into play. Here, in general, the electron process is the bottleneck. This explains, why the high-voltage arm (*orange* dashed line) of the *orange* V-shape fades, by comparing (b) with the other two sketches. In (b), the electron tunneling processes take place at energies at which only states in the decaying shoulder of the BCS coherence peak are available. In (c) and (d), one of the paths of the fan is always in the

vicinity of the threshold value, which leads to a significantly higher intensity. Since the electron process is the bottleneck, slight variations in the hole rate are irrelevant and will not be reproduced by spectral features. Conclusively, as long as these variations occur around the threshold, the hole process will never become the limiting contribution. The reasoning can be applied one-to-one to the comparison between points (h) and (i).

Next, we want to explain why the purple hatched intersection of the two V-shapes is strongly pronounced. The explanation for this can be seen in (c) and (d). The branches of the fan of the electron process are now energetically in the range of the threshold energy, i.e. the increased density of states of the BCS coherence peak is available for tunneling as they are close to being on-threshold.

The last observation to be discussed is the double structure, which is explained by (d). The crucial point for this argument is that the BCS gap is not infinitely sharp, but broadened mainly due to depairing and instrumental broadening. With the further reduction of the bias voltage proceeding from the situation shown in (d), the hole rate will decrease continuously and reach the point where it becomes smaller than the electron rate. For this reason, there are features in this area along the low voltage arm that are due to the changes in $\Gamma_{\mathrm{e,eff}}$ as well as features that are due to the changes in $\Gamma_{\mathrm{h,eff}}$. This results in the particular double structure. If the bias is reduced even further, the hole processes no longer have any density of states available and the Andreev processes stop being possible. Following the same argument, point (j) can be explained, accordingly.

For the explanation of the Y-shape, we have now finally used the same approach as we used in the previous section for simulating the low conductance data, namely transferring the model from Tien-Gordon to individual tunneling rates. In Fig. 8.1(d) the rate-based simulation for the high conductance case is shown. A comparison once again demonstrates the excellent agreement with our data. It correctly simulates the Y-shape in which both the double structure and the sideband spacing are reproduced. A detailed discussion of this simulation follows in the next Section 8.2.

Now that we have explained in detail how the Y-shape is formed, the question arises why this does not apply equally for positive bias voltages. This process is also dominated by resonant Andreev processes and therefore the influence of the single-electron processes by inelastic relaxation is negligible. The question to be answered is, why for positive bias voltages the splitting does not also exhibit a Y-shaped form but returns to a V-shaped appearance.

In Fig. 8.2(a) the V-shape expected from the electron threshold is centered around $eV = \Delta + \epsilon_0$ and is again hatched in *blue*. The inner V-shape at $eV = \Delta - \epsilon_0$ is based on the hole threshold and hatched in *orange*. An observation of the Andreev processes is again only possible within the outer (blue) V-shape because only here both processes are above-threshold. The asymmetry $|u_\epsilon| \ll |v_\epsilon|$ of the YSR wave functions remains unchanged so that in contrast to the negative polarity, the rate-limiting electron processes are now associated with the outer V-shape. This finding directly explains the differences in the splitting pattern for positive and negative bias voltages. Strongly pronounced sidebands occur in the entire outer V-shape, only due to changes in $\Gamma_{e,\mathrm{eff}}$. Since the shape of these

spectral features is determined again by only one rate, this is also reflected in the splitting $\hbar\Omega/e$ of the sidebands.

This can also be seen when looking at the individual processes outlined for positive bias voltages in Fig. 8.2. The processes presented in Figs. 8.2(k)-(m) are equivalent to those in (h)-(j), with the difference that the variations in the hole rate have no influence, as it is not the limiting process within the Andreev reflections. The same applies to points (e)-(g). Here $\Gamma_{\mathrm{h,eff}}$ and $\Gamma_{\mathrm{e,eff}}$ are not comparable, so that the shape is still determined exclusively by $\Gamma_{\mathrm{e,eff}}$.

The V-shape is also nicely reproduced in our theoretical calculations, on which the simulation in Fig. 8.1(d) is based. It is important to note that for large junction conductivities, these V-forms are also due to resonant Andreev reflections and therefore different from those at low conductivities and should not be confused with them. Thermal processes require an inelastic relaxation and are therefore much weaker than resonant Andreev reflections.

In summary, the analysis of the sub-processes has demonstrated the following: The limiting electron tunneling rate leads to a fading-high voltage branch at negative bias voltages. As soon as these limiting rates come close to being on-threshold, they mainly determine the shape of the spectrum. When the rates become comparable, the influence of the asymmetry is lifted and both tunneling processes leave their traces in the spectrum. All things considered, the Y-shape can be described entirely including the double structure, as well as the V-shape for positive bias voltages.

## 8.2 Simulating the Photon-Assisted Current Through the YSR States

In this section, we describe in detail the simulations performed to describe the photon-assisted differential conductance through the YSR state used for Fig. 8.1(c) and (d). Our rate-based simulation relies on only a few input parameters that can be extracted from the experiment. This is new and distinguishes it from previous theoretical descriptions of photon-assisted tunneling. So far, the simple Tien-Gordon model required a complete spectrum without HF radiation as input in order to simulate the influence of HF radiation (see Chapter 7). The following is a summary of the calculation's formal basis and a detailed description of how the required parameters are obtained.

The tunneling processes through the YSR states are described using rate equations. Eq. (8.1) already describes how these rates were modified using the model of Tien and Gordon. Together with the thermal population of the states, these rate equations form the basis to simulate the currents, i.e. the differential conductance. Section 6.3 discusses the detailed derivation resulting in the two equations Eq. (6.52) and Eq. (6.47): For single-electron processes, where inelastic excitations and relaxations are required, the current is

given by

$$I_\mathrm{s} = \frac{e}{h}\int \mathrm{d}\omega \sum_n \mathcal{J}_n^2\left(\frac{eV_\mathrm{HF}}{\hbar\Omega}\right)\Gamma_1 \frac{\Gamma_\mathrm{e}^{n_\mathrm{F}}(\omega_{-n}) - \Gamma_h^{n_\mathrm{F}}(\omega_{+n})}{[\omega-\epsilon_0-\Lambda(\omega)]^2+[\Gamma(\omega)/2]^2} - \sum_m \mathcal{J}_m^2\left(\frac{eV_\mathrm{HF}}{\hbar\Omega}\right)\Gamma_2 \frac{\Gamma_\mathrm{e}^{1-n_\mathrm{F}}(\omega_{-m}) - \Gamma_h^{1-n_\mathrm{F}}(\omega_{+m})}{[\omega-\epsilon_0-\Lambda(\omega)]^2+[\Gamma(\omega)/2]^2}\,. \tag{8.2}$$

The current of the resonant Andreev processes is given by

$$I_\mathrm{a} = \frac{2e}{h}\int \mathrm{d}\omega \sum_{n,m} \mathcal{J}_n^2\left(\frac{eV_\mathrm{HF}}{\hbar\Omega}\right)\mathcal{J}_m^2\left(\frac{eV_\mathrm{HF}}{\hbar\Omega}\right) \frac{\Gamma_e^{n_\mathrm{F}}(\omega_{-n})\Gamma_h(\omega_{+m}) - \Gamma_e(\omega_{-n})\Gamma_h^{n_\mathrm{F}}(\omega_{+m})}{[\omega-\epsilon_0-\Lambda(\omega)]^2+[\Gamma(\omega)/2]^2}\,. \tag{8.3}$$

To obtain the expressions for the conductance required for the simulations, we have to perform the derivative of the two currents with respect to the voltage. The voltage dependence can be found in the expression $\omega_{\pm i} = \omega \pm (eV + i\hbar\omega)$.

### 8.2.1 Simulation Parameters

Here we describe, how we determined the input parameters needed for the rate-based simulation. Practically all parameters can be determined from the HF radiation-free $\mathrm{d}I/\mathrm{d}V$ spectrum at low junction conductance (compare with Fig. 5.3(a)). The only exception is the overall tunnel strength at large conductance.

General material quantities like the superconducting gap, but also the normal density of states $\rho_0$ can be assumed to be the same for tip and substrate. Consequently, we can determine the dimensionless product of $\rho_0\,|T|$ from the normal-state differential conductance $G_\mathrm{N}$ using equation Eq. (3.10). A normal-state conductance of $G_\mathrm{N}^\mathrm{low} = 2.6\times10^{-5}\,\mathrm{G}_0$ gives $\rho_0 t^\mathrm{low} = 8.1\times10^{-4}$. We select the remaining parameters so that the peak heights and the broadening in the $\mathrm{d}I/\mathrm{d}V$ spectra in the absence of HF radiation, shown in Fig. 5.3, are well represented by equation Eq. (8.2). We find that the following parameter set provides the best results for reproducing the experimental $\mathrm{d}I/\mathrm{d}V$ spectra:

$$\epsilon_0 = 0.25\,\mathrm{meV}\,, \tag{8.4}$$
$$\Gamma_1 = 0.70\,\mu\mathrm{eV}\,, \tag{8.5}$$
$$\Gamma_2 = 0.11\,\mu\mathrm{eV}\,, \tag{8.6}$$
$$|u_\epsilon|^2/\rho_0 = 0.21\,\mathrm{meV}\,, \tag{8.7}$$
$$|v_\epsilon|^2/\rho_0 = 0.83\,\mathrm{meV}\,. \tag{8.8}$$

The YSR state energy $\epsilon_0$ is read from the spectrum by eye and iteratively corrected in the simulation process, so that the energetic positions of the peaks are reflected in the best possible way. A similar approach was used for the thermal relaxation rates. Here, the thermal peaks in this spectrum are a very sensitive measure of these rates $\Gamma_1$ and $\Gamma_2$, as they

account for the broadening of the spectra at low conductance. By assuming the spectrum in Fig. 5.3(a) to reflect mainly single-electron tunneling, it can be used to determine $|u_\epsilon|^2/\rho_0$ at positive bias voltage and $|v_\epsilon|^2/\rho_0$ at negative bias voltage. In particular, the YSR wave functions reflect the ratio $|u_\epsilon|^2/|v_\epsilon|^2 = 0.253$ between the peak intensities at $\pm(\Delta + \epsilon_0)$. Therefore the electron tunneling process exhibits smaller intensities than the hole tunneling process.

Moreover, the superconducting gap, the HF frequency, the temperature, and two broadening parameters are used:

$$\Delta = 1.35\,\mathrm{meV}, \tag{8.9}$$
$$f = 40\,\mathrm{GHz}, \tag{8.10}$$
$$T = 1.35\,\mathrm{K}. \tag{8.11}$$
$$\Gamma_\mathrm{s} = 20\,\mu\mathrm{eV}, \tag{8.12}$$
$$\Gamma_\mathrm{system} = 60\,\mu\mathrm{eV}, \tag{8.13}$$
$$\tag{8.14}$$

The superconducting gap is the result of fitting the superconducting coherence peaks of a clean Pb/Pb junction. In the superconducting density of states in Eq. (5.1) the Dynes parameter $\Gamma_\mathrm{s}$ is inserted to describe the depairing of the Cooper pairs. It is determined in the same fit as the gap, together with the instrumental broadening. This is included to compensate for broadening of unknown source as a Gaussian averaging of the simulated $\mathrm{d}I/\mathrm{d}V$ spectra with a width of $\Gamma_\mathrm{system} = 60\,\mu\mathrm{eV}$ (see Section 3.2.3). Frequency and temperature are recorded during the experiment.

In Fig. 8.3 single selected $\mathrm{d}I/\mathrm{d}V$ spectra are compared to the simulations based on the parameters given above. This is done for four different HF amplitudes, respectively, for low conductance in Fig. 8.3(a) and high conductance in Fig. 8.3(b). The spectra are taken from the same data set as the data shown in Fig. 8.1. For both conductances, the lowest of the four spectra are recorded with almost no HF amplitude. Here it is evident that all the important characteristics of the spectrum are represented in the simulation, namely the position and shape (i.e. width and height) of the YSR resonances. Additionally, the simulation also shows effects like the well-established negative differential conductances (NDCs). Despite a further increase in the voltage, there is a reduction in the current after a process was on-threshold and therefore, in the simulation, an NDC also mathematically follows as a result of a convolution between the YSR state with the coherence peak density of states (DoS) of the tip. The other spectra in Fig. 8.3(a) reflect nicely in which detail the simulation can reproduce the photon-assisted splitting. Note that the simulations do not take the substrate's coherence peaks into account. This is why the simulations are always flat towards the edges and do not share the increase at large bias seen in the data.

The simulations in Fig. 8.3(b) with high junction conductance required only the adjustment of one parameter compared to the parameter set for the low conductance case, namely $\rho_0 t$. We choose this parameter with $\rho_0 t^\mathrm{high} = 39 \times \rho_0 t^\mathrm{low}$ so that we have a good overall

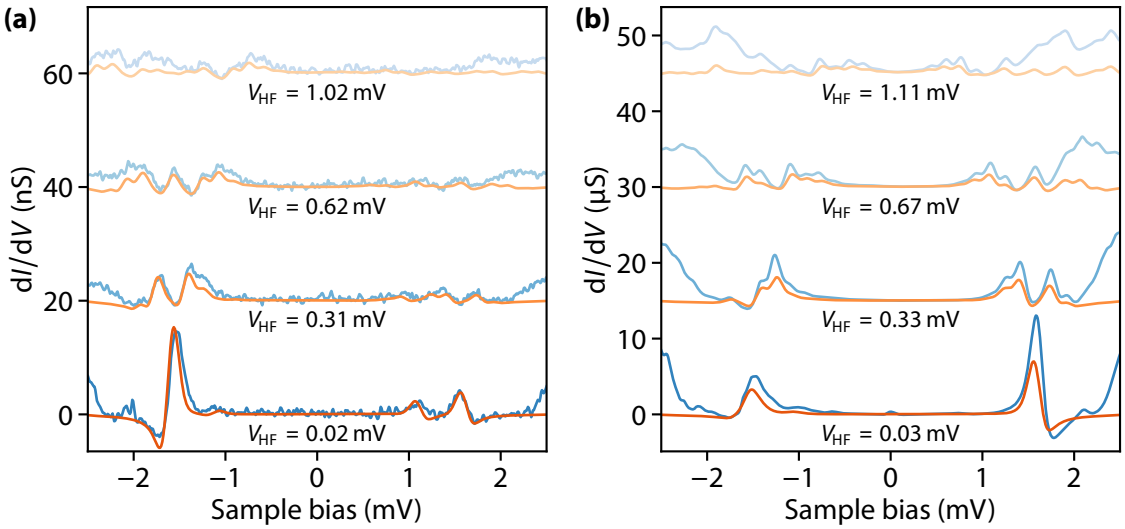


**Figure 8.3 | Individual spectra of the HF splitting of the YSR states at small and large junction conductance together with the corresponding simulations of photon-assisted tunneling.** We show individual spectra of the experimental data from Fig. 8.1 (*blue*) and the corresponding rate-based simulations (*orange*) at different HF amplitudes. **(a)** shows the data in the low-conductance and **(b)** in the high-conductance regime. The spectra are offset for clarity.

agreement between Eq. (8.3) and the measured data for high junction conductance for the case without HF radiation. When choosing this parameter we tried to find the balance so that peaks developing from the YSR state at $\epsilon_0$ are reflected as well as possible in their energetic position, leading to a small underestimation of their amplitudes. We explicitly do not use Eq. (3.10) as before to calculate the value from the normal state conductance. However, both values lie within a range of 15 % and are therefore comparable. After all, the simulated results for high junction conductances in Fig. 8.1(d) is based on the same parameter set as the simulation in Fig. 8.1(b) for low junction conductances.

In summary, this just discussed comparison of single spectra with simulation shows a good agreement between experiment and theory. In particular, this representation method is well suited for the evaluation of the amplitudes and thus for a peak-by-peak comparison. In contrast, the previously discussed 2D color maps in Fig. 8.1(c) highlight other features. Although the amplitudes of the $\mathrm{d}I/\mathrm{d}V$ signal are more difficult to comprehend here, it is possible to follow the shifting and splitting of the individual peaks in great detail.

We can now check this parameter set for consistency against our previous interpretation. It should show that electron and hole tunneling is slow compared to the relaxation rates $\Gamma_1$ and $\Gamma_2$ at low junction conductance and fast at high conductance. The extracted numerical values for the electron and hole tunneling rate are

$$\Gamma_\mathrm{e} = 4.0\,\mathrm{neV} \tag{8.15}$$

$$\Gamma_\mathrm{h} = 15.8\,\mathrm{neV} \tag{8.16}$$

at low junction conductance, and

$$\Gamma_e = 6.2\,\mu eV \tag{8.17}$$
$$\Gamma_h = 24.5\,\mu eV \tag{8.18}$$

at large junction conductance. These values significantly differ from $\Gamma_1 = 0.70\,\mu eV$ and $\Gamma_2 = 0.11\,\mu eV$ by at least one order of magnitude. This is in agreement with the observation of the crossover between single-electron and resonant Andreev tunneling. Here an inversion in the amplitudes $\alpha_\pm$ of the YSR resonances at $\epsilon_0 = 0.25\,meV$ takes place, when the tip is approached (demonstrated in Fig. 5.5). The extracted rates thus confirm our interpretation numerically that in the two extreme cases shown we can assume either dominant single-electron tunneling or dominant Andreev tunneling. Both simulations contain nonetheless always the total current $I_{tot} = I_s + I_a$. The only point where it was relevant that there is no mixing is in the determination of the electron and hole wave functions $u$ and $v$. Here, the assumption that we can derive these from the ratio of the amplitudes $\alpha_+/\alpha_-$ applies only in the case of pure single-electron tunneling.

## 8.3 Advanced Data Analysis Supported by the Rate-Based Simulation

The rate-based simulation allows us to investigate the expected characteristics of the spectra in more detail. Since the simulation is no longer based on input spectra but concrete physical quantities, it is possible to investigate their influence individually. By varying the input parameters we can efficiently simulate spectra for different asymmetries in the YSR wave function, YSR state energies, or frequencies. Thus, we can make predictions for experimental situations that we cannot realize in our Mn/Pb system, which leads to the enormous potential of rate-based simulation.

### 8.3.1 Advanced Simulations for a Better Understanding of the Double Structure in the Y-Shape

So far we have discussed the splitting due to photon-assisted tunneling at only one single frequency of $f = 40\,GHz$. The choice of this particular frequency was not physically motivated but based on technical aspects. To make the best use of our energy resolution, we wanted to maximize the spacing between the sidebands. Since this spacing is directly proportional to the frequency, we took the highest possible frequency that our signal generator provides. This however is a special case for the investigated system. The frequency is such that two times the YSR state energy and the photon energy are an integer multiple of each other. In our case $2\epsilon_0 = 3\hbar\Omega$, where $2\epsilon_0$ just describes the distance between the two V-shapes as shown in Fig. 8.2(a). In Fig. 8.4 we show theoretical simulations of the double

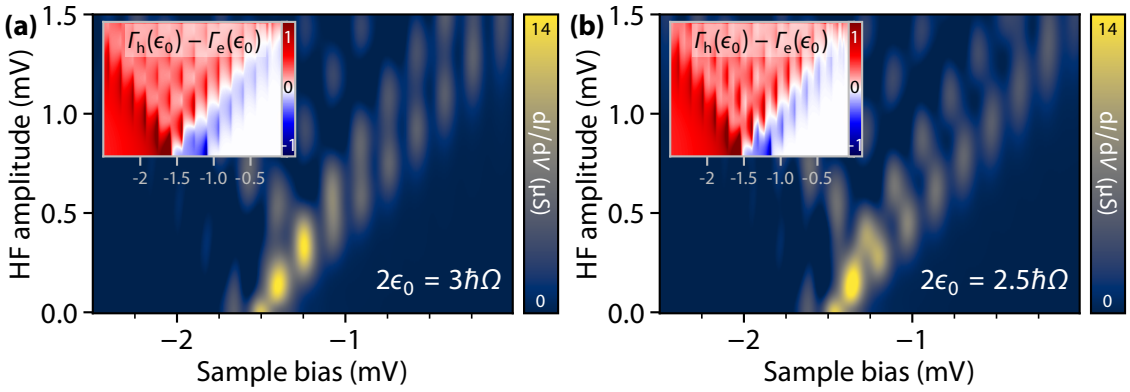


**Figure 8.4 | Study of the origin of the double structure by comparing the electron and hole threshold.** Simulated d$I$/d$V$ spectra of the YSR state under HF irradiation at negative bias voltage. The parameters are chosen such that the Y-shape of the experiment is reflected in its main characteristics. Along the low-voltage arm of the Y-shape, the double structure is formed, in which the outer peaks, forming already at smaller HF amplitudes, are to be associated with the hole threshold, while the peaks just above those are associated with the electron threshold. In panel **(a)** with $2\epsilon_0 = 3\hbar\Omega$ we have chosen the photon energy to be an integer multiple of the distance $2\epsilon_0$ between the origins of the electron and hole thresholds. As a consequence, the peaks of the two branches form at the same sample bias voltages. This situation is very close to the actual experimental data. For comparison, panel **(b)** shows the situation where $2\epsilon_0 = 2.5\hbar\Omega$ no longer corresponds to an integer multiple, but the thresholds are shifted by $0.5\hbar\Omega$. The two insets show the difference between hole and electron tunneling rates in arbitrary units. This illustrates nicely which of the two rates limits the Andreev process. The peaks based on the hole threshold are only visible in regions where electron and hole tunneling rates are comparable and both are non-zero, i.e. exactly in the white region between the blue and red areas in the insets.

structure on the low-voltage arm of the Y-shape. For most combinations of bias voltage and HF amplitude, the large asymmetry between hole and electron wave function of the YSR state means that only the electron threshold is significant for the changes in current and is therefore mainly responsible for the shape of the spectrum. The reason for this is that electron tunneling is weaker than hole tunneling due to the smaller wave function and therefore effectively the rate-limiting process. This can be seen in the two insets in Fig. 8.4, where the difference $\Gamma_h(\epsilon_0) - \Gamma_e(\epsilon_0)$ of hole and electron rates is plotted. The *blue-red* color scale can accordingly be understood as a metric indicating which process is dominant and which is the rate-limiting process. The red areas indicate that the electron process is rate-limiting, while in the blue area the hole process is rate-limiting. However, this latter case occurs mainly along the low-voltage branch of the Y-shape, i.e. along the boundary of the hole tunneling threshold for negative bias voltages. Here the rate for electron tunneling is already high, while hole tunneling is still very weak since the process is just beginning

to be energetically allowed. Thus, features become visible due to both thresholds, ergo the double structure is formed.

The simulation gives us the freedom to reproduce this behavior within the experiment. In the case that the distance between the hole and electron thresholds and the photon energy are integer multiples of each other, both processes are always on-threshold at the same voltages, as shown in Fig. 8.4(a). This simulation comes close to the situation shown in Fig. 8.1(b). In contrast, Fig. 8.4(b) shows the situation where the thresholds are shifted by $0.5\hbar\Omega$, since photon energy and YSR state energy are in the relation $2\epsilon_0 = 2.5\hbar\Omega$. Remarkably, the lower structure, i.e. the one connected to the hole tunneling, has a smaller apparent slope than the structure directly above in the double structure connected to the electron tunneling. This difference in slope is also clearly visible in the experimental data in Fig. 8.1(b).

### 8.3.2 Investigating the YSR Wave Functions Asymmetry

Based on our full theoretical results obtained from the rate-based simulations, we can study the influence a change in the ratio between electron and hole wave function $u_\epsilon$ and $v_\epsilon$ has on the splitting pattern observed under HF radiation. Fig. 8.5 shows the corresponding simulations for different ratios. Along the horizontal direction, the relationship between the YSR wave functions changes. Along the vertical direction, we have again varied the ratio between YSR state energy $\epsilon_0$ and photon energy $\hbar\Omega$. The overall shape of the splittings depends only on the wave function ratio. In the middle column of panels, the ratio of the two wave functions is balanced ($u_\epsilon^2 = v_\epsilon^2$). Accordingly, the spectra are axis-symmetric around the chemical potential, since electron and hole tunneling into the YSR state are equivalent. In the far left column, the hole wave function predominates. This corresponds to our experimental situation with a Y-shape at negative bias voltages and a V-shape at positive bias voltages (exemplarily highlighted in Fig. 8.5(c1)). A reversal of the wave-function ratio to a regime of dominant electron character is shown in the far right column. Here Y- and V-shape exchange sides. This demonstrates that only the asymmetry in the YSR wave functions determines the overall spectral form. The relationship between YSR state energy and frequency does not influence this but is important for the inner structures of the splitting. A change in this ratio is evident in the region where both processes are above-threshold (overlapped by dashed and dotted V-shapes). In this region, the two inner structures shift against each other as the number of sidebands fitting into $2\epsilon_0$ is changed. Especially if the frequency and two times the YSR state energy are integer multiples of each other (thus divisible without remainder) the electron and hole processes are on-threshold at the same time and their sidebands often overlap (see middle column). If the divisibility is not given, both structures are continuously visible and shifted against each other. This divisibility condition does not play a role in all cases with strong asymmetry in the electron and hole wave functions (see outer columns). Here one type of sideband dominates, which is expressed by a regular voltage spacing of $\hbar\Omega$.

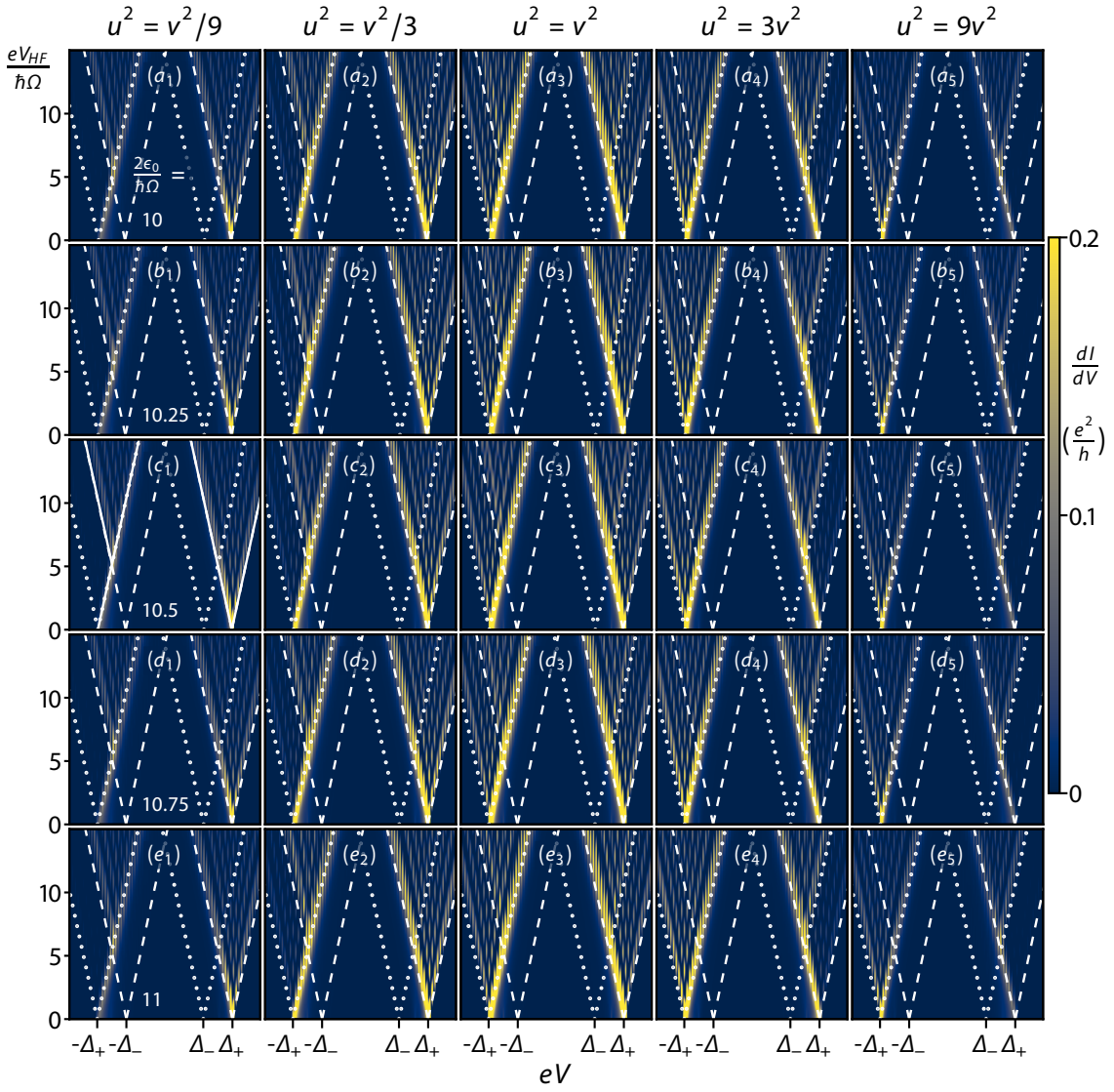


**Figure 8.5 | Investigation of the influence of the YSR-state wave functions ratio and YSR-state energy to frequency ratio on the photon-assisted splitting.** Shown is the differential conductance as a function of bias voltage $eV$ and HF amplitude $eV_{\mathrm{HF}}$ for resonant Andreev tunneling from the superconducting tip into the YSR-state. Along the horizontal axis, the panels differ in the ratio of the electron and hole wave function $u_\epsilon$ and $v_\epsilon$. For all panels $u_\epsilon^2 + v_\epsilon^2$ is kept constant for the sake of comparability. Along the vertical, the ratio between YSR state energy $\epsilon_0$ and photon energy $\hbar\Omega$ is changed. The electron and hole thresholds are indicated by corresponding dashed and dotted V-shapes. These are centered at $e|V| = \Delta_\pm = \Delta \pm \epsilon_0$. In (c1) the resulting Y- and V-shaped regions are exemplarily highlighted. Parameters for the simulation: $\Omega/\Delta = 0.05$, $\rho_0|t| = 0.04$. From [186]

## 8.4 Summary and Conclusion

In this chapter, we have studied the influence of HF-radiation on the tunneling processes through a YSR-state. These states were induced by Mn adatoms on a superconducting Pb surface. By varying the tip-substrate distance we had access to two fundamentally distinct tunneling processes, the single-electron tunneling, and the resonant Andreev reflections. All in all, these resonant Andreev reflections also transfer electron pairs, just as we have previously discussed for Andreev reflections and Josephson tunneling on pristine superconductors. Here, however, we have seen that HF radiation influences these resonant Andreev reflections qualitatively quite differently. In the simple Tien-Gordon-like expressions (7.2) and (7.3) for photon-assisted tunneling of electron pairs, the energy denominator of the intermediate state and thus the pair tunnel amplitude is assumed to be energy independent, and therefore only a $\delta$-function in time. This leads to a reduction of the two time-dependent phase factors associated with the two tunnel electrons to one. The one phase factor alone thus halves the distance between the sidebands compared to the single-electron tunneling. We have shown that this assumption is no longer true if we consider resonant Andreev reflections by a bound state at energy $\epsilon_0$. That is because the amplitude of the tunneling electron-pair has a sharp resonance that is connected to the bound state. In pristine superconductors, it was possible to describe the tunneling processes in the context of low-order perturbation theory in the tunneling Hamiltonian. As we have shown, this is generally no longer possible for resonant Andreev reflections. The rates for tunneling over the junction also determine the width of the bound-state resonance. As a consequence, we have to use all orders of perturbation theory for the description. In the experiment, the width is dominated by inelastic relaxation processes for small tunneling amplitudes (large tip-substrate distances) and by tip-substrate tunneling for large tunneling amplitudes (small tip-substrate distances). In the first case, the current is caused by single-electron transfers. This process can therefore still be described with the low-order perturbation theory in the tunneling Hamiltonian and thus within the scope of spectrum-based simulation. In the second case, the width of the bound state resonance is now dominated by the electron and hole tunneling rates, so that the description of this process must include all orders in perturbation theory. We have successfully described this process based on the rate-based simulation.

Although we have concentrated on YSR-states, the theory used here is by no means specific to them and is also valid for other subgap states. Thus, one of our proposed applications is the possibility to distinguish Andreev from Majorana bound states. Since already small deviations of the YSR-state energy $\epsilon_0$ from zero, lead to a splitting of the sidebands, we can distinguish such YSR-states from Majorana states at zero energy. This is possible even if the deviations are far below our normal energy resolution. Furthermore, an extension of the theory to several subgap states would be interesting. One would expect to see additional spectroscopic features if the photon energy becomes comparable to the level spacing between the subgap states.

# 9

# Implementation of Josephson Spectroscopy to Investigate the Superconducting Order Parameter

It is theoretically predicted that for several non-classical superconducting materials the order parameter is not constant but has a spatial modulation on atomic scales. Examples of such materials are heavy fermion materials, high-$T_c$ superconductors, or disordered superconductors [39]. Different mechanisms could lead to this change, such as the inhomogeneity of disordered materials [191–194], a momentum-dependent pairing interaction in heavy fermion materials [195–197], or the interaction of different electronic orders in the pairing densities as proposed for high-$T_c$ cuprates [198–200]. Scanning tunneling microscopy is intrinsically sensitive to local density of states (LDoS) by quasi-particle tunneling and therefore not sensitive to changes in the superconducting order parameter even with the use of, for example, YSR states [201, 202]. On the other hand, the critical current of the Josephson effect should be related to the BCS ground state, because it is based on Cooper-pair tunneling. If it were possible to monitor the changes of Cooper pair tunneling locally at the atomic level, this would allow the direct investigation of the local pairing parameter and high-resolution studies of novel superconducting phases [203].

Measurements of the Josephson effect in the STM are a challenge because they require a low junction impedance to obtain the best possible coupling between tip and substrate, which in turn enables Cooper pair tunneling and the Josephson effect. Several experiments have been performed using superconducting tips [204] to measure thermal phase fluctuations in the Josephson supercurrent close to point contact [46, 205, 206]. Further measurements have mapped the voltage-biased Josephson effect on the nanometer scale on vortices [207, 208] and high-$T_c$ cuprates [209, 210]. Recent studies have succeeded in imaging variations in the voltage-biased ($I(V)$) Josephson effect across magnetic impurities

[39]. Cooling down to mK-temperatures was the decisive step to image the Cooper pair current at sufficiently stable conditions for atomic resolution.

In voltage-biased junctions, the supercurrent is highly non-linearly depending on the voltage (see $P(E)$-theory in Section 2.4) and therefore do not provide a direct measure of the critical current. Current-biased junctions allow this direct access to the critical current via retrapping and switching current (see Fig. 2.8). They provide a measure of the statistics and hysteresis of the junction which allows direct conclusions about the junctions damping and its capacitive charging. Furthermore, current-biased junctions would be interpretable in the case of coherent Cooper pair tunnels, whereas $P(E)$-theory breaks down because it only describes sequential tunneling. Coherent Cooper pair tunneling might be interesting for applications like locally resolved Shapiro steps (see section 10).

## 9.1 Josephson-Spectroscopy in Pristine Pb/Pb Junctions

Between two superconductors that are brought into close proximity, a supercurrent consisting of Cooper pairs flows according to the Josephson effect (see Section 2.4). This supercurrent scales with the overlap of the superconducting wave function of the two superconducting contacts. We use our Josephson setup (see Section 4.4) to perform current-driven Josephson spectroscopy to determine the critical Josephson current. To achieve an effective current source we have connected an external 1 MΩ resistor in series to the junction. Since the normal state resistance of the Josephson junction is much smaller than the external resistor the voltage drops mostly over the latter and the junction can be considered as current-biased. To test this setup we first observed Josephson junctions between two pristine BCS superconductors in the form of a Pb/Pb junction. Establishing stable contacts in the low impedance range on the rather soft lead is challenging. This requires a lot of attention to keep the machine in a low-noise condition, but also time-consuming tip treatments were essential to generate a stable tip geometry.

We were able to obtain the expected $V(I)$ characteristics of the Josephson effect as shown in Fig. 9.1(a). The spectra were recorded on a clean site of the Pb(111) surface at a normal state resistance of $R_N$ = 113 kΩ. All of them have in common that they exhibit a horizontal step at small applied currents. This step is defined by two sharp inclines, with abruptly changing voltage (*grey* areas). These jumps are not symmetrically located around zero and also have a different statistical distribution (different width of the *grey* areas). To illustrate this, Fig. 9.1(b) shows the statistical distribution of such jumps in the form of a histogram for a Pb(110) junction with a normal state resistance of $R_N$ = 35 kΩ. Here the *blue* distributions describe the backward (BW; from positive to negative current) sweep and the *orange* distributions the forward (FW; from negative to positive current) sweep. The jumps for smaller currents have a significantly smaller width in their distributions than the jumps for larger currents. Also, the junction shows a clear hysteresis between forward sweep and backward sweep.

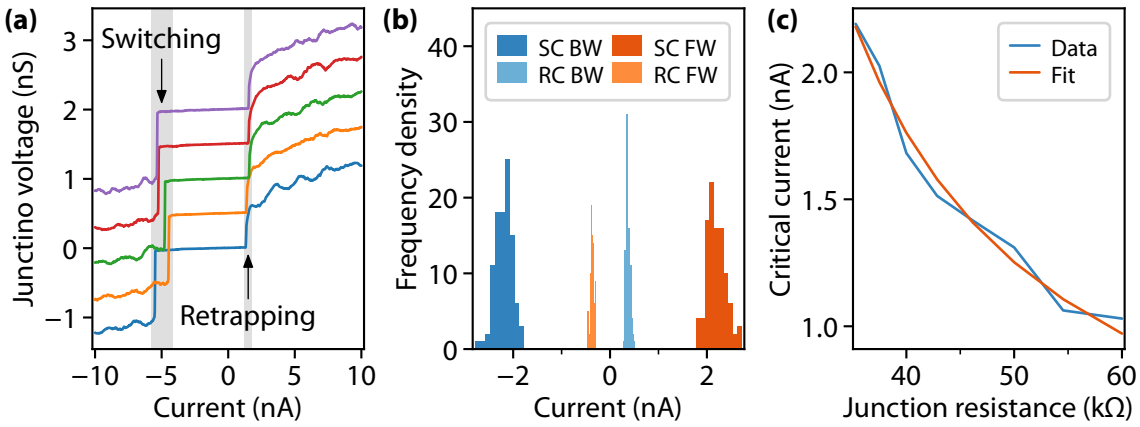


**Figure 9.1 | Determination of the critical Josephson current on pristine Pb. (a)** Junction voltage as a function of the driving current applied to a Pb(111) junction with a resistance of 113 kΩ. Setpoint: $V_{\mathrm{Bias}}$ = 3 mV, $I$ = 26.5 nA. Sweep direction is from positive to negative currents. The offset of the voltage amplifier is corrected and subsequently, the spectra are shifted for clarity. Visible is the characteristic Josephson step of an underdamped junction. It exhibits hysteresis and a statistically scattered switching current, whereas the retrapping current is nearly constant. **(b)** Histogram of retrapping and switching current of a Pb(110) junction. The total number of spectra evaluated here is $n$ = 100, all taken at a junction resistance of 35 kΩ. Setpoint: $V_{\mathrm{Bias}}$ = 6 mV, $I$ = 170 nA. Both sweep directions are shown, where forward sweeps (FW) are recorded from negative to positive current and backward sweeps (BW) vice versa. **(c)** Extracted critical current as a function of junction resistance on Pb(110). A fit of the form $A/(x - x_0)$ shows the inverse proportionality. We get a positive x-offset, which means the fit underestimates the experimental junction resistance. For all measurement points, the feedback was opened at $V_{\mathrm{B}}$ = 6 mV.

The response of the Josephson junction can be described in the context of the RCSJ model as outlined in Section 2.4. In this model, the junction is described by its phase, which can be viewed as a mass particle under the influence of friction in a sinusoidal potential landscape. Without an applied current, the potential has no preferred direction and has a multitude of local minima. The phase will be located in one of these minima, the trapped phased junction state. Only by applying a current, the potential will tilt. This leads to a reduction of the potential barriers until the minima disappear completely when the critical current is reached. Hence, the phase begins to move down the potential landscape. By reducing the current and thus restoring the minima, the junction is ultimately trapped again. Exiting and re-entering this trapped state takes place at two currents characterizing the junction, the switching and retrapping current. These currents are represented in the spectra by the jumps, as marked. The retrapping current is always smaller than the switching current because the phase still contains inertia and therefore gives information about the mass and friction associated with the phase. The larger the mass or smaller the friction, the longer the junction will stay in the running state. The distinctly different size of the two

and the resulting hysteresis suggests that our junctions are underdamped. The different width in the distribution of the currents is a result of the different statistics of the underlying processes. As the mass and friction associated with the phase are approximately constant, the distribution of the retrapping current is very small. The switching current, however, is a thermally activated process, combined with the increased possibility of tunneling when the potential barrier becomes lower, which both lead to an increased spread.

In general, we can state that we can observe steps in the $V(I)$ spectra when the normal state resistance is about $R_N = 100\,k\Omega$ and smaller. We are able to stabilize some junctions down to $R_N = 20\,k\Omega$, which is close to point contact at $R_0 = 1/G_0 = 12.9\,k\Omega$. The stability allowed us to realize measurements of up to $n = 100$ sweeps, which form the basis for our statistical evaluation, like the histogram in Fig. 9.1(b). For the evaluation of this large amount of data, we have automated the process with a peak detection algorithm written in Python. This algorithm determines the characteristic currents from the derivative of the $V(I)$ measurements. As both characteristic currents are subject to statistical broadening, the only way to increase the accuracy is by increasing the sample number $n$. Up to now the stability and therefore this number is limited by the drift and creep of the piezos. In order to minimize these effects, we let the STM settle for several hours after the tunnel contact is established to reach a state of equilibrium. Still, it remains a limiting factor that we have to retract the tip once a day to refill the 1 K pot with helium.

In Fig. 9.1(a) and Fig. 9.1(b) we were able to show that the measured current biased Josephson junctions follow the expected behavior. If we now take these two measurements on Pb(111) and Pb(110) to determine the switching current, we get from Fig. 9.1(a) at a resistance of $R_N = 113\,k\Omega$ a current of $I_S \approx 5\,nA$, and for Fig. 9.1(b) at a resistance of $R_N = 35\,k\Omega$ a current of $I_S \approx 2\,nA$. This does not satisfy the relation we expect between the normal state conductance and the switching current which is proportional to the critical Josephson current. According to the Ambegaokar-Baratoff relation, the critical current and the resistance should be inversely proportional to each other (see Eq. (2.61)). The surface orientation should not have a significant influence on this, because the crystal orientation does not play a decisive role in the superconducting order parameter. We rather assume that capacitive changes might contribute because we could observe that tip-formings and thus changes of the junction geometry affect the switching current as well.

For a closer look at the relationship between switching current and normal state resistance, we have done a distance-dependent measurement series on Pb(110), which is shown in Fig. 9.1(c). The measured data (blue curve) follow here an inverse proportionality as required by the Ambegaokar-Baratoff relation, demonstrated by the fit (orange curve) of the form $A/(x - x_0)$. However, the resulting amplitude $A$ with ~60 μV is orders of magnitude smaller than the value of $\pi\Delta/2e \approx 2\,mV$ expected from Eq. (2.61). We explain this deviation by our relatively large measurement temperature compared to the Josephson energy that determines the amplitude of the potential landscape. This has a direct influence on the thermally activated switching current. Furthermore, changes in the junction capacitance are also of importance, since these changes are reflected by the mass associated with the phase and thus also influence the thermal activation.

In summary, we are not able to compare absolute values of the switching current for different measurements between which the measurement conditions have changed due to variations in the tip or substrate. Also, we have seen that capacitive changes are likely to influence the switching current as different tip configurations alter the results. However, we can detect with the current-biased Josephson spectroscopy changes in the switching current within a measurement series.

## 9.2 Influence of Magnetic Impurities on the Critical Josephson Current

Next, we want to use the Josephson spectroscopy to study magnetic perturbations on superconductors and map their influence on the superconducting ground state. Similar measurements were attempted by Randeria *et al.* in the group of A. Yazdani [39]. They proposed a slightly different approach than ours. Without the use of an additional resistor, they work in the voltage-driven regime of the Josephson effect. Here, the Josephson effect is reflected as zero-bias differential conductance in the $\mathrm{d}I/\mathrm{d}V$ spectra (see Fig. 2.9(b) in Section 2.4). The critical current enters the differential conductance of the Josephson peak within the $P(E)$-theory together with other parameters like junction fluctuations and temperature. This makes qualitative statements about the critical current difficult and susceptible to co-influencing and one needs to take great care to obtain qualitatively meaningful results. In contrast, the advantage of the voltage-dependent measurement is that it is very effective for spatial mapping. This is possible with the STM's usual high spatial resolution. Using the voltage-biased spectroscopy, they were able to detect changes in the zero-bias differential conductance near Fe adatoms on a Pb(110) surface in a 20 mK STM [39]. They attribute these observations to possible changes in the critical current. They quantified this proposition by a $P(E)$-theory fit of single selected voltage biased Josephson spectra. Unfortunately, we were not able to form stable current-biased Josephson contacts above Fe adatoms on Pb(110) for a direct comparison of our current-biased approach to their results. Therefore we used again the Mn adatoms on Pb(111) to perform the first tests of the current-biased approach on magnetic impurities.

### Mn adatoms on Pb(111)

In this section, we want to apply the current-biased Josephson spectroscopy to investigate the critical current above Mn-adatom on the Pb(111) surface. We have established a procedure using current-biased Josephson spectroscopy to measure changes in the superconducting order parameter on the local scale by being sensitive to changes in the switching current. The YSR-states occurring in the spectra of the Mn adatoms on Pb(111) make a Josephson spectroscopy study interesting for investigating the influences of the Mn magnetic moment on the superconducting order parameter. In contrast to the previous chapters, we investigate the Mn atoms in the *down* adsorption side (see section 5.2). In this configuration, the

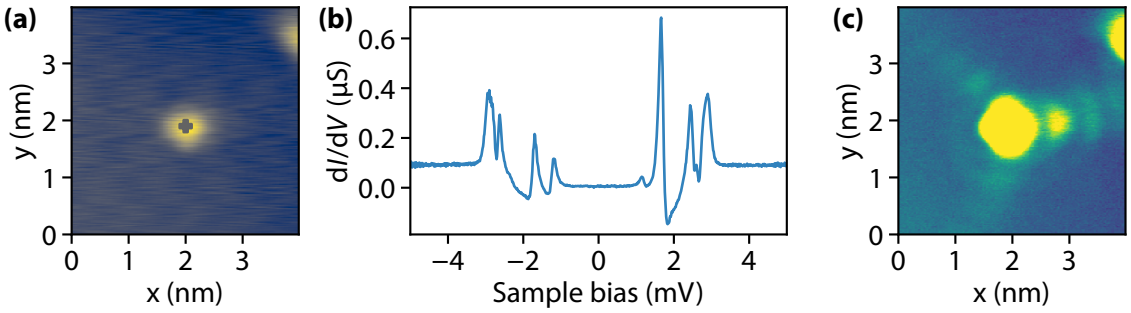


**Figure 9.2 | YSR states of $Mn_{down}$ atom on Pb(111). (a)** Topography of the $Mn_{down}$ adatom on the Pb(111) surface. Setpoint: $V_{Bias}$ = 6 mV, $I$ = 1 nA. **(b)** d$I$/d$V$ spectrum on top of the $Mn_{down}$ adatom. Several YSR states are visible as a result of the magnetic interaction with the superconductor. From the energetically lowest ones, the corresponding thermal peaks are visible at $e|V| < \Delta$ as well. Setpoint: $V_{Bias}$ = 6 mV, $I$ = 300 pA. **(c)** d$I$/d$V$ map of the YSR state at –1.6 mV. The topography from (a) was replayed while recording the d$I$/d$V$ signal. It can be seen that this state is most pronounced above the atom additionally also has oscillating long-range features with three-fold symmetry. This symmetry reflects the symmetry of the spin-carrying orbital. Accordingly, this long-range effect comes from the self-focusing of the scattering electrons on the corresponding Fermi surface.

interaction between the magnetic moment and the superconductor leads to five YSR states [161], seen in the d$I$/d$V$ spectrum in Fig. 9.2(b). The spectrum is taken above the center of the atom shown in Fig. 9.2(a). Just like the spectrum of the *up* configuration, the thermal replicas of the YSR states are shown at voltages $e|V| < \Delta$.

The YSR-states are not only detectable directly above the atoms but have a spatial extent. The distribution of the state at –1.6 mV is shown in Fig. 9.2(c) and was recorded using a d$I$/d$V$ multipass-measurement. In this measurement, the tip is moved along the surface contour lines by replaying the previously recorded topographic data while the d$I$/d$V$ signal is recorded. Thus no topographic effects are influencing the measurement but only those due to the magnetic interaction. The measurement demonstrates that this interaction propagates in oscillating beams along the surface. The beams exhibit a three-fold symmetry along with the three ⟨110⟩ directions. Thereby, the YSR state reflects the symmetry of the Mn $d$-levels, which are split by the surrounding crystal field [161]. The spatial extent can be explained by the self-focusing of scattered electrons perpendicular to the low-curvature regions of the Fermi surface [161]. The oscillations are expected to have a spacing of $2k_F$ which can be seen in the expression for the YSR wave function in Eq. (2.70). With this spacing, the structure can be explained by the coupling to the outer $p$-$d$-like Fermi-sheet of the two-band superconductor.

Having shown that magnetic interaction is indeed present, we can now apply the current-biased Josephson spectroscopy to map the magnetic interactions. We see a change in the switching current over the Mn atom (Fig. 9.3). A line-scan over the adatom (Fig. 9.3(b) at the *orange* positions marked in (a)) shows a reduction of up to 60 % in switching current.

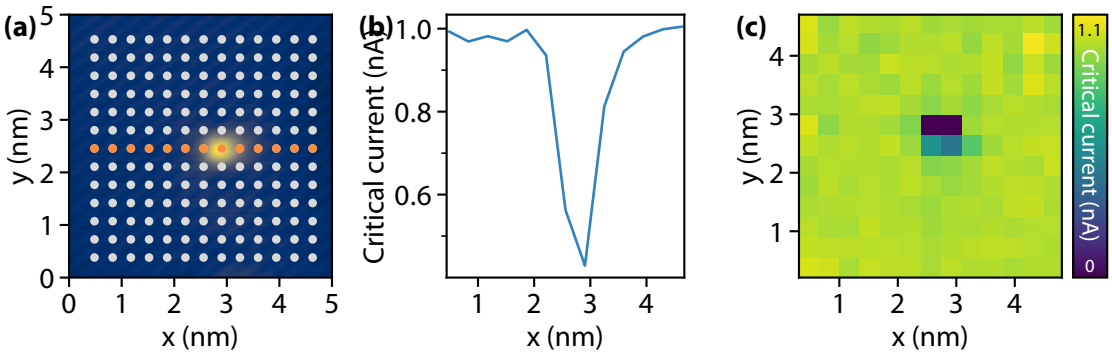


**Figure 9.3 | Mapping of the critical Josephson current of the $Mn_{down}$ adatoms. (a)** Topography of the Mn adatom with the corresponding markings of the measuring positions of the line spectrum (red crosses) and the spacial resolved color-map (complete set of crosses). Setpoint: $V_{Bias}$ = 10 mV, $I$ = 1 nA. **(b)** Line spectrum of the switching currents across the manganese adatom (at *orange* positions in (a)). A clear reduction of the switching current is visible. **(c)** Spacial resolved 2D color-map of the switching current (at grid positions in (a)). No long-range response is visible. For two measuring points, there were no step detectable at all in the $V(I)$ curves and we have manually set these points to zero. In (b) and (c) each data point is based on 60 sweeps of the current biased Josephson junction. Setpoint: $V_{Bias}$ = 10 mV, $I$ = 110 nA.

This large reduction is a strong indication that there has been a change in the superconducting order parameter. Thus we have successfully implemented a method to measure the magnetic influence on the superconducting ground state. A comparison with the signal changes in voltage-biased spectroscopy of Randeria *et al.* [39] shows a higher sensitivity of the technique we have established.

Finally, we want to use this sensitivity to investigate the spatial distribution of the switching current. Therefore we performed single current-biased measurements along the points of a grid covering the Mn atom, with the extracted switching currents shown in the 2D map in Fig. 9.3(c). The map again shows the clear drop of the switching current over the atom. Effects due to the self-focusing arms of the YSR state (see Fig. 9.2(c)) are not seen. Further development of the technique with more stable junctions, larger statistics, and faster measurement routines will hopefully increase the resolution of the technique in the future. It will then become apparent whether quantifiable statements about the scale on which the superconducting ground state changes are possible.

## 9.3 Conclusion

We showed in this chapter that Josephson spectroscopy can be used to study the superconducting ground state directly. This has not been possible using quasiparticle-spectra. We first established and tested the method on pristine Pb surfaces. Retrapping and switching current followed the expected reverse proportional behavior and could therefore be linked

to the critical current. However, we have seen that these currents are influenced by thermal and capacitive effects. We could demonstrate, that all of our junctions are underdamped. Finally, we were able to show a reduction of the switching currents above Mn adatoms on Pb(111), which suggests a reduction of the critical current.

In conclusion, we were able to successfully establish this technology and show its potential. The next direct step will be to increase the resolution. On the one hand, richer statistics would increase the spectral resolution and on the other hand, faster measurement routines would increase the spatial resolution by making finer maps less time-consuming. We expect the method will also be sensitive to non-magnetic influences, although this will need to be demonstrated in the course of future studies. Subsequently, it will be of interest to explore other superconducting systems. These include not only magnetic structures on classical superconductors but also the investigation of the order parameter in strongly coupled superconductors, high-temperature superconductors, and disordered superconductors.

# 10

# Conclusions and Outlook

In this thesis, we have successfully established two new spectroscopic methods to study the physics of YSR states. For this purpose, we mainly focused on the YSR states induced by the magnetic moment of Mn adatoms on a superconducting Pb surface. Using HF radiation and photon-assisted tunneling, we were able to learn more about the transport through these states. Using Josephson spectroscopy we were able to show the influence of the magnetic moment on the superconducting order parameter.

For the realization of these spectroscopic methods, we have worked out the specifications of a specially designed STM, put the new system into operation, and added coax cabling to shine high-frequency radiation in the range from 0.3 GHz to 40 GHz into the junction. This combination of STM with HF radiation required a sophisticated design and is one of the very latest technologies implemented in STMs. The main challenge here is to ensure that the STM is not restricted in its functionality by the installed HF cables. This is inherently difficult, as typical coaxial cables cannot simultaneously conduct high-frequency well while still being compatible with UHV, ultra-cold, and low-vibration conditions. Despite the many compromises that had to be made, we have succeeded in installing coaxial cables that exceed our requirements by far with an attenuation of 10 dB to 60 dB over the complete spectral range up tp 40 GHz. Especially the low attenuations for the upper part of the frequency range from 30 GHz to 40 GHz with an average attenuation of <20 dB is very good. This range is mostly no longer accessible in comparable realizations of HF radiations in STMs [131, 157] and its attenuation is more than two orders of magnitude smaller than their overall average attenuation. The access to this frequency range enabled us to perform the experiments on photon-assisted tunneling. In the course of our experiments we investigated different approaches to introduce the HF signal into the junction and found that, due to the lower electrical noise, the introduction over an antenna is superior to adding it to the tip line via a bias tee.

Next, we could use the HF radiation to study the transport processes through our junction by using photon-assisted tunneling. In this process, the tunneling electron can emit energy

to, or receive energy from the present photon field, whereby the effective density of states is split into sidebands accordingly by multiples of the photon energy. This splitting leads to V-shaped patterns. We have used the splitting to analyze our frequency response using the non-linearities in the current-voltage characteristic of the pristine superconductor-superconductor junctions. Subsequently, we could use these junctions as a reference system to determine the amount of absorbed and emitted photons from the sideband splitting using high-resolution spectroscopy as a function of the HF amplitude. This required our resolution of ~80 μeV of the superconducting tip and the highest possible frequencies in order to identify the individual processes in the splitting structures. From these splittings, we were able to extract the information about the tunnel processes as a multiple of the HF frequency per electron. We demonstrated this capability of resolving the individual processes at frequencies of 40 GHz using the three typical tunnel processes for pristine superconducting junctions: The tunneling of single electrons from the coherence peaks and the tunneling of Cooper pairs in the form of Andreev reflections and the Josephson effect. The resulting 2D maps provide direct information about the resulting sideband patterns.

This experimental method is further supported by simulations based on the simple Tien-Gordon model. With these simulations starting from the unperturbed density of states, we have succeeded in reproducing the experimental data in great detail. The combination of experiment and simulation has enabled us to implement an extremely sensitive measurement procedure. We could identify that quasiparticles form the charge carriers in the case of the coherence peaks and Cooper pairs in the Andreev reflections and the Josephson effect as expected. Although these are already known results, these measurements show that we can successfully irradiate the junction with HF radiation and illustrate the potential of photon-assisted tunneling.

A new aspect was the investigations on the splitting of the conductance through manganese induced YSR states also with a frequency of 40 GHz. Here we have exploited the tunability of the junction conductance over several orders of magnitude to specifically obtain insights into the contributions of resonant Andreev processes to subgap tunneling. As the tip approaches the Mn adatom, there is a change in the tunneling regime from predominantly single-electron tunneling to predominantly resonant Andreev tunneling through the YSR state. This can be described theoretically within a rate-based model. We have reworked this rate-based model under the very same assumption that Tien and Gordon used in their model, creating a rate-based model for describing the phonon-assisted current through subgap states. Central aspects of this theory are the independent sideband conditions for the tunneling of electrons and holes. They lead to two sets of sidebands whose relative distance in bias voltage depends on the ratio of subgap states energy to photon energy. Due to the asymmetry in the YSR wave functions, we see Y-shaped splittings instead of the typical V-shaped splittings as for the pristine junctions. This sideband spacing of the Y-shape indicated a single-electron process, contrary to our assumption of resonant Andreev processes. Using our rate-based model, we were able to simulate these sideband structures in all their details. We learned to interpret the Y-shaped structures as the result of the YSR wave-function asymmetry, meaning that one of the two tunneling processes

of the resonant Andreev reflection is rate-limiting and therefore dominating the splitting in its form. Thus, we found that the distance between the sidebars must be considered in connection with the shape in order to make reliable statements about the number of charge carriers. From the rate-based model, it can be derived that the observation of these photon-assisted sideband patterns of resonant Andreev reflections is determined by two constraints. First, the tunneling must be weak enough so that the tunneling-induced broadening is small compared to the sideband spacing so that it can be resolved well. At the same time, the resonant Andreev reflections require that the tunneling processes are fast compared to the inelastic relaxation processes. The latter leads to competing channels that conduct electrons into the quasiparticle continuum of the substrate and thus enable single-electron tunneling through the subgap state. We fulfill both of these requirements with high enough HF-frequencies and low enough temperatures to reduce the thermal excitations. Thus, photon-assisted tunneling not only shows us the number of electrons involved in the elementary tunneling processes but also helps us to understand the process of resonant Andreev tunneling and to determine the associated tunneling rates from the sideband patterns. These tunneling rates confirmed our understanding of the transition between single-electron tunneling and resonant Andreev tunneling during the increase of junction conductance.

Finally, we were able to establish and use Josephson spectroscopy to measure changes in the critical current of the Josephson effect above magnetic impurities. The detection of these changes cannot be achieved with traditional scanning tunneling spectroscopy using quasiparticles. By adding a 1 MΩ resistor we could perform current-biased measurements of the junction voltage. We succeeded in establishing stable Josephson contacts and we could observe that below a junction resistance of ~100 kΩ the Josephson steps are formed. From these steps, we were able to directly extract the switching and retrapping current. Both of these currents characterize the Josephson junction. They are statistically distributed and follow a hysteresis. We concluded, that we are dealing with underdamped junctions. We showed that the switching current reflects changes in the critical current. We used this to examine Mn atoms on Pb(111) and observe a reduction of the switching current above the atoms and therefore a reduction in critical current. This can be related to a change in the superconducting order parameter. The long-range spatial oscillations of the YSR-states could not be resolved by Josephson spectroscopy so far. We believe that this technique will not only be sensitive to magnetically induced changes but to changes in the superconducting ground state in general.

## Outlook: ESR-STM

After the successful demonstration of our ability to apply HF radiation into the STM junction, one of the next steps is the establishment of electron spin resonance (ESR). The combination of the ESR with the spatial resolution of STM holds great potential for locally resolved measurements of single localized spins, e.g. on adsorbates or lattice defects. This

opens up a whole spectrum of applications for the research of spintronics and quantum computing.

All previous successful implementations of an ESR-STM are based on the possibility of spin sensitive detection of currents. This requires spin-polarized tips that can measure the spin orientation by atomic-scale tunneling magnetoresistance. Baumann *et al.* [131] were the first to demonstrate this in an STM and also reported that without spin polarization they could not measure ESR signal. Without this spin contrast, it is not possible to detect the change in the population of split levels caused by the microwaves. Furthermore, an external magnetic field was used to show the shift in the ESR signal due to the changing Zeeman splitting.

To obtain spin contrast, a stable spin-polarized density of state at the tunneling apex is required [211]. One possibility to realize this is the vapor deposition of thin magnetic films on the tip. A common method is the coating with cobalt [212]. As a ferromagnetic material, cobalt retains the magnetization due to remanence. However, such films require an external magnetic field to maximize spin contrast by aligning the tip magnetization in the desired surface direction. Due to the malfunction of our magnetic field, this is not possible for our system.

Alternatives to this are antiferromagnetic materials. The advantage of these materials is that they have intrinsic spin polarization and a low stray field [213–215]. This allows the entire tip to be made of antiferromagnetic material without affecting the sample as is the case with large amounts of ferromagnetic material. A lot of research is focused on the use of Cr, but due to its fragility, it is quite difficult to prepare. A way that might be feasible for us has recently been demonstrated by Forrester *et al.* [216] with the use of commercially available $Mn_{88}Ni_{12}$ foil as a tip.

Another promising approach was recently shown by Willke *et al.* [217]. They have demonstrated that it is possible to achieve ESR without the use of an external magnetic field. They found that the local field of the tip was sufficient to perform ESR measurements without the need for an additional external magnetic field. This would make this method accessible to our existing STM systems.

### Outlook: Shapiro-Steps – a Majorana State Detector

Besides photon-assisted tunneling, the combination of the Josephson effect with HF-radiation leads to another effect, the so-called Shapiro steps. These are created when the phase dynamics of the *ac* Josephson effect is synchronous with the externally applied ac voltage or one of its multiples. Shapiro steps occur at voltages $V_n^{\mathrm{dc}} = n\hbar\Omega/2e$, as the phase is locked and thus becomes time-independent. When this happens, a *dc* supercurrent occurs at the corresponding voltages [77].

Shapiro steps can be used to identify Majorana fermions [218–220]. When Majorana fermions are present in the junction, there should be a transition from the conventional Josephson relation to an unconventional one: $I_s \propto \sin(\varphi) \rightarrow I_s \propto \sin(\varphi/2)$. Therefore the characteristic voltage in the *ac* Josephson effect should be doubled [219].

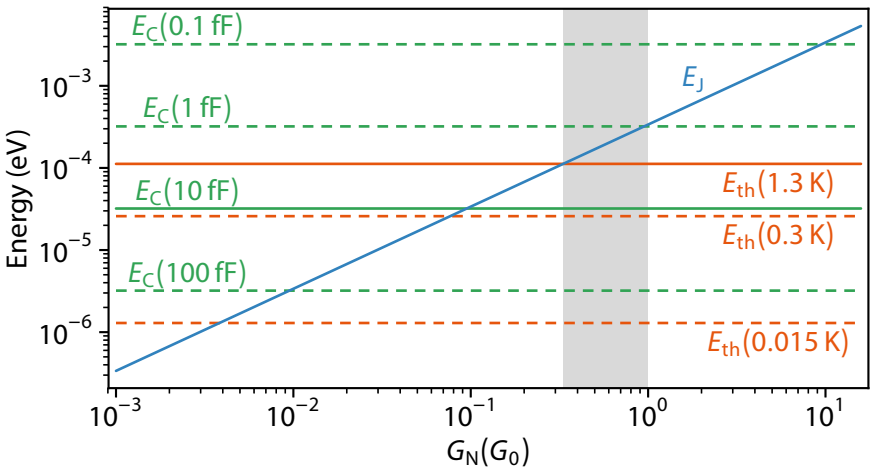


**Figure 10.1 | Comparison between Josephson, thermal, and charging energy.** Comparison of the Josephson energy (*blue*) as a function of the normal state conductance normalized to the conductance quantum $G_0$ with the thermal energy (*red*) and charging energy (*green*). For the latter two, different exemplary values are shown. The solid lines correspond to the realistic conditions for our junction. The *grey* conductance window outlined is the potential range in which the ratios between Josephson energy and thermal energy would allow coherent Cooper pair tunneling.

Shapiro steps can be distinguished from steps based on photon-assisted tunneling by their different behavior. For example, in the steps of the photon-assisted tunneling the square of the Bessel function is considered in its width, whereas in the Shapiro step of the same order the Bessel function is considered only linear. Unfortunately, we have not been able to observe Shapiro steps yet. We attribute this to the fact that due to either thermal fluctuations or the charging energy caused by the junction capacity, the coherence in the tunneling Cooper pair is destroyed when crossing the junction and we only detect sequential Cooper pair tunneling, as also reported by other groups for their STM junctions [189, 221]. An estimation of the energy scales involved is shown in Fig. 10.1. It becomes apparent that at our temperatures only a small conductance window is available so that on the one hand the thermal fluctuations do not destroy the coherence of the Cooper pairs and on the other hand the tip is not contacting the sample at $G_0$. Depending on the capacity of the junction the window closes completely. Further investigations are necessary where it is advisable to try to use larger tip diameter and blunt tip apexes to minimize the charging energy.

### Outlook: Identifying True Zero-Energy States by Photon-Assisted Tunneling

Resonant Andreev reflections are used to investigate presumed Majorana zero modes, [222, 223], for example in chains of magnetic adatoms on *s*-wave superconductors [28, 97, 224–227]. Photon-assisted tunneling can be used not only to determine the type of tunneling processes but also to distinguish true zero-energy states from states with a small but finite

energy $\epsilon_0$. Based on our experiments, we have focused our model on YSR states, although the approach is by no means specific to YSR states, but applies equally to other subgap states. In fact, finite energy states with electron and hole wave functions of the same order show splits due to the separated electron and hole thresholds. Because of their great multiplicity, this splitting should be detectable in the whole V-shaped region with high resolution [186].

## Resumé – The Long and Winding Road Towards Topological Quantum Computing

The presented results in this thesis illustrate the potential of two new spectroscopic methods to study subgap states in superconductors. These methods provided fundamental insights into the electronic and magnetic interactions between magnetic moments with superconductors. In particular, both of our established methods have potential applications in the identification of Majorana zero modes. Due to its spatial resolution, STM may play an important role in the research towards possible topological quantum states. However, it should be noted that the theoretical concepts are more mature than the experimental implementations. Even if the realization of Majorana zero modes in the STM has already been successful, it would first require the entanglement of at least two of them to generate a qubit. A lot of research is still needed to realize controlled bottom-up structures of such Majorana zero mode networks, and as always, STM will not be a platform to scale up applications due to its complexity. However, the methods presented by us may be helpful on the long road within basic research, so that someday user-suitable devices can be realized.

# A

# Appendix

## A.1 Determination of the Distances in the Internal Structure of the HF Induced Splittings

In Chapter 7 the spacing between the sidebands is determined, which arises from the splitting of all features in the $\mathrm{d}I/\mathrm{d}V$ spectra due to photon-assisted tunneling. This section describes how we determine these distances.

A first approach to determine the distances is based on the analysis of one single spectrum showing the splitting. Here the distances between the maxima can be determined directly. However, the variance is quite high when determining the maxima only from one individual spectrum since the sidebands do not reach their maximum at the same HF amplitude. To overcome this difficulty one can use the 2D color maps. In these, the maxima can be determined much better because the overall amplitude dependence can be used to locate the maxima within the splitting.

Also, the maxima are repeated with increasing HF amplitude. We use this to place vertical lines per eye through the maxima, as shown in Fig. A.1. The determination of the distances from the color maps allows us to minimize the spread as well as to determine at least twice as many maxima compared to the single spectra, where only every second maximum is formed. Both of these improvements lead to an increase in the accuracy of the statistics and thus to a reduction of the uncertainty of the extracted value.

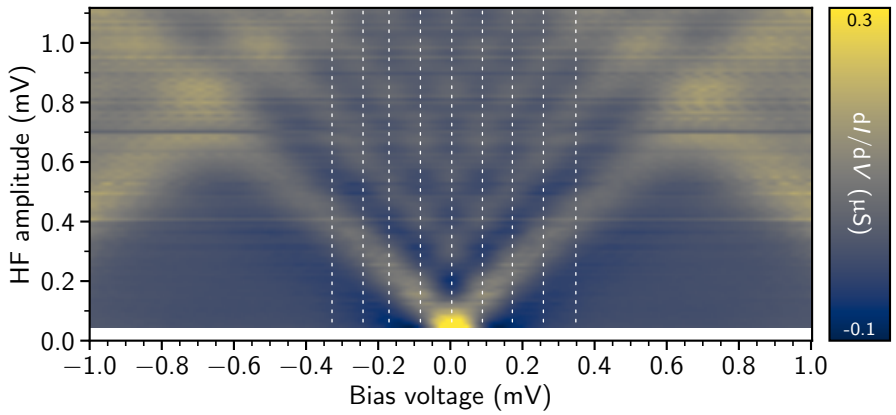


**Figure A.1 | Illustration of the determination of photon-sideband periodicities and their error margins.** Exemplarily, the determination is shown using the Josephson peak with HF radiation of 40 GHz (same data as in Fig. 7.2(a)). Vertical dashed lines are placed by eye along the lines of maximum intensity with increasing HF amplitude.

# References


[1] Benioff, P. The computer as a physical system: A microscopic quantum mechanical Hamiltonian model of computers as represented by Turing machines. *Journal of Statistical Physics* (1980).

[2] Benioff, P. Quantum mechanical hamiltonian models of turing machines. *Journal of Statistical Physics* (1982).

[3] Feynman, R. P. Simulating physics with computers. *International Journal of Theoretical Physics* (1982).

[4] Boixo, S., Isakov, S. V., Smelyanskiy, V. N., Babbush, R., Ding, N., Jiang, Z., Bremner, M. J., Martinis, J. M. & Neven, H. Characterizing quantum supremacy in near-term devices. *Nature Physics* **14,** 595–600 (2018).

[5] Pednault, E., Gunnels, J., Maslov, D. & Gambetta, J. *IBM Research Blog: On "Quantum Supremacy"* 2019.

[6] Gerjuoy, E. Shor's factoring algorithm and modern cryptography. An illustration of the capabilities inherent in quantum computers. *American Journal of Physics* **73,** 521–540 (2005).

[7] Mermin, N. D. *Breaking RSA Encryption with a Quantum Computer: Shor's Factoring Algorithm* in *LECTURE NOTES: ON QUANTUM COMPUTATION* (Cornell University, 2006).

[8] Rivest, R. L., Shamir, A. & Adleman, L. A method for obtaining digital signatures and public-key cryptosystems. *Communications of the ACM* **21,** 120–126 (1978).

[9] Grover, L. K. *A fast quantum mechanical algorithm for database search* in *Proceedings of the Annual ACM Symposium on Theory of Computing* (1996).

[10] Bennett, C. H., Bernstein, E., Brassard, G. & Vazirani, U. Strengths and weaknesses of quantum computing. *SIAM Journal on Computing* (1997).

[11] Ambainis, A. Quantum search algorithms. *ACM SIGACT News* **35,** 22–35 (2004).

[12] Georgescu, I. M., Ashhab, S. & Nori, F. Quantum simulation. *Reviews of Modern Physics* **86,** 153–185 (2014).

[13] Kelly, J. *A Preview of Bristlecone, Google's New Quantum Processor* 2018.

[14] Arute, F. *et al.* Quantum supremacy using a programmable superconducting processor. *Nature* **574,** 505–510 (2019).

[15] Cho, A. The biggest flipping challenge in quantum computing. *Science* (2020).

[16] Mooij, J. E., Orlando, T. P., Levitov, L., Tian, L., Van Der Wal, C. H. & Lloyd, S. Josephson persistent-current qubit. *Science* (1999).

[17] Nadj-Perge, S., Frolov, S. M., Bakkers, E. P. & Kouwenhoven, L. P. Spin-orbit qubit in a semiconductor nanowire. *Nature* (2010).

[18] Kielpinski, D., Meyer, V., Rowe, M. A., Sackett, C. A., Itano, W. M., Monroe, C. & Wineland, D. J. A decoherence-free quantum memory using trapped ions. *Science* (2001).

[19] Imamoglu, A., Awschalom, D. D., Burkard, G., DiVincenzo, D. P., Loss, D., Sherwin, M. & Small, A. Quantum information processing using quantum dot spins and cavity qed. *Physical Review Letters* **83,** 4204–4207 (1999).

[20] Anderlini, M., Lee, P. J., Brown, B. L., Sebby-Strabley, J., Phillips, W. D. & Porto, J. V. Controlled exchange interaction between pairs of neutral atoms in an optical lattice. *Nature* **448,** 452–456 (2007).

[21] Beenakker, C. W. Search for majorana fermions in superconductors. *Annual Review of Condensed Matter Physics* (2013).

[22] Vepsäläinen, A. P., Karamlou, A. H., Orrell, J. L., Dogra, A. S., Loer, B., Vasconcelos, F., Kim, D. K., Melville, A. J., Niedzielski, B. M., Yoder, J. L., Gustavsson, S., Formaggio, J. A., VanDevender, B. A. & Oliver, W. D. Impact of ionizing radiation on superconducting qubit coherence. *Nature* **584,** 551–556 (2020).

[23] Chiaverini, J., Leibfried, D., Schaetz, T., Barrett, M. D., Blakestad, R. B., Britton, J., Itano, W. M., Jost, J. D., Knill, E., Langer, C., Ozeri, R. & Wineland, D. J. Realization of quantum error correction. *Nature* (2004).

[24] Takahashi, S., Tupitsyn, I. S., Van Tol, J., Beedle, C. C., Hendrickson, D. N. & Stamp, P. C. Decoherence in crystals of quantum molecular magnets. *Nature* (2011).

[25] Freedman, M. H., Kitaev, A., Larsen, M. J. & Wang, Z. Topological quantum computation. *Bulletin of the American Mathematical Society* **40,** 31–38 (2003).

[26] Kitaev, A. Y. Fault-tolerant quantum computation by anyons. *Annals of Physics* (2003).

[27] Kitaev, A. Y. Unpaired Majorana fermions in quantum wires. *Physics Uspekhi* **44,** 131 (2001).

[28] Nadj-Perge, S., Drozdov, I. K., Li, J., Chen, H., Jeon, S., Seo, J., MacDonald, A. H., Bernevig, B. A. & Yazdani, A. Observation of Majorana fermions in ferromagnetic atomic chains on a superconductor. *Science* **346,** 602–607 (2014).

[29] Nadj-Perge, S., Drozdov, I. K., Bernevig, B. A. & Yazdani, A. Proposal for realizing Majorana fermions in chains of magnetic atoms on a superconductor. *Phys. Rev. B* **88,** 20407 (2013).

[30] Yu, L. U. H. Bound state in superconducors with paramagnetic impurities. *Acta Physica Sinica* **21,** 75–91 (1965).

[31] Shiba, H. Classical Spins in Superconductors. *Progress of Theoretical Physics* **40,** 435–451 (1968).

[32] Rusinov, A. I. On the theory of gapless superconductivity in alloys containing paramagnetic impurities. *Sov. Phys. JETP* **29,** 1101–1106 (1969).

[33] Sakurai, A. Comments on Superconductors with Magnetic Impurities. *Progress of Theoretical Physics* **44,** 1472–1476 (1970).

[34] Yazdani, A., Jones, B. A., Lutz, C. P., Crommie, M. F. & Eigler, D. M. Probing the local effects of magnetic impurities on superconductivity. *Science* **275,** 1767–1770 (1997).

[35] Heinrich, B. W., Pascual, J. I. & Franke, K. J. Single magnetic adsorbates on s-wave superconductors. *Progress in Surface Science* **93,** 1–19 (2017).

[36] Ji, S.-H., Zhang, T., Fu, Y.-S., Chen, X., Ma, X.-C., Li, J., Duan, W.-H., Jia, J.-F. & Xue, Q.-K. High-Resolution Scanning Tunneling Spectroscopy of Magnetic Impurity Induced Bound States in the Superconducting Gap of Pb Thin Films. *Physical Review Letters* **100,** 226801 (2008).

[37] Ruby, M., Pientka, F., Peng, Y., von Oppen, F., Heinrich, B. W. & Franke, K. J. End States and Subgap Structure in Proximity-Coupled Chains of Magnetic Adatoms. *Phys. Rev. Lett.* **115,** 197204 (2015).

[38] Albrecht, S. M., Hansen, E. B., Higginbotham, A. P., Kuemmeth, F., Jespersen, T. S., Nyg\aard, J., Krogstrup, P., Danon, J., Flensberg, K. & Marcus, C. M. Transport Signatures of Quasiparticle Poisoning in a Majorana Island. *Phys. Rev. Lett.* **118,** 137701 (2017).

[39] Randeria, M. T., Feldman, B. E., Drozdov, I. K. & Yazdani, A. Scanning Josephson spectroscopy on the atomic scale. *Physical Review B* **93,** 161115 (2016).

[40] Ménard, G. C., Guissart, S., Brun, C., Pons, S., Stolyarov, V. S., Debontridder, F., Leclerc, M. V., Janod, E., Cario, L., Roditchev, D., Simon, P. & Cren, T. Coherent long-range magnetic bound states in a superconductor. *Nature Phys.* **11,** 1013 (2015).

[41] Choi, D.-J., Rubio-Verdú, C., De Bruijckere, J., Ugeda, M. M., Lorente, N. & Pascual, J. I. Mapping the orbital structure of impurity bound states in a superconductor. *Nature Commun.* **8,** 15175 (2017).

[42] Dayem, A. H. & Martin, R. J. Quantum interaction of microwave radiation with tunneling between superconductors. *Physical Review Letters* **8,** 246–248 (1962).

[43] Rowell, J. M., Chynoweth, A. G. & Phillips, J. C. Multiphonon effects in tunnelling between metals and superconductors. *Physical Review Letters* **9,** 59–61 (1962).

[44] Chynoweth, A. G., Logan, R. A. & Thomas, D. E. Phonon-assisted tunneling in silicon and germanium Esaki junctions. *Physical Review* **125,** 877–881 (1962).

[45] Josephson, B. Possible new effects in superconductive tunnelling. *Physics Letters* **1,** 251–253 (1962).

[46] Naaman, O., Teizer, W. & Dynes, R. C. Fluctuation dominated josephson tunneling with a scanning tunneling microscope. *Physical Review Letters* **87** (2001).

[47] Bastiaans, K. M., Cho, D., Chatzopoulos, D., Leeuwenhoek, M., Koks, C. & Allan, M. P. Imaging doubled shot noise in a Josephson scanning tunneling microscope. *Physical Review B* (2019).

[48] Schrieffer, J. R., Scalapino, D. J. & Wilkins, J. W. Effective tunneling density of states in superconductors. *Physical Review Letters* **10,** 336–339 (1963).

[49] Taylor, B. N. & Burstein, E. Excess Currents in Electron Tunneling Between Superconductors. *Phys. Rev. Lett.* **10,** 14–17 (1963).

[50] Andreev, A. F. The thermal conductivity of the intermediate state in superconductors. *Sov. Phys. JETP* **19,** 1228 (1964).

[51] Ternes, M., Schneider, W.-D., Cuevas, J.-C., Lutz, C. P., Hirjibehedin, C. F. & Heinrich, A. J. Subgap structure in asymmetric superconducting tunnel junctions. *Phys. Rev. B* **74,** 132501 (2006).

[52] Tien, P. K. & Gordon, J. P. Multiphoton process observed in the interaction of microwave fields with the tunneling between superconductor films. *Physical Review* **129,** 647–651 (1963).

[53] Bardeen, J. Tunnelling from a Many-Particle Point of View. *Physical Review Letters* **6,** 57–59 (1961).

[54] Cohen, M. H., Falicov, L. M. & Phillips, J. C. Superconductive Tunneling. *Physical Review Letters* **8,** 316–318 (1962).

[55] Mahan, G. D. *Many-Particle Physics* (Springer US, Boston, MA, 2000).

[56] Wentzel, G. Eine Verallgemeinerung der Quantenbedingungen für die Zwecke der Wellenmechanik. *Zeitschrift für Physik* **38,** 518–529 (1926).

[57] Kramers, H. A. Wellenmechanik und halbzahlige Quantisierung. *Zeitschrift für Physik* **39,** 828–840 (1926).

[58] Brillouin, L. La mécanique ondulatoire de Schrödinger; une méthode générale de resolution par approximations successives. *Compt. Rend. Hebd. Seances Acad. Sci.* **183,** 24–26 (1926).

[59] Lang, N. D. Spectroscopy of single atoms in the scanning tunneling microscope. *Physical Review B* **34,** 5947–5950 (1986).

[60] Selloni, A., Carnevali, P., Tosatti, E. & Chen, C. D. Voltage-dependent scanning-tunneling microscopy of a crystal surface: Graphite. *Physical Review B* **31,** 2602–2605 (1985).

[61] Bruus, H. & Flensberg, K. *Many-Body Quantum Theory in Condensed Matter Physics* (Oxford University Press, United Kingdom, 2004).

[62] Jishi, R. A. *Feynman diagram techniques in condensed matter physics* (Cambridge University Press, United Kingdom, 2011).

[63] Feynman, R. P. The Theory of Positrons. *Physical Review* **76,** 749–759 (1949).

[64] Feynman, R. P. Space-Time Approach to Quantum Electrodynamics. *Physical Review* **76,** 769–789 (1949).

[65] Dyson, F. J. The Radiation Theories of Tomonaga, Schwinger, and Feynman. *Physical Review* **75,** 486–502 (1949).

[66] Dyson, F. J. The S matrix in quantum electrodynamics. *Physical Review* **75,** 1736–1755 (1949).

[67] Onnes, H. K. The superconductivity of mercury. *Comm. Phys. Lab. Univ. Leiden* **122,** 124 (1911).

[68] Maxwell, E. Isotope Effect in the Superconductivity of Mercury. *Physical Review* **78,** 477 (1950).

[69] Reynolds, C. A., Serin, B., Wright, W. H. & Nesbitt, L. B. Superconductivity of Isotopes of Mercury. *Physical Review* **78,** 487 (1950).

[70] Ginzburg, V. L. & Landau, L. D. No Title. *Zh. Eksp. Teor. Fiz.* **20,** 1064 (1950).

[71] Bardeen, J., Cooper, L. N. & Schrieffer, J. R. Theory of Superconductivity. *Physical Review* **108,** 1175–1204 (1957).

[72] Cooper, L. N. Bound Electron Pairs in a Degenerate Fermi Gas. *Physical Review* **104,** 1189–1190 (1956).

[73] Bednorz, J. G. & Müller, K. A. Possible high Tc superconductivity in the Ba-La-Cu-O system. *Zeitschrift für Physik B Condensed Matter* **64,** 189–193 (1986).

[74] Lindley, D. Landmarks: Superconductivity Explained. *Focus* **18,** 8 (2006).

[75] Fröhlich, H. Theory of the Superconducting State. I. The Ground State at the Absolute Zero of Temperature. *Physical Review* **79,** 845–856 (1950).

[76] Ruby, M. *Electron Momentum Anisotropy investigated by Superconductivity* PhD thesis (Freie Universität Berlin, 2012).

[77] Tinkham, M. *Introduction to Superconductivity: Second Edition* (Dover Publications, 2004).

[78] Bogoliubov, N. N. On a new method in the theory of superconductivity. *Nuovo Cimento* **7,** 794 (1958).

[79] Valatin, J. G. Comments on the theory of superconductivity. *Nuovo Cimento* **7,** 843 (1958).

[80] Nambu, Y. Quasi-Particles and Gauge Invariance in the Theory of Superconductivity. *Physical Review* **117,** 648–663 (1960).

[81] Balatsky, A. V., Vekhter, I. & Zhu, J.-X. Impurity-induced states in conventional and unconventional superconductors. *Reviews of Modern Physics* **78,** 373–433 (2006).

[82] Von Oppen, F., Peng, Y. & Pientka, F. *Topological superconducting phases in one dimension* in *Topological Aspects of Condensed Matter Physics* 387–450 (Oxford University Press, 2017).

[83] Josephson, B. D. Coupled superconductors. *Reviews of Modern Physics* **36,** 216–220 (1964).

[84] Gross, R. *Physics of the Josephson Junction: The Voltage State* in *Lecture Notes; Applied Superconductivity: Josephson Effect and Superconducting Electronics* 89–151 (Walther-Meissner Institut & TU Munich, 2005).

[85] Ambegaokar, V. & Baratoff, A. Tunneling Between Superconductors. *Physical Review Letters* **11,** 104–104 (1963).

[86] Falci, G., Bubanja, V. & Schön, G. Quasiparticle and Cooper pair tunneling in small capacitance Josephson junctions - Effects of the electromagnetic environment. *Zeitschrift für Physik B Condensed Matter* **85,** 451–458 (1991).

[87] Ingold, G.-L. & Nazarov, Y. V. *Charge Tunneling Rates in Ultrasmall Junctions* in *Single Charge Tunneling* (eds Grabert, H. & Devoret, M. H.) 21–107 (Plenum Press, New York, 1992).

[88] Timm, C. *Theory of Superconductivity (Lecture Notes)* (Institute of Theoretical Physics, TU Dresden, Dresden, 2011).

[89] Blonder, G. E., Tinkham, M. & Klapwijk, T. M. Transition from metallic to tunneling regimes in superconducting microconstrictions: Excess current, charge imbalance, and supercurrent conversion. *Physical Review B* **25,** 4515–4532 (1982).

[90] Yazdani, A., Howald, C. M., Lutz, C. P., Kapitulnik, A. & Eigler, D. M. Impurity-induced bound excitations on the surface of Bi2Sr2CaCu2O8. *Physical Review Letters* **83,** 176–179 (1999).

[91] Hudson, E. W., Pan, S. H., Gupta, A. K., Ng, K. W. & Davis, J. C. Atomic-scale quasi-particle scattering resonances in Bi2Sr2CaCu2O(8+$\delta$). *Science* **285,** 88–91 (1999).

[92] Hudson, E. W., Lang, K. M., Madhavan, V., Pan, S. H., Eisaki, H., Uchida, S. & Davis, J. C. Interplay of magnetism and high-Tc superconductivity at individual Ni impurity atoms in Bi2Sr2CaCu2O8+$\delta$. *Nature* **411,** 920–924 (2001).

[93] Ji, S.-H., Zhang, T., Fu, Y.-S., Chen, X., Jia, J.-F., Xue, Q.-K. & Ma, X.-C. Application of magnetic atom induced bound states in superconducting gap for chemical identification of single magnetic atoms. *Applied Physics Letters* **96,** 073113 (2010).

[94] Maki, K. *Gapless Superconductvity* in *Superconductivity: In Two Parts* (ed Parks, R. D. (Dekker, N. Y.) chap. 18 (1969).

[95] Farinacci, L., Ahmadi, G., Reecht, G., Ruby, M., Bogdanoff, N., Peters, O., Heinrich, B. W., von Oppen, F. & Franke, K. J. Tuning the Coupling of an Individual Magnetic Impurity to a Superconductor: Quantum Phase Transition and Transport. *Physical Review Letters* **121,** 196803 (2018).

[96] Maki, K. Motion of the vortex lattice in a dirty type II superconductor. *Journal of Low Temperature Physics* **1,** 45–58 (1969).

[97] Ruby, M., Pientka, F., Peng, Y., von Oppen, F., Heinrich, B. W. & Franke, K. J. Tunneling Processes into Localized Subgap States in Superconductors. *Physical Review Letters* **115,** 087001 (2015).

[98] Binnig, G., Rohrer, H., Gerber, C. & Weibel, E. Tunneling through a controllable vacuum gap. *Applied Physics Letters* **40,** 178–180 (1982).

[99] Binnig, G., Rohrer, H., Gerber, C. & Weibel, E. Surface Studies by Scanning Tunneling Microscopy. *Physical Review Letters* **49,** 57–61 (1982).

[100] Madhavan, V., Chen, W., Jamneala, T., Crommie, M. F. & Wingreen, N. S. Tunneling into a single magnetic atom: Spectroscopic evidence of the Kondo resonance. *Science* (1998).

[101] Gambardella, P., Rusponi, S., Veronese, M., Dhesi, S. S., Grazioli, C., Dallmeyer, A., Cabria, I., Zeller, R., Dederichs, P. H., Kern, K., Carbone, C. & Brune, H. Giant magnetic anisotropy of single cobalt atoms and nanoparticles. *Science* **300,** 1130–3 (2003).

[102] Otte, A. F., Ternes, M., von Bergmann, K., Loth, S., Brune, H., Lutz, C. P., Hirjibehedin, C. F. & Heinrich, A. J. The role of magnetic anisotropy in the Kondo effect. *Nature Physics* **4,** 847–850 (2008).

[103] Repp, J., Meyer, G., Stojković, S. M., Gourdon, A. & Joachim, C. Molecules on insulating films: Scanning-tunneling microscopy imaging of individual molecular orbitals. *Physical Review Letters* (2005).

[104] Repp, J. Imaging Bond Formation Between a Gold Atom and Pentacene on an Insulating Surface. *Science* **312,** 1196–1199 (2006).

[105] Donati, F., Dubout, Q., Autès, G., Patthey, F., Calleja, F., Gambardella, P., Yazyev, O. V. & Brune, H. Magnetic moment and anisotropy of individual Co atoms on graphene. *Physical Review Letters* (2013).

[106] Hirjibehedin, C. F., Lin, C.-Y., Otte, A. F., Ternes, M., Lutz, C. P., Jones, B. A. & Heinrich, A. J. Large magnetic anisotropy of a single atomic spin embedded in a surface molecular network. *Science* **317,** 1199–203 (2007).

[107] Bartels, L., Meyer, G. & Rieder, K.-H. Basic Steps of Lateral Manipulation of Single Atoms and Diatomic Clusters with a Scanning Tunneling Microscope Tip. *Physical Review Letters* **79,** 697–700 (1997).

[108] Otte, A. F., Ternes, M., Loth, S., Lutz, C. P., Hirjibehedin, C. F. & Heinrich, A. J. Spin excitations of a kondo-screened atom coupled to a second magnetic atom. *Physical Review Letters* (2009).

[109] Loth, S., Baumann, S., Lutz, C. P., Eigler, D. M. & Heinrich, A. J. Bistability in atomic-scale antiferromagnets. *Science* **335,** 196–199 (2012).

[110] Stipe, B. C., Rezaei, M. A. & Ho, W. Single-molecule vibrational spectroscopy and microscopy. *Science* (1998).

[111] Stipe, B. C., Rezaei, M. A. & Ho, W. Localization of Inelastic Tunneling and the Determination of Atomic-Scale Structure with Chemical Specificity. *Physical Review Letters* **82,** 1724–1727 (1999).

[112] Qiu, X. H., Nazin, G. V. & Ho, W. Vibronic States in Single Molecule Electron Transport. *Physical Review Letters* **92,** 206102 (2004).

[113] Franke, K. J. & Pascual, J. I. Effects of electron–vibration coupling in transport through single molecules. *Journal of Physics: Condensed Matter* **24,** 394002 (2012).

[114] Tsukahara, N., Noto, K.-I., Ohara, M., Shiraki, S., Takagi, N., Takata, Y., Miyawaki, J., Taguchi, M., Chainani, A., Shin, S. & Kawai, M. Adsorption-induced switching of magnetic anisotropy in a single iron(II) phthalocyanine molecule on an oxidized Cu(110) surface. *Physical review letters* **102,** 167203 (2009).

[115] Grobis, M., Khoo, K. H., Yamachika, R., Lu, X., Nagaoka, K., Louie, S. G., Crommie, M. F., Kato, H. & Shinohara, H. Spatially dependent inelastic tunneling in a single metallofullerene. *Physical Review Letters* (2005).

[116] Lee, J., Fujita, K., McElroy, K., Slezak, J. A., Wang, M., Aiura, Y., Bando, H., Ishikado, M., Masui, T., Zhu, J.-X., Balatsky, A. V., Eisaki, H., Uchida, S. & Davis, J. C. Interplay of electron–lattice interactions and superconductivity in Bi2Sr2CaCu2O8+$\delta$. *Nature* **442,** 546–550 (2006).

[117] Gawronski, H., Mehlhorn, M. & Morgenstern, K. Imaging phonon excitation with atomic resolution. *Science* (2008).

[118] Lee, H. J. & Ho, W. Single-bond formation and characterization with a scanning tunneling microscope. *Science* (1999).

[119] Lauhon, L. J. & Ho, W. Control and characterization of a multistep unimolecular reaction. *Physical Review Letters* (2000).

[120] Kim, Y., Komeda, T. & Kawai, M. Single-Molecule Reaction and Characterization by Vibrational Excitation. *Physical Review Letters* (2002).

[121] Komeda, T., Kim, Y., Kawai, M., Persson, B. N. & Ueba, H. Lateral hopping of molecules induced by excitation of internal vibration mode. *Science* (2002).

[122] Heinrich, A. J., Gupta, J. A., Lutz, C. P. & Eigler, D. M. Single-atom spin-flip spectroscopy. *Science* **306,** 466–9 (2004).

[123] Loth, S., Etzkorn, M., Lutz, C. P., Eigler, D. M. & Heinrich, A. J. Measurement of Fast Electron Spin Relaxation Times with Atomic Resolution. *Science* **329,** 1628–1630 (2010).

[124] Shirato, N., Cummings, M., Kersell, H., Li, Y., Stripe, B., Rosenmann, D., Hla, S. W. & Rose, V. Elemental fingerprinting of materials with sensitivity at the atomic limit. *Nano Letters* (2014).

[125] Birk, H., de Jong, M. J. M. & Schönenberger, C. Shot-Noise Suppression in the Single-Electron Tunneling Regime. *Physical Review Letters* **75,** 1610–1613 (1995).

[126] Herz, M., Bouvron, S., Ćavar, E., Fonin, M., Belzig, W. & Scheer, E. Fundamental quantum noise mapping with tunnelling microscopes tested at surface structures of subatomic lateral size. *Nanoscale* **5,** 9978 (2013).

[127] Burtzlaff, A., Weismann, A., Brandbyge, M. & Berndt, R. Shot noise as a probe of spin-polarized transport through single atoms. *Physical Review Letters* (2015).

[128] Cocker, T. L., Jelic, V., Gupta, M., Molesky, S. J., Burgess, J. A., Reyes, G. D. L., Titova, L. V., Tsui, Y. Y., Freeman, M. R. & Hegmann, F. A. An ultrafast terahertz scanning tunnelling microscope. *Nature Photonics* (2013).

[129] Cocker, T. L., Peller, D., Yu, P., Repp, J. & Huber, R. Tracking the ultrafast motion of a single molecule by femtosecond orbital imaging. *Nature* (2016).

[130] Peller, D., Kastner, L. Z., Buchner, T., Roelcke, C., Albrecht, F., Moll, N., Huber, R. & Repp, J. Sub-cycle atomic-scale forces coherently control a single-molecule switch. *Nature* **585,** 58–62 (2020).

[131] Baumann, S., Paul, W., Choi, T., Lutz, C. P., Ardavan, A. & Heinrich, A. J. Electron paramagnetic resonance of individual atoms on a surface. *Science* **350,** 417–420 (2015).

[132] Paul, W., Baumann, S., Lutz, C. P. & Heinrich, A. J. Generation of constant-amplitude radio-frequency sweeps at a tunnel junction for spin resonance STM. *Review of Scientific Instruments* (2016).

[133] Yang, K., Bae, Y., Paul, W., Natterer, F. D., Willke, P., Lado, J. L., Ferrón, A., Choi, T., Fernández-Rossier, J., Heinrich, A. J. & Lutz, C. P. Engineering the Eigenstates of Coupled Spin- 1/2 Atoms on a Surface. *Physical Review Letters* **119,** 227206 (2017).

[134] Yang, K., Willke, P., Bae, Y., Ferrón, A., Lado, J. L., Ardavan, A., Fernández-Rossier, J., Heinrich, A. J. & Lutz, C. P. Electrically controlled nuclear polarization of individual atoms. *Nature Nanotechnology* **13,** 1120–1125 (2018).

[135] Bae, Y., Yang, K., Willke, P., Choi, T., Heinrich, A. J. & Lutz, C. P. Enhanced quantum coherence in exchange coupled spins via singlet-triplet transitions. *Science Advances* **4,** eaau4159 (2018).

[136] Willke, P., Bae, Y., Yang, K., Lado, J. L., Ferrón, A., Choi, T., Ardavan, A., Fernández-Rossier, J., Heinrich, A. J. & Lutz, C. P. Hyperfine interaction of individual atoms on a surface. *Science* **362,** 336–339 (2018).

[137] Tobias R. Umbach. *Magnetic and Electronic Properties of Supermolecular Architectures on Metal Surfaces* PhD thesis (Freie Universität Berlin, 2013).

[138] Zandvliet, H. J. & van Houselt, A. Scanning Tunneling Spectroscopy. *Annual Review of Analytical Chemistry* **2,** 37–55 (2009).

[139] Tersoff, J. & Hamann, D. R. Theory and Application for the Scanning Tunneling Microscope. *Physical Review Letters* **50,** 1998–2001 (1983).

[140] Buisset, J. *Tieftemperatur Rastertunnelmikroskopie : Entwicklung eines hochstabilen Gerätekonzepts zur Untersuchung dynamischer Oberflächenprozesse und zur Analyse und Handhabung einzelner Atome und Moleküle zwischen 4 und 300 Kelvin* PhD thesis (Technische Universität, Wissenschaft und Technik Verlag, Berlin, 1996).

[141] Heinrich, B. W., Braun, L., Pascual, J. I. & Franke, K. J. Protection of excited spin states by a superconducting energy gap. *Nature Physics* **9,** 765–768 (2013).

[142] Wiesendanger, R. *Scanning Probe Microscopy and Spectroscopy: Methods and Applications* (Cambridge University Press, 1994).

[143] *Application Notes 3: About Lock-In Amplifiers* (Stanford Research Systems, Inc., Sunnyvale, CA, USA, 2004).

[144] Fernández Torrente, I. *Local spectroscopy of bi-molecular assemblies: screening, charge transfer, and magnetism at the molecular scale* PhD thesis (Freie Universität Berlin, 2008).

[145] *Principles of lock-in detectionand the state of the art* Zürich, Schweiz, 2016.

[146] Klein, J., Léger, A., Belin, M., Défourneau, D. & Sangster, M. J. L. Inelastic-Electron-Tunneling Spectroscopy of Metal-Insulator-Metal Junctions. *Physical Review B* **7,** 2336–2348 (1973).

[147] Kröger, J., Limot, L., Jensen, H., Berndt, R., Crampin, S. & Pehlke, E. Surface state electron dynamics of clean and adsorbate-covered metal surfaces studied with the scanning tunnelling microscope. *Progress in Surface Science* **80,** 26–48 (2005).

[148] Singh, U. R., Enayat, M., White, S. C. & Wahl, P. Construction and performance of a dilution-refrigerator based spectroscopic-imaging scanning tunneling microscope. *Review of Scientific Instruments* **84,** 013708 (2013).

[149] Pan, S. H., Hudson, E. W. & Davis, J. C. 3He refrigerator based very low temperature scanning tunneling microscope. *Review of Scientific Instruments* **70,** 1459–1463 (1999).

[150] Drevniok, B., Paul, W. M. P., Hairsine, K. R. & McLean, A. B. Methods and instrumentation for piezoelectric motors. *Review of Scientific Instruments* **83,** 033706 (2012).

[151] Charifoulline, Z. Residual Resistivity Ratio (RRR) Measurements of LHC Superconducting NbTi Cable Strands. *IEEE Transactions on Applied Superconductivity* **16,** 1188–1191 (2006).

[152] Berlincourt, T. G. Emergence of NbTi as supermagnet material. *Cryogenics* **27,** 283–289 (1987).

[153] Brittles, G. D., Mousavi, T., Grovenor, C. R. M., Aksoy, C. & Speller, S. C. Persistent current joints between technological superconductors. *Superconductor Science and Technology* **28,** 093001 (2015).

[154] Halbritter, J. On the oxidation and on the superconductivity of niobium. *Applied Physics A Solids and Surfaces* **43,** 1–28 (1987).

[155] Aspart, A. & Antoine, C. Study of the chemical behavior of hydrofluoric, nitric and sulfuric acids mixtures applied to niobium polishing. *Applied Surface Science* **227,** 17–29 (2004).

[156] Liu, J., Cheng, J. & Wang, Q. Evaluation of NbTi superconducting joints for 400 MHz NMR magnet. *IEEE Transactions on Applied Superconductivity* (2013).

[157] Natterer, F. D., Patthey, F., Bilgeri, T., Forrester, P. R., Weiss, N. & Brune, H. Upgrade of a low-temperature scanning tunneling microscope for electron-spin resonance. *Review of Scientific Instruments* **90,** 013706 (2019).

[158] Friedlein, J., Harm, J., Lindner, P., Bargsten, L., Bazarnik, M., Krause, S. & Wiesendanger, R. A radio-frequency spin-polarized scanning tunneling microscope. *Rev. Sci. Instrum.* **90,** 123705 (2019).

[159] Seifert, T. S., Kovarik, S., Nistor, C., Persichetti, L., Stepanow, S. & Gambardella, P. Single-atom electron paramagnetic resonance in a scanning tunneling microscope driven by a radio-frequency antenna at 4 K. *Phys. Rev. Research* **2,** 13032 (2020).

[160] Ruby, M., Heinrich, B. W., Pascual, J. I. & Franke, K. J. Experimental Demonstration of a Two-Band Superconducting State for Lead Using Scanning Tunneling Spectroscopy. *Physical Review Letters* **114,** 157001 (2015).

[161] Ruby, M., Peng, Y., von Oppen, F., Heinrich, B. W. & Franke, K. J. Orbital Picture of Yu-Shiba-Rusinov Multiplets. *Physical Review Letters* **117,** 186801 (2016).

[162] Ruby, M., Heinrich, B. W., Peng, Y., von Oppen, F. & Franke, K. J. Wave-function hybridization in Yu-Shiba-Rusinov dimers. *Physical Review Letters* (2018).

[163] Franke, K. J., Schulze, G. & Pascual, J. I. Competition of superconducting phenomena and Kondo screening at the nanoscale. *Science* **332,** 940–944 (2011).

[164] Bauer, J., Pascual, J. I. & Franke, K. J. Microscopic resolution of the interplay of Kondo screening and superconducting pairing: Mn-phthalocyanine molecules adsorbed on superconducting Pb(111). *Physical Review B - Condensed Matter and Materials Physics* **87,** 75125 (2013).

[165] Heinrich, B. W., Braun, L., Pascual, J. I. & Franke, K. J. Tuning the Magnetic Anisotropy of Single Molecules. *Nano Letters* **15,** 4024–4028 (2015).

[166] Hatter, N., Heinrich, B. W., Ruby, M., Pascual, J. I. & Franke, K. J. Magnetic anisotropy in Shiba bound states across a quantum phase transition. *Nature Communications* **6,** 8988 (2015).

[167] Hatter, N., Heinrich, B. W., Rolf, D. & Franke, K. J. Scaling of Yu-Shiba-Rusinov energies in the weak-coupling Kondo regime. *Nature Communications* (2017).

[168] Ruby, M., Heinrich, B. W., Peng, Y., von Oppen, F. & Franke, K. J. Exploring a Proximity-Coupled Co Chain on Pb(110) as a Possible Majorana Platform. *Nano Lett.* **17,** 4473–4477 (2017).

[169] Buckel, W. & Kleiner, R. *Supraleitung* (Wiley-VCH Verlag GmbH & Co. KGaA, Weinheim, Germany, 2012).

[170] Dynes, R. C., Narayanamurti, V. & Garno, J. P. Direct measurement of quasiparticle-lifetime broadening in a strong-coupled superconductor. *Physical Review Letters* **41,** 1509–1512 (1978).

[171] Jaworski, F., Parker, W. H. & Kaplan, S. B. Quasiparticle and phonon lifetimes in superconducting Pb films. *Physical Review B* **14,** 4209–4212 (1976).

[172] Mikhailovsky, A., Shulga, S., Karakozov, A., Dolgov, O. & Maksimov, E. Thermal pair-breaking in superconductors with strong electron-phonon interaction. *Solid State Communications* **80,** 511–515 (1991).

[173] Herman, F. & Hlubina, R. Microscopic interpretation of the Dynes formula for the tunneling density of states. *Physical Review B* **94,** 144508 (2016).

[174] Szabó, P., Samuely, T., Hašková, V., Kačmarčík, J., Žemlička, M., Grajcar, M., Rodrigo, J. G. & Samuely, P. Fermionic scenario for the destruction of superconductivity in ultrathin MoC films evidenced by STM measurements. *Physical Review B* **93,** 014505 (2016).

[175] White, A. E., Dynes, R. C. & Garno, J. P. Destruction of superconductivity in quench-condensed two-dimensional films. *Physical Review B* (1986).

[176] Sherman, D., Pracht, U. S., Gorshunov, B., Poran, S., Jesudasan, J., Chand, M., Raychaudhuri, P., Swanson, M., Trivedi, N., Auerbach, A., Scheffler, M., Frydman, A. & Dressel, M. The Higgs mode in disordered superconductors close to a quantum phase transition. *Nature Physics* **11,** 188–192 (2015).

[177] Abrikosov, A. A. & Gorkov, L. P. On the Problem of the Knight Shift in Superconductors. *Sov. Phys. JETP* **12,** 337 (1961).

[178] Feigel'man, M. V. & Skvortsov, M. A. Universal Broadening of the Bardeen-Cooper-Schrieffer Coherence Peak of Disordered Superconducting Films. *Physical Review Letters* **109,** 147002 (2012).

[179] Giaever, I., Hart, H. R. & Megerle, K. Tunneling into superconductors at temperatures below 1°K. *Physical Review* **126,** 941–948 (1962).

[180] Rowell, J. M., Anderson, P. W. & Thomas, D. E. Image of the phonon spectrum in the tunneling characteristic between superconductors. *Physical Review Letters* **10,** 334–336 (1963).

[181] Floris, A., Sanna, A., Massidda, S. & Gross, E. K. Two-band superconductivity in Pb from ab initio calculations. *Physical Review B - Condensed Matter and Materials Physics* (2007).

[182] Choy, T. S., Naset, J., Hershfield, S., Stanton, C. & Chen, J. A Database of Fermi Surfaces in Virtual Reality Modeling Language. *Bull. Am. Phys. Soc.* **45** (2000).

[183] Sklyadneva, I. Y., Heid, R., Echenique, P. M., Bohnen, K. B. & Chulkov, E. V. Electron-phonon interaction in bulk Pb: Beyond the Fermi surface. *Physical Review B - Condensed Matter and Materials Physics* (2012).

[184] Martin, I. & Mozyrsky, D. Nonequilibrium theory of tunneling into a localized state in a superconductor. *Physical Review B* **90,** 100508 (2014).

[185] Kozorezov, A. G., Golubov, A. A., Wigmore, J. K., Martin, D., Verhoeve, P., Hijmering, R. A. & Jerjen, I. Inelastic scattering of quasiparticles in a superconductor with magnetic impurities. *Physical Review B* **78,** 174501 (2008).

[186] González, S. A., Melischek, L., Peters, O., Flensberg, K., Franke, K. J. & von Oppen, F. Photon-assisted resonant Andreev reflections: Yu-Shiba-Rusinov and Majorana states. *Physical Review B* **102,** 045413 (2020).

[187] Peters, O., Bogdanoff, N., Acero González, S., Melischek, L., Simon, J. R., Reecht, G., Winkelmann, C. B., von Oppen, F. & Franke, K. J. Resonant Andreev reflections probed by photon-assisted tunnelling at the atomic scale. *Nature Physics* (2020).

[188] Zimmermann, U. & Keck, K. Multiple Andreev-reflection in superconducting weak-links in the interaction with external microwave-fields. *Zeitschrift für Physik B Condensed Matter* **101,** 555–560 (1996).

[189] Roychowdhury, A., Dreyer, M., Anderson, J. R., Lobb, C. J. & Wellstood, F. C. Microwave photon-assisted incoherent cooper-pair tunneling in a Josephson STM. *Physical Review Applied* **4** (2015).

[190] Kot, P., Drost, R., Uhl, M., Ankerhold, J., Cuevas, J. C. & Ast, C. R. Microwave-assisted tunneling and interference effects in superconducting junctions under fast driving signals. *Physical Review B* **101,** 134507 (2020).

[191] Sacépé, B., Dubouchet, T., Chapelier, C., Sanquer, M., Ovadia, M., Shahar, D., Feigel'Man, M. & Ioffe, L. Localization of preformed Cooper pairs in disordered superconductors. *Nature Physics* **7,** 239–244 (2011).

[192] Bouadim, K., Loh, Y. L., Randeria, M. & Trivedi, N. Single- and two-particle energy gaps across the disorder-driven superconductor-insulator transition. *Nature Physics* **7,** 884–889 (2011).

[193] Gomes, K. K., Pasupathy, A. N., Pushp, A., Ono, S., Ando, Y. & Yazdani, A. Visualizing pair formation on the atomic scale in the high-Tc superconductor Bi2Sr2CaCu2O8+$\delta$. *Nature* **447,** 569–572 (2007).

[194] Pasupathy, A. N., Pushp, A., Gomes, K. K., Parker, C. V., Wen, J., Xu, Z., Gu, G., Ono, S., Ando, Y. & Yazdani, A. Electronic origin of the inhomogeneous pairing interaction in the high-Tc superconductor Bi2Sr2CaCu 2O8+$\delta$. *Science* **320,** 196–201 (2008).

[195] Fulde, P. & Ferrell, R. A. Superconductivity in a strong spin-exchange field. *Physical Review* **135,** A550 (1964).

[196] Larkin, A. I. & Ovchinnikov, Y. N. Nonuniform state of superconductors. *Zh. Eksp. Teor. Fiz.* **47,** 1136 (1964).

[197] Matsuda, Y. & Shimahara, H. Fulde-Ferrell-Larkin-Ovchinnikov state in heavy fermion superconductors. *Journal of the Physical Society of Japan* **76** (2007).

[198] Chen, H. D., Vafek, O., Yazdani, A. & Zhang, S. C. Pair density wave in the pseudogap state of high temperature superconductors. *Physical Review Letters* **93,** 187002 (2004).

[199] Berg, E., Fradkin, E. & Kivelson, S. A. Charge-4e superconductivity from pair-density-wave order in certain high-temperature superconductors. *Nature Physics* **5,** 830–833 (2009).

[200] Lee, E. J. H., Jiang, X., Houzet, M., Aguado, R., Lieber, C. M. & De Franceschi, S. Spin-resolved Andreev levels and parity crossings in hybrid superconductor-semiconductor nanostructures. *Nature Nanotechnology* **9,** 79–84 (2014).

[201] Flatté, M. E. & Byers, J. M. Local electronic structure of a single magnetic impurity in a superconductor. *Physical Review Letters* **78,** 3761–3764 (1997).

[202] Flatté, M. E. & Byers, J. M. Local electronic structure of defects in superconductors. *Physical Review B - Condensed Matter and Materials Physics* **56,** 11213–11231 (1997).

[203] Balatsky, A. V., Šmakov, J. & Martin, I. Josephson scanning tunneling microscopy. *Physical Review B - Condensed Matter and Materials Physics* **64,** 212506 (2001).

[204] Rodrigo, J. G. & Vieira, S. *STM study of multiband superconductivity in NbSe2 using a superconducting tip* in *Physica C: Superconductivity and its Applications* **404** (North-Holland, 2004), 306–310.

[205] Rodrigo, J. G., Suderow, H. & Vieira, S. On the use of STM superconducting tips at very low temperatures. *Eur. Phys. J. B* **40,** 483–488 (2004).

[206] Levy, N., Zhang, T., Ha, J., Sharifi, F., Talin, A. A., Kuk, Y. & Stroscio, J. A. Experimental evidence for s-wave pairing symmetry in superconducting CuxBi2Se3 single crystals using a scanning tunneling microscope. *Physical Review Letters* **110,** 117001 (2013).

[207] Proslier, T., Kohen, A., Noat, Y., Cren, T., Roditchev, D. & Sacks, W. Probing the superconducting condensate on a nanometer scale. *Europhysics Letters* **73,** 962–968 (2006).

[208] Bergeal, N., Noat, Y., Cren, T., Proslier, T., Dubost, V., Debontridder, F., Zimmers, A., Roditchev, D., Sacks, W. & Marcus, J. Mapping the superconducting condensate surrounding a vortex in superconducting V3Si using a superconducting MgB2 tip in a scanning tunneling microscope. *Physical Review B - Condensed Matter and Materials Physics* **78,** 140507 (2008).

[209] Kimura, H., Barber, R. P., Ono, S., Ando, Y. & Dynes, R. C. Josephson scanning tunneling microscopy: A local and direct probe of the superconducting order parameter. *Physical Review B - Condensed Matter and Materials Physics* **80** (2009).

[210] Hamidian, M. H., Edkins, S. D., Joo, S. H., Kostin, A., Eisaki, H., Uchida, S., Lawler, M. J., Kim, E. A., Mackenzie, A. P., Fujita, K., Lee, J. & Davis, J. C. Detection of a Cooper-pair density wave in Bi2Sr2CaCu2O8+x. *Nature* **532,** 343–347 (2016).

[211] Wiesendanger, R. Spin mapping at the nanoscale and atomic scale. *Reviews of Modern Physics* **81,** 1495–1550 (2009).

[212] Heinrich, B. W., Iacovita, C., Rastei, M. V., Limot, L., Ignatiev, P. A., Stepanyuk, V. S. & Bucher, J. P. A spin-selective approach for surface states at Co nanoislands. *The European Physical Journal B* **75,** 49–56 (2010).

[213] Shvets, I. V., Wiesendanger, R., Bürgler, D., Tarrach, G., Güntherodt, H. J. & Coey, J. M. Progress towards spin-polarized scanning tunneling microscopy. *Journal of Applied Physics* (1992).

[214] Maris, G., Jdira, L., Hermsen, J. G., Murphy, S., Manai, G., Shvets, I. V. & Speller, S. Towards spin-polarized scanning tunneling microscopy on magnetite (110). *Japanese Journal of Applied Physics, Part 1: Regular Papers and Short Notes and Review Papers* (2006).

[215] Murphy, S., Ceballos, S. F., Mariotto, G., Berdunov, N., Jordan, K., Shvets, I. V. & Mukovskii, Y. M. Atomic scale spin-dependent STM on magnetite using antiferromagnetic STM tips. *Microscopy Research and Technique* (2005).

[216] Forrester, P. R., Bilgeri, T., Patthey, F., Brune, H. & Natterer, F. D. Antiferromagnetic MnNi tips for spin-polarized scanning probe microscopy. *Review of Scientific Instruments* **89,** 123706 (2018).

[217] Willke, P., Singha, A., Zhang, X., Esat, T., Lutz, C. P., Heinrich, A. J. & Choi, T. Tuning Single-Atom Electron Spin Resonance in a Vector Magnetic Field. *Nano Letters* **19,** 8201–8206 (2019).

[218] Rokhinson, L. P., Liu, X. & Furdyna, J. K. The fractional a.c. Josephson effect in a semiconductor–superconductor nanowire as a signature of Majorana particles. *Nature Physics* **8,** 795–799 (2012).

[219] Williams, J. R. & Goldhaber-Gordon, D. Doubling down on Majorana. *Nature Physics* (2012).

[220] Choi, S.-J., Calzona, A. & Trauzettel, B. Majorana-induced DC Shapiro steps in topological Josephson junctions. *Physical Review B* **102,** 140501 (2020).

[221] Jäck, B., Eltschka, M., Assig, M., Etzkorn, M., Ast, C. R. & Kern, K. Critical Josephson current in the dynamical Coulomb blockade regime. *Physical Review B* (2016).

[222] Law, K. T., Lee, P. A. & Ng, T. K. Majorana Fermion Induced Resonant Andreev Reflection. *Phys. Rev. Lett.* **103,** 237001 (2009).

[223] Flensberg, K. Tunneling characteristics of a chain of Majorana bound states. *Phys. Rev. B* **82,** 180516 (2010).

[224] Pawlak, R., Kisiel, M., Klinovaja, J. A., Meier, T., Kawai, S., Glatzel, T., Loss, D. & Meyer, E. Probing atomic structure and majorana wavefunctions in mono-atomic fe chains on superconducting Pb surface. *npj Quantum Inf.* **2,** 16035 (2016).

[225] Feldman, B. E., Randeria, M. T., Li, J., Jeon, S., Xie, Y., Wang, Z., Drozdov, I. K., Andrei Bernevig, B. & Yazdani, A. High-resolution studies of the Majorana atomic chain platform. *Nat. Phys.* **13,** 286–291 (2017).

[226] Jeon, S., Xie, Y., Li, J., Wang, Z., Bernevig, B. A. & Yazdani, A. Distinguishing a Majorana zero mode using spin-resolved measurements. *Science* **358,** 772–776 (2017).

[227] Kim, H., Palacio-Morales, A., Posske, T., Rózsa, L., Palotás, K., Szunyogh, L., Thorwart, M. & Wiesendanger, R. Toward tailoring Majorana bound states in artificially constructed magnetic atom chains on elemental superconductors. *Science Advances* **4,** eaar5251 (2018).

# Acknowledgement

As so often in life, nothing is possible without the help of dear colleagues and friends, especially during a PhD. I am very grateful to all people for their support during this time and would like to take the opportunity to express my appreciation.

First and foremost, my thanks go to *Prof. Katharina Franke*. Not only for giving me the opportunity to do my PhD but especially for being an extraordinary good doctoral mother. Just as every student could wish for. Back then, the good atmosphere and empathy in your research group motivated me to apply for a master's thesis and this decision was never disappointed. I would make the same choice again at any time. You contribute enormously to the group's atmosphere through your way of leadership, you take time for everyone and you are willing to give input when needed. Without you, this thesis would not have been possible for me to accomplish.

I would also like to thank my second supervisor *Prof. Robert Bittl*. I appreciate your truly sincere interest in my work over the years and your help in overcoming all sorts of minor drawbacks regarding HF frequencies. I also thank your entire research group, who were always willing to share their valuable HF knowledge with me and who helped me out in an uncomplicated way when I needed components to test an idea of mine. Here *Dr. Christian Teutloff* is especially mentioned.

I am especially grateful to *Prof. Felix von Oppen* for the great support of the photon-assisted tunneling project from a theoretical point of view, together with your PhD students *Sergio Acero González* and *Larissa Melischek*. – It was a very rewarding collaboration where many enlightening discussions with you gave me completely new perspectives on our experiments.

I want to thank *Prof. Clemens Winkelmann* of the Université Grenoble Alpes for his ideas and support for both, the HF experiments and the Josephson spectroscopy. Especially your expertise on the Josephson effect and the experimental input during your visits as well as the provision of equipment were essential for this work.

Much of the experimental work takes place in the laboratory and therefore a special thanks to my lab colleagues with whom I conducted the experiments and worked and screwed on Kili[1]. I would like to thank *Nils Bogdanoff*, whom I supervised as a master student, which was a great joy and led to very fruitful results. I was very happy to be able to profit from your incredible wealth of knowledge. I am also grateful to *Gaël Reecht*

[1]Short for Kilimanjaro: Name of the STM we established

for his support of the experiments and the many hours we spent together working on improvements to the machine. The same is true for *Rika Simon*, who accompanied the project during her master thesis with a lot of passion. And when it comes to the laboratory work, a big thank you to *Dr. Christian Lotze* cannot be missing. In our group, you are and always will be the master craftsman and the person to call in case of an emergency, whether it's technical support in the lab or IT questions. You are so important for the group and I think it is admirable how you always manage to help everyone. And finally, I'm glad to know that my machine is in good hands and wish my successor *Martina Trahms* much success – I believe in you and I'm sure you'll rock the Josephson spectroscopy.

Working is essential, but not everything, and as I have already mentioned, I paid a lot of attention to the group's climate when I was looking for a master's thesis. Therefore I am grateful to all current and former members of the AG-Franke for the wonderful time we spend together. First of all *Nils Krane*, my long-time office colleague – I enjoyed charing an office with you very much, we had a lot of fun[2], and I am grateful for all the valuable input even if our research interests were diametrically opposed. A big thank you also goes to the former members *Dr. Benjamin Heinrich*, *Michael Kleinert (Ruby)* and *Nino Hatter*, who welcomed me into the group and introduced me to STM. Many thanks to *Daniela Rolf*, who was one of the good souls of the group for a long time and who accompanied me throughout my studies. You have always been a driving force for the group' s solidarity and an important initiator of coffee and volleyball clubs, which were an important place of exchange even for non-coffee drinkers. I also want to thank *Eva Liebhaber*, who with her warm spirit has taken on this linking role in the group. I really enjoyed your infectious good mood during the time we spent together in an office, even though it was way too short due to Corona. A special thanks of course to *Eva Liebhaber*, *Martina Trahms*, *Sergey Trishin* and *Nils Bogdanoff* for proofreading. Finally, I would also like to thank all the other current and former members of the AG-Franke: *Gelavizh Ahmadi*, *Laëtitia Farinacci*, *Jennifer Hartfiel*, *Lisa Rütten*, *Paul Stoll*, *Idan Tamir*, and *Asieh Yousofnejad*.

Finally, I would like to express my gratitude to the most important people in my life, my family and my friends. My mother *Hildegard* for her unconditional support throughout my life. You are wonderful. The same goes for my second family with my best and longtime friend *Till* and his parents *Viola* and *Raimund*. A big thank you also goes to all my great friends who have supported me on this long journey and especially in the past weeks, especially to *Philip* for proofreading. You enrich my life incredibly, as do all my dear fellow musicians. And finally, I would like to express my deepest gratitude to my partner *Anneke*. I am so grateful for all your support and understanding during this time. Your emotional support has been invaluable and I am so grateful to have you by my side and so excited about the coming time with you.

[2]The influence of loud music was fortunately mutual and the advancement of Noise Canceling was a great blessing for both of us ;-)

# Curriculum Vitae

*For reasons of data protection, the curriculum vitae will not published in the electronic version.*

## List of Publications


- Peters, O., Bogdanoff, N., Acero González, S., Melischek, L., Simon, J. R., Reecht, G., Winkelmann, C. B., von Oppen, F. & Franke, K. J. Resonant Andreev reflections probed by photon-assisted tunnelling at the atomic scale. *Nature Physics* (2020)
- González, S. A., Melischek, L., Peters, O., Flensberg, K., Franke, K. J. & von Oppen, F. Photon-assisted resonant Andreev reflections: Yu-Shiba-Rusinov and Majorana states. *Physical Review B* **102,** 045413 (2020)
- Farinacci, L., Ahmadi, G., Reecht, G., Ruby, M., Bogdanoff, N., Peters, O., Heinrich, B. W., von Oppen, F. & Franke, K. J. Tuning the Coupling of an Individual Magnetic Impurity to a Superconductor: Quantum Phase Transition and Transport. *Physical Review Letters* **121,** 196803 (2018)

# Conference Contributions

## 2015

- DPG Spring Meeting of the Condensed Matter Section, Berlin, Germany, 2015-Mar
  (Poster) *Tuning the Magnetic Anisotropy and the Coupling to the Surface in Fe-Octaethylporphyrin-Cl Complexes on Au(111)*
- SPICE Workshop: Magnetic Adatoms as Building Blocks for Quantum Magnetism, Mainz, Germany, 2015-Aug
  (Poster) *Tuning the Kondo coupling strength of a single molecule*
- 598$^{th}$ WE-Heraeus-Seminar: Magnetic Adatoms as Building Blocks for Quantum Magnetism, Bad Honnef, Germany, 2015-Nov
  (Poster) *Tuning the Kondo coupling strength of a single molecule*

## 2016

- DPG Spring Meeting of the Condensed Matter Section, Regensburg, Germany, 2016-Mar
  (Oral contribution) *Tuning the Kondo coupling strength of a single molecule*
- DIPC Workshop: Spins on Surfaces, Donostia International Physics Centre, San Sebastián, Spain, 2016-Sep
  (Oral contribution) *Weak vs. strong coupling Kondo*

## 2018

- DPG Spring Meeting of the Condensed Matter Section, Berlin, Germany, 2018-Mar
  (Oral contribution) *Influence of microwave radiation on an STM Josephson junction*
- International Focus Workshop: New Platforms for Topological Superconductivity with Magnetic Atoms, Max Planck Institute for the Physics of Complex Systems, Dresden, Germany, 2018-Mar
  (Poster) *Influence of microwave radiation on an STM Josephson junction*

# Selbständigkeitserklärung

Ich erkläre gegenüber der Freien Universität Berlin, dass ich die vorliegende Dissertation selbstständig und ohne Benutzung anderer als der angegebenen Quellen und Hilfsmittel angefertigt habe. Die vorliegende Arbeit ist frei von Plagiaten. Alle Ausführungen, die wörtlich oder inhaltlich aus anderen Schriften entnommen sind, habe ich als solche kenntlich gemacht. Diese Dissertation wurde in gleicher oder ähnlicher Form noch in keinem früheren Promotionsverfahren eingereicht.

Mit einer Prüfung meiner Arbeit durch ein Plagiatsprüfungsprogramm erkläre ich mich einverstanden.

Berlin, den 26. Oktober 2020